Studies of Radiation Levels in the Large Hadron Collider and of Radiation Damage to Silicon Detectors

Grant William Gorfine

School of Physics
The University of Melbourne
Parkville Victoria 3052

Australia

September 1994

Thesis submitted for the degree of
Doctor of Philosophy

Abstract

A study has been made of the degradation of silicon detectors expected at the proposed Large Hadron Collider (LHC) at CERN.

A review of radiation damage to silicon detectors is given. The increase in leakage current as a function of neutron fluence has been measured with two irradiations. In these experiments leakage currents were monitored in silicon detectors held under bias both during and after the irradiation. The reduction in leakage currents after the irradiation due to self annealing was measured for up to 80 days. This annealing was parameterized and damage coefficients were determined which were corrected for this self annealing.

The FLUKA Monte Carlo cascade code has been used to calculate the particle fluxes expected in the inner tracking region of the ATLAS detector (one of two general purpose detectors proposed for the LHC). Fluxes have been calculated in terms of the equivalent 1 MeV neutron flux. A number of detector configurations have been considered investigating the effects of moderating material. Two designs have been simulated; one with silicon layers and Transition Radiation Tracker (TRT) modules interspersed, the other with all silicon layers within the inner radius of a single TRT module.

Two experiments were carried out to test the validity of the FLUKA code. In the first experiment, neutron fluxes were measured using fission counters during regular operation involving $\overline{p}p$ collisions in the UA2 detector at CERN. These measurements were compared with calculations made with FLUKA. The second experiment used a calorimeter-like structure comprised of lead plates immersed in a tank of liquid argon. It was irradiated by 205 GeV/c hadrons and the production of ^{41}Ar by low energy neutrons was measured. The experiment was also simulated with FLUKA. The production rate of ^{41}Ar obtained from the simulation agreed with the measured quantity to within 20%. Other tests of the FLUKA code have been reviewed.

Projections have been made for a 10 year operating scenario at the LHC. A number of temperature and luminosity scenarios are considered. The degradation of the silicon in terms of leakage current and depletion voltage has been determined. This showed that it is feasible to operate silicon layers at radii greater than 40 cm for 10 years at the LHC.

I declare that the length of this thesis does not exceed 100,000 words.

Acknowledgements

I would like to thank my supervisor, Dr. Geoffrey Taylor, and also Dr. Stuart Tovey for their help and advice.

I thank the members of the Experimental Particle Physics group at the University of Melbourne for their friendship and assistance.

I thank Burkhard Schmidt with whom I worked installing and calibrating the fission counters used in UA2. I also thank the members of the UA2 collaboration for their assistance.

I would like to thank the many who helped with the BEDLAM experiment. I thank Dr. Graham Stevenson whose guidance was invaluable. I also thank him for his help with assaying the aluminium disks. I would like to acknowledge the assistance of the following people: Dr. Alberto Fassò for assaying the gold, indium and copper foils; Martin Hooper for assaying the aluminium disks; Alain Bonifas for his general help and for the argon activity calibration; Guy Roubaud for his help with the calibration; Gilbert Bertuol for his general help; Murray Ross for his useful advice and help; Robin Dillon for handling the liquid argon; and Rasmus Raffnsøe for beam monitoring. I would also like to thank Dr. Graham Robinson and Dr. Brian McGregor for their useful suggestions.

I thank Dr. Alfredo Ferrari for his helpful discussions and advice regarding FLUKA. I am also grateful to Dr. Jan Zazula for his quick response to my frequent questions regarding FLUKA.

The financial assistance from CRA Ltd. and the Australian Research Council, which enabled me to spend a substantial time at CERN, is gratefully acknowledged.

Finally, I thank very much the support from my family and friends. In particular I thank my parents and Melissa Black.

Contents

List of Figures

List of Tables

Chapter 1

Introduction

The Large Hadron Collider (LHC) proposed to be built at CERN will provide the opportunity to study many exciting topics in particle physics and hopefully some unexpected physics will be discovered. To provide such potential, protons circling in opposite directions in a 27 km circumference ring will collide with an interaction rate of about 10^9 per second and with a centre of mass energy of 15.4 TeV. The consequence, however, is a high radiation environment; about 3 orders of magnitude greater than in existing colliders. The survivability of detector components in such an environment is a major issue.

One of two general purpose detectors to be built at the LHC is ATLAS. A description of the LHC and the ATLAS detector is given in Chapter 2. Radiation levels up to an equivalent 1 MeV neutron flux of 10^{14} n/cm^2 per year are expected in the inner detector regions of ATLAS. Silicon detectors provide high resolution and fast response and it is planned that they will be used as an integral part of the tracking system for ATLAS. The survivability of silicon detectors in ATLAS is a key question studied in this thesis.

Radiation damage to silicon detectors results in an increase of the leakage current, a change in the effective impurity concentration which leads to an increased voltage required for full depletion, and a degradation of the charge collection efficiency. In order to understand the damage to silicon resulting from high radiation levels, silicon detectors have been irradiated to known fluxes of neutrons. The analysis of two neutron irradiations is given in Chapter 3. In these experiments the silicon detectors were reverse biased and leakage currents were measured at frequent intervals

both during and after irradiation.

In order to predict the extent of the damage it is necessary to have an accurate estimate of the radiation levels expected in ATLAS. The Monte Carlo computer code FLUKA has been used to determine this. The source of particles making up the particle fluxes in the inner detector can be roughly divided into two categories. The first is the particles coming directly from the proton-proton collisions. The second is the particles resulting from showers in the calorimeters which make their way into the inner detector region. The majority of the particles in the second category are neutrons, referred to as "albedo" neutrons. FLUKA is capable of simulating the transport of neutrons down to low energies and so is able to calculate the fluxes of these "albedo" neutrons.

In order to have confidence in FLUKA predictions, tests of FLUKA have been performed. These are described in Chapter 4. To test FLUKA in a realistic detector environment neutron measuring devices were placed in the UA2 detector at CERN. The results were then compared to FLUKA. Despite uncertainties making the comparisons inconclusive the results are of interest.

Liquid argon calorimeters are being developed for ATLAS. When exposed to low energy neutrons (from thermal up to about 1 MeV) ^{41}Ar is produced which decays via beta and gamma emission with a half-life of 1.8 hours. FLUKA is capable of simulating neutrons down to thermal energies and has been used to calculate the expected activity of ^{41}Ar in ATLAS [1]. In order to have confidence in these predictions an experiment was carried out where, to emulate a lead/liquid argon calorimeter, a lead plate structure was immersed in a container of liquid argon. Once in place it was irradiated by a 205 GeV/c hadron beam. After the irradiation, measurements were made of the production rate of ^{41}Ar. A number of activation detectors, that were placed throughout the calorimeter-like structure, were also assayed. Measured data was then compared with FLUKA calculations. The experiment and FLUKA calculations are described in Chapter 4.

Chapter 5 describes a calculation of neutron and other hadron fluxes expected

in the inner tracking detectors of ATLAS. The equivalent 1 MeV neutron flux that would produce the same damage in silicon has been calculated. A number of different detector configurations have been studied.

In Chapter 6 predictions are made of the degradation of silicon detectors operating at the LHC. These are based on the fluxes calculated in Chapter 5 along with information obtained from the neutron irradiations given in Chapter 3 and from radiation damage studies made by other groups. Predictions are made of the leakage current and depletion voltage increases expected in possible 10 year operating scenarios. In this way, the viability of using silicon detectors in the high radiation environment expected at the LHC is ascertained.

Chapter 2

The LHC and the ATLAS Detector

2.1 The Large Hadron Collider

The Large Hadron Collider (LHC) is proposed to be built at CERN[1]. The accelerator will collide protons circling in opposite directions in two 27 km circumference rings. This will be built within the tunnel of the current LEP (Large Electron Positron) collider. Figure 2.1 shows a schematic of the layout of accelerators at CERN including the Proton Synchrotron (PS) and Super Proton Synchrotron (SPS) which will be used as injectors for the LHC.

Superconducting magnets will be used to obtain the magnetic fields of 10 Tesla required to maintain the 7.7 TeV protons in orbit. The magnet system uses a novel design where the two beam pipes (for the counter circling protons) are incorporated into the same mechanical structure and cryostat.

Protons will be grouped into bunches with bunches crossing every 25 ns. The luminosity $\mathcal{L}$ is a measure of the intensity of the beams and is given by

$$\mathcal{L} = \frac{N^2 f k}{4\pi\sigma_R^2} \tag{2.1}$$

where N is the number of protons in each bunch, k is the number of bunches, f is the revolution frequency, and σ_R is the RMS radius of the beam at the interaction point.

The maximum design luminosity is 1.7×10^{34} cm^{-2}s^{-1}. It is likely that the machine will run at a lower luminosity for the first few years, gradually building up

[1]CERN is the European Laboratory for Particle Physics which is located near Geneva, Switzerland.

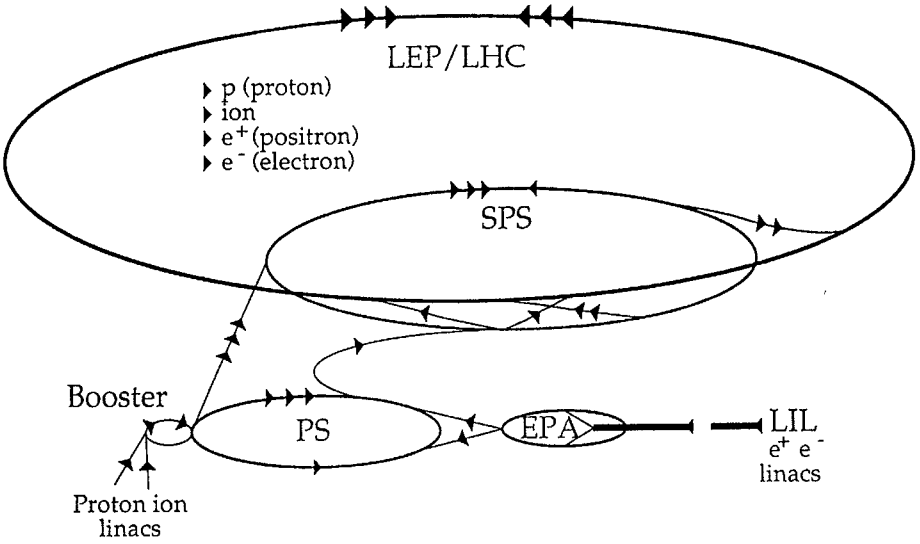

Figure 2.1: CERN accelerator complex.

to the maximum luminosity.

The number of proton-proton inelastic interactions per unit time is given by

$$R = \mathcal{L}\,\sigma_{inel} \tag{2.2}$$

where σ_{inel} is the inelastic cross section. Assuming $\sigma_{inel} = 60$ mb[†], then at a luminosity of 10^{34} cm^{-2}s^{-1} one expects about 15 interactions per bunch crossing.

2.2 The ATLAS Detector

There will be detectors at three interaction points. One of the detectors proposed is ATLAS (A Toroidal LHC ApparatuS). The other two detectors are CMS which will be a general purpose detector, and ALICE which will be a heavy ion experiment.

[†]Recent results indicate that $\sigma_{inel} \simeq 71$ mb [55, 56]

2.2.1 Physics Goals

The ATLAS detector is being designed to be a general purpose detector capable of studying a wide range of physics topics with the potential for discovering new physics.

The primary physics goal is to search for the Standard Model Higgs boson. The Higgs mechanism allows the electroweak symmetry to be broken and allows particles to have mass. The mass of the Higgs boson, which is unspecified by the theory, is expected to be in the range 50 GeV $\lesssim m_{\mathrm{H}} \lesssim$ 1 TeV. Some of the best experimental signatures for observing the Higgs are expected to be:

$$\begin{aligned} &\mathrm{H} \rightarrow \gamma + \gamma && \text{if } m_{\mathrm{H}} < 150 \text{ GeV}/c^2 \\ &\mathrm{H} \rightarrow \mathrm{Z} + \mathrm{Z}^* \rightarrow 4 \text{ leptons} && \text{if } 120 < m_{\mathrm{H}} < 180 \text{ GeV}/c^2 \\ &\mathrm{H} \rightarrow \mathrm{Z} + \mathrm{Z} \rightarrow 4 \text{ leptons} && \text{if } m_{\mathrm{H}} > 180 \text{ GeV}/c^2 \end{aligned}$$

where Z* is a virtual Z boson. Other physics topics that will be investigated include:

- Supersymmetry: an extension of the Standard Model where every particle has a supersymmetric partner. Many of the supersymmetric particles are expected to have masses in the discovery range of the LHC.
- Compositeness: to study if quarks and leptons have substructure.
- Top quark physics. Although confirmation of the top quark is likely to come before the LHC is built, the LHC will allow precise measurement of its mass and extensive studies of top quark decays. At a luminosity of 10^{32} cm^{-2}s^{-1} of the order of 10^6 $t\bar{t}$ pairs are expected to be produced each year.
- B meson physics: Around 10^{11} $b\bar{b}$ pairs are expected to be produced per year at a luminosity of 10^{32} cm^{-2}s^{-1}.

The latter two areas, for which a large number of events occur even at a luminosity of 10^{32} cm^{-2}s^{-1}, can be investigated during the initial low luminosity running.

The design requirements and optimization of the detector have been studied by the ATLAS collaboration by investigating the capability of the detector to study topics such as those listed above.

2.2.2 The Detector

A diagram of the ATLAS detector is shown in figure 2.2. There are three major components: the inner tracking region containing both continuous and discrete tracking; the calorimeter providing energy and position measurement; and muon chambers which will be in a toroidal magnetic field generated using an air core superconducting toroidal magnet. The inner region and calorimeter will be described in more detail below.

The Inner Detector

The inner tracker is essential for the identification and reconstruction of electrons. Also, information is provided for triggering by matching tracks in the inner detector with a cluster in the calorimeter. One of the initial designs for the inner detector was the "Cosener's House" design [2] as shown in figure 2.3.

Silicon detectors are used extensively in high energy physics as they provide high spatial resolution and fast response. A description of how they operate is given in Section 3.2. In the Cosener's House design, silicon tracking layers are located at several radii. A summary of these layers is given in table 2.1. The layers designated ϕ and z provide an accurate measure of the azimuthal and longitudinal positions respectively. A few layers use double sided silicon with accurate ϕ and z measurements on each side respectively. The layers close to the beam pipe provide the high precision vertex measurements required for physics that can be done in the initial low luminosity running. These layers will be exposed to extreme radiation levels and are likely to be removed after a few years of operation.

Radiation hard detectors (most likely GaAs) in the form of wheels are located at $z = 58.5$, 70, 96, and 109 cm.

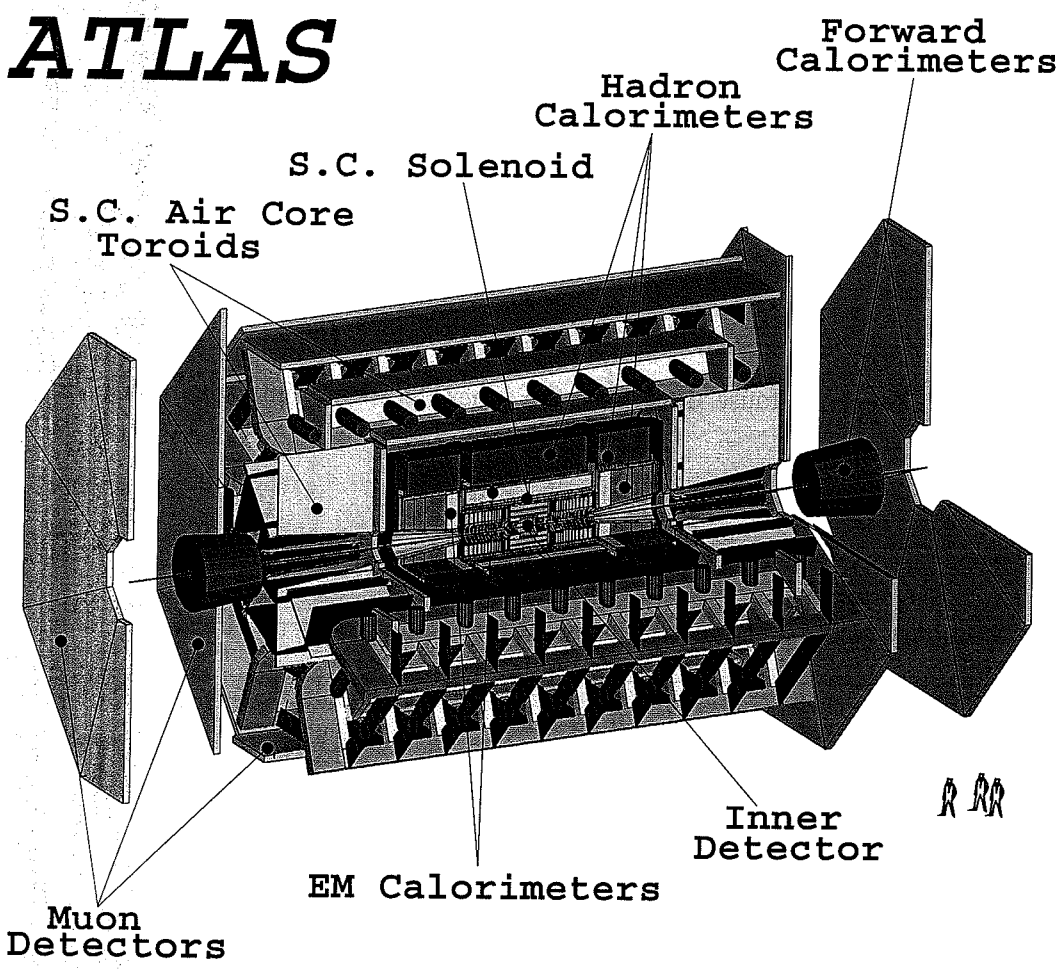

Figure 2.2: The ATLAS detector.

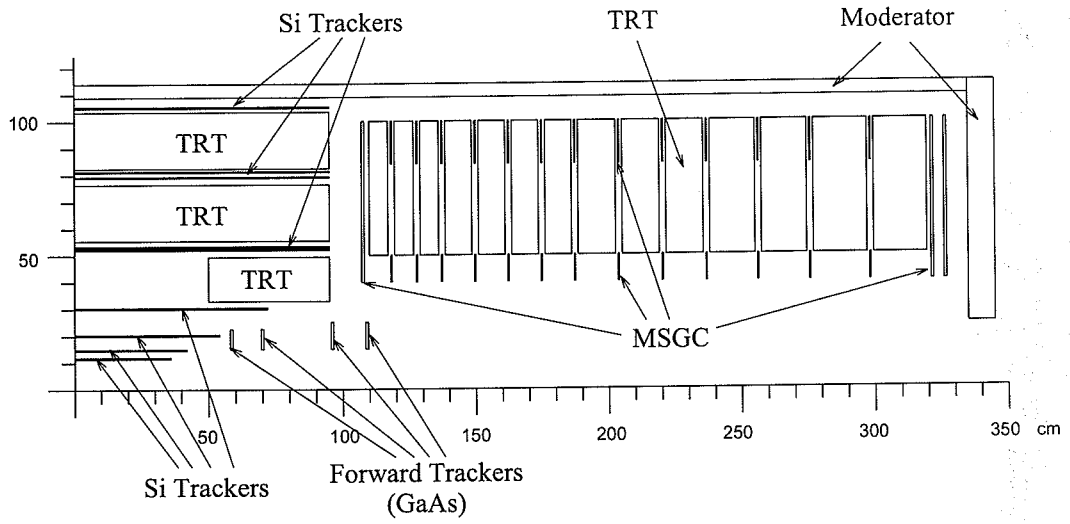

Figure 2.3: The Cosener's House design for the inner detector. Only one quarter segment is shown.

Table 2.1: Summary of the geometry of silicon layers in the Cosener's House design.

Layer	Radius (cm)	Length (cm)	Type	Pad Size[a]	Thickness (μm)	Sensitive Vol. (cm^3)
1	11.5	72	pixel	$50\mu m \times 200\mu m$	150	1.50×10^{-6}
2	14.5	84	pixel	$50\mu m \times 200\mu m$	150	1.50×10^{-6}
3	20	108	2-sided	$2 \times 6cm \times 25\mu m$	300	9.00×10^{-4}
4	30	144	2-sided	$2 \times 6cm \times 25\mu m$	300	9.00×10^{-4}
5	52	190	ϕ	$2 \times 6cm \times 195\mu m$	300	7.02×10^{-3}
6	53	190	z-pad	$23mm^2$	300	6.90×10^{-3}
7	79	190	ϕ	$2 \times 6cm \times 195\mu m$	300	7.02×10^{-3}
8	81	190	z-pad	$23mm^2$	300	6.90×10^{-3}
9	105	190	ϕ	$2 \times 6cm \times 195\mu m$	300	7.02×10^{-3}

[a] The factor 2 in the pad size for some layers indicates that the pads from two adjacent detectors are connected.

A number of transition radiation tracker (TRT) modules are located in both the barrel and end-cap regions of the inner detector as shown in figure 2.3. The TRT in the barrel region contains straws embedded in a polyethylene foam. The end-cap TRT will possibly consist of polypropylene foils and straws. Microstrip gas counters (MSGC) are located throughout the end-cap TRT.

Neutron fluxes can be reduced by the introduction of hydrogenous material. To achieve this a layer of 5–10 cm thick polyethylene moderator may be placed on the inside of the calorimeter vessel.

The inner detector region will be in a 2 Tesla solenoidal magnetic field. The solenoid will be incorporated into the cryostat of the electromagnetic calorimeter.

Other designs for the inner detector are being considered. One such variation consists of a single TRT unit in the barrel region with all the silicon layers within the inner radius of the TRT. Such a design is shown in figure 2.4.

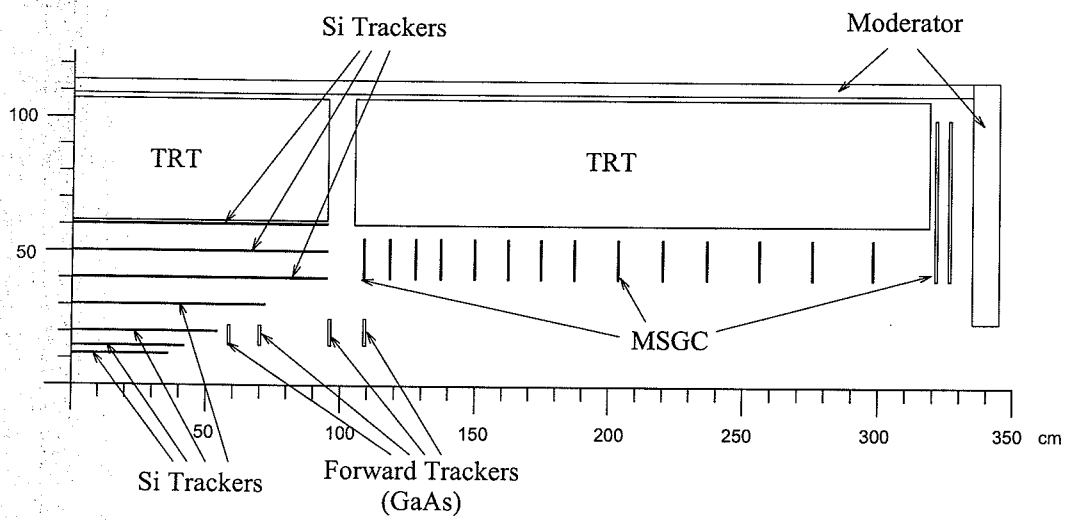

Figure 2.4: An inner detector design with a single TRT in the barrel region.

The Calorimeter

The calorimeter design is shown in figure 2.5. The electromagnetic calorimeter, in both the barrel region and the end-caps, is made up of lead/liquid argon. The

hadronic calorimeters are made up of iron/scintillator, except for the end-cap plug which contains iron/liquid argon. The calorimeter modules containing liquid argon (which has a boiling point of 87 K) are within a cryostat. The electromagnetic calorimeter uses a novel accordion design as depicted in figure 2.6. The calorimeters in the end plug region use a similar design.

To increase the coverage of the detector, forward calorimeters are located close to the beam pipe about 15 m from the interaction point. (See figure 2.2.)

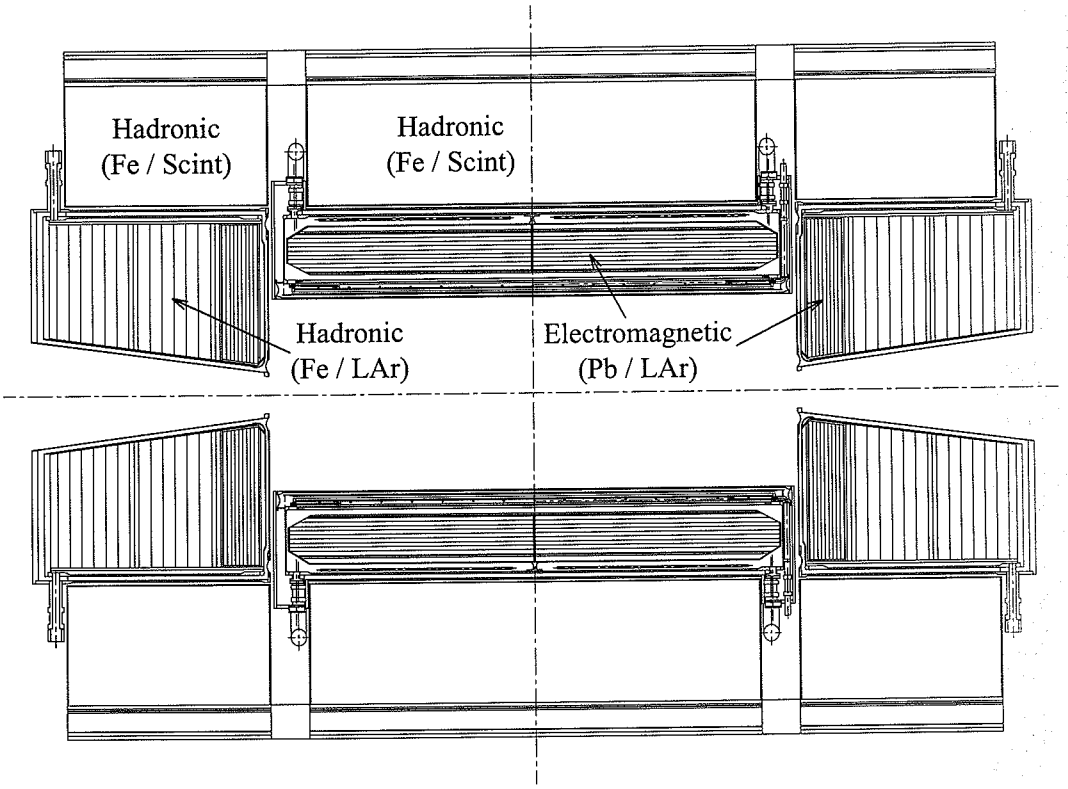

Figure 2.5: The ATLAS calorimeter.

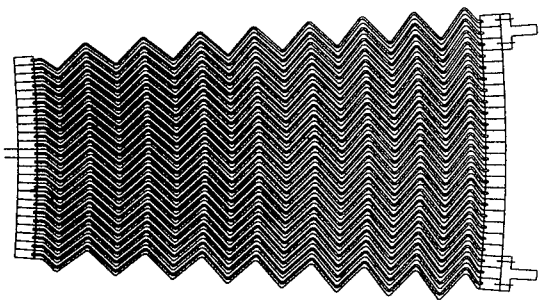

Figure 2.6: A prototype module of the accordion electromagnetic calorimeter.

Chapter 3

Radiation Damage to Silicon Detectors

3.1 Introduction

Silicon detectors, as planned to be used for tracking in ATLAS, will be exposed to high radiation levels. This chapter gives an overview of how silicon is damaged by high energy particles and what effect this damage has on the performance of silicon detectors. Two experiments involving the neutron irradiation of silicon detectors are described. These experiments give valuable information about the increase in leakage current produced as a result of the irradiation. Other aspects of radiation damage studies are also reviewed.

3.2 Silicon Detectors in High Energy Physics

A silicon detector is essentially a p-n diode operated under reverse bias. The cross section of a detector is shown in figure 3.1. The bulk of the silicon, in this case, is n-type. (P-type silicon can also be used.) A highly doped p^+ layer forms the p-n junction. A n^+ layer on the reverse side aids in making ohmic contact. The p^+ layer is often segmented. The region under each segment acts as a separate detector allowing for high position resolution.

A reverse bias voltage is applied which produces a region depleted of mobile charge carries. This depletion region constitutes the sensitive volume of the detector and grows as the voltage is increased. A large enough bias voltage is applied so that the depletion region extends the full volume of the detector. That is, the detectors are operated at full depletion. When a charged particle passes through the detector a

number of electron-hole pairs are created. (The average energy required to create an electron-hole pair in silicon is 3.6 eV.) For a minimum ionizing particle (mip) passing through 300 μm of silicon, about 23,000 electron-hole pairs are created. The electrons and holes are swept out by the electric field. A charge pulse results which is converted to a voltage pulse using a charge sensitive preamplifier.

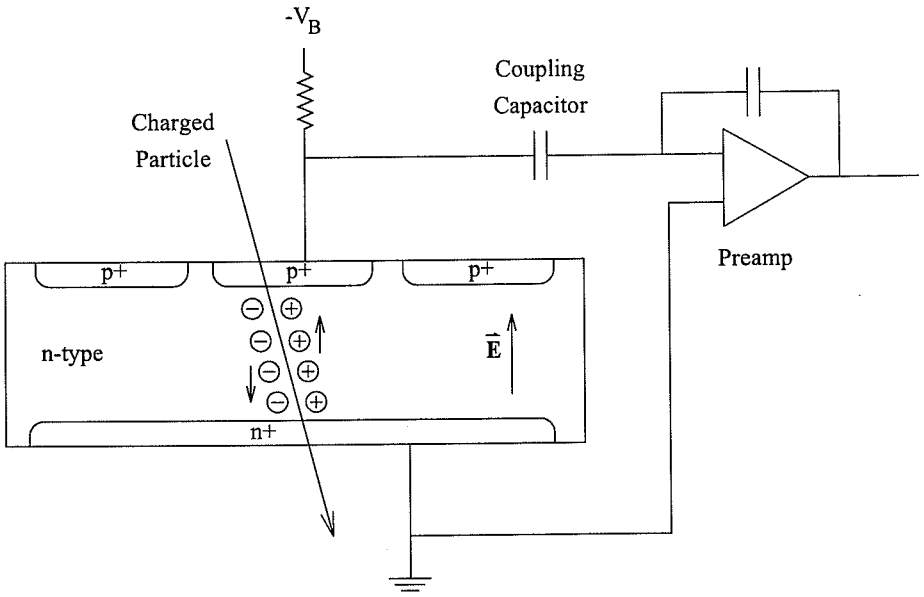

Figure 3.1: Schematic of a silicon detector.

3.3 Displacement Damage in Silicon.

Radiation damage can be roughly divided into two types: ionizing energy loss which mainly produces surface damage effects such as charge trapping in the oxide layer and non-ionizing energy loss which results in displacement damage in the bulk of the silicon. The latter of these has the greatest effect on the performance of silicon as a detector. [3]

The following discussion will concentrate on neutron damage, but as discussed in Section 3.4 below, the damage by other particles can be described by an equivalent

neutron flux.

Some of the neutrons that pass through the silicon will have a collision with one of the silicon atoms. This silicon atom recoils and is referred to as the primary knock on atom (PKA). The PKA loses energy rapidly, striking a number of silicon atoms along its way and producing a number of point defects. This continues until its energy drops below the displacement threshold ($\sim$ 15 eV). Some of the silicon atoms knocked out by the PKA will displace other silicon atoms and a few "terminal clusters" are formed with a high density of defects. Typically the PKA track is less than 100 nm long and 1–3 terminal clusters are formed [4]. The defects consist of interstitial atoms and lattice vacancies. A large number of these are within a few atomic spacings of each other and immediately recombine removing around 95% of the damage. A number of "stable" defects are formed such as vacancy-phosphor ("E centres"), vacancy-oxygen ("A centres") and divacancies. Due to the thermal motion of the silicon atoms some of this damage is removed by the recombination of interstitials and vacancies. Annealing at high temperatures is a common method for removing damage. This annealing can also occur at room temperature and below (although at a much slower rate) and is referred to as self annealing. Section 3.6 discusses self annealing further.

3.4 Non-Ionizing Energy Loss by Different Particles

The displacement damage described above is to a good approximation proportional to the non-ionizing energy loss (NIEL) of the radiation [5]. The NIEL in silicon as a function of energy for protons, neutrons, pions, muons, electrons and photons is shown in figure 3.2. These are from the NIEL set calculated by Van Ginneken [5]. By using these curves it is possible to relate the damage by other particles and neutrons of different energies to neutrons of a specific energy. Normally this is given as the equivalent 1 MeV neutron flux.

As can be seen from the figure, the displacement damage produced by electrons and photons is at least an order of magnitude less than the damage produced by

hadrons. Because of this difference, hadron fluxes are the dominating component responsible for bulk damage to silicon detectors in ATLAS.

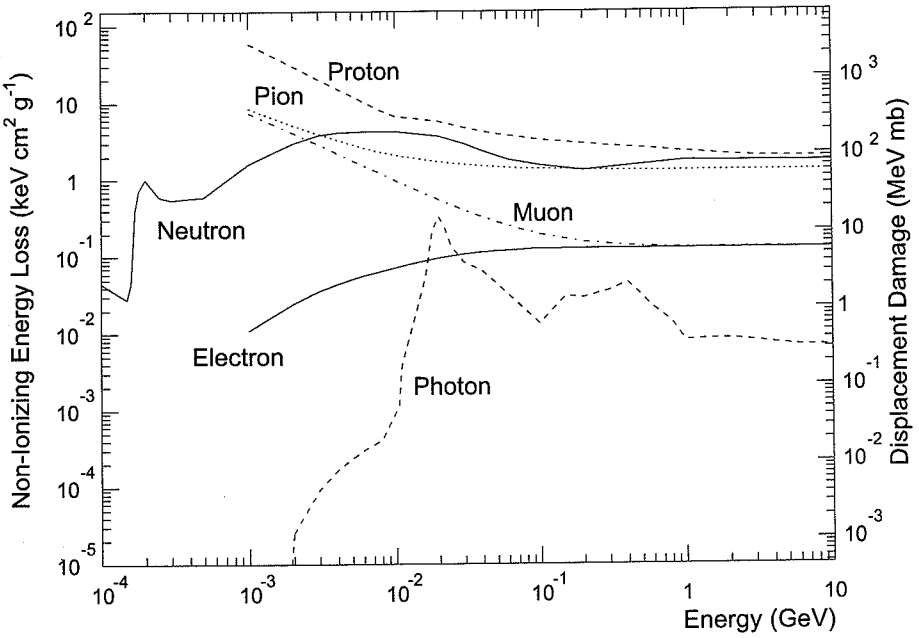

Figure 3.2: Non-ionizing energy loss in silicon. The right hand scale shows the corresponding displacement damage cross section. [5]

3.5 The Effect of Damage on Detector Characteristics

The "stable" defect complexes provide effective recombination/generation levels which results in an increase in the reverse bias current. This increase in current produces an increased shot noise across the diode junction, hence the signal to noise ratio is reduced.

The defects provide effective sites for charge trapping and electron-hole recombination. When an ionizing particle passes through the detector, the charge trapping causes some charge to be collected over a longer time than usual as charges are released slowly following thermal emissions from the traps. The defects also serve as

scattering sites which result in a reduced carrier mobility and hence an increase in the time needed to collect the charge. Since there is a limited time to collect the charge (of the order of the LHC "bunch crossing time") not all of the charge will be collected. Some charge will also be lost due to recombination. The above factors decrease the charge collection efficiency and hence degrade the signal to noise ratio.

The defects can produce effective donor or acceptor levels in the silicon crystal. This results in a change in the effective impurity concentration which in turn produces a change in the voltage required for full depletion.

3.5.1 Increase of the Reverse Leakage Current

Some of the defects give rise to energy levels in the forbidden band gap and are effective recombination/generation centres. These energy states act like stepping stones between the valence band and conduction band, allowing electrons and holes to be more easily thermally excited over this gap.

The reverse bias leakage current is made up of three components; the bulk or volume current, diffusion currents, and surface currents. In a radiation damaged detector the main contribution is generally from the volume current which is a result of recombination/generation in the bulk.

An increase in the displacement damage results in an increase in the volume current I_{Vol}. This contribution is given by

$$I_{Vol} = q\, G_v\, Vol \tag{3.1}$$

where G_v is the thermal generation rate per unit volume, Vol is the depleted volume, and q is the electron charge. If we assume that the recombination/generation centres are located in the middle of the forbidden gap then G_v is given by

$$G_v = \frac{n_i}{2\tau_p} \tag{3.2}$$

where n_i is the intrinsic charge carrier density and τ_p is the minority charge carrier

lifetime. (The minority charge carriers are holes in the case of n-type material.) The lifetime τ_p is inversely proportional to the density of the recombination/generation centres N_t, where N_t will be proportional to the density of defects. The increase in leakage current is therefore proportional to the number of defects in the depleted volume.

In the absence of annealing the number of defects and hence the leakage current are expected to increase linearly with particle fluence Φ. (The definitions of flux and fluence are given in Appendix A.) This linearity is expressed via a damage coefficient α defined as

$$\alpha = \frac{\Delta I}{\Phi \cdot Vol} \,. \tag{3.3}$$

The effects of self annealing on the leakage current are given in Section 3.6.

The shot noise due to the leakage current I is given by

$$\sigma_{\text{shot}}\,(\text{RMS electrons}) = \sqrt{\frac{I \cdot \tau_s \cdot A}{q}} \tag{3.4}$$

where q is the electron charge. The constant A is a dimensionless quantity which depends on the shaping used by the preamplifier and filter, and the shaping time τ_s is a characteristic time whose definition depends on the shaping. Typically A is about 2 and so equation (3.4) becomes

$$\sigma_{\text{shot}}\,(\text{RMS electrons}) = 112\sqrt{I(\mu\text{A}) \cdot \tau_s(ns)} \,. \tag{3.5}$$

For a shaping time of 25 ns and a leakage current of 5 μA the resulting noise is about 1250 electrons. The noise produced by the electronics proposed for the ATLAS experiment is about 1500 electrons. This gives a total noise (adding the contributions in quadrature) of about 2000 electrons. A minimum ionizing particle passing through 300 μm of silicon produces a most probable signal of about 23,000 electrons. The signal to noise ratio for a leakage current of 5 μA is therefore better than 11:1.

As well as an increase in the noise, the increase in the leakage current results in an increased power consumption. This is potentially a problem due to the heat

generated and will affect the amount of cooling required.

3.5.2 Change in the Effective Impurity Concentration

The depletion width is given by

$$W = \sqrt{\frac{2\epsilon_{\mathrm{Si}}(V + V_{bi})}{q|N_{eff}|}} \tag{3.6}$$

where ϵ_{Si} (equal to $11.9\,\epsilon_0$) is the permittivity in silicon, q is the electron charge, V is the applied bias voltage (positive for reverse bias), V_{bi} is the built in voltage, and $|N_{eff}| = |N_D - N_A|$ is the effective impurity concentration. Usually V is much larger than V_{bi} and the latter term is ignored. The quantities N_D and N_A are the donor and acceptor concentrations.

For a fully depleted detector, W equals the physical width of the detector d. Therefore the relationship between the voltage required for full depletion V_{dep} and the effective impurity concentration is given by

$$|N_{eff}| = \frac{2\epsilon_{\mathrm{Si}} V_{dep}}{qd^2}\,. \tag{3.7}$$

A model for the dependence of the effective impurity concentration with fluence as described in Ref. [6] is given by

$$N_{eff}(\Phi) = N_{eff,0} - N_0^*(1 - \exp(-c\Phi)) - b\Phi \tag{3.8}$$

where $N_{eff,0}$ is the initial concentration, N_0^* is the part of the donor concentration which is removed during irradiation, c is the donor removal constant, b is the production rate of acceptor like defects, and Φ is the 1 MeV neutron equivalent fluence. The second term corresponds to donor removal and is likely to be due to the formation of vacancy-phosphorus complexes. The last term is due to the creation of acceptor like defect centres. Acceptor removal is assumed not to contribute due to the fact that vacancy-boron complexes anneal out rapidly. Figure 3.3, taken from Ref. [6], shows

experimental data with a fit according to equation (3.8).

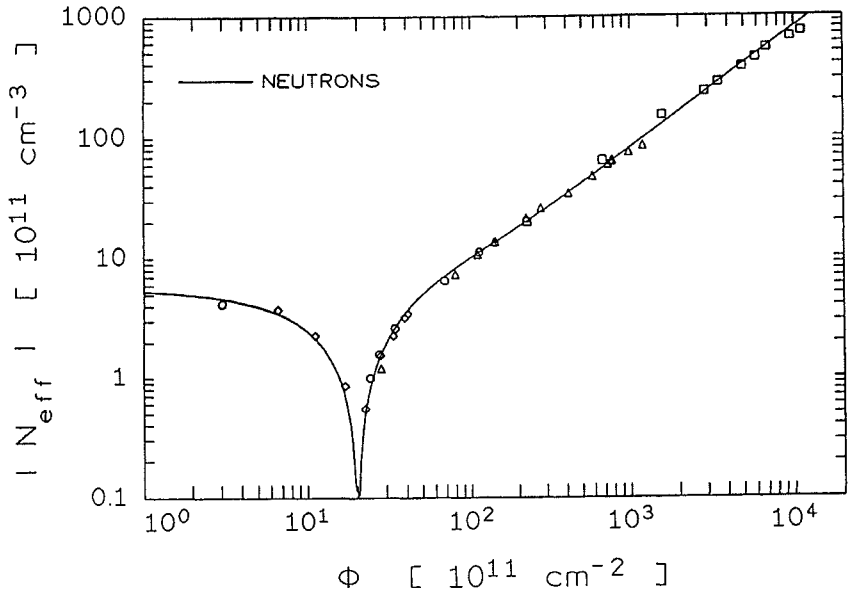

Figure 3.3: Absolute value of the effective impurity concentration versus fluence up to 10^{15} n/cm^2. The solid curve represents a fit according to equation (3.8). [6]

The depletion voltage is observed to initially decrease and then increase. This change over corresponds to the acceptor concentration exceeding the donor concentration, (initially it is the reverse for n-type material). That is, the detector is changing from n-type to p-type. This type inversion occurs for a neutron fluence of about 2×10^{12} cm^{-2}. The detectors are still operable after type inversion. This is because the diodes are actually an n^+-n-p^+ junction. (See Section 3.2.) The n^+ and p^+ are highly doped regions and so their doping concentrations are not significantly changed in the irradiation. The n-type region has almost equal donor and acceptor concentrations and the balance is changed from effective n-type to effective p-type when irradiated. When type inversion occurs the detectors become an n^+-p-p^+ junction and so an n-p junction still exists. Hence the detectors can still be operated with the same polarity that they had before inversion.

The model described by equation (3.8) is not sufficient to explain the long term behaviour. After a period of several months "reverse annealing" of the effective

impurity concentration is observed and the rate is dependent on the fluence received. This effect is shown in figure 3.4 taken from Ref. [7].

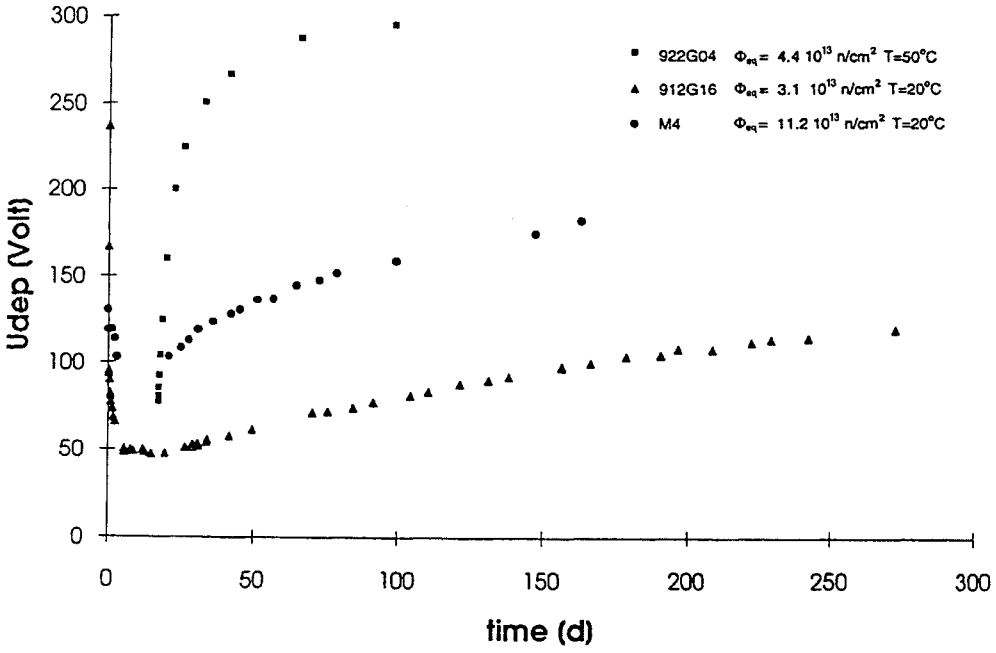

Figure 3.4: Increase in depletion voltage with time after irradiation due to reverse annealing of the effective impurity concentration. The annealing is 50 times faster at 50°C than at room temperature. [7]

A possible explanation of this process, as described in Ref. [8], is the production of two neutral defects X_1 and X_2 which then combine to form a single acceptor like defect Y. Assuming that both neutral defects have approximately the same concentration or are physically identical such that $N_x = N_{x1} = N_{x2}$, then the rate of removal of N_x is equal to the production rate of defect Y and is given by the second order process:

$$\mathrm{d}N_y = -\mathrm{d}N_x = k\,N_x^2\,\mathrm{d}t \tag{3.9}$$

where k is the reaction constant. It follows that the increase in the concentration of Y defects is given by

$$N_y(t) = N_{x,0}(t/(t+\tau)) \tag{3.10}$$

where $N_{x,0} \equiv N_{y,\infty}$ is the initial concentration of the defects X_1 or X_2, and

$$\tau = (kN_{x,0})^{-1} \tag{3.11}$$

is the "half life" time. The temperature dependence of k was found by a study of the temperature dependence of reverse annealing [8] to obey the Arrhenius relation:

$$k = k_o \exp\left(\frac{-E_a}{k_B T}\right) \tag{3.12}$$

where E_a is the activation energy found to be 1.31 ± 0.04 eV, k_0 is a constant related to the most abundant phonon frequency in the lattice, and k_B is Boltzmann's constant.

Incorporating the reverse annealing into equation (3.8) gives rise to the following fluence and time dependence of N_{eff}:

$$N_{eff}(\Phi, t) = N_{eff,0} - N_0^*(1 - \exp(-c\Phi)) - \beta_s \Phi - \beta_n R(t, \tau)\Phi \tag{3.13}$$

where $\beta_{s,n}$ are production rates of the "stable" and "neutral" defects respectively. The last term is due to the reverse annealing and is described by the function $R(t, \tau)$. From equation (3.10),

$$R(t, \tau) = t/(t + \tau) \ . \tag{3.14}$$

Note that equation (3.13) assumes that all electrically active defects except those that are "stable" have annealed out, and those that are "stable" never anneal. Some relatively fast annealing is observed after a short irradiation. In the LHC, however, where the irradiation is over a long time, damage with short annealing times will not contribute significantly.

Table 3.1 summarizes the parameters for calculating N_{eff} as compiled by the RD2 Collaboration [9].

Table 3.1: Effective impurity concentration parameters.

$N_{eff,0}$ (10^{11} cm^3)	5.4
N_0^* (10^{11} cm^3)	3.15 ± 0.38
c (10^{-13} cm^2)	4.11 ± 1.25
β_s (cm^{-1})	0.017 ± 0.001
β_n (cm^{-1})	0.044 ± 0.016
E_a (eV)	1.31 ± 0.04
$k(T = 0°\text{C})$ (cm^3/s)	$3.45^{+0.94}_{-0.68}$

3.5.3 Charge Collection

The defects act as sites for recombination and trapping and so decrease the charge collection efficiency. Carrier mobility is also reduced, increasing the time required to collect charge. Due to the 25 ns bunch crossing time the charge must be collected within this time. An example of a detector's response before and after an irradiation of 1.1×10^{14} n/cm^2 is shown in figure 3.5 (taken from Ref. [10]). In this case, a 12% collection deficiency was observed for the irradiated detector. For a shaping time of 25 ns and a leakage current of 5 μA the signal to noise ratio is expected to be greater than 11:1. (See Section 3.5.1.) For a 30% charge collection deficiency this is reduced to 8:1, which should be acceptable.

3.6 Self Annealing

Some of the defects in the silicon lattice can repair themselves due to the thermal motion of the silicon atoms. This can occur at room temperature and is referred to as self annealing.

This annealing is an advantage as it reduces the damage and hence prolongs the life of the detector. It is desirable to model this annealing in order to predict the operation of silicon detectors in a long term running period of ATLAS. When measurements are taken under different conditions, if no correction is made for the

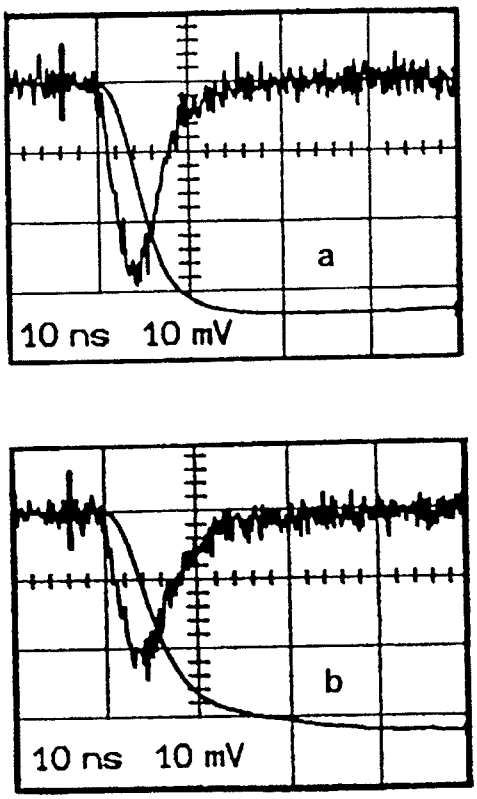

Figure 3.5: Current pulse response for 2 MeV electrons from a ^{106}Ru source. (a) Not irradiated ($V_{dep} = 30$ V). (b) Irradiated with 1.12×10^{14} n/cm^2 ($V_{dep} = 130$ V). Both detectors biased at 160 V. [10]

self annealing, comparison is difficult. For example, when calculating the damage coefficient defined in equation (3.3) the increase in current is what would be obtained immediately after an "instantaneous" irradiation. If the irradiation was over a long period of time then annealing occurs during the irradiation and so the resulting current increase, without correction for self annealing, will be lower.

Following the method outlined in Ref. [11] the self annealing can be modelled as described below. The following will describe the self annealing of the leakage current increase but can be applied in the same manner for any quantity proportional to the density of defects which increases linearly with fluence in the absence of annealing. Silicon detectors will generally have a small reverse current before they are irradiated. In the following, reference to the leakage current will refer to the increase in bulk current ΔI and be denoted I.

There is likely to be more than one type of defect contributing to the leakage current each with contribution I_i such that

$$I = \sum_{i=1}^{n} I_i \,. \tag{3.15}$$

Each of these contributions will have different rates of production and annealing. The rate of production is expected to be proportional to the flux with production rate a_i. The rate of annealing is assumed to be proportional to the number of the type of defect responsible, with time constant τ_i. The time differential for I_i is therefore given by

$$\frac{\mathrm{d}I_i}{\mathrm{d}t} = a_i \frac{\mathrm{d}\Phi(t)}{\mathrm{d}t} - \frac{1}{\tau_i} I_i(t) \tag{3.16}$$

where $\Phi(t)$ is the fluence at time t. Before irradiation it is assumed that there is no contribution to I, i.e., $I_i(0) = 0$. The leakage current increase if no self annealing occurred I_0, after an irradiation of fluence Φ, is given by

$$I_0 = \left(\sum_{i=1}^{n} a_i \right) \Phi \,. \tag{3.17}$$

The interesting quantity is the value $\sum a_i$ which in this case is the damage coefficient

α multiplied by the depleted volume of the detector.

Defining fractional damage factors A_i for each contribution such that

$$A_i = a_i / \sum a_i \tag{3.18}$$

and solving equation (3.16) leads to the following time variation of the leakage current:

$$\begin{aligned} \frac{I(t)}{I_0} &= \sum_{i=1}^{n} A_i \frac{1}{\Phi(t)} \left[\int_0^t \frac{\mathrm{d}\Phi(t^*)}{\mathrm{d}t^*} e^{t^*/\tau_i} \mathrm{d}t^* \right] e^{-t/\tau_i} \quad \text{for } 0 \le t \le T \\ \frac{I(t)}{I_0} &= \sum_{i=1}^{n} A_i \frac{1}{\Phi(T)} \left[\int_0^T \frac{\mathrm{d}\Phi(t^*)}{\mathrm{d}t^*} e^{t^*/\tau_i} \mathrm{d}t^* \right] e^{-t/\tau_i} \quad \text{for } t \ge T \end{aligned} \tag{3.19}$$

where t is the time since the beginning of the irradiation, and T is the duration of the irradiation.

In order to extract the self annealing parameters A_i and τ_i it is useful to calculate the ratio $I(t)/I(T)$. Given that $t' = t - T$ is the time after the end of irradiation, and $I(T)$ is the leakage current at the end of the irradiation, then using equation (3.19) it follows that

$$\frac{I(t')}{I(T)} = \sum_{i=1}^{n} A_i^* e^{-t'/\tau_i} \tag{3.20}$$

where

$$A_i^* = \frac{A_i c_i}{\sum A_i c_i} \tag{3.21}$$

and

$$c_i = \frac{1}{\Phi(T)} \left[\int_0^T \frac{\mathrm{d}\Phi(t^*)}{\mathrm{d}t^*} e^{t^*/\tau_i} \mathrm{d}t^* \right] e^{-T/\tau_i} \,. \tag{3.22}$$

For the case of a single irradiation of constant flux with a duration time T, this simplifies to

$$c_i = \frac{\tau_i}{T}(1 - e^{-T/\tau_i}) \,. \tag{3.23}$$

The self annealing parameters can be determined after fitting the data according to equation (3.20) and extracting A_i^* and τ_i. The A_i may be obtained from the

A_i^* via the relation (which follows from equation (3.21) and $\sum A_i = 1$):

$$A_i = \frac{A_i^*/c_i}{\sum A_i^*/c_i} . \tag{3.24}$$

Equation (3.20) may be used to obtain $I(T)$ from any measurement after the end of irradiation. Assuming the self annealing parameterization is correct, all measurements should result in obtaining the same $I(T)$. Finally, to obtain I_0 the following relation can be used:

$$\frac{I(T)}{I_0} = \sum_{i=1}^{n} A_i c_i . \tag{3.25}$$

3.6.1 Calculation for Non-Uniform Irradiations

For the more complex irradiations described in Sections 3.9 and 3.10 the analysis for a single irradiation with constant flux must be generalized. To calculate c_i according to equation (3.22) the irradiation was separated into a number of constant irradiations. Consider the time limits $t_0 = 0$, t_1, ..., $t_m = T$ covering the total duration of the irradiation with corresponding fluence $\Phi_0 = 0$, Φ_1, ..., $\Phi_m = \Phi(T)$. The flux between times $t_j - 1$ and t_j is given by

$$\phi_j = \frac{\Phi_j - \Phi_{j-1}}{t_j - t_{j-1}} . \tag{3.26}$$

It follows from equation (3.22) that the c_i are then given by

$$c_i = \frac{1}{\Phi(T)} \left[\sum_{j=1}^{m} \phi_j \tau_i (e^{t_j/\tau_i} - e^{t_{j-1}/\tau_i}) \right] e^{-T/\tau_i} . \tag{3.27}$$

3.7 Temperature Dependence of Leakage Current

The leakage current depends strongly on temperature. Assuming all defect levels are in the middle of the forbidden gap, the temperature dependence is given by

$$I \propto (k_B T)^2 \exp(-E_g/2k_B T) \tag{3.28}$$

where T is the temperature in Kelvin and E_g is the width of the forbidden gap (equal to 1.12 eV for silicon). Better agreement is seen with experiment if E_g is replaced with 1.21 eV [11]. To normalize leakage currents to the current at 20°C, I_{20}, the following relation can be used:

$$\frac{I_{20}}{I_T} = \left(\frac{293.2}{T}\right)^2 \exp\left[\frac{1.21}{2k_B}\left(\frac{1}{T} - \frac{1}{293.2}\right)\right] \tag{3.29}$$

where I_T is the current at temperature T. Equation (3.29) corresponds roughly to a doubling of the leakage current for a 7°C increase.

3.8 Neutron Irradiations of Silicon

The two neutron irradiations of silicon detectors described here were performed by the Melbourne group [12, 13]. The analysis for these experiments forms part of the work for this thesis.

The two irradiations were carried out using facilities of the Australian Nuclear Science and Technology Organization (ANSTO) at the Lucas Heights laboratory near Sydney. In the first experiment, referred to as Melbourne Irradiation 1, the irradiation took place over 3 days reaching a maximum fluence of 10^{13} n/cm^2. The temperature in the first experiment was not controlled, but was measured and data was normalized to 20°C. In the second experiment, referred to as Melbourne Irradiation 2, the irradiation lasted around an hour reaching a maximum fluence of about 5×10^{12} n/cm^2. In this experiment the temperature was maintained at 20°C to within ±0.2°C. For both irradiations the silicon detectors were kept under reverse bias and leakage currents were monitored during and after the irradiation.

Corrections for self annealing have been made with parameters determined from the data and damage coefficients have been evaluated.

3.9 First Neutron Irradiation by the Melbourne Group

3.9.1 Experimental Setup

Neutrons were obtained by bombarding a thin Li target with monoenergetic protons of energy 2.9 MeV. Most neutrons are produced via the reaction Li(p,n)Be with $\sim$ 10% produced via Li(p,n)Be*. The proton beam with a current of around 35 μA was produced via a Van de Graf generator.

Two silicon detectors were irradiated. These detectors were previously used in the inner tracking layer of the UA2 experiment. (See Section 4.3.1 for a description of the UA2 detector.) The detectors measure 16×32 mm^2 and are segmented into 16 pads each with a width of 2 mm. The thickness of the detectors is 300 μm. The sensitive volume of each pad is 9.6×10^{-3} cm^3. The detectors had received very little irradiation in the UA2 experiment and had leakage currents before the present irradiation of about 20 nA. (After the irradiation the leakage currents rose to around 10 μA.) The two detectors were kept in their UA2 electrical test boxes. These test boxes consisted of plastic cases with electrical contact made by conductive rubber, allowing connection to be made to each pad separately. The test boxes were mounted in a lightproof box with an aluminised mylar film lid. Dry nitrogen was circulated through the box to ensure minimal humidity. Figure 3.6 shows the box and arrangement of the detectors.

Both silicon detectors were placed in a plane 20 ± 1 mm behind the Li target. The position and numbering scheme for the pads is shown in figure 3.7. The proton beam, with a full width of approximately 3 mm, was centred between pads 8 and 9 of detector 1 and hence these pads received the maximum fluence. Contours of constant neutron fluence in the plane of the detector are shown in figure 3.7. The edge pads of detector 1 received $\sim$ 40% of the maximum fluence. The second detector received fluences ranging from about 30% to 6% of the maximum fluence. For a thin target the neutrons at a given angle are monoenergetic. The neutron energy ranges from 1.2 MeV in the forward direction to 0.9 MeV at the outermost edge pad of detector 2. To monitor the neutron flux a "long counter" was placed 3 m directly behind the

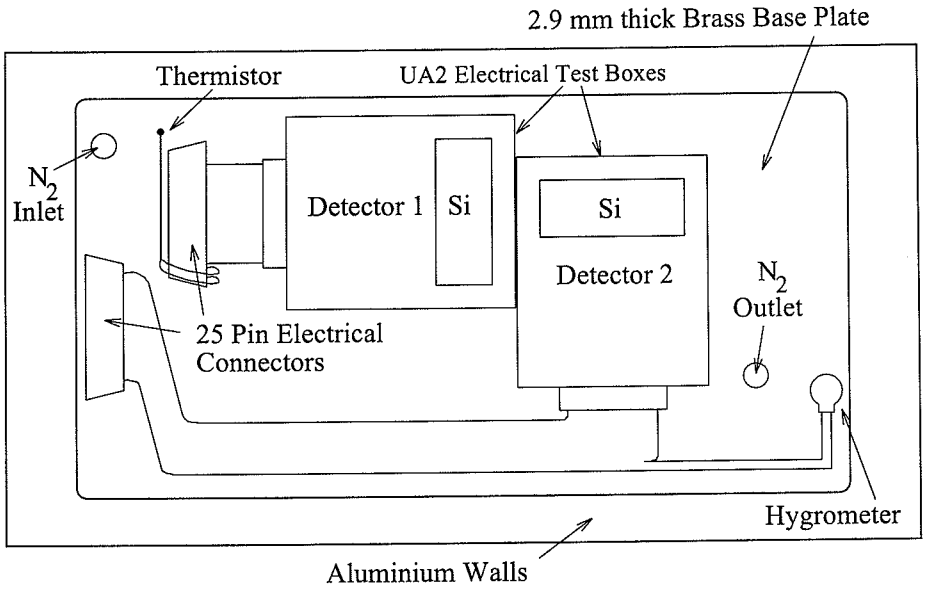

Figure 3.6: The lightproof box for the silicon detectors.

Li target. A "long counter" consists of a thermal neutron detector in a block of moderating material. Figure 3.8 shows the geometry of the experiment.

The detectors were exposed, at an almost constant rate, for 6 hours on the first day and for 14 hours on each of the following two days. Figure 3.9 shows the fluence in the forward direction as a function of time. (Section 3.9.2 describes the calculation of the fluence normalization.) The detectors remained reverse biased at 45 V throughout the exposure and for about 30 hours after the end of the third exposure. Leakage currents were monitored at 3 minute intervals during this period. The detectors were unbiased for 3 days during which time they were transported from Sydney to Melbourne. The bias was then maintained at 45 V and currents were measured at typically 30 minute intervals for a period of 10 weeks.

The currents from the 32 pads along with the current of a thermistor inside the box were recorded with an analog multiplexer/microammeter/IBM-AT arrangement as shown in figure 3.10. The humidity in the box was monitored using a capacitive hygrometer.

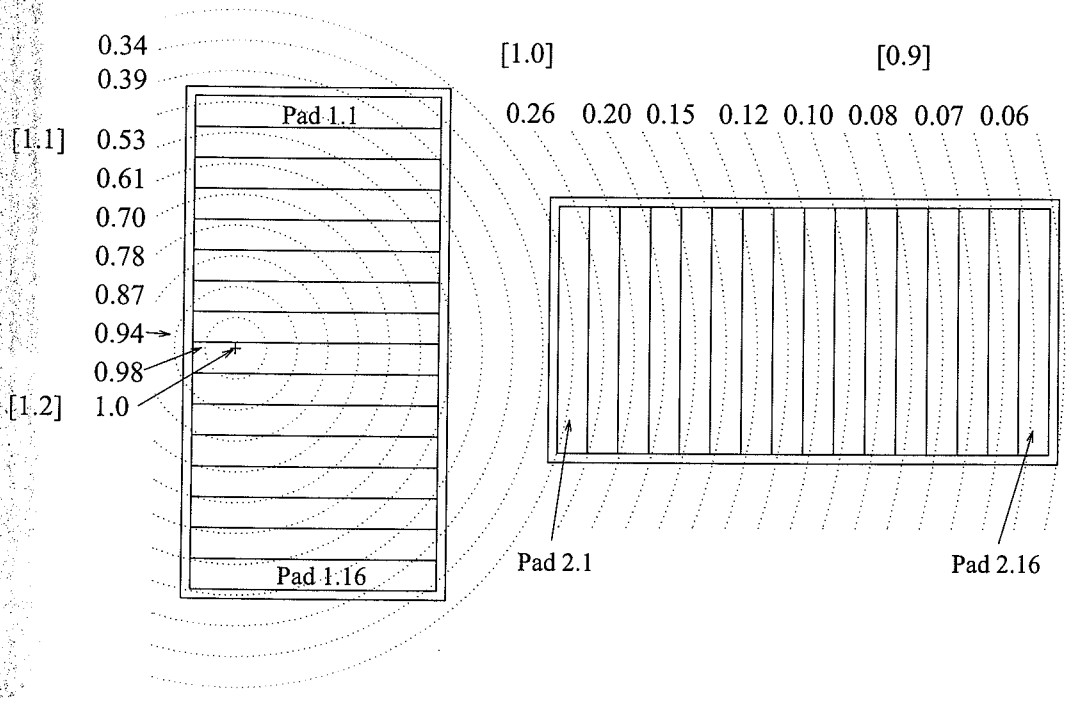

Figure 3.7: Position of the two silicon detectors. Contours of constant neutron fluence are shown with fluence relative to the beam centre. Neutron energies (MeV) are given in square brackets.

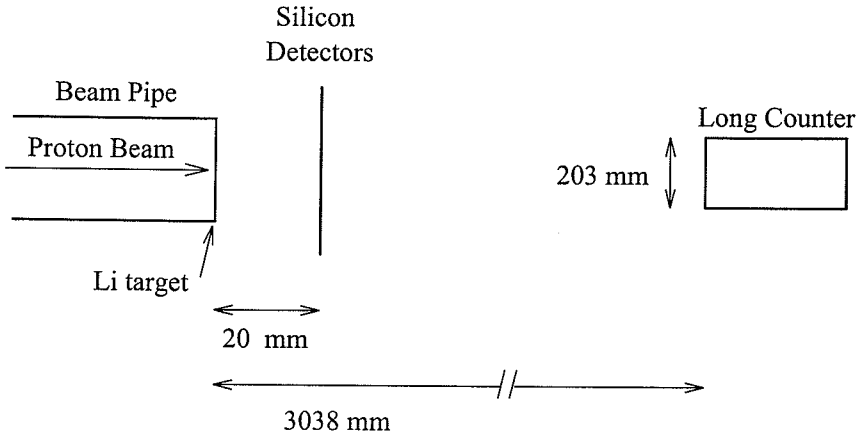

Figure 3.8: Schematic of the experiment geometry.

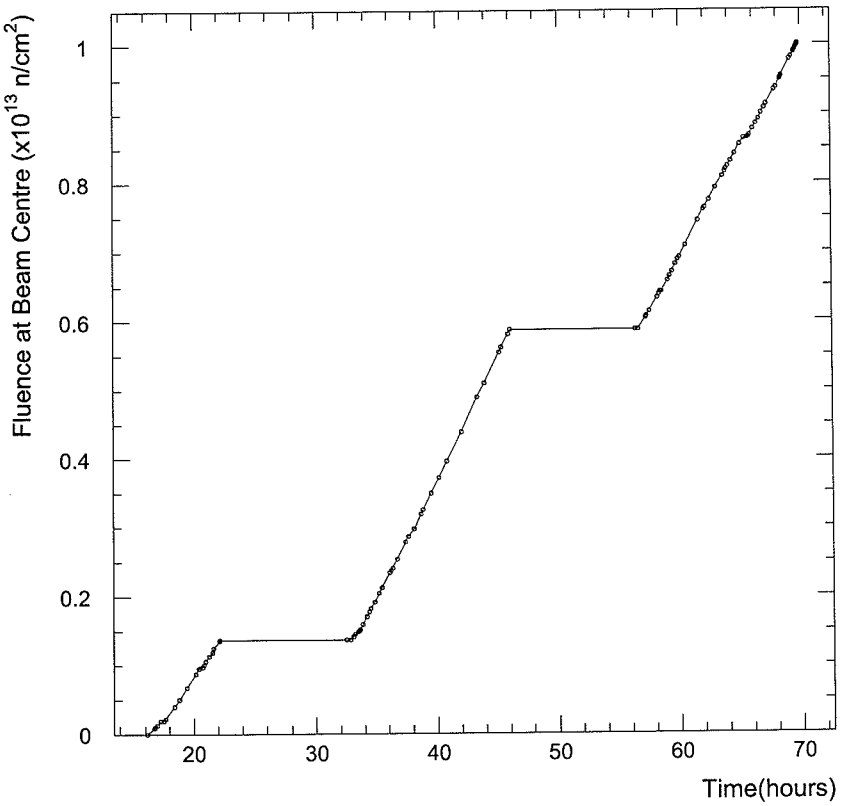

Figure 3.9: Time dependence of the fluence at beam centre.

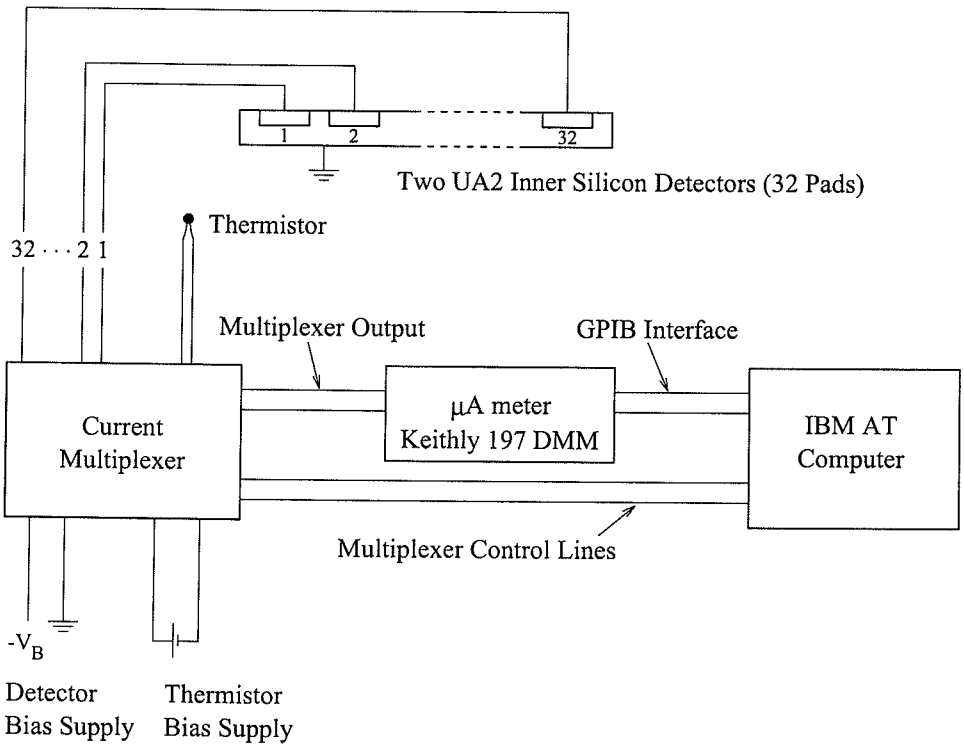

Figure 3.10: Data acquisition system for Melbourne Irradiation 1.

3.9.2 Fluence Calculation

The fluence on each pad was determined from differential cross section data and normalized using the "long counter" measurement.[1] The fluence measured by the "long counter" underestimates the actual fluence due to attenuation in the detectors and the brass backing plate. The attenuation in the 2.9 mm thick brass backing plate (assumed to be the nominal 70% Cu, 30% Zn by weight with a density of 8.5 g/cm^3) was calculated to be 0.07 ± 0.01. The attenuation in the silicon was less than 1%. Neutrons will also be scattered into the "long counter" by the apparatus, increasing the measured fluence. This was estimated to lead to an increase of approximately 2% based on a calculation using a 12 cm diameter circular brass plate of thickness 2.9 mm.

The uncertainty in the distance between the lithium and the silicon leads to a 10% uncertainty in the fluence. Due to the magnitude of this uncertainty, only the attenuation in the brass was considered. The fluence in the "long counter" was measured to be 3.6×10^{13} n/sr. After correction for the attenuation in the brass plate the fluence in the plane of silicon at the beam centre was $(1.0 \pm 0.1) \times 10^{13}$ n/cm^2.

The effective flux at a given angle θ to the normal is greater by $1/\cos(\theta)$ due to the increased path length through silicon that the neutrons must pass. (See Appendix A.) The fluence averaged over the pad's area was obtained via numerical integration using differential cross section data for the Li(p,n)Be reaction [14]. The results are shown in figure 3.11. The contribution from Li(p,n)Be* was ignored. This will only have a small effect since the fluxes were normalized using the "long counter". The contribution from Li(p,n)Be* would give rise to a slightly different angular and energy distribution.

[1] The fluence calculations were done by Robert Bardos of the Melbourne group.

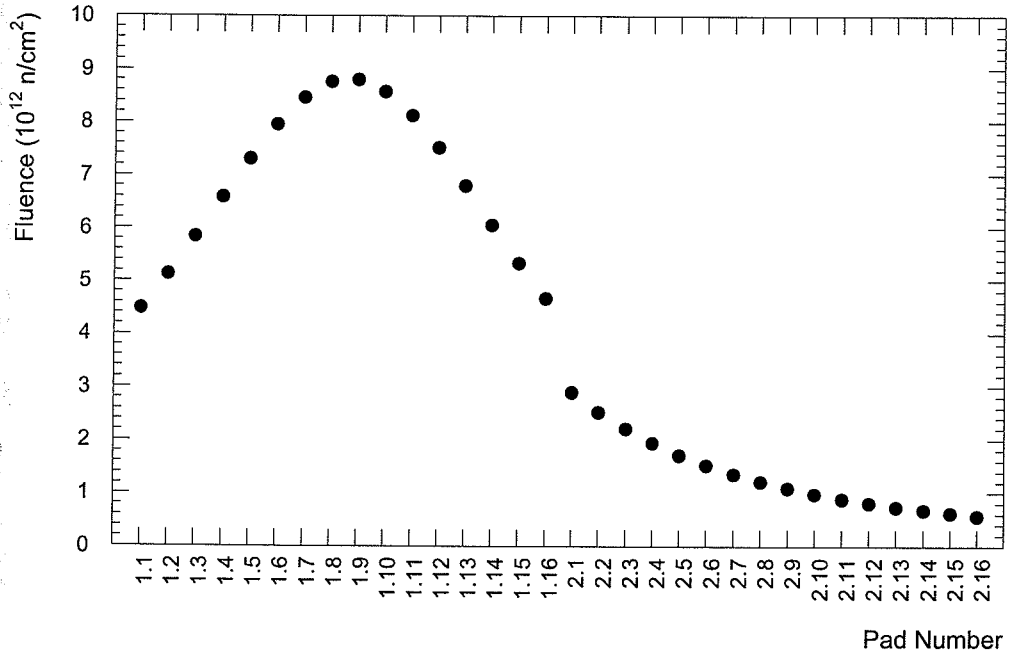

Figure 3.11: Average fluence per pad.

3.9.3 Analysis

Temperature Correction

The variation of leakage current with temperature was assumed to follow equation (3.29). Using this equation the raw data was normalized to 20°C. During the experiment the temperature of the detectors remained within the range 16–24°C. Figures 3.12a and 3.12b show the data for one pad before and after temperature correction. The temperature correction was successful in removing most of the fluctuations.

A possible source for the fluctuations that remain after temperature correction is variations in the thermistor voltage. The temperature was calculated by measuring the current through a thermistor, which depends on the voltage across the thermistor. The thermistor voltage was not monitored continuously, but instead was measured with a multimeter once or twice a day. Different voltage supplies were used from time to time and the voltage was known to fluctuate especially for the first few days of measurements at Melbourne. The fluctuations do follow a daily cycle, but this can be due to the power load which would be expected to decrease overnight, increasing the voltage across the thermistor. An increase in thermistor voltage will give a higher current and hence the calculated temperature will be higher than it actually is. After the temperature correction the leakage current would be underestimated.

One section of the temperature corrected data showed a dip for all the pads at about 12 hours after the end of the final irradiation. This is more evident in figure 3.19 at t =82 hr. At the corresponding time the temperature rose relatively quickly. It is thought that this dip was due to a lag in the temperature change between the silicon and the thermistor.

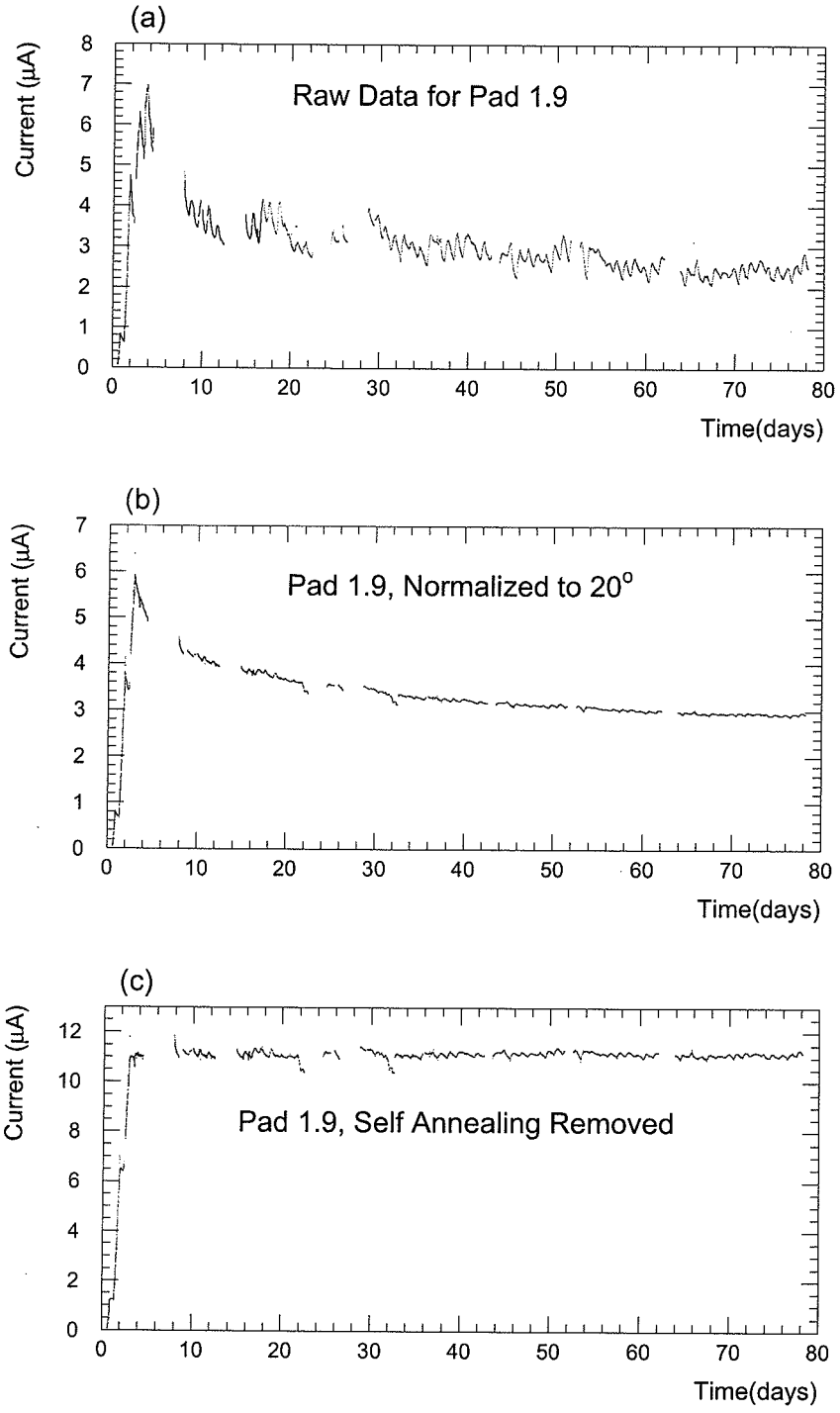

Figure 3.12: Comparison between (a) the raw data, (b) temperature corrected data normalized to 20°C, and (c) data with self annealing removed for a typical pad.

3.9.4 Temperature Corrected Data

The First Detector

Figures 3.13 and 3.14 show leakage currents normalized to 20°C for the first detector, as a function of time from the start of irradiation. The time taken as the start of irradiation is arbitrary and for convenience it has been chosen to be about 16 hours before the actual start of irradiation. The time variation of the leakage currents for the first detector behaved broadly as expected; an increase during the irradiation and a reduction due to self annealing between irradiations and at the end of the final irradiation. There is a three day gap in all the plots due to the lack of monitoring during transportation of the detectors from Sydney to Melbourne.

The largest increase in current was observed in pad 1.8, which along with pad 1.9 was on the beam axis. The edge pads (pads 1.1 and 1.16) showed the next largest increase despite receiving less than half of the maximum fluence. Pad 1.11 had a dead readout channel and hence recorded a null current at all times. Pads 1.3 and 1.7 were originally suspected to be dead. However, these two pads suddenly produced a signal approximately 14 hours after the end of the irradiation. At the same time the pads adjacent to both showed a decrease in current. This occurred at a time when the detector casing was moved. It is suggested that the cause may have been some highly resistive material between the crystal and the conductive rubber which was displaced due to mechanical shock. The reduction in the current in the adjacent pads is probably due to these pads sharing the current that would have been seen in pads 1.3 and 1.7. The reason for this is not clear. One possible explanation is that the depletion volume under the neighbouring pads was extending into the volume under the unbiased pads and hence increasing the reverse current. The adjacent pads 1.4 and 1.8 showed larger decreases after the incident than for pads 1.2 and 1.6. If this explanation is correct, then the depletion region under pads 1.4 and 1.8 must have extending significantly into the volume under pads 1.3 and 1.7. Another explanation is that there may have been a short with the neighbouring pads. Alternatively, the cause may be associated with the multiplexer.

The Second Detector

Figures 3.15 and 3.16 show the leakage current for pads on the second detector. Pads 2.2 and 2.15 behaved as expected and pad 2.13 was dead throughout. Except for these pads this detector exhibited some very unusual behaviour.

Less than 5 hours into the irradiation on the second day all the pads, except pads 2.2, 2.13 and 2.15, showed a rapid increase in apparent leakage current. The effect was worse in pad 2.1 which showed the largest leakage current, up to 15 μA, compared with the other pads on the detector, typically less than 3 μA. Detector 1 behaved normally at this time. Further anomalies occurred about 10 and 28 days after the start of irradiation. No satisfactory explanation has been found for the anomalous behaviour of this detector. It is felt that the behaviour was a readout problem rather than a radiation induced phenomenon.

3.9.5 Self Annealing Correction

Self annealing occurs both during and after irradiation. The expected variation of current due to self annealing is described in Section 3.6.

Given the anomalous behavior of detector 2 discussed above, only the first detector was used to study self annealing. The dead pad, the edge pads and the pads which showed sudden changes in leakage current about 14 hours after the irradiation were excluded. The fractional decrease of leakage currents for the remaining seven pads (1.5, 1.9, 1.10, 1.12, 1.13, 1.14, and 1.15) showed similar time dependence as seen in figure 3.17. In this figure the currents have been normalized by $1/(\Phi \cdot Vol)$ and so represent a measure of the uncorrected damage coefficient as a function of time after the irradiation.

The currents from these seven pads were added up. The time variation after the end of irradiation is expected to be the sum of exponentials as given in equation (3.20). The summed data (normalized to the summed current at the end of the irradiation) was therefore fitted with a sum of exponentials plus a constant. The constant allows for irreparable damage or for time constants too long to be observable in the time

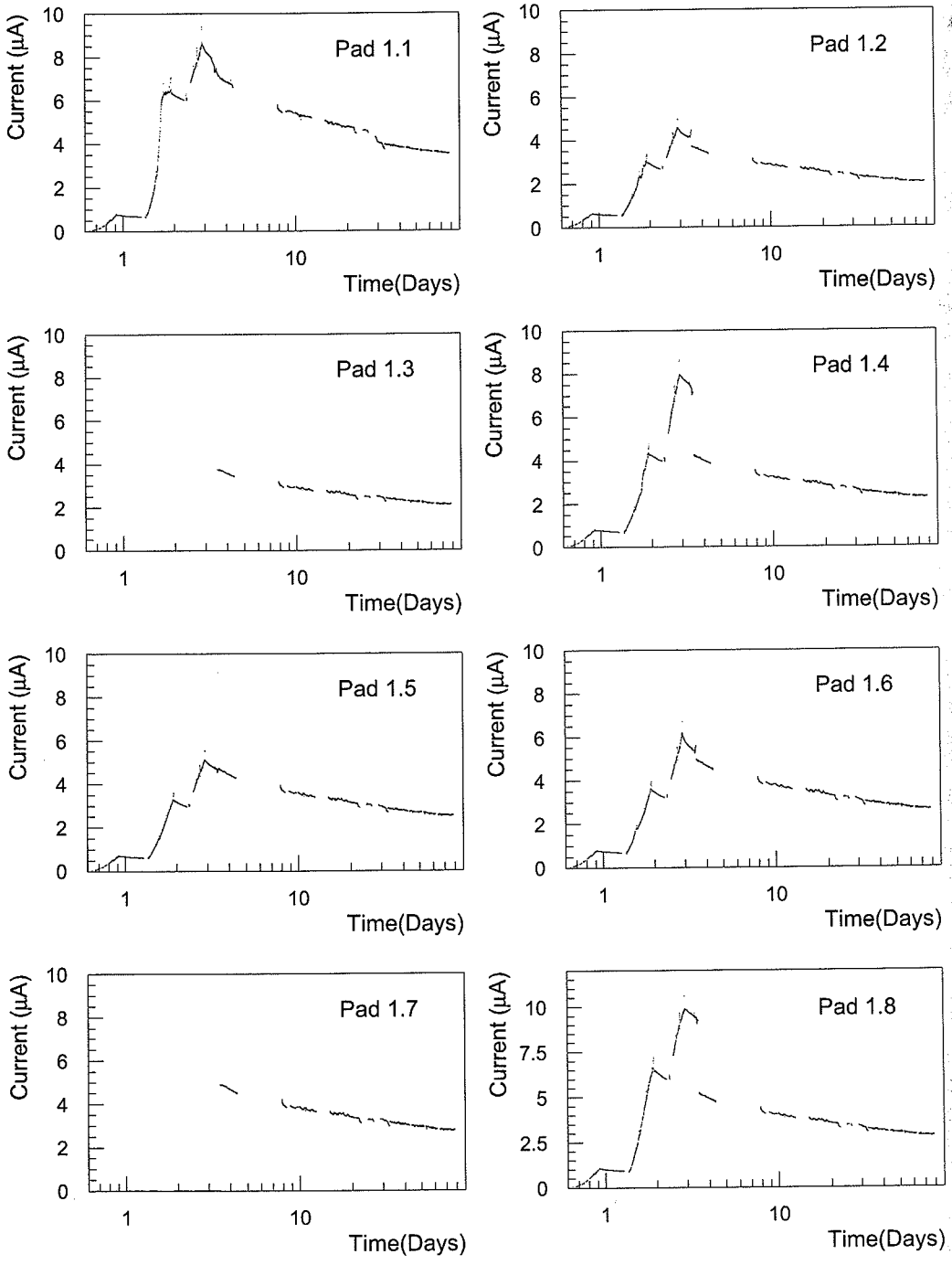

Figure 3.13: Temperature corrected data for pads 1.1–1.8.

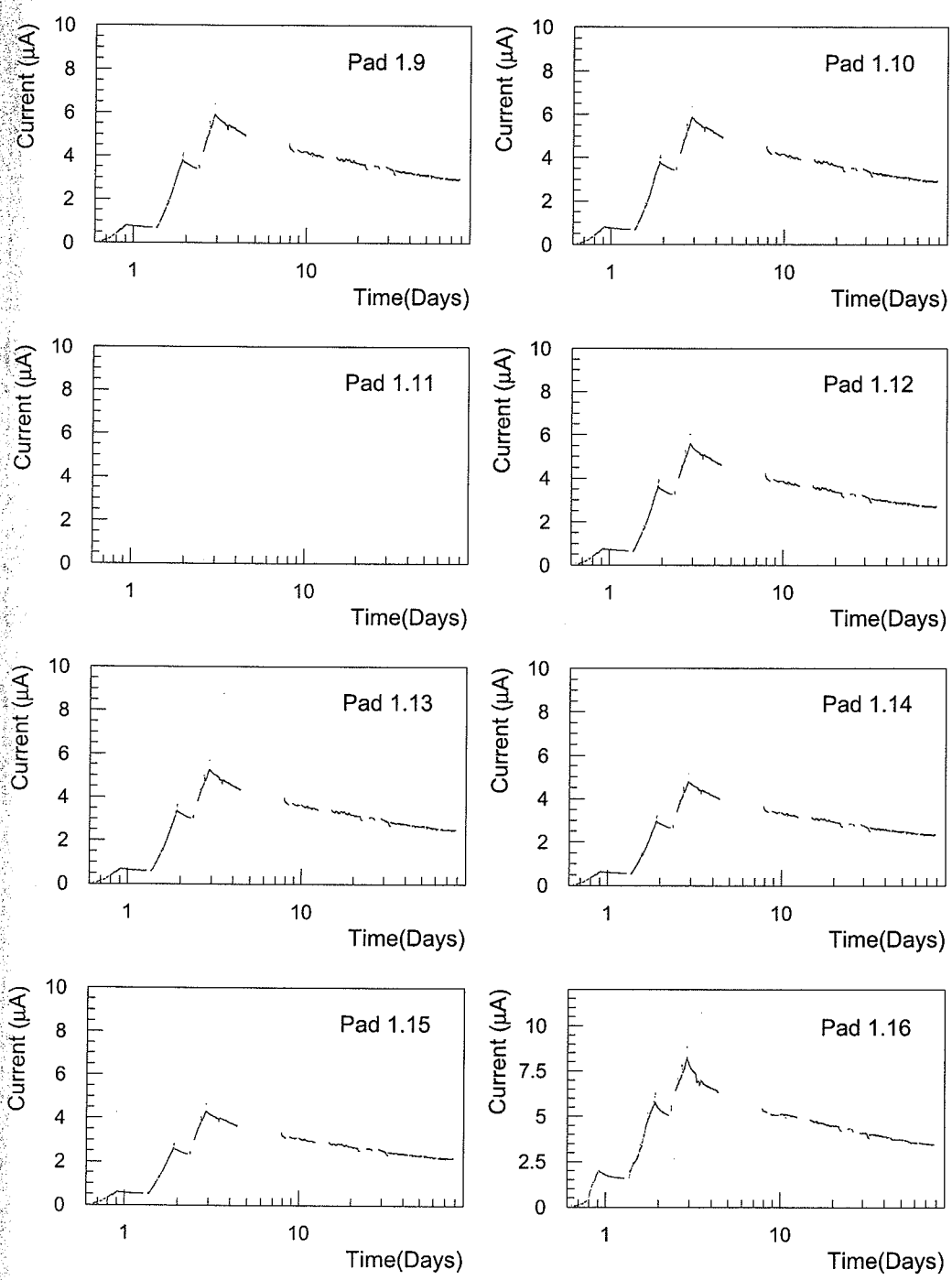

Figure 3.14: Temperature corrected data for pads 1.9–1.16.

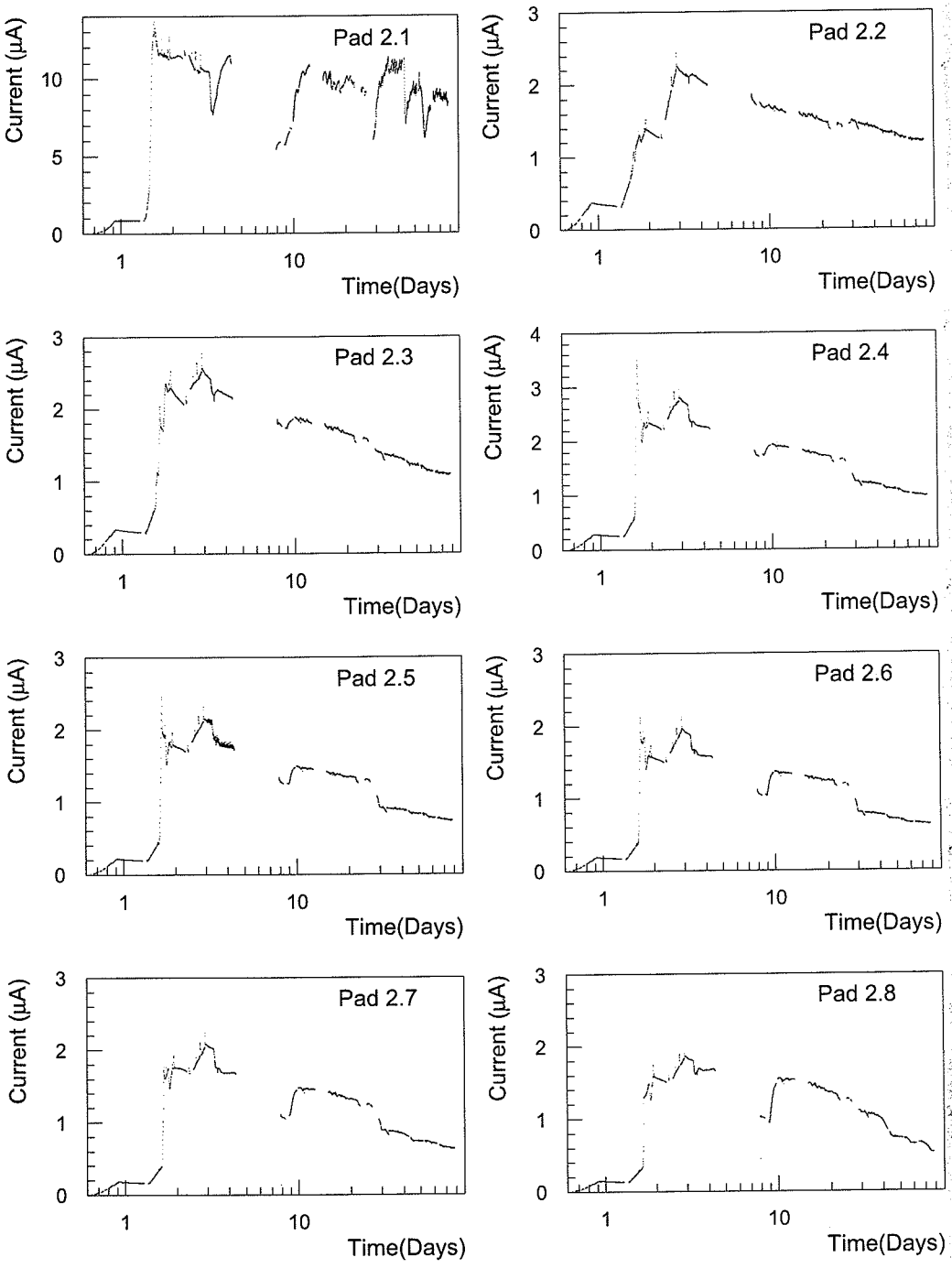

Figure 3.15: Temperature corrected data for pads 2.1–2.8.

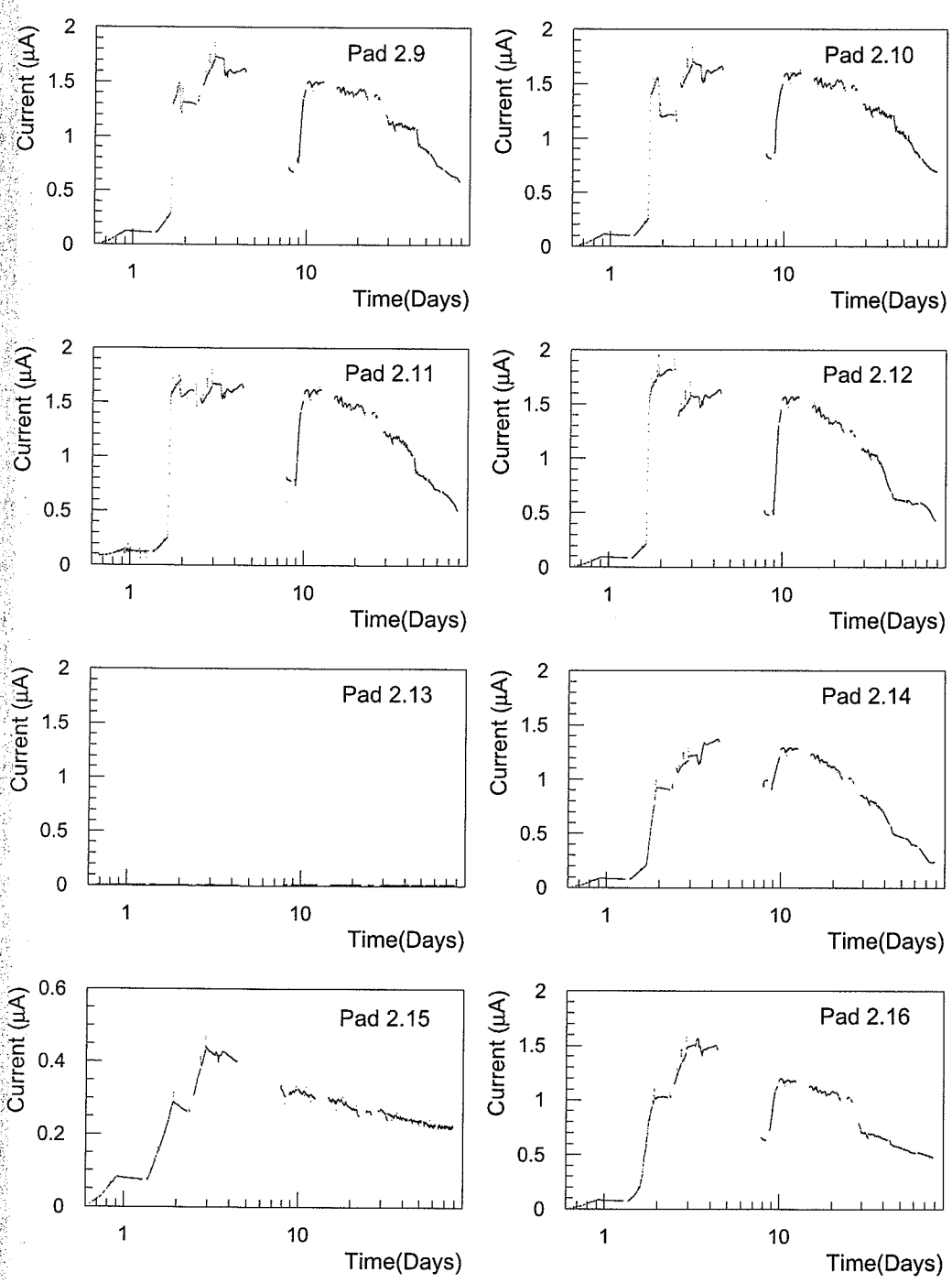

Figure 3.16: Temperature corrected data for pads 2.9–2.16.

over which measurements were made.

The data was found to be adequately fitted with three exponentials plus a constant. MINUIT [15] was use to obtain the parameters in table 3.2. To give meaning to the errors calculated by MINUIT it was necessary to assign errors to the data points. As the fluctuations in the data due to imperfect temperature corrections outweigh any measurement error, the amplitude of these fluctuations was used as an estimate for the errors on the data. The errors in table 3.2 should therefore be treated with caution. It should be noted that there are strong correlations between the parameters in the fit.

The τ_i and A_i^* as obtained from the fit and the calculated A_i are shown in table 3.2. The A_i were calculated with equation (3.24) with c_i calculated as described in Section 3.6.1. Figure 3.18 shows the summed data along with the best fit.

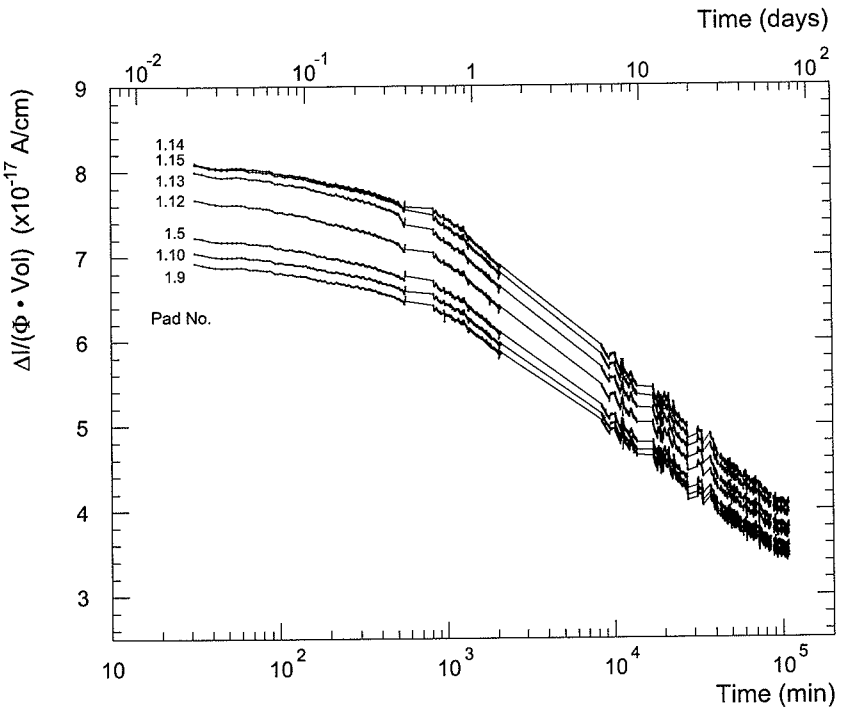

Figure 3.17: Uncorrected damage coefficient as a function of time after the irradiation

Table 3.2: Self annealing parameters for Melbourne Irradiation 1.

i	τ_i	A_i	A_i^*
1	∞	0.2553 ± 0.0004	0.4719 ± 0.0007
2	$(3.54 \pm 0.03) \times 10^4$	0.1590 ± 0.0004	0.2828 ± 0.0006
3	$(2.44 \pm 0.01) \times 10^3$	0.196 ± 0.001	0.2203 ± 0.0009
4	63 ± 7	0.390 ± 0.056	0.0250 ± 0.0025

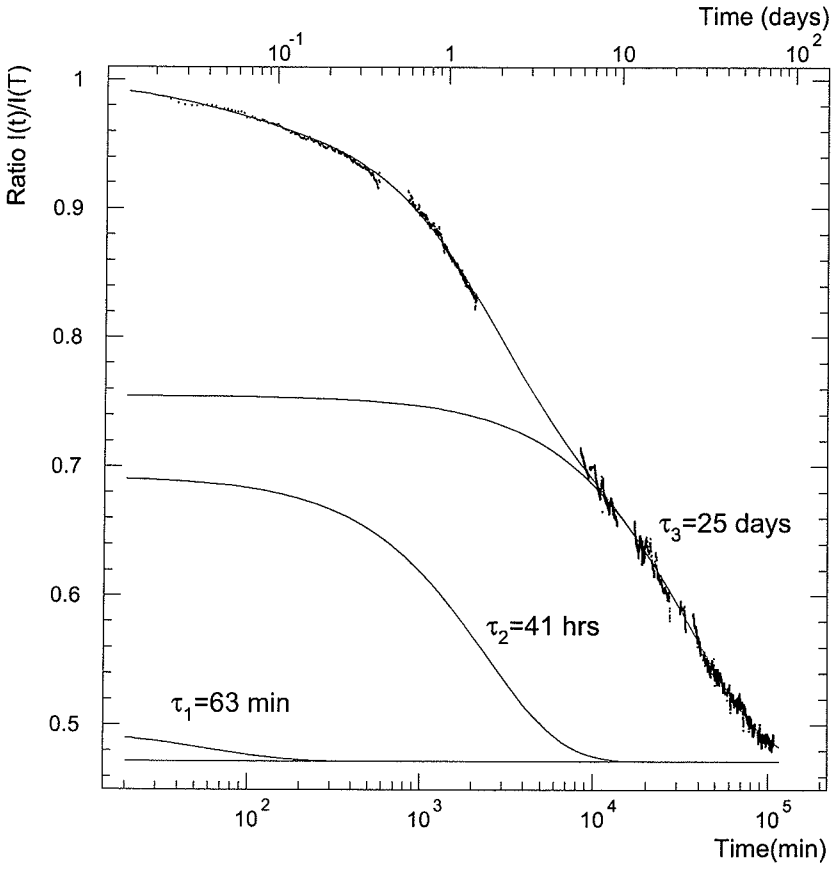

Figure 3.18: The summed data for detector 1 (see text), with fit superimposed.

3.9.6 Current versus Flux and Extraction of Damage Coefficients

Using the parameters obtained from the fit and the temperature corrected data one may calculate I_0, the leakage current expected if no self annealing had occurred. Figure 3.12c shows the data corrected for temperature and self annealing, for a typical pad (1.9) over the long term. Figure 3.19 shows the comparison before and after the self annealing correction for the short term data. It can be seen that the final current would have been almost a factor of 2 higher if no self annealing occurred during irradiation.

Figure 3.20 shows the leakage current corrected for self annealing as a function of the fluence on beam axis for the first detector. The general trend is as expected; the increase in current decreases away from the centre pads (1.8 and 1.9). The main exceptions are the end pads which showed abnormally high current increases. In two cases, pairs of pads (1.4 and 1.13, 1.8 and 1.9) symmetrically located with the beam axis, which therefore receive the same fluence, differ in damage rate by 50%. This is probably due to pads 1.4 and 1.8 sharing current from their neighbouring pads as discussed earlier.

The damage rates with fluence are not quite linear. Since the irradiation was over a number of days, the amplitude of the damage with the shortest time constant was small after the irradiation. This gave rise to a larger uncertainty in this amplitude than for the longer time constant components. It is possible that this component was overestimated which would give rise to an over correction in the self annealing. This may explain the non-linear increase.

Figure 3.21 shows the current corrected for self annealing for detector 2. For this detector, only data from the first day of irradiation and 5 hours of the second day is presented, because thereafter, unexplained variations in current occurred. Pad 2.11 was very noisy and is not shown. The end pads, as for detector 1, showed abnormally high leakage current increases. The other pads showed the expected behaviour with the current increase being proportional to the relative fluence. The linearity is better than for detector 1. However, a shorter time was utilized for detector 2, and so any

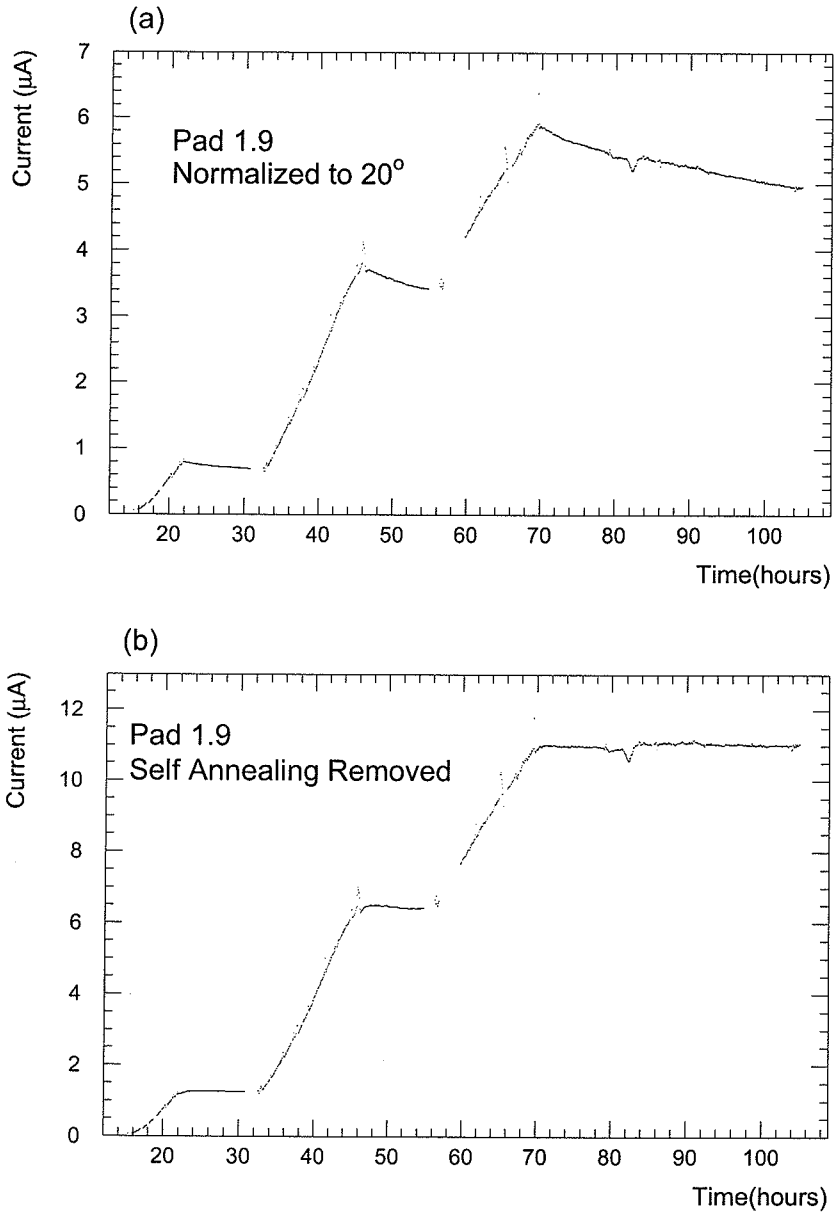

Figure 3.19: Comparison between (a) temperature corrected data normalized to 20°C, and (b) data with self annealing removed for a typical pad. Short term data is shown.

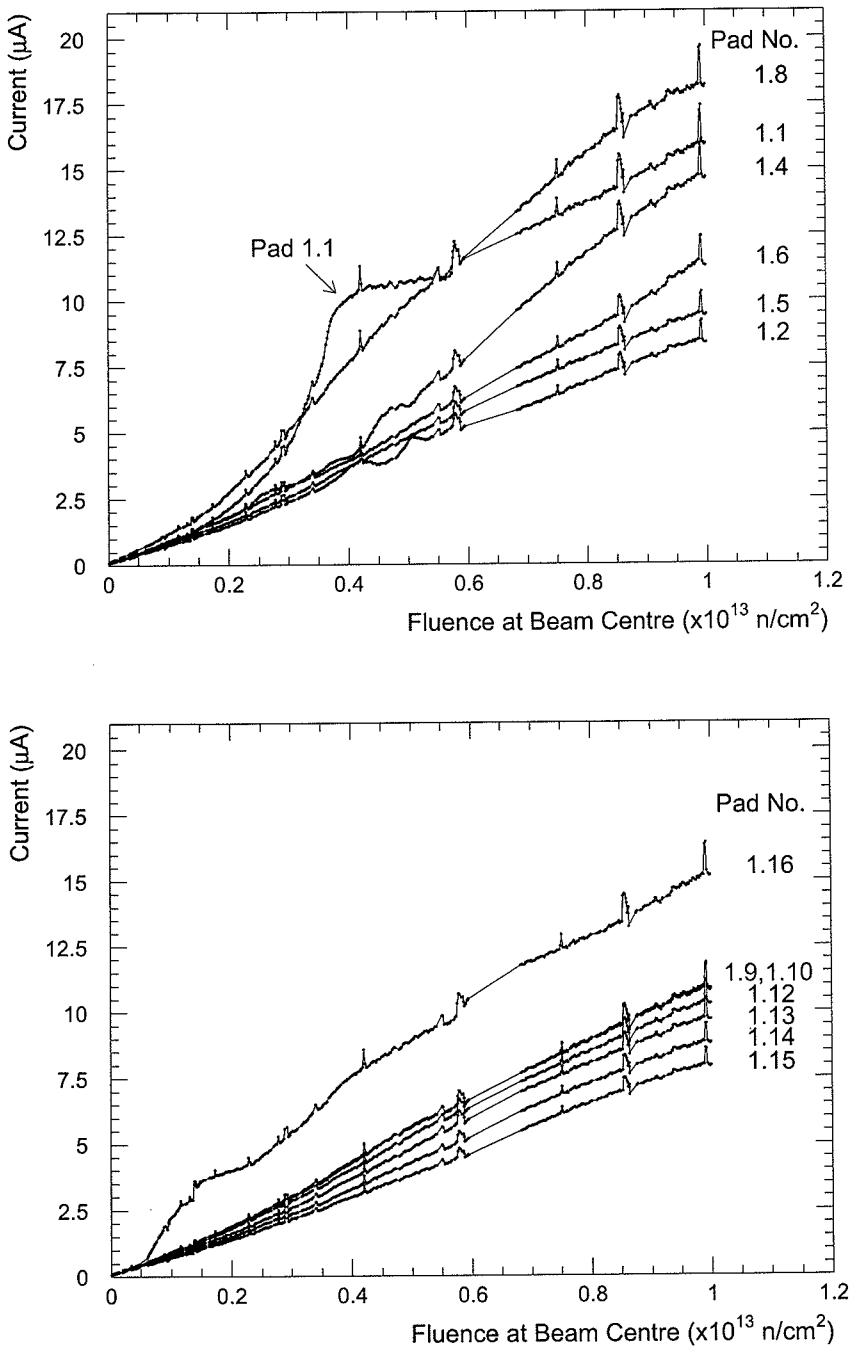

Figure 3.20: Leakage current vs fluence at beam centre for detector 1.

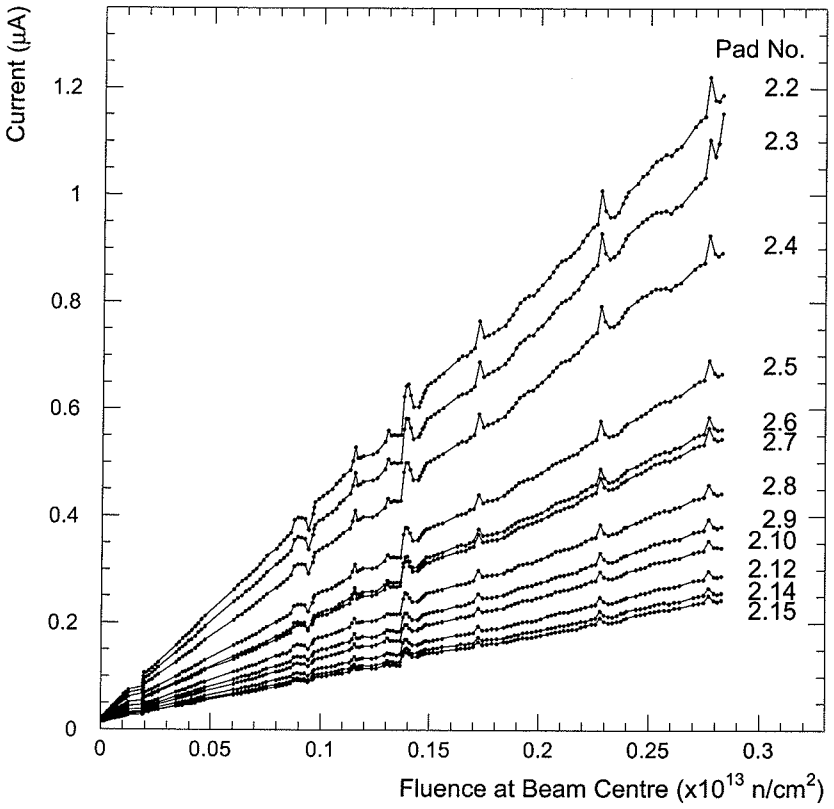

Figure 3.21: Leakage current vs fluence at beam centre for detector 2.

non-linearity is less likely to be apparent.

The spikes in this data, which appear for all pads at given fluence values, are from spikes in the thermistor current. They usually coincided with times when the beam was turned on or off and during beam trips, suggesting that the thermistor was picking up some electrical noise. The spikes are not observed in the raw leakage current data and are not of physical interest.

From these plots the damage coefficients were calculated from the rate of current increase with fluence. For the first detector the whole irradiation time was utilized. For the second detector, only the period before the observed irregularities was utilized. Using the average fluence for each pad a damage coefficient was calculated using

$$\alpha = \frac{\Delta I}{\Phi \cdot Vol} \,. \tag{3.30}$$

The calculated α are plotted in figure 3.22 and tabulated in table 3.3. Apart from the edge pads and pads 1.4 and 1.8, the resulting damage coefficients are fairly consistent.

It is clear that the edge pads behave differently. This is not fully understood and requires further studies. The use of guard rings may eliminate this problem. Since the purpose of these studies is to predict the behaviour of silicon in the LHC where the pad geometries are quite different, the results from the edge pads will not be used here.

Pads 1.4 and 1.8 were next to pads which initially showed no currents. It is possible that the depletion region was extending into these neighbouring pads (that is, their sensitive volumes were larger) thus accounting for their higher damage coefficients.

The average damage coefficient (excluding end pads and pads 1.4 and 1.8) was $(1.4 \pm 0.3) \times 10^{-16}$ A/cm. The error includes systematic errors as well as a 12% error corresponding to the fluctuations in the damage coefficients. The systematic errors are a 10% error in the flux and errors due to the correction for self annealing. The latter has been estimated to be 8% and is mainly due to errors in the contribution from the shortest time constant.

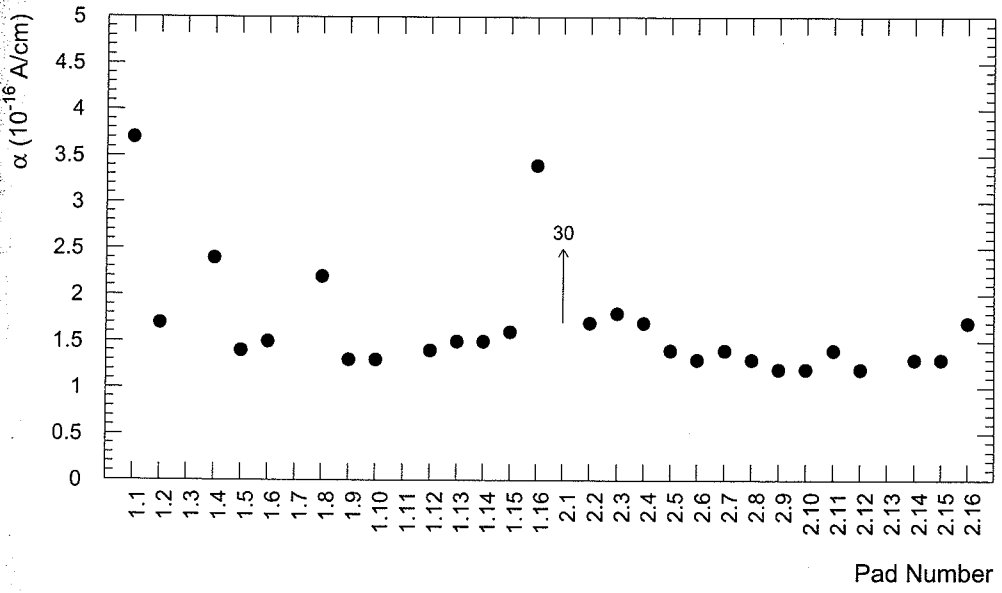

Figure 3.22: Damage coefficients for each pad.

Since the neutrons used were essentially monoenergetic with mean energy of 1.1 MeV there was no need for further correction for the energy spectrum of neutrons.

3.10 Second Neutron Irradiation by the Melbourne Group

3.10.1 Experimental Setup

Neutrons, as in Melbourne Irradiation 1, were produced by bombarding a Li target with protons with an energy of 2.9 MeV. In this irradiation a thick lithium target was used to increase the yield of neutrons. The full lithium target thickness corresponds to a proton energy loss of about 300 keV and the neutrons produced will have a similar range of energies.

The silicon detectors were placed at a perpendicular distance of 12.4 ± 0.7 mm from the target.

Two UA2 segmented silicon detectors were placed next to each other, with the beam centred between them. The layout and numbering scheme are shown

Table 3.3: Current increase for the given average fluence for each pad along with the calculated alphas.

Pad no.	Current Increase (μA)	Average Fluence* (10^{12} n/cm^2)	α (10^{-16} A/cm)
1.1	16.08	4.5	3.7
1.2	8.54	5.1	1.7
1.3	–	5.8	–
1.4	14.86	6.6	2.4
1.5	9.56	7.3	1.4
1.6	11.63	8.0	1.5
1.7	–	8.5	–
1.8	18.28	8.8	2.2
1.9	11.04	8.8	1.3
1.10	10.96	8.6	1.3
1.11	–	8.1	–
1.12	10.43	7.5	1.4
1.13	9.82	6.8	1.5
1.14	8.91	6.1	1.5
1.15	8.04	5.5	1.6
1.16	15.31	4.7	3.4
2.1	23.45	0.82	30.0
2.2	1.17	0.71	1.7
2.3	1.07	0.63	1.8
2.4	0.90	0.55	1.7
2.5	0.66	0.49	1.4
2.6	0.55	0.43	1.3
2.7	0.53	0.38	1.4
2.8	0.43	0.34	1.3
2.9	0.36	0.31	1.2
2.10	0.33	0.28	1.2
2.11	0.33	0.25	1.4
2.12	0.27	0.23	1.2
2.13	–	0.21	–
2.14	0.24	0.19	1.3
2.15	0.23	0.18	1.3
2.16	0.27	0.16	1.7

* NOTE: Average fluence corresponds to the average fluence at which the above leakage current change was observed. For detector 1 this was at the end of irradiation. For detector 2 this was just before the rapid increase.

in figure 3.23. The beam position was such that pads 2 and 3 received the maximum fluence, and corresponding pads on each detector received about the same flux. To achieve electrical connections the silicon detectors were attached to etched copper/kapton foils using conducting epoxy. Electrical connection to the pads was made via bonded gold wires.

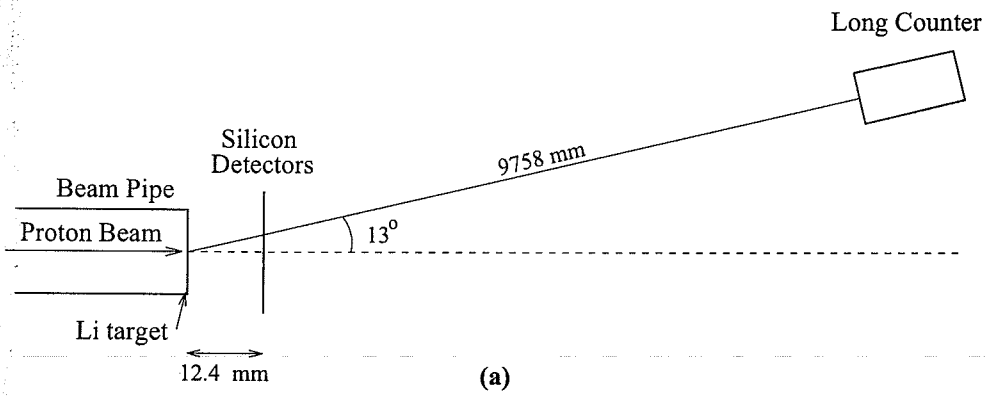

(a)

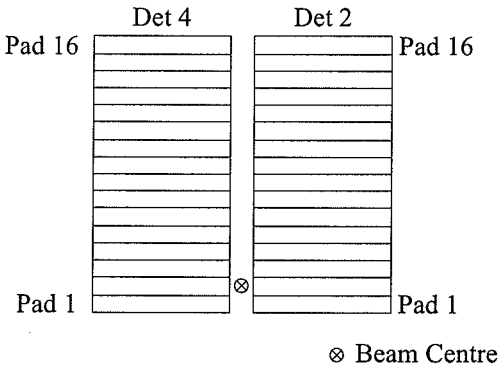

(b)

Figure 3.23: (a) The silicon detectors were placed close to the Li target perpendicular to the proton beam. An off-axis counter at a distance of about 10 m was used to monitor the neutron flux. (b) The beam was centred between detectors 2 and 4, close to pad 2 in each detector.

The detectors were reverse biased at 50 Volts both during and after the irradiation. Multiplexing the signals enabled the measurement of leakage currents on each

pad at two to eight minute intervals. In addition I-V curves were taken regularly. Figure 3.24 shows a schematic of the acquisition system.

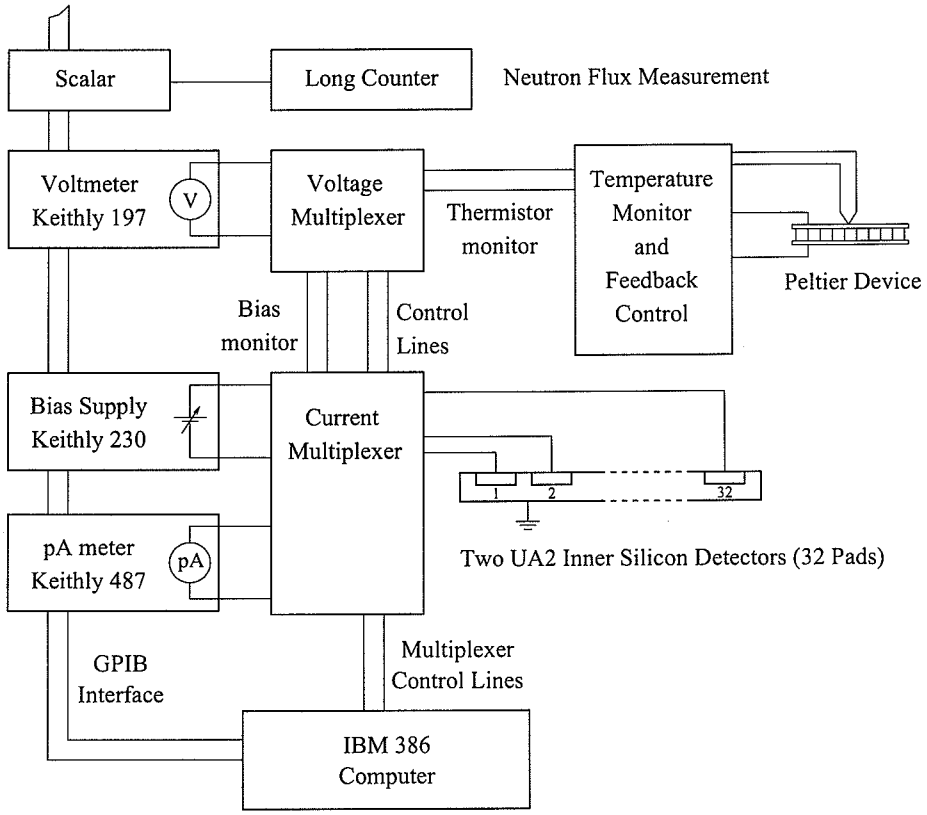

Figure 3.24: Data acquisition system for Melbourne Irradiation 2.

For purposes of temperature control and dehumidification, the detector/kapton assemblies were placed in a vacuum chamber. The temperature of a copper substrate plate, in thermal contact with the kapton, was maintained within 0.2°C of 20°C by use of a thermoelectric heat pump (Peltier device) and servo-control system. A diagram of the apparatus is shown in figure 3.25.

The irradiation took place in two stages. A short irradiation of 13 minutes was followed three hours later by an irradiation for about 65 minutes. The fluence versus time for one pad is shown in figure 3.26. Leakage currents were monitored continuously, at three minute intervals during the exposure and at eight minute intervals

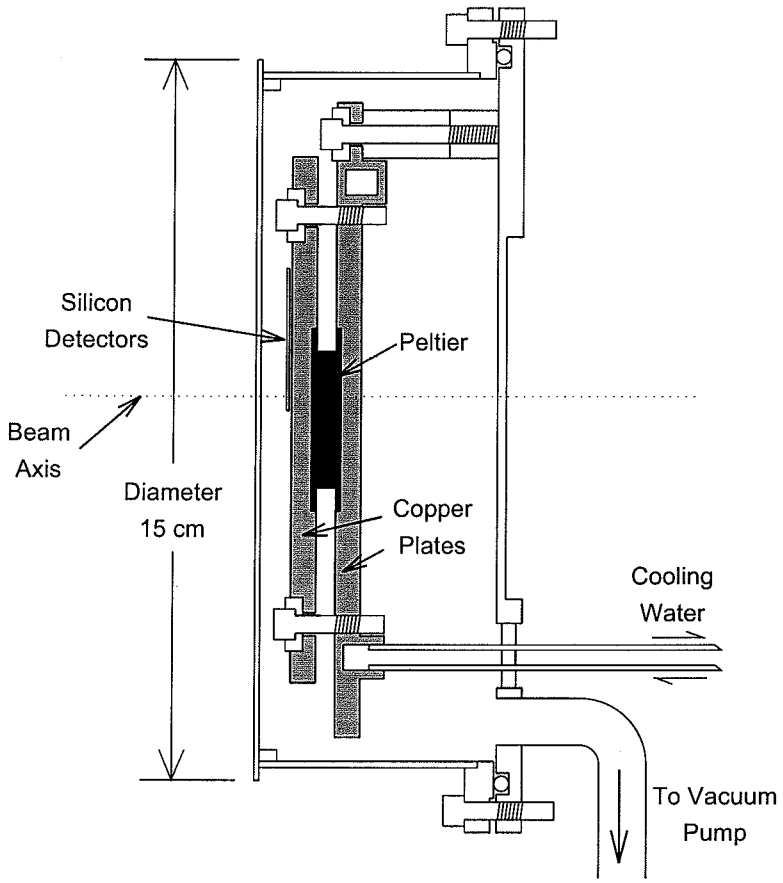

Figure 3.25: Side view of the vacuum chamber used for Melbourne Irradiation 2.

after the irradiation. The data being reported here was collected for ten hours after the irradiation.

Figure 3.27 shows the data obtained for a typical pad. Of the thirty-two pads irradiated, only sixteen showed the expected behaviour during and after irradiation. Data from these sixteen "good" pads is shown in figures 3.28 and 3.29. Other pads exhibited erratic behaviour. This is possibly due to bad connections caused during the transport of the detectors from Melbourne to Sydney, and is not thought to be a problem associated with radiation damage. Consequently further analysis is restricted to the sixteen "good" pads.

The temperature was maintained at 20°C throughout and hence no temperature correction was required.

3.10.2 Flux Calculations

When producing neutrons via protons on a thick Li target, the protons lose energy in the target resulting in a range of energies for the neutrons. The cross section will also vary as the proton loses energy. To calculate the resulting neutron flux and energy distribution a method based on the one described in Ref. [16] was used. Only neutrons produced via Li(p,n)Be were computed; the small contribution from Li(p,n)Be* was ignored.

The flux for each pad was calculated by means of a numerical integration over the area of the pad, allowing for the finite size of the proton beam spot. The flux is given by

$$\int_{beam}\int_{pad} f(\theta)\cos\theta \times \frac{1}{(l\sec\theta)^2} \times \sec\theta \tag{3.31}$$

where $f(\theta)$ is the flux at a given angle θ to the normal and l is the perpendicular distance from the target to the silicon. The first factor $\cos\theta$ in the integrand corrects for the obliquity of the neutron flux away from the axis, the second factor allows for the inverse square law, and the $\sec\theta$ corrects for the longer path length in the silicon for neutrons at large angles. The effective flux is larger due to this inclination. The limits of integration were determined by the positions of the corners of each pad. The

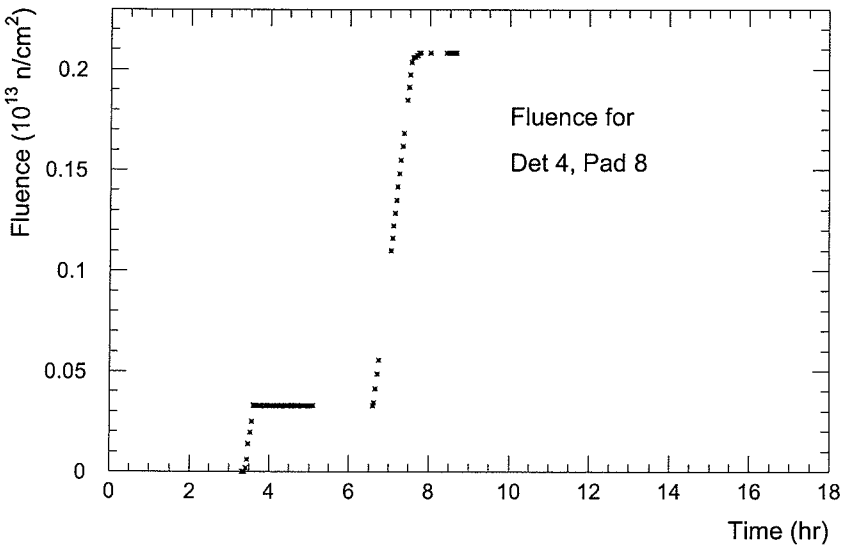

Figure 3.26: The fluence received by a typical pad as a function of time (the origin of the time axis is arbitrary).

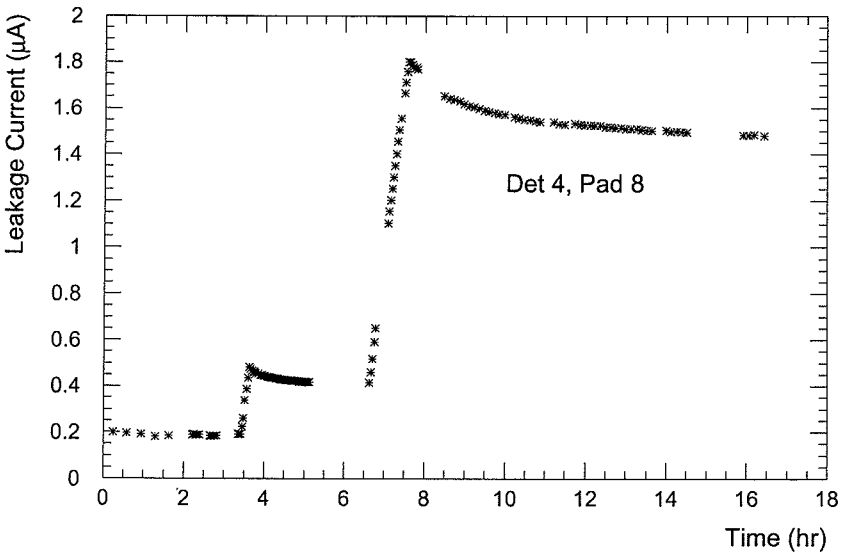

Figure 3.27: The variation of leakage current of a typical pad as a function of time (the origin of the time axis is arbitrary).

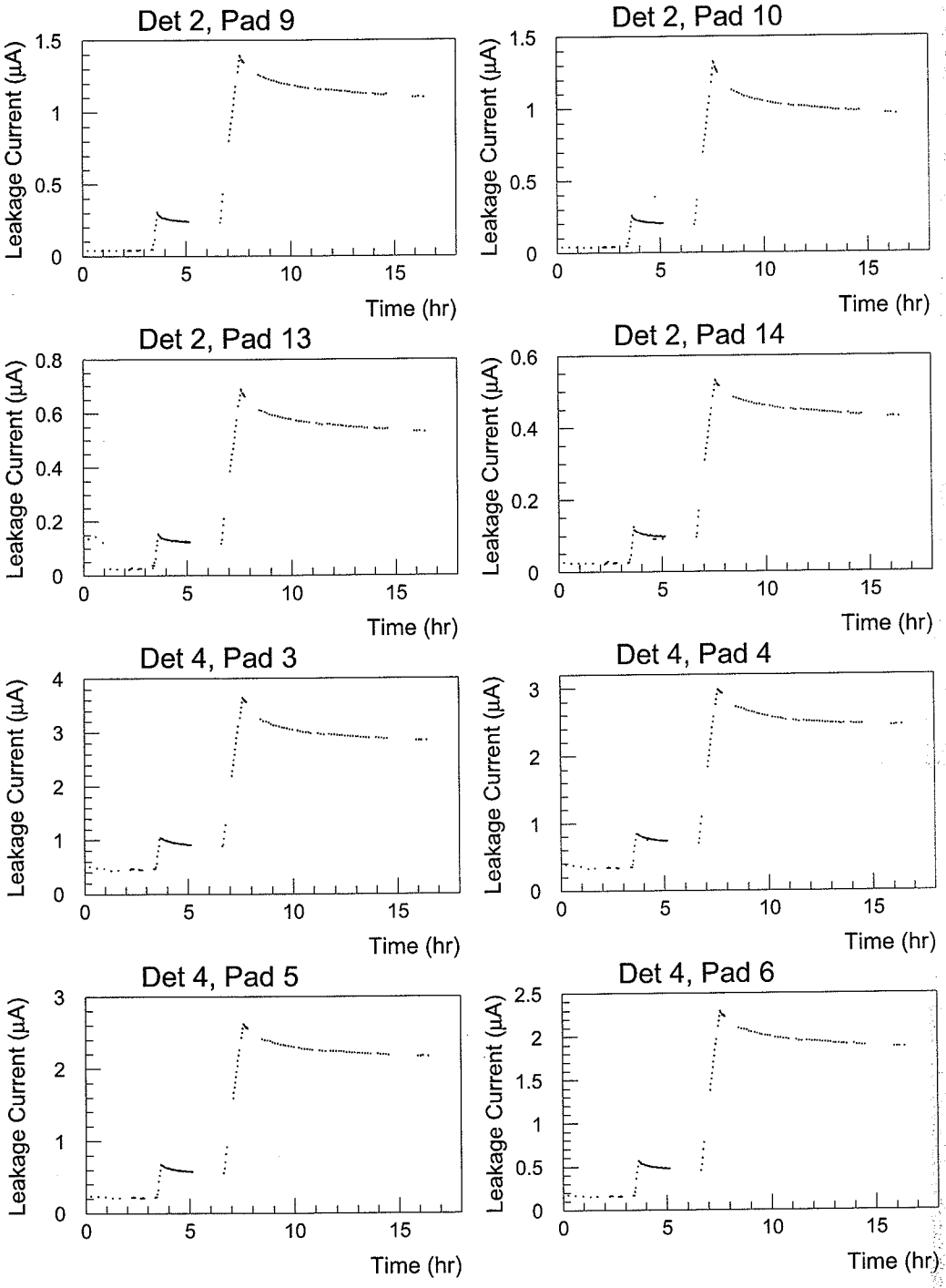

Figure 3.28: The leakage current as a function of time for the first eight good pads.

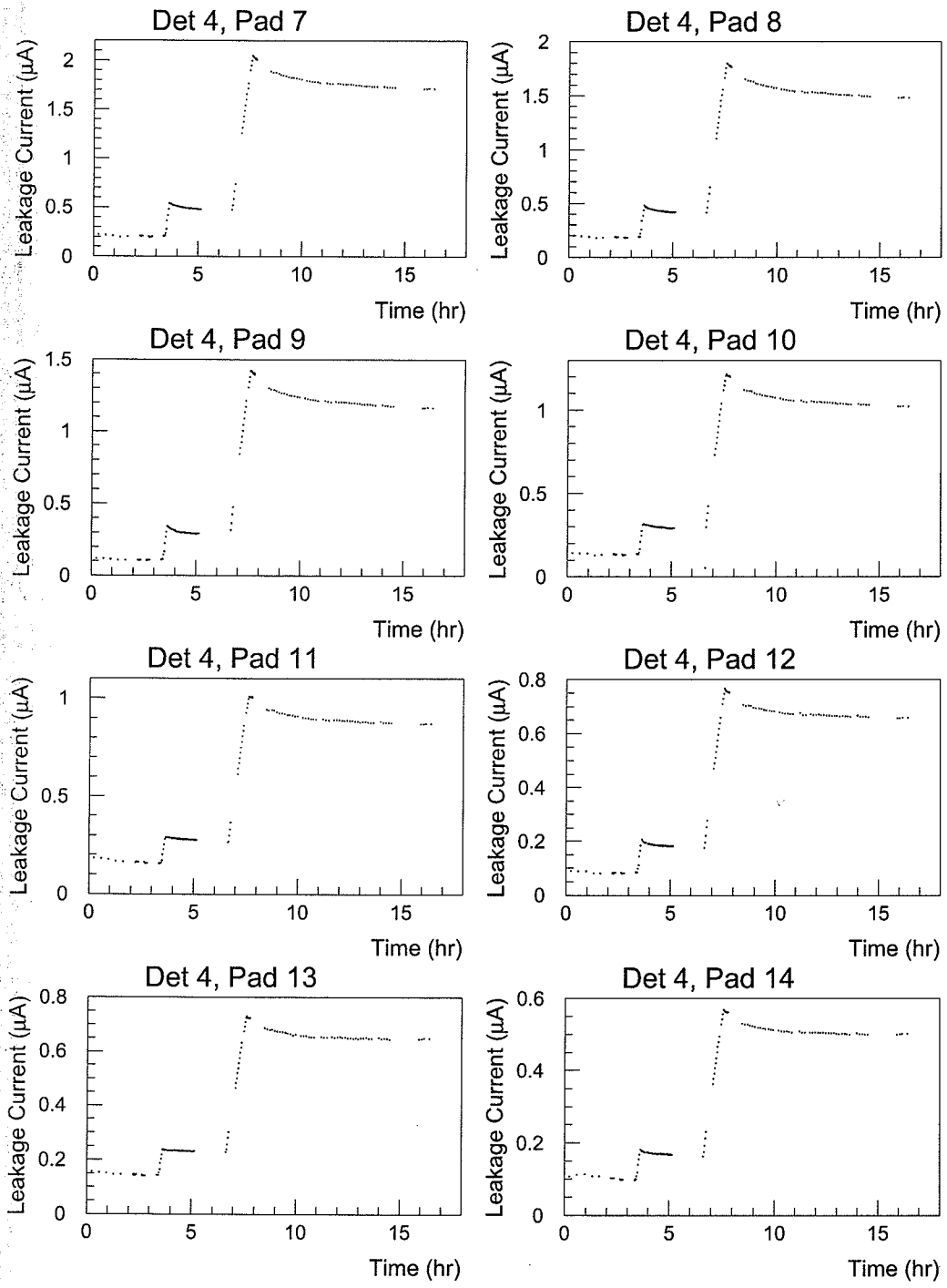

Figure 3.29: The leakage current as a function of time for the remaining eight good pads.

beam spot size was 3 mm in diameter.

The energy range and relative neutron flux for each pad were determined. A "long counter" was used to provide a normalization and to measure the time profile of the flux. The "long counter" was placed approximately 10 metres from the target at an angle of 13° from the beam line, as shown in figure 3.23. This geometry was needed to avoid large dead times in the counter at the high flux rates utilized.

In order to determine the effect of the scattering of neutrons away from the "long counter" by the silicon detectors and their supports, and of scattering into the "long counter", short runs were taken with and without the chamber present. These runs were taken for the same integrated beam current. This resulted in a reduction of about 10% in the "long counter" reading with the chamber in place. The fluxes quoted have been corrected for this. However, this does not correct for any minor variation in the flux distribution over the pads that the presence of the chamber itself may produce.

The calculated fluence achieved at the end of irradiation is shown in figure 3.30 and the energy distributions are shown in figure 3.31. Note that as detectors 2 and 4 were almost symmetric about the beam axis, corresponding pads obtained similar fluences. The differences are due to the beam not being exactly centred.

The uncertainty of the target-to-silicon distance produces a systematic error in the flux of 11%.

3.10.3 Analysis

The change in leakage current due to the irradiation is shown in figure 3.27 for a typical pad. The neutron fluence received for this pad is shown in figure 3.26.

The silicon detectors used in this experiment had been previously irradiated which accounts for their high initial leakage currents, ranging from 100 to 500 nA for detector 4 and 25 to 50 nA for detector 2. It was assumed that the damage associated with this initial leakage current was no longer annealing over the time scale of this experiment. This is a valid assumption as the previous irradiation occurred about one

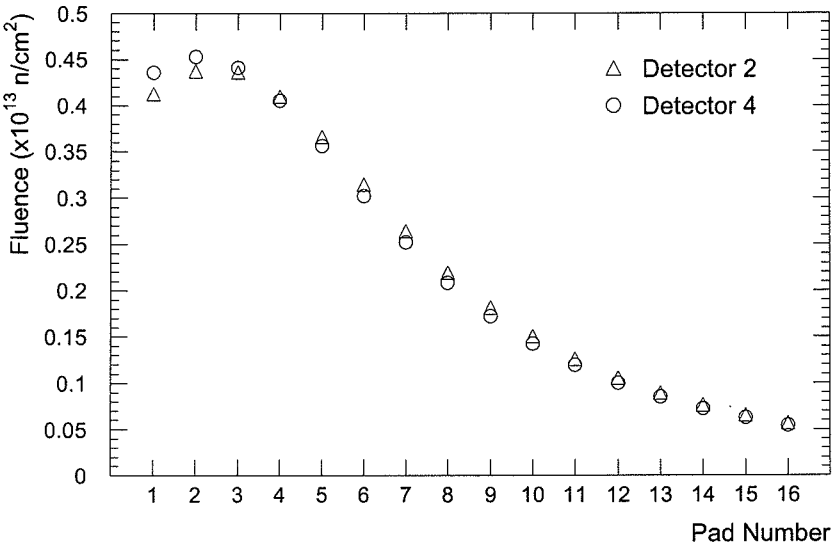

Figure 3.30: The fluence at the end of irradiation, for all 32 pads, calculated as described in the text.

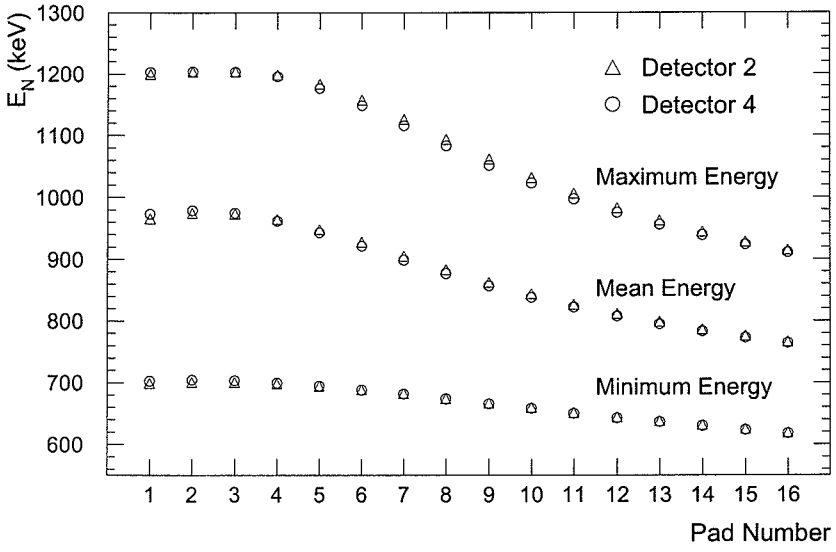

Figure 3.31: The mean energy of the neutrons striking each pad. Also shown are the extreme values.

month before this exposure, and the period over which the present data was taken was much shorter. The quantity of interest is the increase in leakage current and so these initial currents were subtracted. Henceforth all references to the leakage current refer to the increase in leakage current during the irradiation described here.

If the self annealing occurs at the same rate for all pads then one expects the ratio $I(t)/I(T)$, where $I(T)$ is the leakage current at the end of the irradiation and $t > T$, to be the same for all pads. Figure 3.32 show the ratio $I(t)/I(T)$ for the sixteen good pads. It is evident that the rate of self annealing varies significantly between pads. Figure 3.33 shows this ratio for the averaged currents of all the good pads, and for the two extreme pads. Also shown are the expected current decreases predicted using the self annealing parameters obtained by the Hamburg group (Set 1 in Ref. [17]) and from Melbourne Irradiation 1 described in Section 3.9.

In order to study if this spread depended on the fluence received, values of $I(t)/I(T)$ at a time (t = 16 hours) near the end of data collection were plotted against the fluence received by that pad. See figure 3.34. No significant evidence for a fluence dependence is observed.

Self annealing parameters were obtained for the averaged current ratio and for the extreme pads. The minimum annealing was seen in pad 14 of detector 4. The maximum was seen in pad 10 of detector 2. The parameters were found using MINUIT [15] to fit data for the period after the final irradiation with a sum of exponentials. The data was found to be best fit with the sum of two exponentials plus a constant term. The constant term allows for any irrecoverable damage and for annealing with time constants much greater than the time period over which data is being fitted. Due to the relatively short period over which data was collected it was not possible to determine any time constants greater than about ten hours. Therefore it was decided to fix one time constant at the value of 2440 minutes as obtained in Melbourne Irradiation 1. (See Section 3.9.)

The fits have the form given in equation (3.20). The A_i^* must be converted to the A_i, the amplitudes that would be obtained for an instantaneous irradiation.

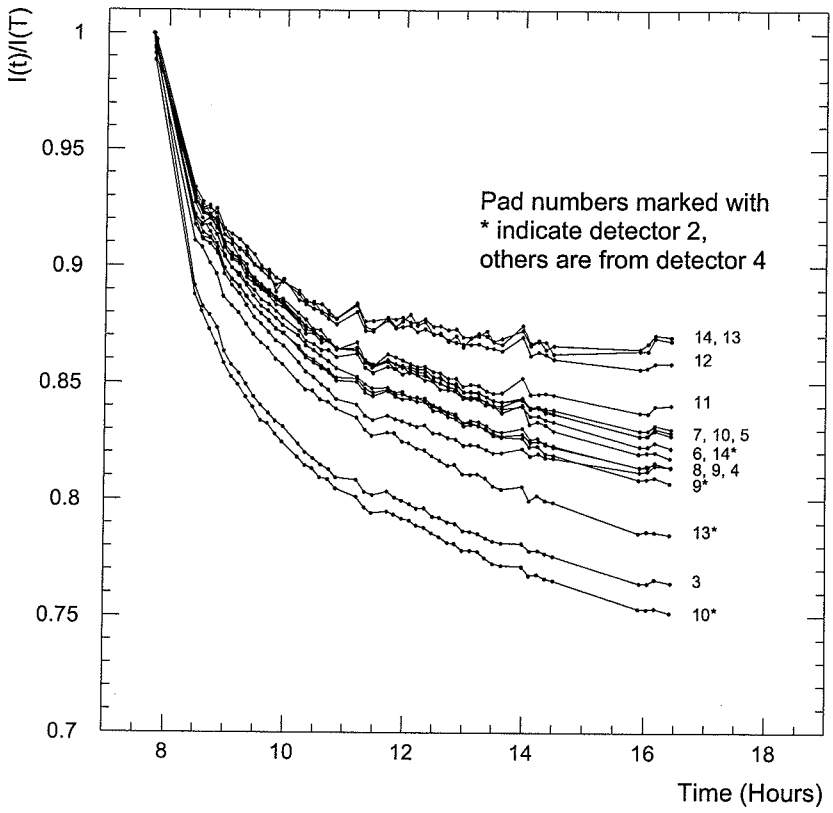

Figure 3.32: The ratios of currents after the end of exposure to the currents at the end of exposure for the sixteen good pads.

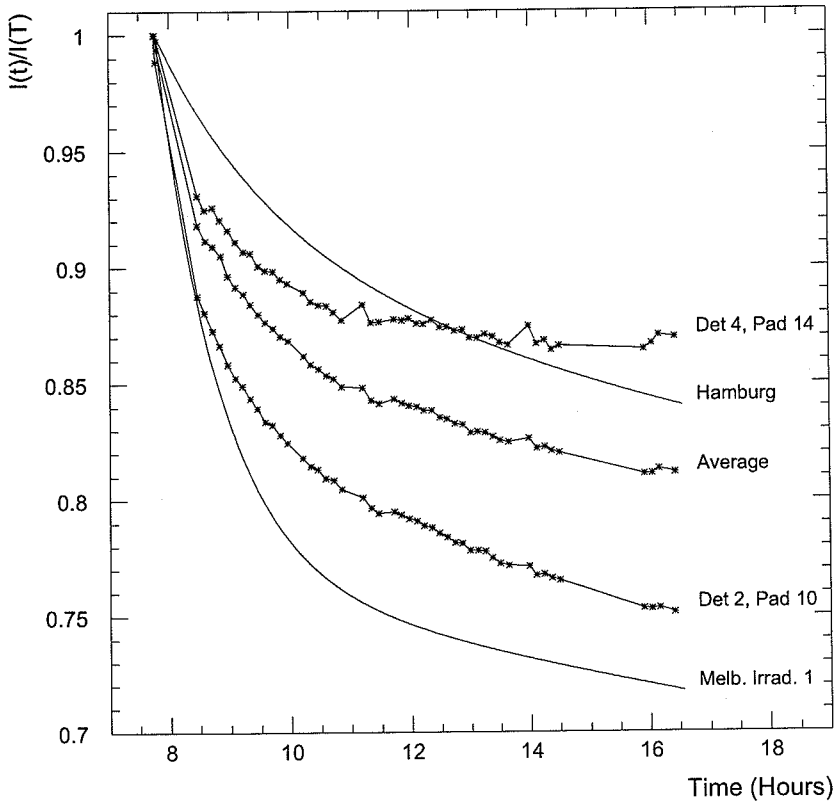

Figure 3.33: The ratios of currents after the end of exposure to the currents at the end of exposure for the average of the sixteen good pads and the two pads showing the most extreme ratios. The curves are described in the text.

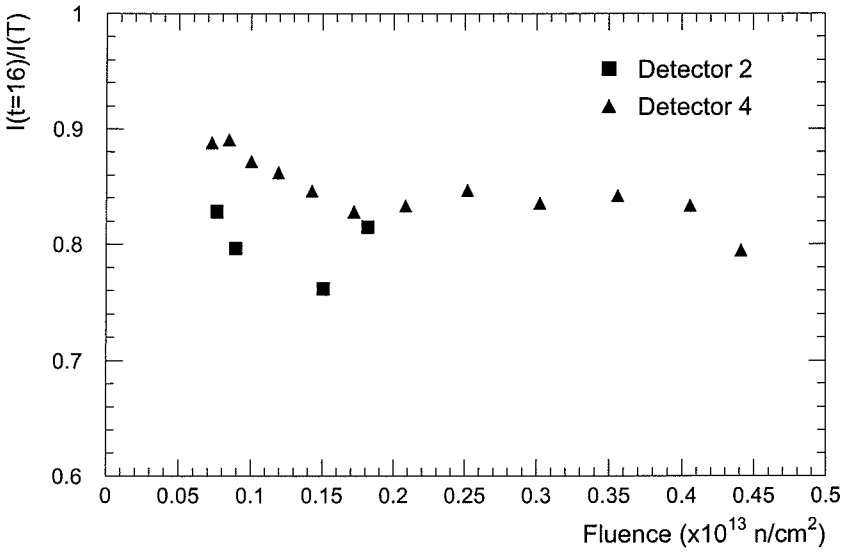

Figure 3.34: The ratios of currents about seven hours after the end of exposure to the currents at the end of exposure as a function of fluence received.

These were calculated with equation (3.24) where c_i was calculated as described in Section 3.6.1. The resulting three sets of self annealing parameters, along with those from Melbourne Irradiation 1 and the Hamburg group, are shown in table 3.4.

Figure 3.35 shows data for pad 8 of detector 4 corrected using the five sets of self annealing parameters using the method described in Section 3.6. The current ratio after irradiation for this pad was close to the average data and hence the correction is good for that set of parameters.

The current increase, if there was no self annealing during irradiation (or for an instantaneous irradiation), would be given by

$$I_0 = I(T)/f \tag{3.32}$$

where according to equation (3.25):

$$f = I(T)/I_0 = \sum A_i c_i \tag{3.33}$$

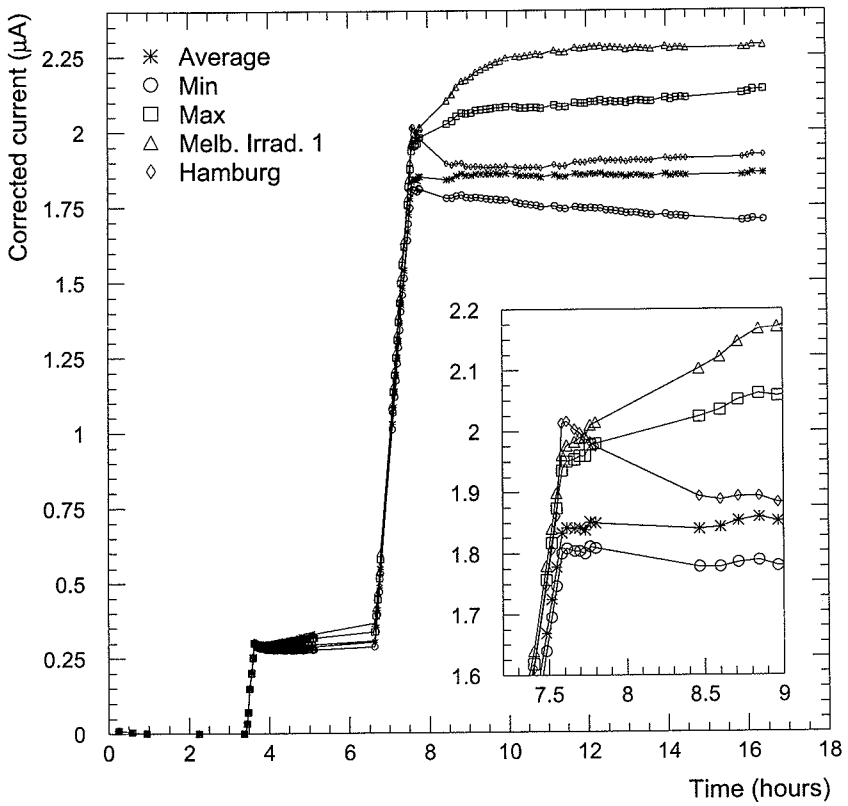

Figure 3.35: The current, corrected for self annealing, as a function of time for five sets of annealing parameters. Inset shows an expanded view about a time near the end of irradiation.

Table 3.4: Self annealing parameters for Melbourne Irradiation 2. Also given are the parameters from Melbourne Irradiation 1 and the Hamburg group.

Average		
i	τ_i (min)	A_i
1	∞	0.473
2	2440*	0.281
3	57.4	0.245

Minimum		
i	τ_i (min)	A_i
1	∞	0.686
2	2440*	0.091
3	58.1	0.222

Maximum		
i	τ_i (min)	A_i
1	∞	0.305
2	2440*	0.381
3	48.9	0.314

Melb. Irrad. 1		
i	τ_i (min)	A_i
1	∞	0.255
2	3.54×10^4	0.159
3	2440	0.196
4	63	0.390

Hamburg		
i	τ_i (min)	A_i
1	6.70×10^5	0.396
2	1.47×10^4	0.201
3	1090	0.131
4	119	0.116
5	17.8	0.156

* Parameter Fixed

and c_i is given in equation (3.27).

The c_i depend only on the flux profile, the time of the irradiation and the τ_i, but not on the fluence. Therefore, for a given set of annealing parameters, f will be independent of fluence and so be equal for all pads.

It is necessary to make some choice of the time used to calculated f and hence I_0. If the self annealing parameters describe a given data set well, then the choice is not important, as the same value should be obtained for all times after the end of irradiation. For an incorrect set of self annealing parameters the time chosen will make a difference. It was decided to take the time corresponding to the actual end of irradiation. In figure 3.35 this time was 7.8 hours.

The values of f^{-1} for the five sets of parameters are given in table 3.5.

A plot of the leakage current increase at the end of irradiation versus fluence is given in figure 3.36 for the sixteen good pads. No corrections have been applied to these currents. The data is consistent with a linear dependence. The slope is a

measure of the uncorrected damage coefficient, which was measured to be

$$\alpha_{un} = \frac{\Delta I}{\Phi \cdot Vol} = 7.2 \times 10^{-17}\ \mathrm{A\,cm^{-1}}\ . \tag{3.34}$$

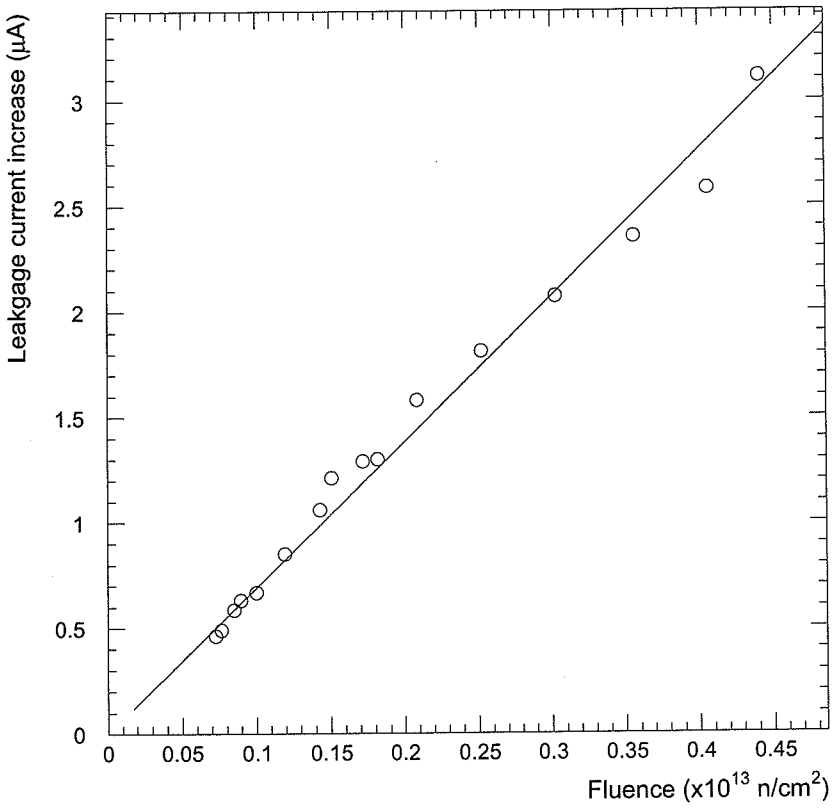

Figure 3.36: The increases in leakage currents for all good pads with respect to the fluence received.

As f will be the same for all pads for a given set of annealing parameters, an alpha corrected for self annealing, α_{cor}, can be obtained using

$$\alpha_{cor} = \alpha_{un}/f\ . \tag{3.35}$$

The resulting corrected damage coefficients are given in table 3.5. The spread of values represents the systematic uncertainty involved in correcting for self anneal-

ing. The mean neutron energy was 0.8 MeV. (See figure 3.31.) The linearity shown in figure 3.36 indicates that the damage coefficient is not strongly dependent on neutron energy in the range studied here. No correction for neutron energy has been applied.

Table 3.5: Damage coefficients for Melbourne Irradiation 2.

Self annealing parameter set	f^{-1}	α ($\times 10^{-17}$) A/cm
Average	1.17	8.4
Minimum	1.14	8.2
Maximum	1.25	9.0
Melb. Irrad. 1	1.27	9.1
Hamburg	1.25	9.0

The variation in the current decrease for different pads, as seen here, is indicative of the variation in self annealing that can occur in supposedly identical pads. It should be regarded as an additional uncertainty in all studies of this type.

3.10.4 I-V Characteristics

I-V curves were taken for all pads at various times before, during and after the irradiations. The timing of these is shown in figure 3.37. Figure 3.38 shows a typical set of curves, while figures 3.39 and 3.40 show the full set. All values of leakage currents reported above were taken at a bias voltage of 50 V. As may be seen from these figures this voltage was always sufficient to achieve full depletion and was never high enough to cause breakdown. A common feature of the I-V characteristics, both before and after irradiation, is a small positive slope after depletion has been obtained.

The Hamburg group have found that the damage coefficient and annealing rate can depend on whether the currents are taken at V_{dep} or at a fixed bias above V_{dep} [18]. They have found that better consistency is obtained when measurements are taken at V_{dep}. Since the first point was taken at a bias voltage of 10 V it is difficult to determine the exact voltage at which the detectors become fully depleted. The

slopes of the I-V curves are not significantly different before and after irradiation and consequently the effect on the determination of the damage coefficient is expected to be second order.

3.11 Discussion and Comparison with Results from Other Groups

Table 3.6 compares the damage coefficients found by several groups. All values have been corrected for self annealing and have either been measured at 20°C or have been measured at room temperature and normalized to 20°C. The irradiations have been carried out with neutron sources with energies near 1 MeV or the data have been corrected to 1 MeV using NIEL data. These corrections have been performed by the groups reporting the data.

Table 3.6: Comparison of damage coefficients obtained in this thesis and by other groups.

α ($\times 10^{-17}$ A/cm)	Reference
14 ± 3[a] 8.4 ± 1.0[a]	Melb. Irrad. 1 Melb. Irrad. 2
8 ($\Phi < 8 \times 10^{12}$) ~ 20 ($\Phi > 8 \times 10^{12}$)	Hamburg [6]
9[a]	Cambridge [17]
9[a] 8	Dortmund [17] [19]
6.7 ± 0.4 7.4 ± 0.4[b]	Lemeilleur, *et al.* [10]
5.3 ± 0.6	Gill, *et al.* [20]

[a] Measured with UA2 inner silicon detectors.
[b] Measured with p-type silicon. Others measured with n-type silicon.

The damage coefficients are observed to have some variation, with most being around 8×10^{-17} A/cm. A number of the measurements were performed with UA2

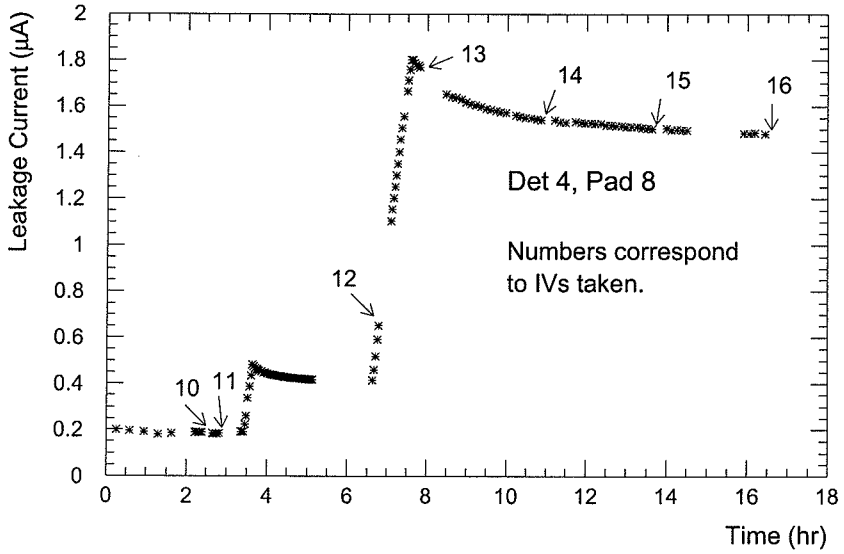

Figure 3.37: The current time profile for one pad showing the times at which I-V characteristics were studied.

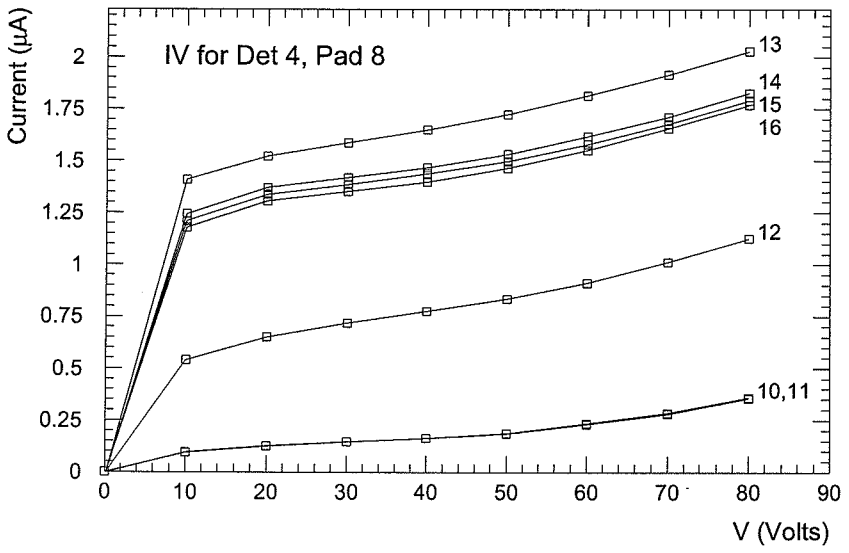

Figure 3.38: The I-V characteristics for a typical pad taken at the times indicated in figure 3.37.

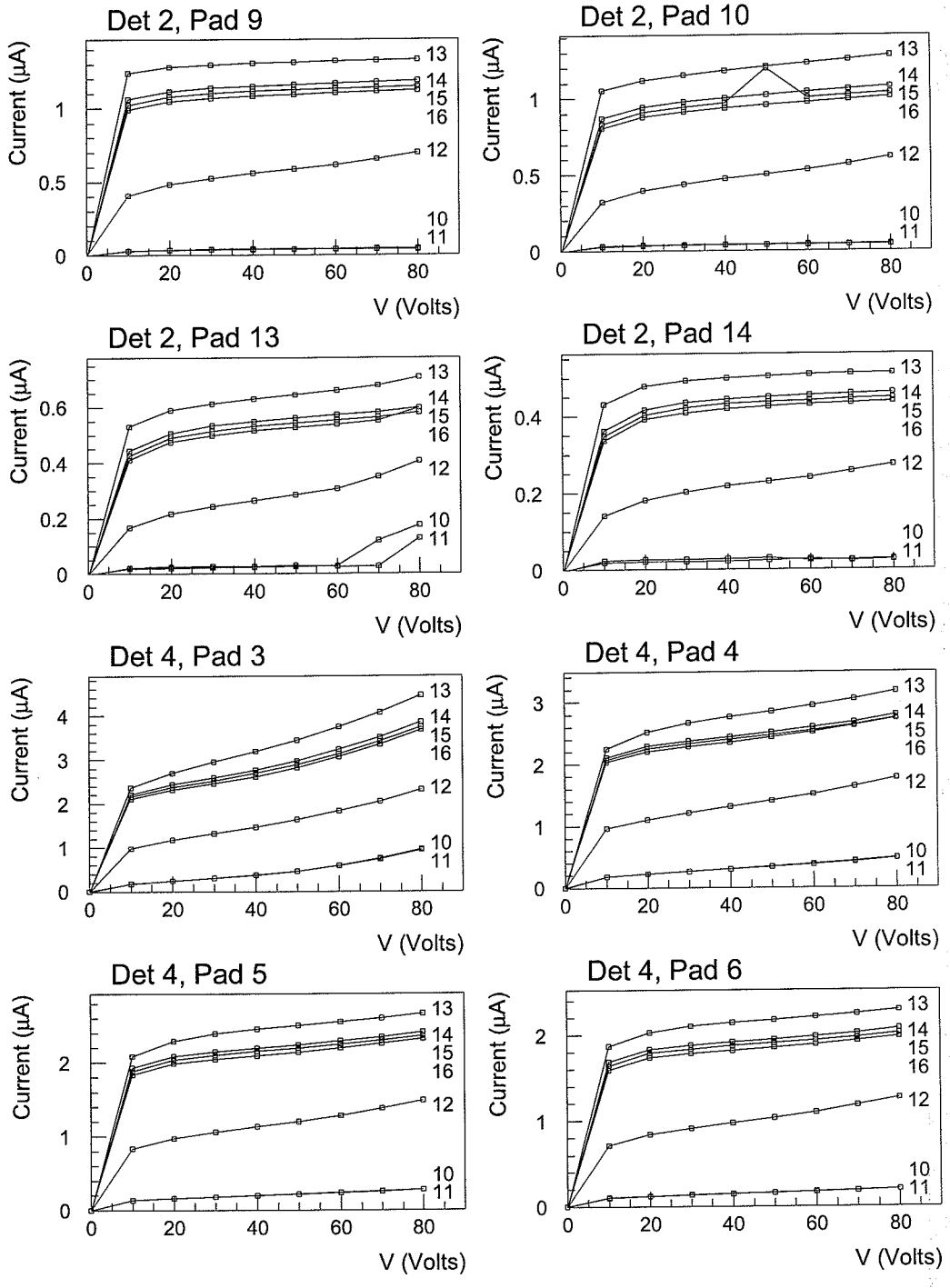

Figure 3.39: The I-V characteristics for the first eight good pads taken at the times indicated in figure 3.37.

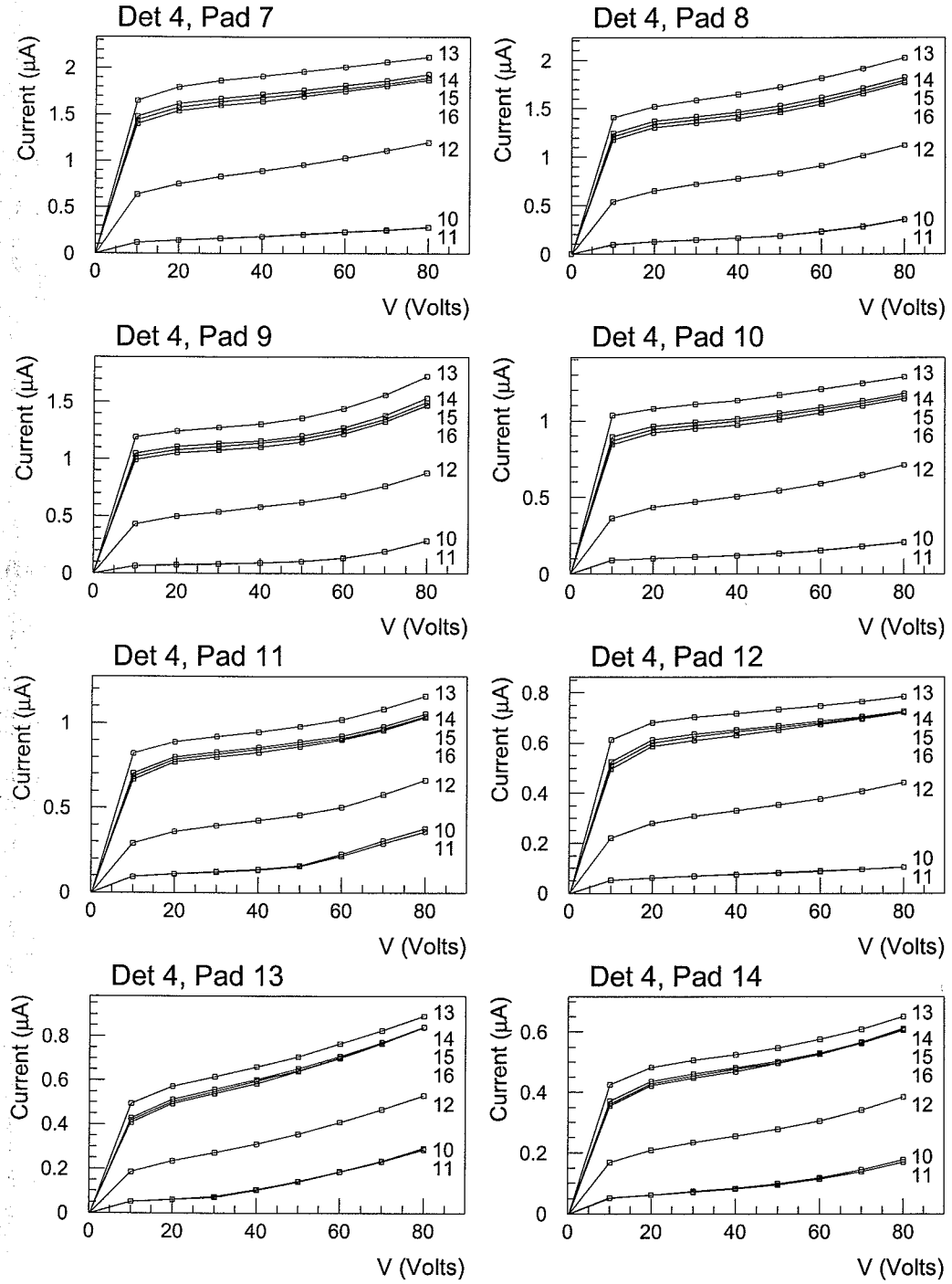

Figure 3.40: The I-V characteristics for the remaining eight good pads taken at the times indicated in figure 3.37.

inner silicon detectors. These are indicated in the table. Apart from the measurement made in Melbourne Irradiation 1, these gave consistent results. The measurements cover a range of detector types, different neutron energies and fluences and different measurement conditions such as having the detectors biased or unbiased. No consistent differences have been observed with any of these variations.

The Hamburg group observed a different damage coefficient for high and low fluence which they consider to be associated with type inversion [6]. After substantial self annealing this discrepancy is reduced. This behaviour, however, is not observed by other groups (e.g. [19]).

During the operation of the LHC where the irradiation is taking place over several months, contributions to the leakage current which anneal with short time constants will not be seen. It is of more interest to compare the damage coefficient after long term annealing. Figure 3.41 shows a number of annealing curves from different groups. These have been normalized to the damage coefficient reported with the annealing parameters and so represent the damage coefficient expected at times after a short irradiation. For Melbourne Irradiation 2 the three sets obtained (average, minimum and maximum) are shown normalized with their respective damage coefficient. Also shown are some measurements taken by Baldini *et al.* [21] at 1 week and 6 months after irradiation. The Dortmund group have obtained results [19] consistent with the curve obtained by Hamburg.

There is a large amount of spread in the data. Some of this may be due to errors in the fluence determination which is generally of the order 10–20%. Apart from this it is not clear why the results deviate. The results from Melbourne Irradiation 2 and the Hamburg curve are not too different. After some annealing the comparison between Melbourne Irradiation 1 and the Hamburg curve is better than for the damage coefficient corrected for self annealing as given in table 3.6. For example, the damage coefficient after 80 days is 3.7×10^{-17} A/cm for Melbourne Irradiation 1. This can also be seen in figure 3.17 where for times much longer than the irradiation time the damage coefficient can be obtained directly. The value from Melbourne Irradiation 1

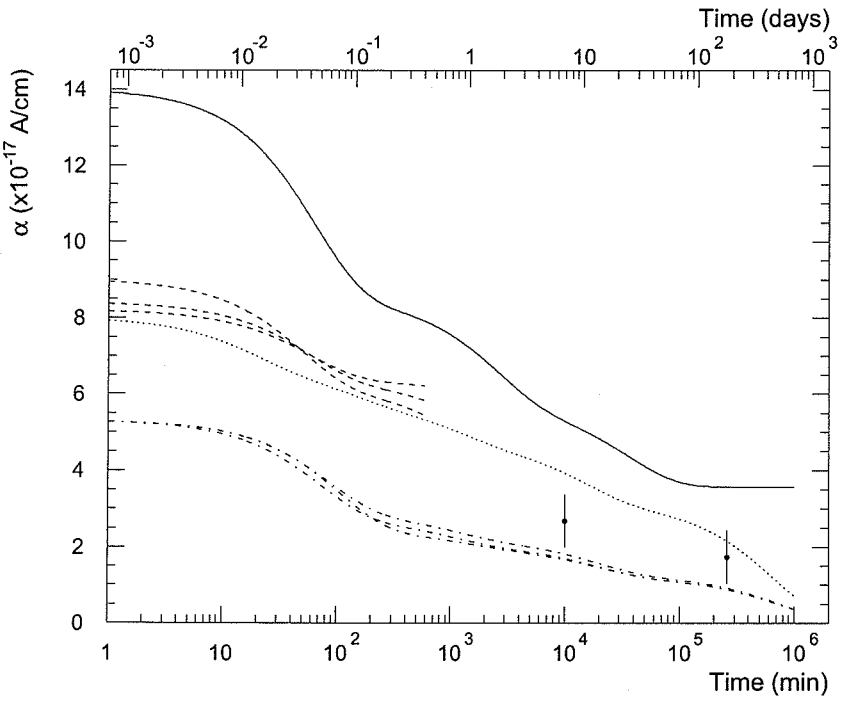

Figure 3.41: Comparison of self annealing curves from Melbourne Irradiation 1 (solid line), Melbourne Irradiation 2 (dashed lines), Hamburg group (dotted line), and Gill *et al.* [20] (dash-dotted lines). Also shown are data points from Baldini *et al.* [21].

is 40% higher than the corresponding Hamburg value which is 2.7×10^{-17} A/cm. This is compared with a 75% difference for the self annealing corrected value.

The data from Melbourne Irradiation 2 only covered 10 hours after the irradiation and so not much can be concluded about the long term behaviour. Since the irradiation was short, a good measurement of the short term annealing could be obtained and consequently this measurement provided a more accurate determination of the damage coefficient corrected for self annealing. For Melbourne Irradiation 1, which took place over three days, the shortest time constant could not be accurately determined. It is quite possible that this component was overestimated which in turn would overestimate the damage coefficient obtained. This may partly explain the discrepancy between the two measurements.

As observed in Melbourne Irradiation 2, the short term annealing can vary substantially. This has also been observed by the Hamburg group [18] where they found deviations for times less than 1 hour. After this, however, data tended to fall on the same annealing curve.

The long term data is insensitive to the determination of the short time constants and to the details of the irradiation (i.e., whether it is a 5 minute or a week long exposure). Therefore the damage coefficient at, for example, 100 days is a better value to compare. It is also a more important quantity when considering LHC predictions, for which the short time constant terms do not contribute. Since Melbourne Irradiation 1 gave information about the long term behaviour these results have been used in Chapter 6 to predict leakage currents expected in LHC operation. Comparisons are also made with the parameters obtained by Hamburg.

3.12 Measurements at Other Temperatures

Several groups have made measurements at various temperatures. Figure 3.42, taken from Ref. [7], shows a comparison of measurements taken at 0°C, 10°C, and

20°C. The ratios of currents at 1 week after irradiation are

$$I(20) : I(10) : I(0) = 1 : 0.82 : 0.23 .$$

These ratios are observed to be higher than the ratios calculated using the temperature dependence given in equation (3.29):

$$I(20) : I(10) : I(0) = 1 : 0.40 : 0.15 .$$

This is likely to be due to the temperature dependence of the annealing process. Defects that anneal out at room temperature may be "frozen in" or anneal at a much slower rate at low temperatures. Also, some contributions that appear when irradiated at low temperatures may anneal too rapidly at warm temperatures to be observed.

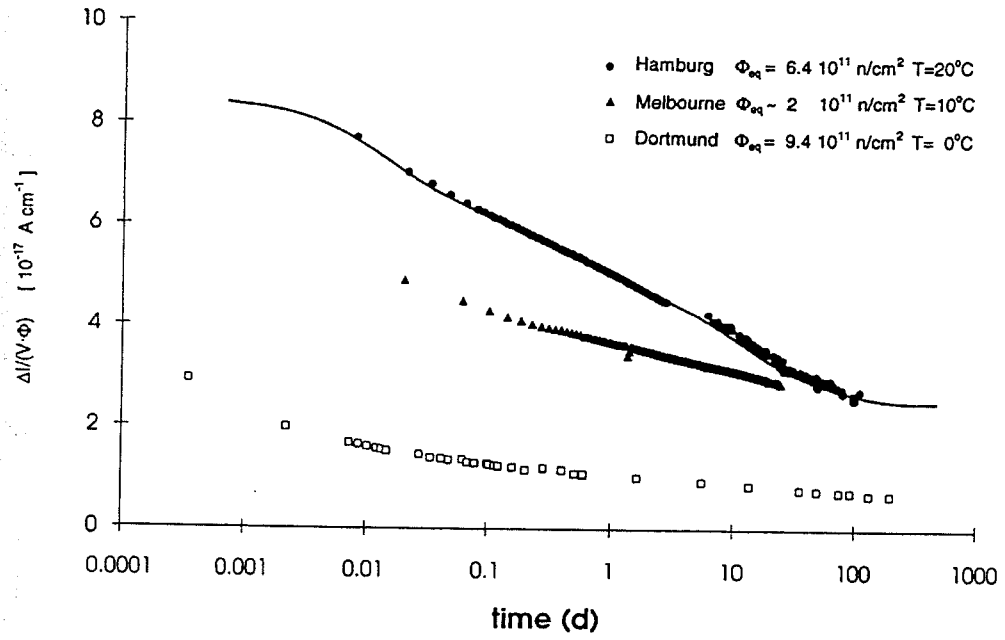

Figure 3.42: Comparison of the leakage current annealing at different temperatures. [7]

When detectors are irradiated at low temperature and are later warmed up,

then after some initial rapid annealing the leakage currents are observed to approach the value expected if irradiated at room temperature [17]. This indicates that the processes producing the damage are not significantly dependent on the temperature. The annealing rates, however, are affected.

The cooling of the detectors is an effective way of reducing the leakage currents. The self annealing, however, is reduced and so there is an advantage of having some warm up time to allow further annealing. Some of the consequences of operating at different temperatures are seen in Chapter 6.

Chapter 4

Comparisons between FLUKA and Experiment

4.1 Overview of FLUKA

FLUKA [22] is a Monte Carlo code which is well suited to simulating cascades initiated by high energy hadrons or leptons. The code has undergone many improvements since its 1986 release [23]. A description of these improvements can be found in Refs. [24, 25, 26, 27].

Most of the improvements relevant to calculations carried out in this thesis are associated with the inelastic event generator. FLUKA is able to simulate in detail inelastic nuclear interactions in the energy range 20 MeV to 10 TeV. A major improvement to this part of the code has been the incorporation of a nuclear evaporation model which accounts for the emission of neutrons, protons, and heavy fragments from the excited nuclei, and the de-excitation of the nucleus by gamma emission.

The electromagnetic part of FLUKA has been extensively improved as described in Ref. [24]. Calculations in this thesis have been mainly concerned with quantities which are relatively unaffected by electrons and photons. Therefore, to save in computer processing time, no use has been made of the electromagnetic part of FLUKA.

The improvement to FLUKA which has the most bearing on the calculations presented in this thesis is the incorporation of code to transport low energy neutrons below 20 MeV. This code is similar to MORSE [28], using a multigroup cross section

library. The cross section library contains around 40 elements which are commonly used in accelerator and detector applications. The cross section sets are comprised of 37 neutron energy groups. The lowest energy group is the thermal group covering the energy range 10^{-5}–0.4 eV. Doppler reduced broadening has been taken into account for a few materials at liquid argon (87 K) and liquid helium (4 K) temperatures. Neutrons can be transported down to optionally defined thresholds which can be as low as thermal neutrons (i.e. the thermal group). The survival probability (that is, the probably that a particle will continue to be transported after it interacts with a nuclei in the medium) can be set for neutrons in the energy group corresponding to the chosen threshold. If not set, the survival probability will depend on the neutron absorption cross section. Neutrons affected by the forced survival probability will be given an appropriate weighting. Setting the survival probability is useful for the thermal group where if the neutron absorption cross section is low, excessive computer time may be spent transporting the thermal neutrons. If the neutron absorption cross section is high, too few thermal neutrons might make it to the region of interest, resulting in poor statistics.

Transport of charged hadrons is possible down to an energy of 20 MeV. Below this, particles are ranged out to rest. This is done in a straight line regardless of whether or not the particle is in a magnetic field. If applicable the particle eventually decays or is captured. Antiprotons and π^-s that are ranged out to rest are made to annihilate on a nucleus. All other forms of transport, such as multiple scattering, delta ray production, inelastic or elastic collisions, and allowing particles to decay during flight, are ignored below this energy.

FLUKA uses combinatorial geometry. This involves defining a number of bodies such as cylinders, spheres, cones, and regions bounded by a plane. Complex 3-dimensional geometries can be created by adding and subtracting these bodies.

A number of "scoring options" are included in FLUKA. The track-length scoring option has been used extensively in this work. This option sums the track-lengths of the required particle in a requested region. The average flux is given by the

summed track-length divided by the region's volume. (See Appendix A.) A boundary crossing option is available with optional inverse cosine weighting, allowing the flux on region boundaries to be determined. In many of the calculations in this thesis a user written routine has been used, which is called at each boundary crossing, allowing more flexibility in scoring.

All FLUKA simulations in this thesis have been carried out with the March 1993 version of FLUKA on CERN's IBM VM computing facility.

4.2 Review of Tests of FLUKA

One of the tests of FLUKA has come from comparison with a series of experiments referred to as the "Rösti Runs". These experiments were designed to measure the radial and longitudinal shower development, initiated by high energy particles, in a block of material. They provide a benchmark for programs such as FLUKA. Data from three experiments have been compared with FLUKA in Ref. [25]. The three experiments were:

1. The irradiation of an iron structure by a 200 GeV/c hadron beam [29].
2. The irradiation of the same iron structure by a 24 GeV/c proton beam [30].
3. The irradiation of a lead structure by a 200 GeV/c hadron beam [31].

The irradiated structures consisted of 20 plates of lead or iron of 5 cm thickness with thin Al detector support plates placed in the 7 mm deep slots between the plates. The transverse dimensions were 30×30 cm^2 for the iron structure and 50×50 cm^2 for the lead structure.

The production rates of isotopes in a number of activation detectors were measured which were sensitive to neutrons with energies between about 0.8 and 25 MeV and hadrons with energies above about 35 MeV. Table 4.1 summarizes the main contributing reactions, the sensitive energy range, and sample sizes.

The above structures were simulated with FLUKA and production rates were calculated using known cross sections for the reactions given in table 4.1. Figures 4.1

Table 4.1: Summary of activation techniques.

Main contributing reaction	Sample size (thickness × diameter)	Nominal energy range
$^{115}In(n,n')^{115m}In$	0.3 mm × 10 mm	0.8–15 MeV
$^{32}S(n,p)^{32}P$	6 mm × 23 mm	3–25 MeV
$^{27}Al(n,x)^{24}Na$	0.5 mm × 10–30 mm	6–25 MeV
$^{27}Al(h,x)^{18}F$	0.5 mm × 10–30 mm	> 35 MeV

and 4.2 taken from Ref. [25] show the longitudinal and radial comparisons with data from the ^{115}In (n,n') ^{115m}In reaction. The points are the measured data and histograms are the FLUKA values.

Agreement within 20% of the measured results was observed in most cases, although up to 40% disagreement was seen. Table 4.2 taken from Ref. [25] gives the ratio of FLUKA simulations to measured data. The values given are the average of ratios for detectors which were at different radial positions and on different plates. Also given are the averages for the different detector types and for the three experiments. The absorbed dose as measured by RPL (radiophotoluminescent) dosimeters is also given.

4.3 Comparison of Neutron Fluxes in UA2 with FLUKA

In order to obtain measured values of neutron flux in a realistic detector environment "fission counters" were installed in the UA2 detector. Neutron and other radiation detecting dosimeters had previously been installed in the UA2 detector but these only gave an integrated dose. The fission counters measured the variation in neutron flux in real time. This allowed the neutron flux produced during stable beam conditions, as well as at other times, to be monitored. These measurements have been compared with neutron fluxes calculated using FLUKA.

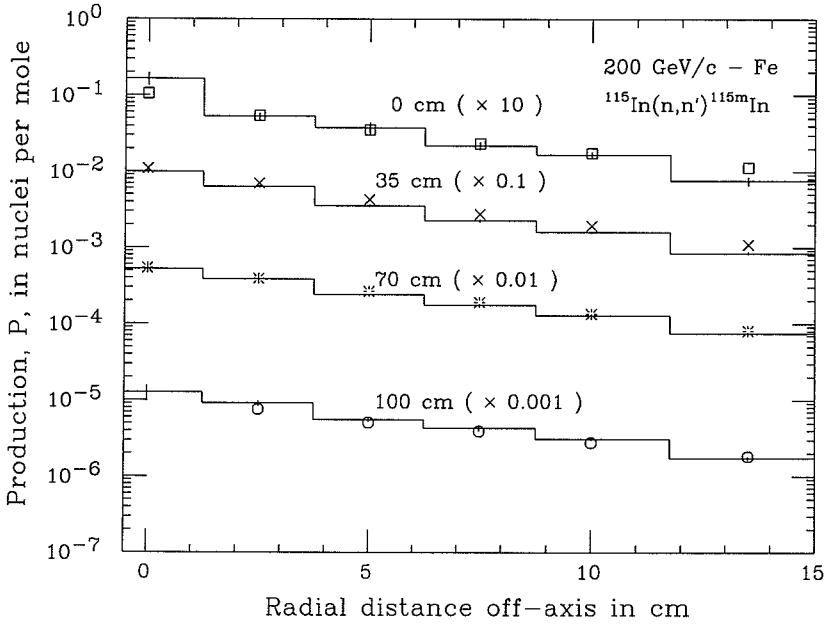

Figure 4.1: Comparison of the calculated and measured production of ^{115m}In from ^{115}In as a function of radial distance off-axis at different depths in an iron structure irradiated by 200 GeV/c hadrons. The data are scaled as indicated in brackets for the sake of clarity. [25]

Table 4.2: Ratios of the results from FLUKA simulations to the measured data, averaged over detector positions, for the different measurement techniques and experiments. [25]

Detector system	200 GeV/c Fe	24 GeV/c Fe	200 GeV/c Pb	Mean over experiments
^{115}In(n,n')^{115m}In	0.91±0.02	1.20±0.05	1.34±0.09	1.12±0.03
^{32}S(n,p)^{32}P	0.96±0.03	1.35±0.05	0.70±0.02	0.85±0.03
^{27}Al(n,x)^{24}Na	0.85±0.02	1.03±0.02	0.63±0.01	0.82±0.01
^{27}Al(h,x)^{18}F	1.30±0.04	1.32±0.05	1.04±0.03	1.17±0.03
Mean over detectors	0.92±0.02	1.14±0.02	0.76±0.02	0.91±0.01
RPL dosimeters	0.91±0.06	0.93±0.07	–	0.92±0.05

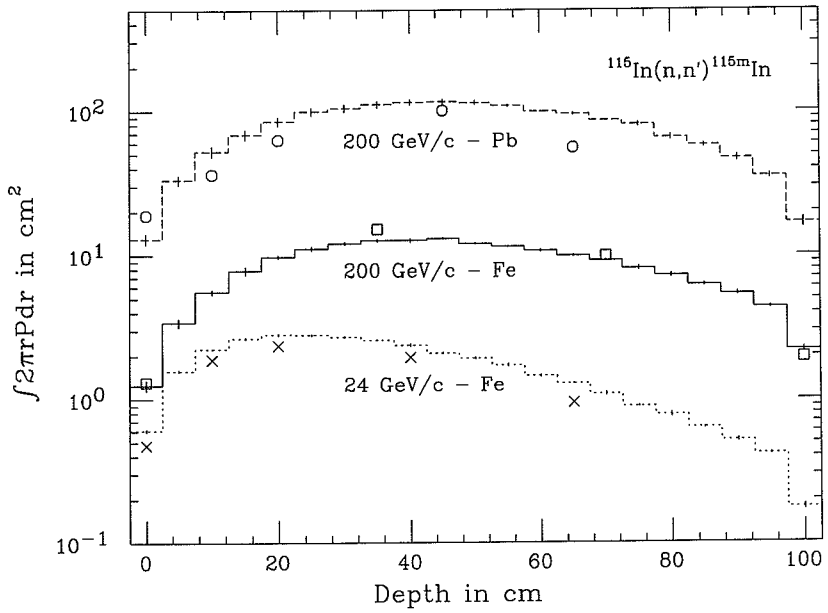

Figure 4.2: Comparison of the calculated and measured variation of the radially integrated production of ^{115m}In from ^{115}In as a function of depth in iron and lead structures irradiated by 200 GeV/c and 24 GeV/c hadrons. [25]

4.3.1 Description of the UA2 Detector and Geometric Modelling with FLUKA

The UA2 detector was located at CERN in the SPS accelerator with protons and antiprotons being collided with a centre of mass energy of 630 GeV. A full description of the detector is given in Ref. [32]. A schematic of the detector is show in figure 4.3. Details given here are mainly concerned with aspects relevant to geometric modelling with FLUKA. The geometry used in the FLUKA calculations is shown in figure 4.4.

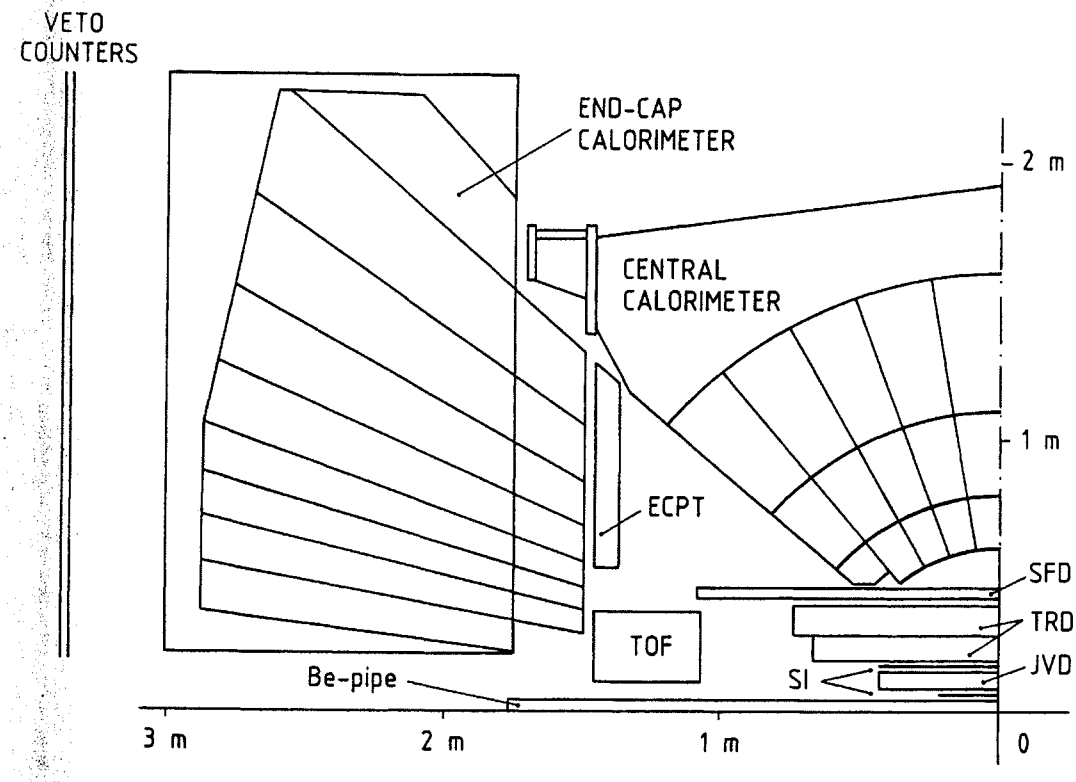

Figure 4.3: Schematic of the UA2 detector. One quarter segment is shown.

The inner detector region is comprised of silicon layers at radii of about 3 cm and 15 cm, a Jet Vertex Detector (JVD) between 3.5–13.5 cm, a Transition Radiation Detector (TRD) between 17–38 cm, and a Scintillator Fiber Detector (SFD) between 38–44 cm. The two silicon layers have been simulated each by a 1 mm thick layer

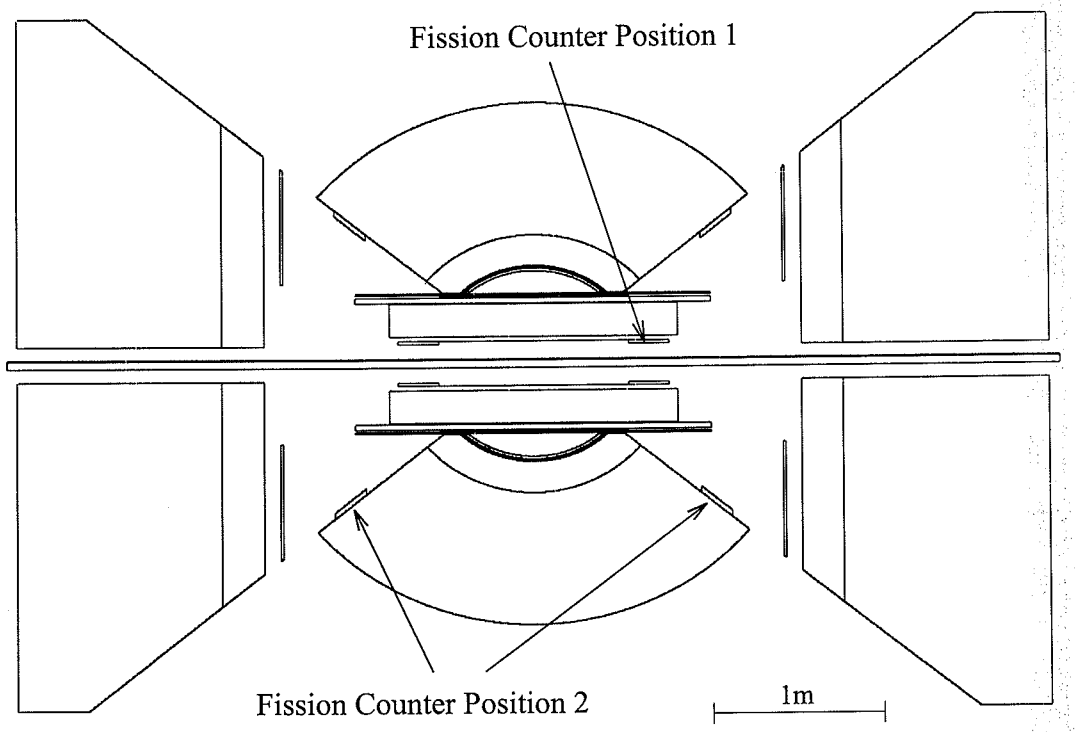

Figure 4.4: FLUKA geometry for the UA2 detector. The positions of the fission counters are indicated.

of silicon of length 160 cm. The thickness is greater than the actual thickness of the detectors (300 μm) to take into account the presence of material in the supports and electronics. However, these layers are not expected to have a significant effect on the simulation and their actual length is smaller. The JVD is a drift chamber. It contains negligible material as concerns the calculations here and has not been included. The TRD is comprised of about 800 propylene foils in two stacks of length 160 and 180 cm. This has been simulated as one region of length 170 cm with CH_2 of density 0.08 g/cm^3 corresponding to the approximate fraction of the volume occupied by the foils. The SFD contains around 60,000 scintillator fibers with a diameter of 1 mm and a length of 2.1 m. This has been simulated with two sections, with radial extent 38.6–41.8 cm and 43.3–44.3 cm, containing scintillator with reduced density of 0.44 g/cm^3. (Scintillator typically has a H/C ratio of 1.10 and density of 1.032 g/cm^3.) Within the SFD lies a lead converter at a radius of 42.5 cm. It is tapered with an average thickness of 6.8 mm and a length of 110 cm.

The central calorimeter covers the region $40° < \theta < 180°$, with an approximate spherical geometry. The central electromagnetic calorimeter extends radially from 60 cm to 80 cm, with a 18 mm thick layer of aluminium at the front face. It consists of a sandwich of 26 layers of 3.5 mm thick lead and 27 layers of 4 mm thick scintillator. The central hadronic calorimeter extends radially from 80 cm to 166 cm with a sandwich of 40 layers of 15 mm thick iron, 5 mm thick scintillator and 1 mm gaps. The aluminium layer and the first 4 layers of the electromagnetic calorimeter have been included in the simulation while the rest has been approximated by a homogeneous mixture of iron and scintillator with a volume ratio of 3.5 : 4. The reason for this is to simulate more accurately the early stages of the shower development. Deeper into the calorimeter the overall shower development should be reasonably approximated by using a homogeneous mixture of the appropriate materials. The hadronic calorimeter has been simulated with a homogeneous mixture of iron and scintillator with volume ratios of Fe : Scint : vacuum equal to 5 : 15 : 1.

The end-cap calorimeter has angular coverage of $5.6° < \theta < 45°$. The electro-

magnetic part extends longitudinally from 159 to 183 cm, with 32 layers of 3 mm thick lead and 33 layers of 4 mm thick scintillator. The hadronic part extends longitudinally from 183 to about 300 cm, with layers of 25 mm thick iron, 4 mm thick scintillator and 2 mm gaps. The end-cap calorimeters have been simulated with homogeneous mixtures with a volume ratio Pb : Scint equal to 3 : 4 for the electromagnetic part, and volume ratios of Fe : Scint : vacuum equal to 25 : 4 : 2 for the hadronic part.

End Cap Proportional Tubes (ECPT) are located in front of the end-cap calorimeter. They contain a radiator which is located 140 cm longitudinally from the interaction point and extends 50.7–132 cm radially. It contains a 0.8 cm thick layer of lead sandwiched between two 0.25 mm thick iron layers. This has been simulated with a homogeneous mixture of lead and iron with a volume ratio of 8 : 5.

Regions containing no material were set up with locations corresponding to those of the fission counters as given in Section 4.3.3. These regions are indicated in figure 4.4. The regions covered the full azimuth, taking advantage of the azimuthal symmetry of the detector. As far as the simulation was concerned the regions on the forward and backward sides were considered equivalent due to the symmetry. The end from which protons approach is referred to as the forward side and the antiprotons approach from the backward side.

4.3.2 Description of the Fission Counters

A fission counter consists of a fissionable material inside an ionization chamber. The fission counters used (type number FC 165/1000/U238 [33]) consist of concentric cylindrical electrodes with a 10 mm spacing. A cross section of the detector is shown in figure 4.5. The fissionable material (in this case ^{238}U in the form of U_3O_8) is coated on five of the cathode surfaces (the inner surface of the outer cathode, and both surfaces of the inner two). The length of the coated area is 5.1 cm with a total surface area of 165 cm^2. The thickness of the coating corresponds to 1000 $\mu g/cm^2$. The chamber is filled with a suitable gas such as argon.

Neutrons interact with the ^{238}U inducing fission, usually resulting in two heavy

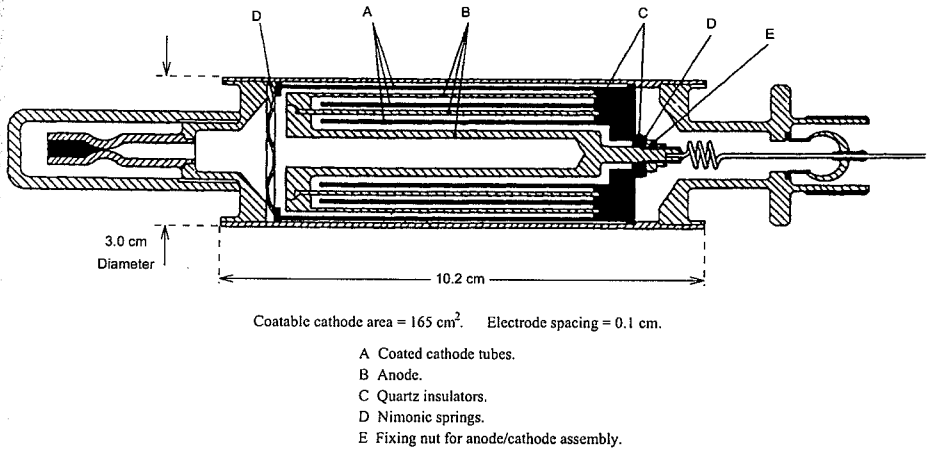

Figure 4.5: Cross section of multiple-plate fission counter type B165. [34]

fission fragments. The charged fragments travelling through the gas will cause ionization producing electron-ion pairs which are collected on the electrodes as a charge pulse.

The ^{238}U is an alpha emitter (as are most fissile coatings used in fission counters) hence these alphas will also produce pulses. To operate the fission counter the discriminator level must be set above the maximum peaks of the α-pulses. This was achieved by increasing the discriminator level, during a period in which there was no beam, until no counts were recorded.

The fission counters are sensitive to neutrons with energies greater than about 1 MeV corresponding to the threshold for fission in ^{238}U. The sensitivity varies with energy as the number of counts depends on the cross section of neutron induced fission of ^{238}U as shown in figure 4.6. The theoretical sensitivity for the fission counters used was 1.08×10^{-4} cps/nv for 3 MeV neutrons [33], where cps is counts per second and nv is a measure of neutron flux in neutrons/cm^2/sec. A calibration of the fission counters was carried out as described in Section 4.3.4.

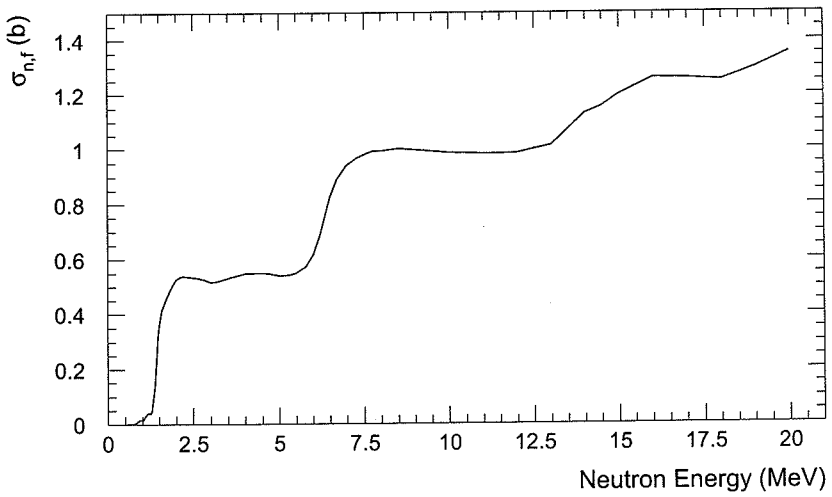

Figure 4.6: Cross section of neutron induced fission of ^{238}U. Data is from ENDF/B-VI [35].

4.3.3 Fission Counter Measurements in UA2

During the final run of UA2 in 1990, fission counters were installed in the UA2 detector to obtain measured values of the neutron flux. The counters were installed in two main positions. Figure 4.4 shows these positions. The first position (referred to as position 1) was just within the outer silicon boards. The location of the counter was approximately 10 cm radially from the beam axis and 80 cm longitudinally from the interaction point. Only one fission counter was installed at this stage, being situated on the forward side of the UA2 detector. The second position (referred to as position 2) was on the side of the central calorimeter a distance of approximately 90 cm longitudinally from the interaction point, and about 75 cm radially. Two fission counters were installed, one on the forward side and the other on the backward side.

The fission counter used in position 1 and on the forward side in position 2 was referred to as fission counter A. The other counter on the backward side in position 2 was referred to as counter B.

For fission counter A when it was in position 1 the discriminator unit was

located in close proximity to the fission counter with only the digital signal going to the control room. In the second position the analog signal was taken to the control room allowing the discriminator level to be adjusted in the control room and the pulse height spectrum to be investigated. The length of the cables was approximately 60 to 80 m and so the signal was attenuated much more than for the first position.

4.3.4 Calibration of the Fission Counters

To calibrate the fission counters a neutron source with known flux output was used. The neutron source used was a ^{238}PuBe source located at CERN. Both fission counters were mounted together on a movable platform so that the distance between the source and detectors could be varied. The count rate was measured at five different separations; 15, 20, 30, 40 and 50 cm. The flux constant of the neutron source was 856 n/cm^2/s at one meter [36]. This excludes corrections for the scattering and absorption. Scattering factors f_S were provided [36] to take into account the neutron flux due to scattering of neutrons from walls and other objects in the room. The f_S ranged from 1.005 at 20 cm to 1.015 at 50 cm. The flux at a distance r from the source is given by

$$\phi = \frac{856 \text{ cm}^{-2}\text{s}^{-1}}{r^2} \times f_S(r) \tag{4.1}$$

where r is in meters.

The sensitivity at each distance was calculated by taking the count rate divided by the calculated flux. The average of these (excluding the measurement at 15 cm) was calculated to give a final sensitivity factor. The measurement at 15 cm was excluded because, for this small separation, the assumption that the detector was a single location with separation r was not a good approximation. The resulting sensitivities are given in table 4.3.

Table 4.3: Fission counter sensitivities.

Fission Counter	Sensitivity (cps/nv)
A	$(1.24 \pm 0.02) \times 10^{-4}$
B	$(1.40 \pm 0.03) \times 10^{-4}$

Calculation of the Sensitivity as a Function of Energy

Since the sensitivity varies with neutron energy, the sensitivities s_{cal} calculated in the above calibration are actually averaged over the neutron spectrum of the ^{238}PuBe source. Figure 4.7 shows the spectrum of neutrons from a PuBe source [37]. Neutrons are emitted with energies up to about 11 MeV with a mean energy of 4.3 MeV. The effect of the scattered neutrons, which will come back with different energies, will not be significant since the scattering corrections are small ($< 1.5\%$).

The sensitivity $s(E)$ of the fission counters is expected to be proportional to the neutron induced fission cross section $\sigma(E)$:

$$s(E) = k\,\sigma(E)\,. \tag{4.2}$$

The count rate N is given by

$$N = \int \frac{\mathrm{d}\phi(E)}{\mathrm{d}E}\, s(E)\,\mathrm{d}E = k \int \frac{\mathrm{d}\phi(E)}{\mathrm{d}E}\, \sigma(E)\,\mathrm{d}E\,. \tag{4.3}$$

The calibration sensitivity s_{cal} is defined as

$$s_{cal} = \frac{N}{\phi} = \frac{k \int \frac{\mathrm{d}\phi(E)}{\mathrm{d}E}\, \sigma(E)\,\mathrm{d}E}{\int \frac{\mathrm{d}\phi(E)}{\mathrm{d}E}\,\mathrm{d}E}\,. \tag{4.4}$$

The proportionality constant k is therefore given by

$$k = \frac{s_{cal}}{\langle \sigma_{n,f} \rangle_{cal}} \tag{4.5}$$

where $\langle\sigma_{n,f}\rangle_{cal}$ is the neutron induced fission cross section averaged over the PuBe neutron spectrum,

$$\langle\sigma_{n,f}\rangle_{cal} = \frac{\int \frac{\mathrm{d}\phi(E)}{\mathrm{d}E}\,\sigma(E)\,\mathrm{d}E}{\int \frac{\mathrm{d}\phi(E)}{\mathrm{d}E}\,\mathrm{d}E}\,. \tag{4.6}$$

The quantity $\langle\sigma_{n,f}\rangle_{cal}$ was found to be 0.577 b by folding the neutron source spectrum as shown in figure 4.7 with the cross section as shown in figure 4.6. Table 4.4 shows the expected sensitivity, based on the theoretical sensitivity at 3 MeV (see Section 4.3.2,) for different energies and for the calibration. These are compared with the sensitivities measured above and with earlier measurements at 14 MeV [36]. The measured sensitivities are in good agreement with the theoretical values. The values of the proportionality constant k are given in table 4.5. It can be seen from this table that the calibration with the PuBe source and the earlier measurements at 14 MeV are in excellent agreement.

Table 4.4: Comparison of theoretical and measured sensitivities.

E_n	$\sigma_{n,f}$	Sensitivity (10^{-4} cps/nv)		
(MeV)	(b)	Theoretical	Counter A	Counter B
3	0.516	1.08	–	–
4.3	0.549	1.15	–	–
PuBe	0.577	1.21	1.24 ± 0.02	1.40 ± 0.03
14	1.13	2.37	2.45 ± 0.20	2.85 ± 0.20

Table 4.5: Values for the proportionality constant k (in 10^{-4} cps/nv/b).

	Counter A	Counter B
Theoretical	2.09	2.09
PuBe	2.15 ± 0.04	2.43 ± 0.05
14 MeV	2.17 ± 0.18	2.52 ± 0.18

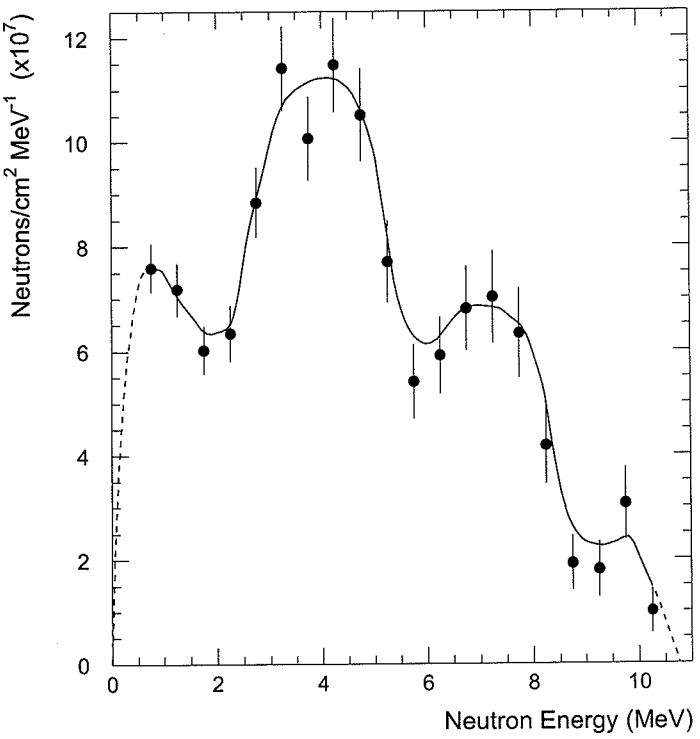

Figure 4.7: Energy distribution of neutrons from a PuBe source. [37]

4.3.5 Results from the Fission Counters

Values of scalers connected to the fission counters were written to tape every five minutes. On the end of run records the accumulated count for a run could be read out. Data was written to tape only during clean beam, so the data does not include counts during a "beam fill" and during beam dumps. A normal running cycle consists of a fill period during which the collider is filled with protons and antiprotons, and the beam is accelerated to the required energy. After the beam stabilizes (clean beam), data taking can commence. Once the beam intensity drops below a useful level the beam is dumped. The cycle is then repeated.

Data will on occasions include counts during times when the beam was lost suddenly or when a radiation trip occured (i.e., the radiation monitors exceed a set level). These are the most likely reasons for runs with counts that did not correlate with the integrated luminosity or other radiation monitoring devices. These radiation monitors (PAX monitors and three litre chambers) were located outside the detector near the beam pipe. For the majority of runs, a good correlation between the fission counters, the integrated luminosity and the radiation monitors was observed.

Plots of the counts from the fission counters versus integrated luminosity are shown in figures 4.8–4.10. Each data point corresponds to a single run.

To compare measured results with FLUKA calculations the flux per $\overline{p}p$ interaction was extracted. This was achieved with a linear fit to the counts versus luminosity data, forcing the fit to pass through the origin. Points that deviated more than four standard deviations from the final fit were excluded from the fit. The resulting slope, which was in counts per nb^{-1}, was converted to counts per interaction by dividing by the number of interactions for an integrated luminosity of 1 nb^{-1}. The number of interactions is given by

$$\sigma_{inel} \int \mathcal{L}\,\mathrm{d}t \tag{4.7}$$

where σ_{inel} is the $\overline{p}p$ inelastic cross section which was taken as 38.3 ± 2.5 mb [38]. The flux was then obtained by dividing the counts per interaction by the sensitivity factor s_{cal} as given in table 4.3.

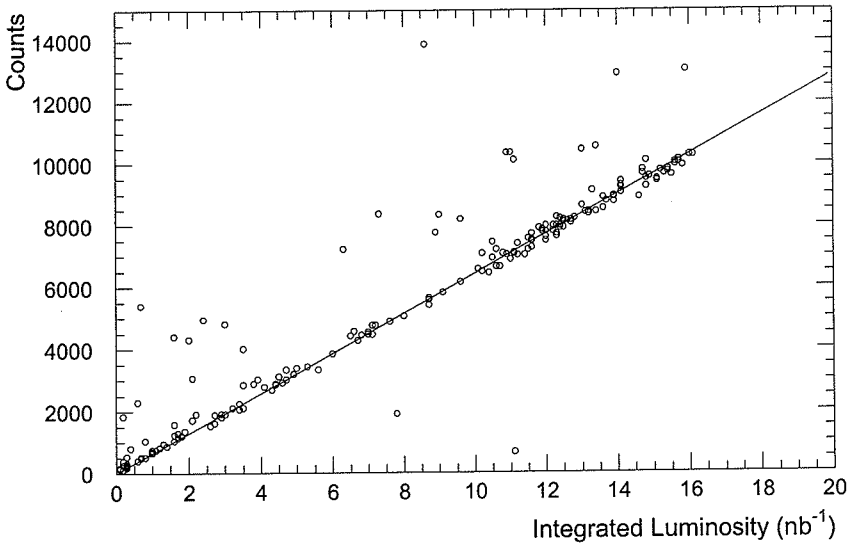

Figure 4.8: Fission Counter A vs Luminosity at Position 1.

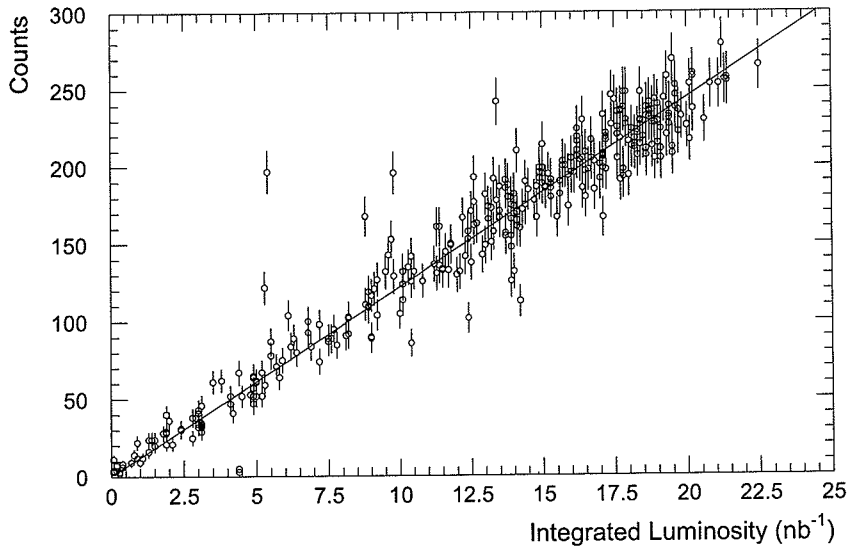

Figure 4.9: Fission Counter A vs Luminosity at Position 2.

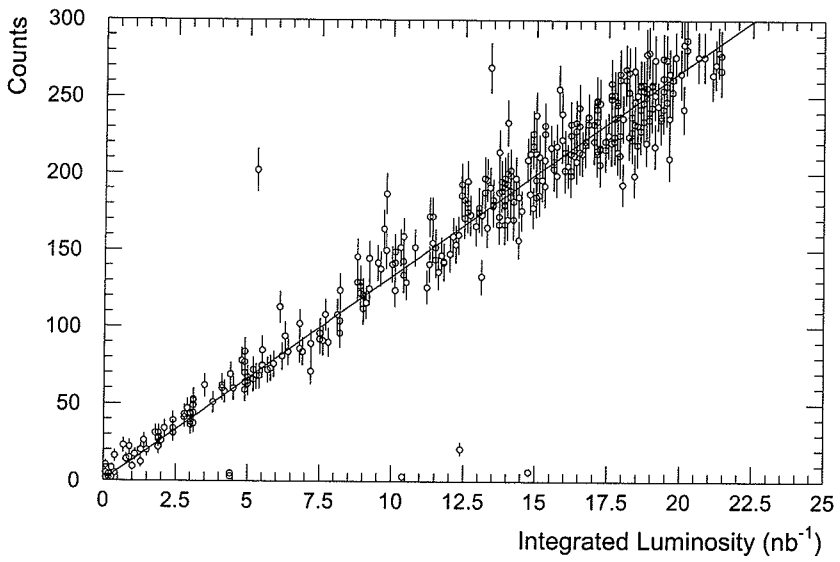

Figure 4.10: Fission Counter B vs Luminosity at Position 2.

The count rates obtained from the fission counter and the resulting neutron flux are given in table 4.6. No significant difference was observed between the fluxes in the forward and backward locations for position 2.

It should be noted that the fluxes given here assume an energy spectrum that is the same as the one in the calibration. This assumption, however, is taken into account by correcting the values obtained with FLUKA. (See Section 4.3.6.)

Table 4.6: Count rates and neutron fluxes as measured by the fission counters.

Position	Fission Counter	Counts per nb^{-1}	Flux n/cm^2/interaction
1	A	644 ± 1	0.14 ± 0.01
2 (Forward)	A	12.2 ± 0.1	$(2.6 \pm 0.2) \times 10^{-3}$
2 (Backward)	B	13.3 ± 0.1	$(2.5 \pm 0.2) \times 10^{-3}$

4.3.6 FLUKA Calculation of Neutron Fluxes in UA2

The source of secondaries from $\overline{p}p$ collisions with parameters appropriate for the SPS collider was generated with the program named DTUJET90 [39]. Around 50,000 secondaries were simulated corresponding to about 850 primary $\overline{p}p$ interactions.

Neutron fluxes were obtained in regions corresponding to the location of the fission counters using the standard track-length scoring option of FLUKA. The mean and error were calculated by doing at least 5 separate runs. Figure 4.11 shows the neutron energy spectrum obtained in the two positions down to an energy of about 10 keV. By plotting $Ed\phi/dE$ (i.e. $d\phi/d(lnE)$) when a logarithmic scale is used the area under the graph is representative of the number of neutrons. The neutron fluxes per beam particle with energy greater than 1.1 MeV (corresponding approximately to the energy threshold of fission in the counters) were 1.2×10^{-3} n/cm^2 in position 1 and 5.1×10^{-4} n/cm^2 in position 2.

In a hadronic cascade a large number of secondaries are produced with progressively lower energy. Many of the charged particles range out leaving a large number of low energy neutrons. The peak at 1 MeV as seen in the spectra in figure 4.11 is typical of neutrons produced in hadronic cascades in calorimeters. Many of the neutrons make their way back into the inner cavity (these are referred to as "albedo" neutrons), and these neutrons may reflect one or more times off the walls of the calorimeter. The net result is like a gas of neutrons with almost uniform flux within the cavity. This uniformity can be seen by the similar neutron spectra in the low energy region for both positions. The flux of low energy neutrons is smaller in position 2 because neutrons passing through position 1 can easily come from either the forward or backward side of the detector as there is not much material to obstruct them. For position 2 most of the neutrons passing through the fission counter would have been produced in the same side of the detector since the central calorimeter shields the counters in this position.

In the high energy region the neutron flux is much higher in position 1 than

in position 2. In position 1 the flux (above about 1 GeV) is dominated by neutrons produced directly from the $\overline{p}p$ interactions. This contribution varies approximately with the inverse of the radial distance squared.

In order to compare the FLUKA calculated fluxes with the fluxes obtained from the fission counters, it was necessary to take into account that the sensitivity is a function of energy. The expected count rate is given by equation (4.3), where $\mathrm{d}\phi/\mathrm{d}E$ is obtained from FLUKA. Dividing the count rate by s_{cal} gives a corrected flux which can be compared with the fluxes obtained in Section 4.3.5. Since $s_{cal} = k\langle\sigma_{n,f}\rangle_{cal}$, this corrected flux can be calculated as

$$\phi_{corr} = \frac{\int \frac{\mathrm{d}\phi(E)}{\mathrm{d}E}\,\sigma(E)\,\mathrm{d}E}{\langle\sigma_{n,f}\rangle_{cal}}\,. \tag{4.8}$$

The corrected FLUKA fluxes were found to be 1.7×10^{-3} n/cm^2 in position 1 and 5.6×10^{-4} n/cm^2 in position 2. This correction has only a small effect in position 2 where most of the neutrons are in a similar energy range to the PuBe spectrum. In position 1 the correction is larger due to the higher flux of high energy neutrons which has a significant contribution due to a larger fission cross section for these energies.

Proton and charged pion fluxes were also calculated with a lower energy threshold of 10 MeV. Their spectra are shown in figure 4.11, and the total fluxes are given in table 4.7. The pion flux is due predominately to pions produced in the $\overline{p}p$ interactions and differ in the two position by approximately $1/\mathrm{r}^2$ (i.e., a factor of 50). The proton flux is also made up partly of protons from the $\overline{p}p$ interactions. In position 1 this contribution accounts for about 30% of the flux (mostly those above 1 GeV), the rest resulting from showers in the calorimeter. In position 2 the proton flux is predominately from showers in the calorimeter. Above about 100 MeV the proton and neutron fluxes are very similar for both positions. Below this energy the charged particles tend to range out.

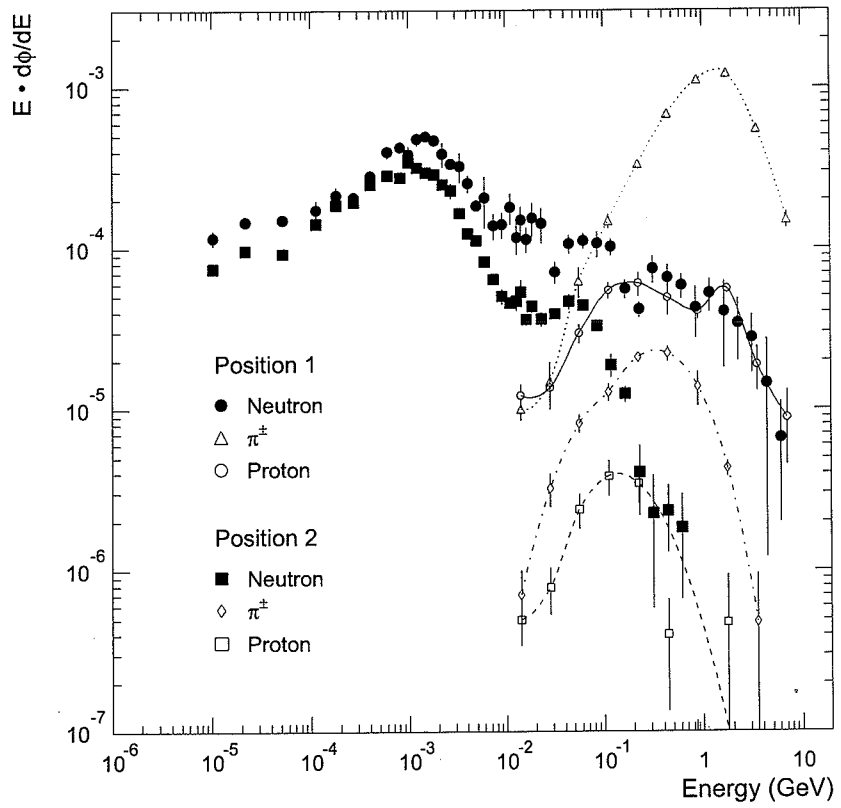

Figure 4.11: Neutron, proton and charged pion spectra in UA2 at position 1 (near outer silicon) and position 2 (side of calorimeter).

Table 4.7: Neutron, proton and pion fluxes in UA2 calculated with FLUKA. Position 1 is just within the outer silicon layer. Position 2 is on the side of the central calorimeter. Fluxes are per cm^2 per beam interaction.

Position	Neutron (> 1.1 MeV)	Proton	Pion
1	1.2×10^{-3}	2.4×10^{-4}	3.0×10^{-3}
2	5.1×10^{-4}	8.3×10^{-6}	6.1×10^{-5}

Table 4.8: Comparison of neutron fluxes calculated with FLUKA with those measured by the fission counters in UA2. Fluxes are in units of 10^{-3} n/cm^2 per $\overline{p}p$ interaction.

Position	FLUKA		Measured
	$E_n > 1.1$ MeV	Corrected	
1	1.2	1.7	140
2	0.51	0.56	2.5

4.3.7 Comparison of FLUKA Calculation with Measurements from the Fission Counters

Table 4.8 shows the comparison between the fluxes measured with the fission counters and those calculated using FLUKA. In both positions the calculated values are much less than those measured, with better agreement in position 2. Possible reasons for the discrepancies include:

- The calculated values only take into account the neutrons produced as a result of hadronic showers initiated by particles from the $\overline{p}p$ interactions. Neutrons will also be produced as a consequence of beam losses. The beam is not perfectly collimated and particles in the beam halo can interact in the beam pipe, magnets and shielding around the beam pipe, and the calorimeter to produce other neutrons. Although it is likely that the beam halo will vary for different luminosities, the correlation plots show the counts versus the integrated luminosity for a run and so it is expected that these variations would average out. It is therefore expected that the contribution from beam losses will be proportional to the integrated luminosity for a run. The disagreement between measured and calculated fluxes in position 2 is less, probably due to this position being further from the beam pipe and because the end caps may have shielded a number of these neutrons.

- The fission counters will also be sensitive to other particles. For example proton, pion and photon induced fission are all possible. The sensitivity to these

other particles is not known. However, using fission cross section data, an estimate of their contribution can be determined. As estimated in Section 4.3.8 below, the FLUKA calculated flux, taking into account the pion contribution, is 0.016 n/cm^2/int. in position 1 and 8.4×10^{-4} n/cm^2/int. in position 2. These are in much better agreement with the measured values, however, the discrepancy is still large with the measured value being higher than the FLUKA value by factors of 9 and 3 in positions 1 and 2 respectively. The charged particles themselves will produce ionization in the fission counter, but these pulses will be below those from the alphas which are doubly charged. Only fission fragments that are multiply charged will produce a signal.

4.3.8 Contribution of Other Particles to the Fission Counter Measurements

Since the fission counters will be sensitive to particles other than neutrons, an estimation of their contribution is helpful. The charged pions and protons have energies in the range 10 MeV to 10 GeV with pions in position 1 peaking at around 1 GeV (see figure 4.11). The proton induced fission cross section in U is generally less than 1.6 b for high energy protons (see for example Refs. [40, 41]). Hicks *et al.* [42] obtain cross sections for π^- roughly decreasing with energy from about 3.0 b at 60 MeV to 2.4 b at 100 MeV. For π^+ the cross sections are around 2.0 b in this energy range. Khan *et al.* [43] obtain cross sections of 2.890 ± 0.054 b for π^- at 80 MeV and 2.260 ± 0.048 b for π^+ at 100 MeV. The pion cross section ($\sigma_{\pi,f}$=2.6 b) has been taken as the average of these last two values and has been used to estimate the contribution of pions to the measured flux from the fission counters. The proton contribution has been ignored because of its much smaller flux (see table 4.7) and the smaller fission cross section than that for pions. The pion contribution $\phi_{\pi,corr}$ has been calculated by

$$\phi_{\pi,corr} = \phi_{\pi} \frac{\sigma_{\pi,f}}{\langle \sigma_{n,f} \rangle_{cal}} \,. \tag{4.9}$$

Table 4.9 summarizes the results.

Table 4.9: Comparison of fluxes measured by the fission counters in UA2 with those calculated with FLUKA. The contribution of pions is included. Fluxes have been corrected to take into account the varying sensitivity with energy. Fluxes are in units of 10^{-3} cm^{-2} per $\overline{p}p$ interaction.

Position	FLUKA Corrected Fluxes			Measured
	Neutron	Pion	Total	
1	1.7	14	16	140
2	0.56	0.28	0.84	2.5

4.3.9 Discussion of UA2 Comparison

The comparison between the measured and calculated neutron fluxes were inconclusive due to the possible contribution of beam losses to the measured flux which were not included in the simulation. The sensitivity of the fission counters to particles other than neutrons also made the comparison difficult. In position 2 where these contributions are expected to have less effect the comparison was better with the measured value being 4.5 times greater than calculated, compared with a discrepancy of a factor 80 in position 1. Including an estimate of the pion contribution gave better agreement, with the measured values being greater by a factor 3 in position 2 and a factor 9 in position 1.

These large discrepancies highlight the importance of eliminating the contribution of beam losses in the LHC. Their contribution in the LHC is considered not to be significant at full luminosity due to the planned use of very efficient collimation. Apart from requiring this to reduce radiation levels in the detector, this collimation is necessary to prevent quenching in the super conducting magnets used for the beam.

Another important observation in the UA2 measurements was that the majority of the counts from the fission counters came from periods during fill, beam dump, and sudden beam losses. The data shown in figures 4.8–4.10 were only taken during clean beam. The improved collimation in the LHC is anticipated to reduce to an insignificant level contributions such as these.

4.4 BEDLAM Experiment

A lead/liquid argon calorimeter is being developed for the ATLAS detector. When exposed to low energy neutrons (from thermal energies up to around 1 MeV) ^{41}Ar is produced in the liquid argon. This isotope is radioactive and decays via beta and gamma emission, the photon having an energy of 1.29 MeV. The half-life of ^{41}Ar is 1.8 hours and if the activity is too high then, for safety reasons, the calorimeter may be required to have double containment in case of leakage in the first container. Also, this activity will contribute to the noise of the calorimeter.

To calculate the activity of ^{41}Ar the program FLUKA has been used to determine the neutron flux and hence the rate of induced activity.

Bench mark experiments such as those described in Section 4.2 have given confidence in FLUKA's predictions down to about 0.8 MeV. To test the predictive capabilities of FLUKA for neutrons down to thermal energies an experiment (BEDLAM, BEam Dump in Liquid Argon Measurement) was carried out in which a lead slab structure in a container of liquid argon was irradiated in a 205 GeV/c hadron beam. The resulting activity was compared with the activity predicted by FLUKA. Neutron activation detectors were also included in the slab structure to test how well the thermal neutron flux (below 0.4 eV) was being calculated by FLUKA.

4.4.1 Description of the Experiment

The experiment was carried out in the H6 line in the North Hall Experimental Area EHN1 of the CERN SPS. Figure 4.12 shows the setup for the experiment. Concrete shielding was used extensively around the experimental setup to minimize radiation levels outside the beam area.

The "calorimeter" consisted of six slabs of lead measuring $50 \times 50 \times 2.5$ cm^3. The slots between the slabs measured 0.8 cm deep. Seven aluminium plates of thickness 0.1 cm where placed in the slots as supports for activation detectors and dosimeters. The plates were numbered 1 to 7 with plate 1 upstream.

The calorimeter was placed in a steel container referred to as the inner con-

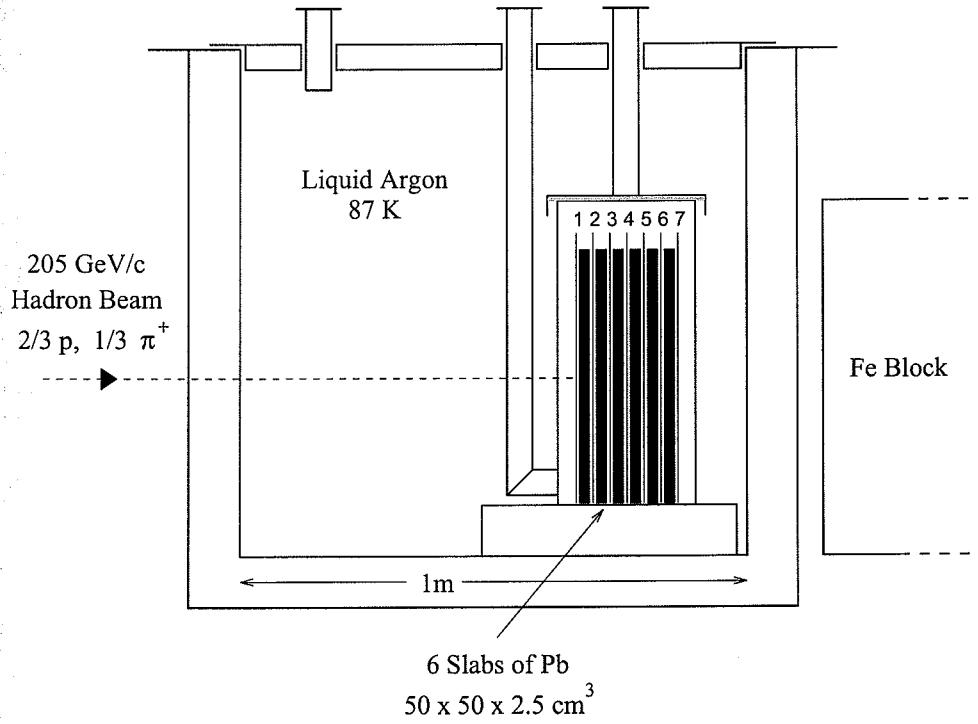

Figure 4.12: Diagram of experimental setup. Aluminium plates were placed in the slots numbered 1–7 as indicated.

tainer. The inner container was designed to provide a reference volume in which to determine the ^{41}Ar activity. This container had dimensions 60 × 60 × 26 cm^3. A steel lid was placed on top of this with a 1 cm thick sheet of expanded polystyrene in between to act as a seal. The lid was secured down with four clamps.

Pipes were attached to the inner container to allow filling and extraction of the liquid argon.

It was necessary to ensure minimal loss of liquid argon in the inner container due to evaporation since this would change the volume of liquid argon during irradiation and hence introduce uncertainties in determining the activity of ^{41}Ar. To achieve this, the inner container was placed in a large insulated container, referred to as the outer container, which was also filled with liquid argon. Any liquid argon which evaporated from the outer container could then be replaced, maintaining the surface level above the top of the inner container, without altering the concentration of activity in the reference volume. During the irradiation the evaporation in the outer container was low and topping up was not required. The outer container had inner dimensions of about one cubic meter. It consisted of a steel frame with an inner lining of steel about 1 cm in thickness. The walls contained expanded polystyrene of thickness 8.2 cm, the whole being contained in a wooden box 2.3 cm thick.

An iron block 160 cm long by 80×80 cm^2 was placed 5 cm behind the outer container in line with the beam in order to increase the fluence of low-energy neutrons and to simulate the ATLAS calorimeter.

4.4.2 Description of the Irradiation

The calorimeter assembly was irradiated with a 205 GeV/c hadron beam which consisted of two thirds protons and one third pions and which had a lateral width of approximately 2 cm FWHM. The irradiation lasted approximately 12.5 hours. The beam intensity was very stable except for a stop of 1.5 hours about 4 hours after the start of irradiation. The intensity of the beam averaged over the nominal irradiation time of 12.5 hours was 2.5 × 10^7 beam particles per second.

The irradiation time profile was monitored by three different methods. A parallel plate ionization chamber was placed directly in the beam, and two other radiation monitors were located outside the concrete shielding. One of these was a neutron counter whose output is shown in figure 4.13.

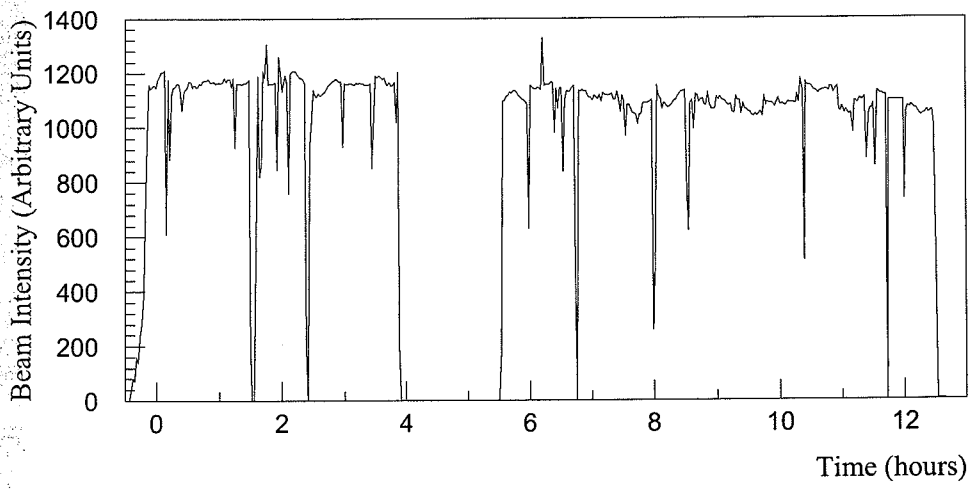

Figure 4.13: Irradiation time profile obtained using a neutron monitor.

Corrections were made for the effect of the non-uniform irradiation in the determinations of induced radioactivity. This was done by calculating Run Uniformity factors which, when multiplied by the production rate calculated assuming uniform intensity over a nominal beam time, gives the corrected production rate. (See Appendix B.) The Run Uniformity factors calculated using the data from the three monitors were found to be consistent, and the values used are shown in table 4.10.

The beam intensity was obtained by measuring the activity of ^{24}Na induced in a 0.5 mm thick sheet of aluminium that was placed directly in the beam 2 m upstream of the calorimeter. This made use of the reaction ^{27}Al (h,x) ^{24}Na which has a cross section of $\sigma = 8.1 \pm 0.6$ mb for a hadron momentum of 205 GeV/c [44]. The average beam intensity is given by

$$\mathcal{I}_{ave} = \frac{a_{sat}\, A}{t\, N_A\, \sigma} \tag{4.10}$$

Table 4.10: Run Uniformity factors.

Isotope	Half-Life	Run Uniformity Factor
^{41}Ar	1.83 hr	0.93
^{64}Cu	12.7 hr	1.00
^{116m}In	54.2 min	0.90
^{115m}In	4.49 hr	0.98
^{198}Au	2.70 days	1.00
^{24}Na	15 hr	1.00

where a_{sat} is the saturation activity (calculated as described in Section 4.4.5), A is the atomic mass of ^{27}Al, t is the thickness of the aluminium sheet in g/cm^2, and N_A is Avagadro's number.

The beam intensity was calculated to be $(2.5 \pm 0.2) \times 10^7$ beam particles per second. The error is dominated by the cross section uncertainty. This value has been used is subsequent calculations of production rates.

A second method for finding the beam intensity used data from the parallel plate ionization chamber. The ionization chamber consisted of five parallel plates spaced 16 mm apart with an aperture of 185 mm in diameter. The centre plate is the collector and the ones either side are at a potential of around 250–300 V. The beam passes through 32 mm of air at atmospheric pressure in the sensitive part of the detector. The mean ambient conditions at CERN are 725 mmHg and 20°C, hence the effective thickness of air is

$$T = 0.001293(\mathrm{g/cm^3}) \times 725/760 \times 3.2(\mathrm{cm}) = 3.95(\mathrm{mg/cm^2}) \; . \qquad (4.11)$$

Taking the mean stopping power as $\epsilon = 2.3$ MeV g^{-1}cm^2, and the mean energy required to create an ion-electron pair as $w = 34.2$ eV, the charge per beam particle (i.e., the current per unit beam intensity) is given by

$$I/\mathcal{I} = (-\epsilon T\, e)/w = 4.25 \times 10^{-17}\mathrm{C} \qquad (4.12)$$

where e is the electron charge. The average current was measured to be 1.02×10^{-9} A, resulting in an average beam intensity of 2.4×10^{7} beam particles per second. This is in close agreement with the intensity measured using the activation method.

4.4.3 Filling and Extraction of the Liquid Argon

Liquid argon was transferred from filling tanks into the outer and inner containers ensuring that both containers were filled to capacity. Beam was started shortly after filling was complete. A rod with a piece of expanded polystyrene attached to the end was used to indicate the level of the liquid in the outer container, which was checked periodically during irradiation.

At the end of the irradiation some liquid was transferred from the outer container into a holding dewar by the use of a cryogenic pump. After the level of the argon was reduced to below the level of the lid of the inner container, liquid argon extraction from the inner container commenced. This was done to reduce the chance of liquid from outside the inner container seeping into the container and diluting the activated argon concentration. About 30 litres of liquid argon from the inner container was transferred to a 50 litre dewar for subsequent measurement.

4.4.4 Efficiency for Argon Activity Measurements

A GeLi detector was used to assay the argon. To determine the efficiency for measuring the argon activity in the gamma spectrometer assembly, a salt containing ^{152}Eu was dissolved in water with an activity of around 50 Bq/l. This was placed in two dewars of 2 litre capacity. The dewars were placed around the GeLi detector in the gamma spectrometer assembly. The gamma spectrum of ^{152}Eu has several peaks for which the efficiency was determined and so an efficiency curve was fitted. For 1.29 MeV (from ^{41}Ar) the interpolated efficiency for water was $(0.059 \pm 0.005)\%$. The efficiency is defined as the counts per second divided by the activity.

Since the efficiency was measured using water, this must be corrected to the efficiency in liquid argon. This was done by performing a Monte Carlo using the

photon attenuation lengths for argon and water. The photon attenuation lengths for 1.29 MeV photons were calculated from photon total cross sections obtained from Ref. [45]. The geometry for the calculation is shown in figure 4.14. The dewar was a cylinder with a diameter of 10 cm and a height of 25.5 cm corresponding to a 2 litre volume. The detector was assumed to be a point located 5 cm above the base of the dewar and 8 cm from the axis of the dewar (point D in the figure). The procedure was then as follows:

1. Obtain a random position P in the dewar as the source position.
2. Calculate the distance to the wall of the cylinder, t, along a line joining the source and the detector ($t = \overline{\mathrm{WP}}$).
3. Calculate the distance between the source and the detector, R=$\overline{\mathrm{DP}}$.
4. Calculate the weight of the event as

$$W = \frac{e^{-t/\lambda}}{R^2}$$

   where λ is the photon mass attenuation length as given below.
5. Accumulate this weight: $W_{\mathrm{tot}} \leftarrow W_{\mathrm{tot}} + W$.
6. Repeat this procedure N_{event} times.
7. Calculate the efficiency as $\epsilon = W_{\mathrm{tot}}/N_{\mathrm{event}}$.

This procedure was done for $\lambda_{\mathrm{H_2O}} = 15.9 \pm 0.5$ cm and $\lambda_{\mathrm{Ar}} = 14.2 \pm 0.4$ cm obtaining efficiencies for water and argon respectively. The ratio of the efficiency in argon over the efficiency in water was found to be 0.97 ± 0.01.

Another correction that was made was the effect of using a different volume of liquid in the calibration from what was used in the argon activity measurement. The initial volume in each dewar for the argon measurements was estimated to be 2.15 l rather than 2 l as used in the calibration. To calculate this effect the above

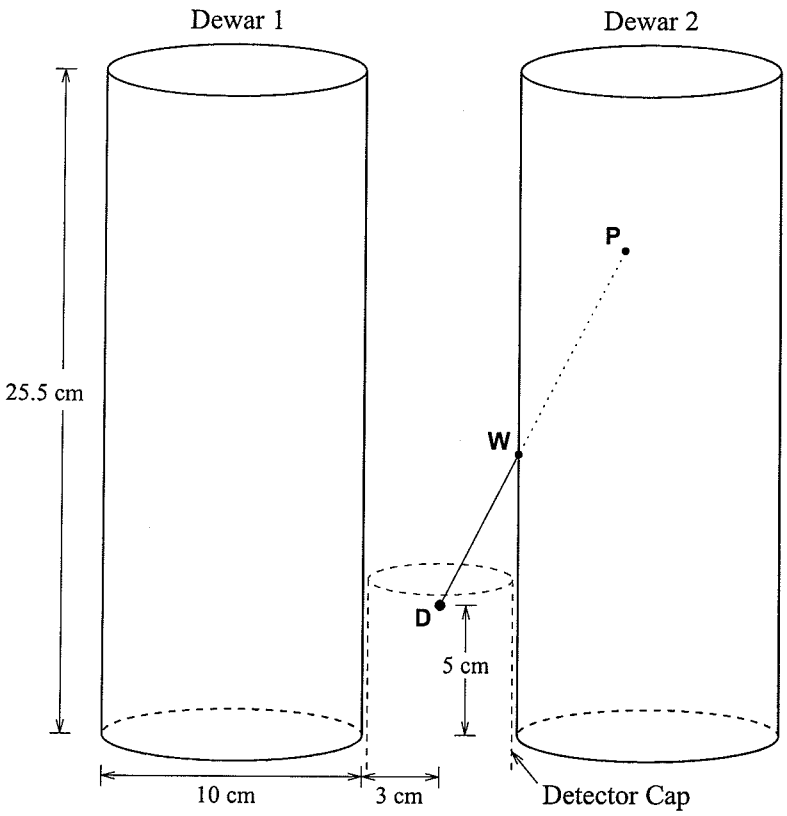

Figure 4.14: Layout of dewars in gamma spectrometer assembly. For the calculation of corrections to the efficiency the detector was assumed to be at point D, $R = \overline{\mathrm{DP}}$, and $t = \overline{\mathrm{WP}}$.

Monte Carlo was performed with a height of 27.4 cm for the dewar, corresponding to a volume of 2.15 l. The ratio of the efficiency for 2.15 l over the efficiency for 2 l was found to be 0.94. This is approximately equal to the inverse of the ratio of the two volumes (equal to 0.93). This is because most of measured activity comes from regions in the dewar close to the detector. The variations in the height will affect the volume (and hence the total activity), but they will have little effect on the counts received. The error on this correction will be dominated by uncertainties in the initial volume estimated to be around 2%. The error was not included here as an overall estimate for the volume error was included when calculating the activity as described in Section 4.4.6.

After these corrections the efficiency for 1.29 MeV photons in argon with a dewar filled with 2.15 l was $(0.054 \pm 0.005)\%$.

4.4.5 Calculation of Activity and Production Rates

The average activity in a counting time t_c is given by

$$\bar{a} = \frac{N_c}{t_c} \frac{1}{\epsilon \cdot (1-d) \cdot b} \tag{4.13}$$

where N_c is the counts in time t_c in a particular peak corresponding to some gamma-ray energy, ϵ is the efficiency for that gamma-ray energy, d is the fractional dead time, b is the branching ratio or decay probability for that gamma-ray energy. In the case of measurements with the liquid argon, the activity was also divided by the volume to give the activity per litre.

To calculate the instantaneous activity at the beginning of counting, the average activity must be multiplied by

$$f_{count} = \frac{\lambda t_c}{1 - \exp(-\lambda t_c)} \tag{4.14}$$

where λ is the decay constant. To calculate the activity at the nominal end of irra-

diation, the activity at the beginning of counting must be multiplied by

$$f_{lapse} = \exp(\lambda t_l) \tag{4.15}$$

where t_l is time lapsed between the nominal end of irradiation and the beginning of counting. To calculate the saturation activity a_{sat} the activity at the end of irradiation must be multiplied by

$$f_{irrad} = \frac{1}{1 - \exp(-\lambda t_i)} \tag{4.16}$$

where t_i is the nominal length of the irradiation. The saturation activity is therefore given by

$$a_{sat} = f_{irrad} \cdot f_{lapse} \cdot f_{count} \cdot \bar{a} \ . \tag{4.17}$$

The production rate (per mole of parent isotope per beam particle) is given by

$$\Psi = \frac{a_{sat} \cdot A \cdot f_{RU}}{\mathcal{I}_{ave}\, m\, x} \tag{4.18}$$

where A is the atomic mass, $\mathcal{I}_{ave}$ is the average beam intensity over the nominal irradiation time, m is the mass of the sample, x is the relative abundance of the isotope being irradiated, and f_{RU} is the Run Uniformity factor. For the case of the argon sample the mass of the sample was given as the mass of one litre of argon, i.e., 1.40 kg.

4.4.6 Measurement of Argon Activity

Some of the liquid argon from the 50 litre dewar was transferred to two dewars, each of 2 litre nominal capacity. These were placed around a GeLi detector and a gamma spectrum was collected. The dewars were of the same type and placed in the same positions as those used in the efficiency determination. Figure 4.15 shows one of the spectra collected. ^{41}Ar decays via beta emission followed by gamma emission with a 1.8 hour half-life. The decay results in a 1.29 MeV gamma ray with absolute emission probability per decay of 99.2%. There is also a 1.68 MeV gamma ray with

a branching ratio of 0.05% but this was not measurable. The ^{41}Ar peak is very prominent. The energies of other peaks have been shown with the isotopes giving rise to these peaks. Section 4.4.7 discusses the isotopes identified and their production rates.

Four measurements were taken. Table 4.11 summarizes the results from these measurements. The volume, assumed to be 2.15 l, was used to calculate the activity per litre. The error on the activity was dominated by the uncertainty in the volume of the liquid and the 8% error on the efficiency. The error on the volume was globally estimated as being 4%. This was based on a 2% uncertainty in the initial volume and on the loss of liquid argon in 20 minutes measured to be about 3%. The statistical errors from counting were less than 0.3% for the first three measurements and was 4.4% for the fourth measurement.

The mean from the first three measurements of the activity at the end of irradiation was $(9.5 \pm 0.9) \times 10^5$ Bq/l. The variation of the three measurements gives rise to a standard deviation of 2%. This is expected to be mainly due to the positioning of the dewar and volume variations. The latter is not expected to have a large effect for reasons discussed in Section 4.4.8. The average production rate per mole of ^{40}Ar per beam particle was $(1.02 \pm 0.12) \times 10^{-3}$. The error on this includes the errors as described above as well as the 7.5% error on the beam intensity.

Only the first three measurements were used because of the larger error in the fourth measurement and because the decrease in volume was significant in the fourth measurement which had a long counting time. The effects on the activity due to evaporation of argon during the measurement are described in Section 4.4.8.

4.4.7 Production Rates of Isotopes Identified in the Argon Sample

The gamma spectra of the argon samples (one of which is shown in figure 4.15) revealed peaks from a number of isotopes. The isotopes identified were ^{24}Na, ^{28}Mg, ^{38}S, ^{38}Cl and ^{39}Cl. The isotope ^{38}S decays to ^{38}Cl and so both isotopes are labelled for peaks resulting from the ^{38}Cl decay. These isotopes are likely to be spallation

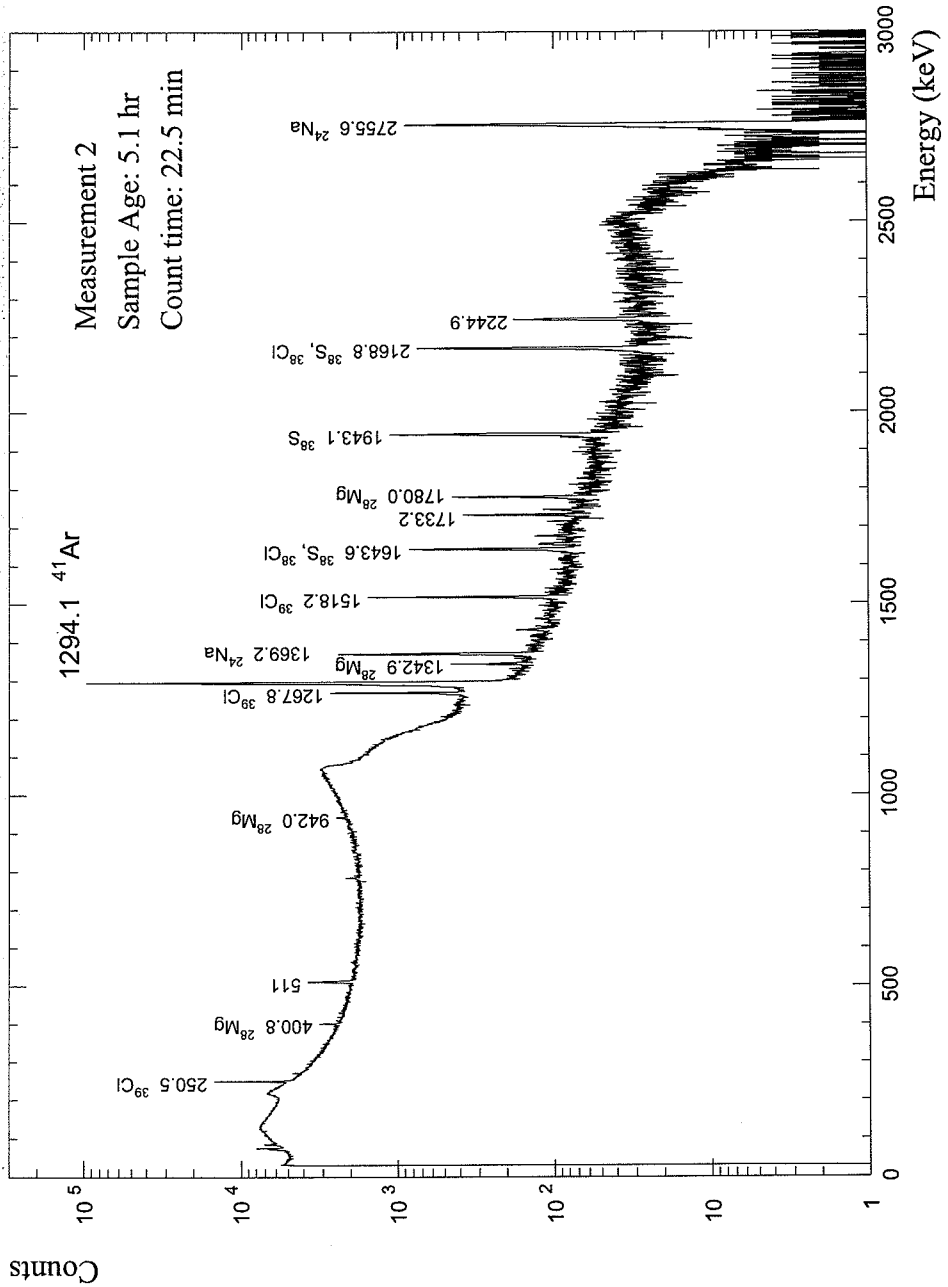

Figure 4.15: Gamma spectrum obtained from argon sample. Energy of prominent peaks are labelled along with identified isotopes.

Table 4.11: Argon Measurements.

Measurement	Sample Age (hrs)	Count Time (min)	Percentage Dead Time	Activity (Bq/l)	Activity at End of Irradiation (Bq/l)
1	2.2	6.3	28%	4.17×10^5	9.60×10^5
2	5.1	22.5	9.5%	1.37×10^5	9.54×10^5
3	7.5	19.4	4.1%	5.31×10^4	9.28×10^5
4	24.7	119	0.1%	71.4	8.31×10^5

products from the argon. Two peaks at 1.733 and 2.245 MeV were not identified. The production rates of the identified isotopes are given in table 4.12. These were calculated in the same manner as for ^{41}Ar, using only the first three measurements. The efficiency curve as determined in Section 4.4.4 was used. The correction factors (see Section 4.4.4) which were calculated for 1.29 MeV gamma rays were used for all energies. The peaks from the source used in the efficiency determination covered the energy range 100–1400 keV. A number of the peaks in the argon spectrum were above this energy range and so extrapolation of the efficiency curve was necessary. The resulting production rates should therefore be treated with caution.

The production of ^{38}Cl is complicated by the fact that apart from direct production it is produced by the decay of ^{38}S. The production rate was estimated from only the first measurement. For the other isotopes the first three measurements gave consistent results. For the fourth measurement, however, results for ^{24}Na and ^{28}Mg (peaks for the other isotopes were no longer measurable) were about half of what they were expected to be based on the first three measurements. This is thought to be due to these isotopes, which are lighter than the surrounding argon, moving toward the top of the 50 litre dewar. The cryogenic pump used to transfer liquid to the 2 litre dewars took liquid from the bottom of the dewar where the concentration of the isotopes may have decreased over time.

During the operation of ATLAS the activities of these isotopes will reach saturation and so will equal the production rates. Because of the similarities between

the materials used in this experiment and the calorimeter proposed for ATLAS, the production rates here are a good indication of the relative activities of these isotopes expected in ATLAS. The ^{41}Ar activity clearly dominates. The ^{39}Cl and ^{38}Cl activities are comparable and their contribution will result in a total activity that is roughly double that of the ^{41}Ar activity alone. Their shorter half-lives, however, will mean their contribution will be small a few hours after beam stops. The other isotopes have production rates two to three orders of magnitude lower and therefore do not present a problem.

Table 4.12: Production rates of isotopes identified in the argon sample. Production rates are per mole per beam particle.

Isotope	Half-Life	Production Rate
^{41}Ar	1.83 hr	1.02×10^{-3}
^{39}Cl	55.6 min	3.7×10^{-4}
^{38}Cl	37.2 min	3.4×10^{-4}
^{38}S	2.84 hr	1.0×10^{-5}
^{24}Na	15 hr	9.6×10^{-6}
^{28}Mg	20.9 hr	3.1×10^{-6}

4.4.8 Effect of Evaporation of Liquid Argon During Assay

Since liquid argon is evaporating during the assay, the volume is decreasing and hence there is an additional decrease in the activity. The geometry is also changing and will affect the efficiency. These two effects tend to cancel out as the efficiency is approximately proportional to the inverse of the volume. In order to get a quantitative estimate of this effect the volume variation as a function of time was required.

A measurement of the volume variation with time was made during the fourth measurement. Since the level of the liquid argon in the two dewars inside the gamma spectrometer assembly could not be monitored during the assay, a third dewar was kept outside. All dewars were initially filled to about the same level. The volume of the third dewar was monitored throughout the measurement, resulting in the time

variation of volume as shown in figure 4.16. At the end of the measurement all dewars were observed to have lost about the same amount of liquid.

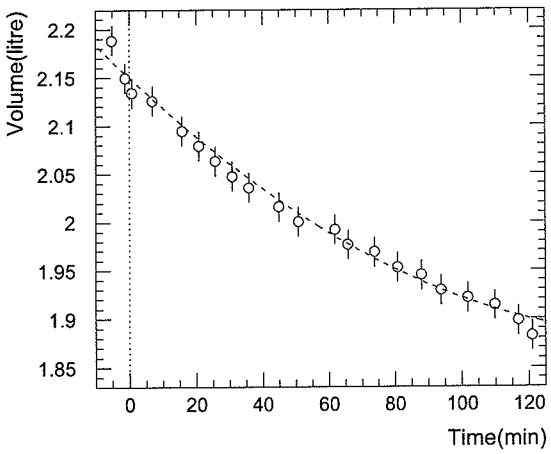

Figure 4.16: Variation of argon volume during assay as a function of time. Dashed line is the parameterization as given in equation (4.19).

The volume variation was parameterized with the following polynomial:

$$V(t) = 2.15 - (3.28 \times 10^{-3})t + (9.97 \times 10^{-6})t^2 \tag{4.19}$$

where t is the time from the start of measurement in minutes and $V(t)$ is the volume in litres at that time.

The efficiency for different volumes was determined as described in Section 4.4.4. Table 4.13 shows the effect of this volume variation on the instantaneous activity at different times during the irradiation. It can be seen that the correction factor is close to unity.

Table 4.13: Effect of changing volume on instantaneous activity.

Time (min)	Volume (litre)	$f_V^{-1} = \frac{V(t)}{V(0)}$	$f_{eff} = \frac{eff(0)}{eff(t)}$	Correction Factor $f_V \cdot f_{eff}$
0	2.15	1.0	1.0	1.00
20	2.09	0.972	0.973	1.00
54	2.00	0.930	0.938	1.01
90	1.94	0.902	0.912	1.01
120	1.90	0.884	0.897	1.02

4.4.9 Activation Detectors

Non-Thermal Reactions

In order to check the position of the beam centre on the calorimeter structure, the ^{24}Na activity was measured in disks that were punched out of two of the aluminium detector support plates. Plates in slots 3 and 5 were used for this purpose. The arrangement of the aluminium disks is shown in figure 4.17. On each plate 21 disks were obtained; one in the middle with a diameter of 14 mm and five in each of the directions: left, right, top and down. These were at radii of 20, 50, 100, 150 and 200 mm with diameters of 14, 18, 24, 26 and 34 mm respectively.

In addition the ^{115m}In activity induced in indium foils was measured. Details of these foils are given below. Both this reaction and the aluminium reaction gave a cross check with previous experiments such as the ones reviewed in Section 4.2. Table 4.14 gives further information for these reactions.

Table 4.14: Aluminium and indium reactions.

Detector	Reaction	Half-Life	Measurement Technique	Energy Range
Aluminium	^{27}Al (n,α) ^{24}Na	15 hr	NaI	6–25 MeV
Indium	^{115}In (n,n') ^{115m}In	4.49 hr	GeLi	0.8–15 MeV

Thermal Reactions

To measure the flux of thermal neutrons, foils of gold, indium, and copper were placed on slot 5. These all have a high cross section for thermal neutrons. Table 4.15 gives a summary of these detectors. The thermal cross section given is the cross section for neutrons having a velocity of 2200 m.s^{-1}. The thicknesses of the foils as given in table 4.15 are thin enough so that the foils themselves do not perturb the surrounding flux. Data for argon is shown in this table for comparison.

Half the foils were placed in a sandwich of cadmium. Cadmium has an extremely high cross section for neutrons below 0.5 eV, the cadmium cut-off. Figure 4.18 shows the cadmium cross section. The foils with cadmium were placed on the left side of the plate (with beam into the page) and those without cadmium on the right side, the intention being that both sides receive the same flux. By taking the difference of the activity one obtains the activity due to neutrons with an energy below the cadmium cut-off. The arrangement of the detectors is shown in figure 4.17. Detectors were placed at radii of 5, 10, 15, and 20 cm from the nominal beam centre. The gold and indium foils were both 16 mm in diameter while the copper foils were 36 mm in diameter. The cadmium cover consisted of two disks each of 1 mm thickness. The foil was placed between the two cadmium disks which were 2 mm greater in diameter than the foils that they surrounded.

Table 4.15: Activation detectors used for thermal neutron measurements. Argon is also included for comparison.

Detector	Reaction	Thickness (μm)	Thermal Cross Section	Half-Life
Gold	^{197}Au (n,γ) ^{198}Au	61	98.8 b	2.70 days
Indium	^{115}In (n,γ) ^{116m}In	106	157 b	54.2 min
Copper	^{63}Cu (n,γ) ^{64}Cu	112	4.5 b	12.7 hr
Argon	^{40}Ar (n,γ) ^{41}Ar	–	0.66 b	1.83 hr

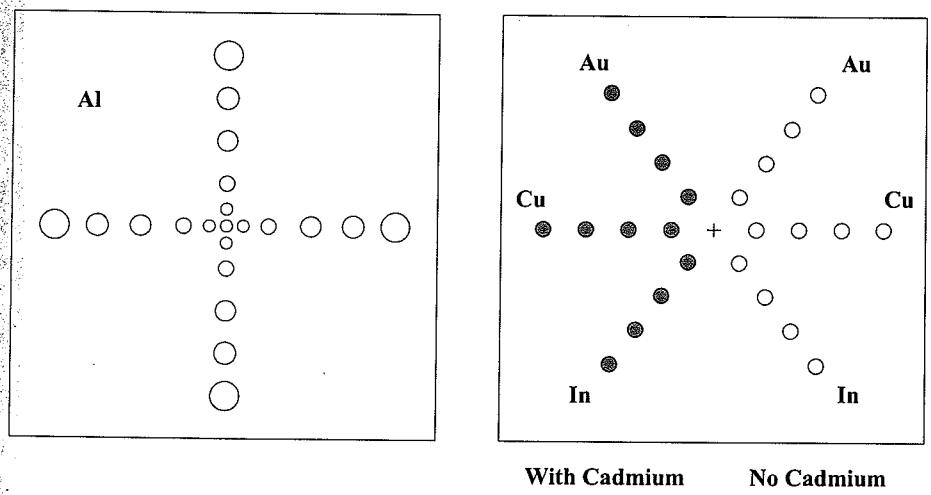

Figure 4.17: Arrangement of aluminium detectors (left) and detectors for thermal neutron measurements (right).

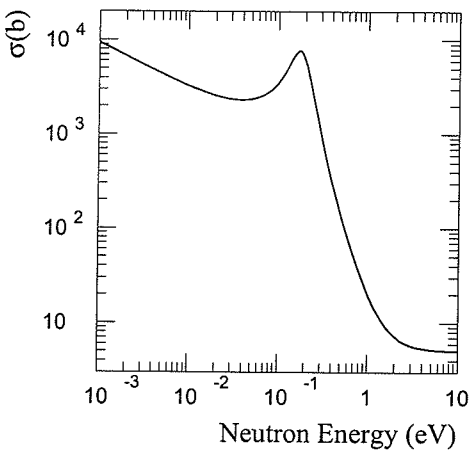

Figure 4.18: Cadmium total neutron cross section.

4.4.10 Measurement of Activation Detectors

After the irradiation the indium, gold, and copper foils were removed from slot 5. Gamma spectra were collected for each foil using a GeLi type detector. The efficiency curve used for these measurements had a 5% uncertainty.

The production rate of the relevant isotope was determined for each of the indium, gold, and copper foils. The results plotted as a function of radius (using the corrected beam centre which was calculated as described in Section 4.4.11 below) are shown in figures 4.19–4.21. Data points on the figures for gold and copper correspond to individual measurements and so where more than one data point is shown for a given radius this corresponds to a repeated measurement. In general those measurements that were repeated agreed well. Error bars (due only to the statistics of the counts) are shown where they are larger than the symbols used. Curves shown on these plots are exponentials fitted to the data.

The aluminium disks punched out from slots 3 and 5 were assayed with a NaI crystal. The production rates of ^{24}Na from ^{27}Al as a function of corrected radius are shown in figure 4.22. The production rates of ^{115m}In from the indium foils are shown in figure 4.23. These plots show the comparison with FLUKA calculations as described in Section 4.4.18.

Indium Foils

Only one measurement was made for each of the indium foils on the first day after irradiation (except for one foil which was not recovered). Two foils were remeasured the following day but there were no measurable amounts of ^{116m}In due to its 54 min half-life. The ^{116m}In decays via β^- decay 100% of the time with subsequent emission of gamma rays at several energies. Three of the main peaks were used to obtain the activity. The peaks used were 1.294 MeV, 1.097 MeV and 0.416 MeV with emission probabilities per decay of 84.4%, 56.2% and 29.2% respectively.

Data from the three main peaks have been plotted in figure 4.20. The original efficiency curve resulted in systematic differences between the results from the three

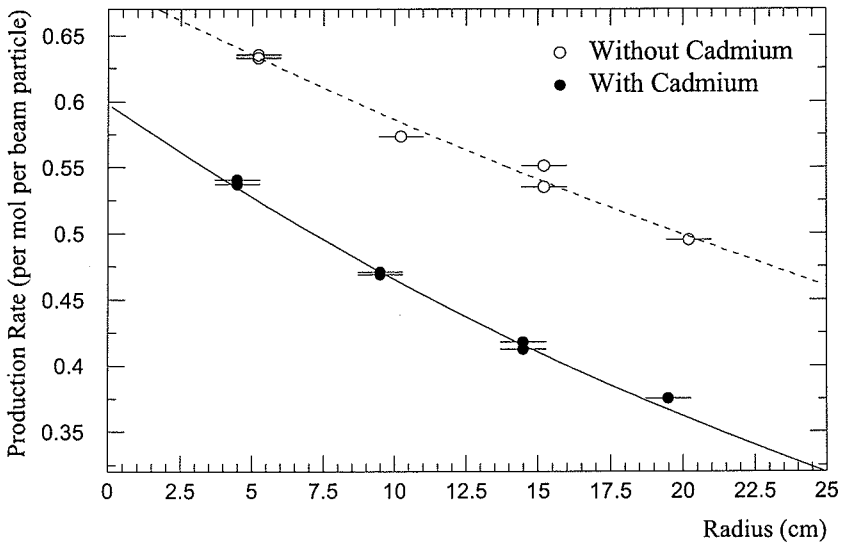

Figure 4.19: Measured production rate of ^{198}Au from ^{197}Au. Curves shown are an exponential fit to the data. Horizontal error bars show width of samples.

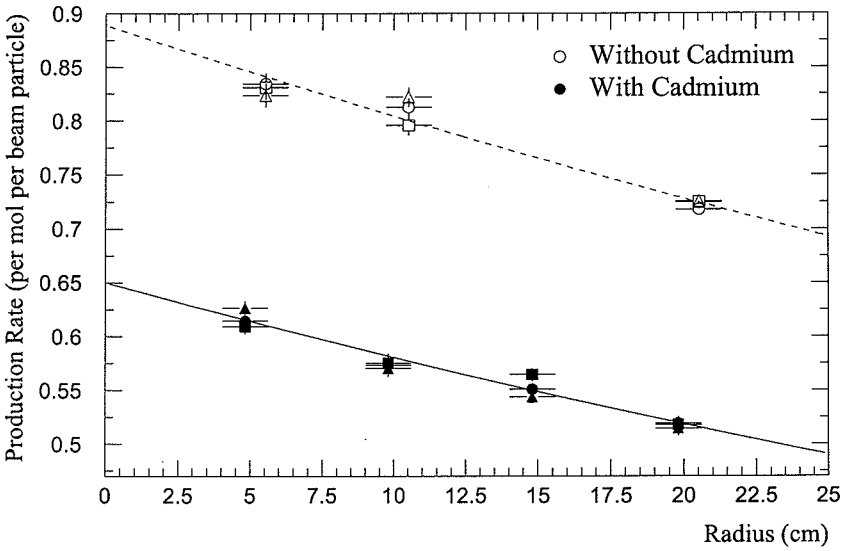

Figure 4.20: Measured production rate of ^{116m}In from ^{115}In. Three peaks were measured: circle 1.29 MeV; square 1.10 MeV; triangle 0.42 MeV. Curves shown are an exponential fit to the data. Horizontal error bars show width of samples.

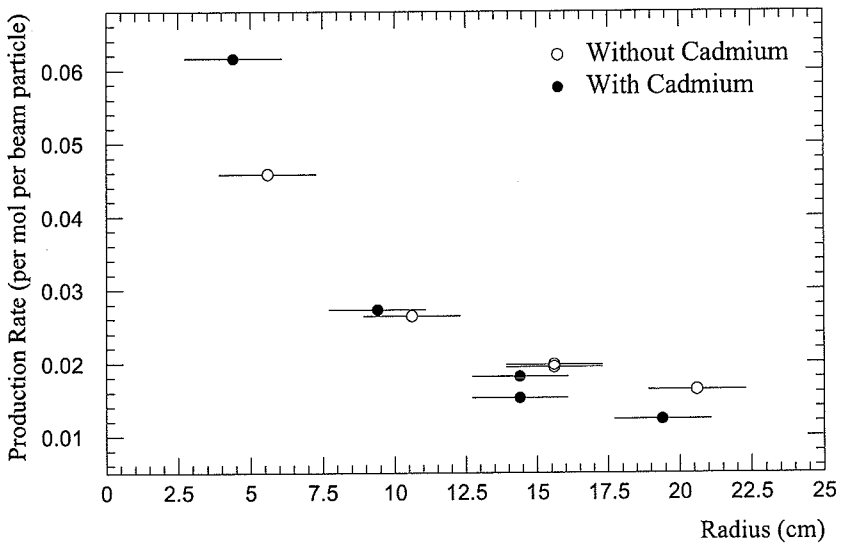

Figure 4.21: Measured production rate of ^{64}Cu from ^{63}Cu. Horizontal error bars show width of samples.

peaks. These efficiencies were modified so that the points were consistent. This was achieved as follows. The original efficiencies are denoted ϵ_i, where $i = 1, 2, 3$ for the three peaks at energies of 1.295, 1.097, and 0.416 MeV respectively. Correction factors f_{ij} were found for each sample j, such that $f_{ij}\Psi_{ij} = \Psi_j$, where Ψ_{ij} is the production rate calculated for peak i, sample j, and $\Psi_j = \frac{1}{3}\sum_{i=1}^{3}\Psi_{ij}$ is the average of three production rates for that sample. The average of these factors was found for each peak: $f_i = \frac{1}{m}\sum_{j=1}^{m} f_{ij}$. New efficiencies $\epsilon_i' = f_i^{-1}\epsilon_i$ were then calculated. The productions rates were then recalculated using these new efficiencies. The values of f_i were found to be 1.004, 0.956, and 1.045. The variations observed here are consistent with the 5% error on the original efficiency curve.

In the indium foils, the isotope ^{115m}In is also produced. ^{115m}In decays via isomeric transition resulting in a 0.336 MeV photon with emission probability per decay of 45.8%. The half-life is 4.49 hours.

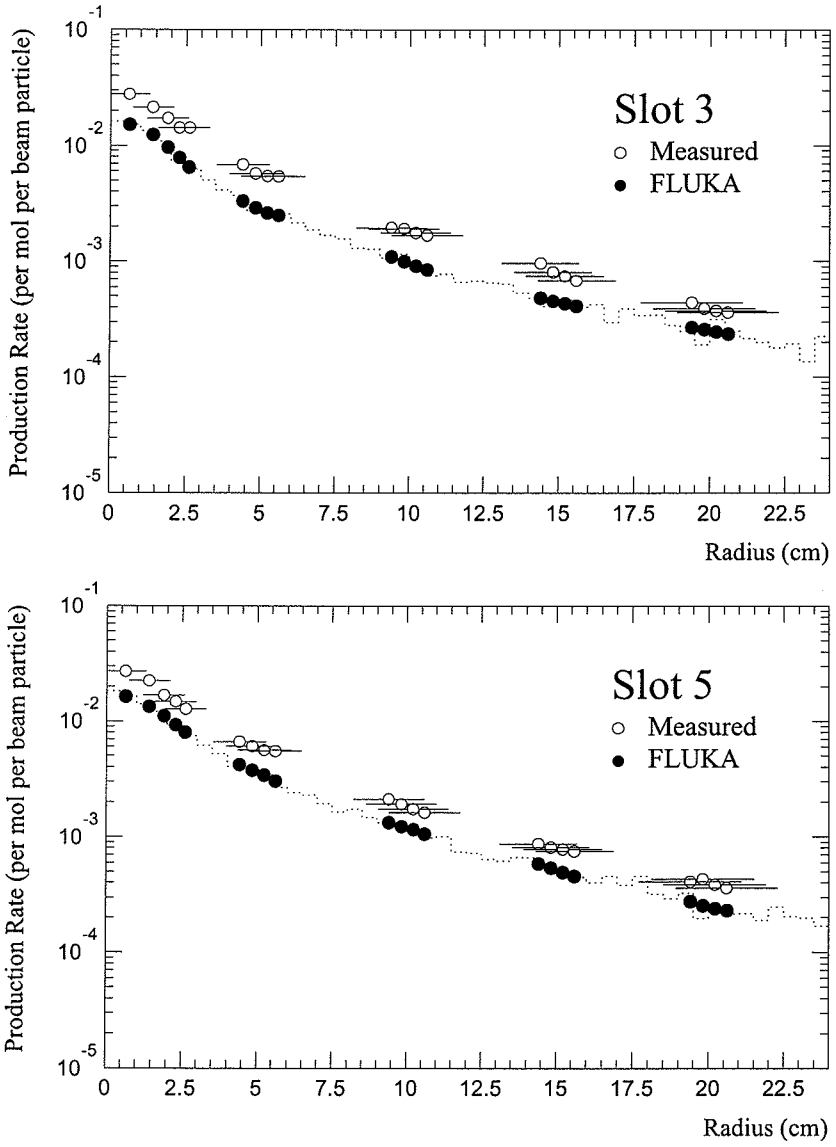

Figure 4.22: Comparison of radial distribution obtained from FLUKA calculation and measured data of production rate of ^{24}Na from ^{27}Al. Horizontal error bars show width of samples.

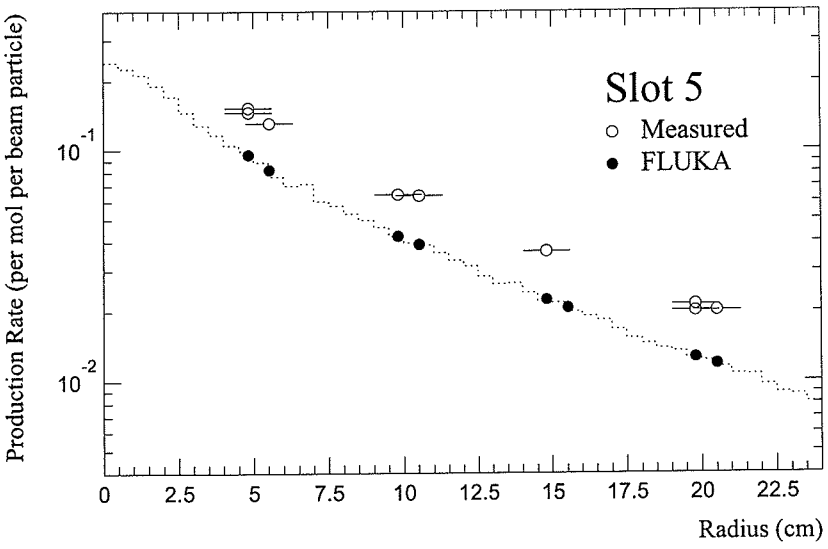

Figure 4.23: Comparison of radial distribution obtained from FLUKA calculation and measured data of production rate of ^{115m}In from ^{115}In. Horizontal error bars show width of samples.

Gold Foils

The ^{198}Au decays 100% via β^- decay with subsequent gamma rays of energy 0.411 MeV (95.6%), 0.676 MeV (0.80%), and 1.09 MeV (0.16%). The half-life is 2.7 days. Only data from the 0.411 MeV peak was used. Five of the eight foils were measured twice and the results were consistent.

Copper Foils

The ^{64}Cu decays via β^-, β^+ and electron capture with a half-life of 12.7 hours. The branching ratio of β^+ is 18.1%. The annihilation of the positron results in two 0.511 MeV gamma rays. A 36.2% gamma emission per decay was used.

Aluminium Disks

The ^{24}Na decays via β^- and gamma emission with a 15 hour half-life. The photons have energies of 1.369 MeV and 2.754 MeV (100%). The isotope was assayed using a NaI crystal by measuring the counts in a window around the 2.754 MeV peak.

4.4.11 Determination of the Beam Position

When plotting data from the aluminium disks from slots 3 and 5, if the beam is assumed to be centred on the plate then the production rates are found not to lie on a smooth curve. That is, the production rates from disks at the same nominal radius were found not to be the same.

The actual beam centre was calculated by fitting the sum of two exponentials to the data allowing the function parameters and the beam coordinates to vary. MINUIT [15] was used to perform the minimization of the χ^2. The procedure was repeated for both slots. The resulting beam coordinates (with beam into the page) were $(-0.6 \text{ cm}, 0.2 \text{ cm})$. Although it is possible for the beam centre to be different for the two slots due to the calorimeter not being exactly normal to the beam, the difference between the beam centres calculated for the two slots was not significant enough to necessitate using different beam coordinates.

Using this new beam centre the resulting radial variation of the production rate of ^{24}Na in aluminium is seen in figure 4.22. The corrected beam centre was used in the FLUKA simulations and also for determining the radial positions of the detectors.

4.4.12 FLUKA Simulations of BEDLAM

The following sections give details of the FLUKA simulations and comparisons with the measured data.

4.4.13 Description of the Geometry used for FLUKA

The geometry used in the FLUKA simulation is shown in figures 4.24 and 4.25. Materials used are indicated. For those regions in contact with the liquid argon the 87 K materials were used. (These take into account the reduced doppler broadening at lower temperatures.) The composition for the non standard materials such as wood, expanded polystyrene and concrete are stated below.

Wood is not a very well defined material. It was assumed to have a density of 0.8 g/cm^3 and a composition of 88% cellulose ($C_6H_{10}O_5$) and 12% water by volume. The resulting composition was H 51.1%, C 23.2%, and O 25.6%. For the expanded polystyrene a density of 0.015 g/cm^3 and a ratio of H/C = 1.0 were used. For concrete the density was 2.35 g/cm^3 and the composition was O 51.1%, Si 35.8%, Ca 8.6%, Al 2.0%, Fe 1.2%, H 0.6%, C 0.4%, and Na 0.3% by weight. Studies of the effects of different wood densities and the inclusion of 4% Sb in the lead are given in Section 4.4.21.

4.4.14 Run Conditions

A user source routine was written which generated 205 GeV/c protons and pions. Protons were generated on average 2/3 of the time and pions 1/3 of the time. The radial profile of the beam was assumed to be Gaussian with standard deviation of 1.2 and 0.9 cm in the horizontal and vertical directions respectively. These correspond to measurements made in a previous experiment carried out under similar conditions [29]. For the main simulation 1200 beam particles were transported. For other configurations the number of beam particles transported were 300 for simulations with different wood densities and 600 for a simulation with 4% Sb in lead.

Electrons, photons, muons, neutrinos and π^0-mesons were immediately discarded. These have an insignificant contribution to the quantities measured here. Protons and pions were transported down to 20 MeV. Neutrons were transported down to the thermal group. Neutrons in the thermal group were set a 95% survival probability. (An explanation of the survival probability is given in Section 4.1.) All

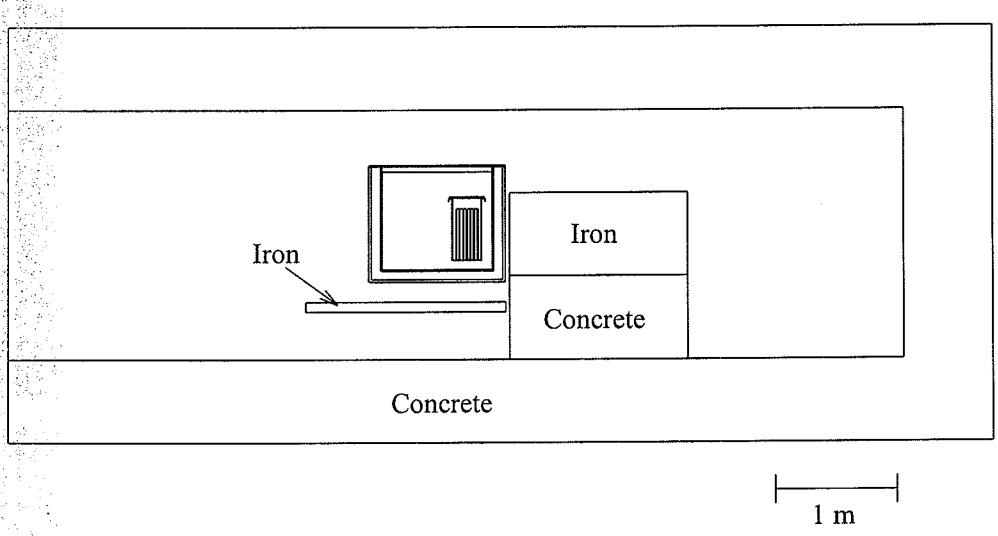

Figure 4.24: Geometry used in FLUKA simulation. Overall view. The iron block under the experiment corresponds to the iron table on which the experiment was placed.

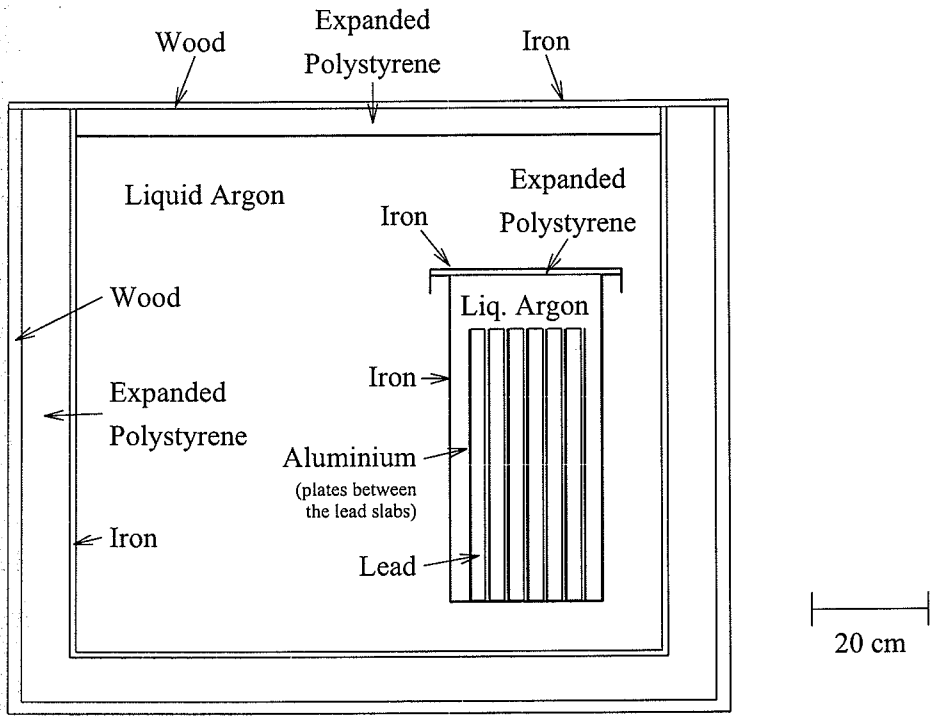

Figure 4.25: Geometry used in FLUKA simulation. View of the outer and inner containers.

other particles were transported down to 50 MeV.

4.4.15 Description of Scoring

To determine the production rate of ^{41}Ar in the reference volume, track-lengths were scored using FLUKA's track-length detector option. The flux is given by the total track-length divided by the regions volume. This was done in the region of liquid argon in the inner container. A spectrum of neutron flux with energy was obtained. Five runs were done to allow a mean and error to be calculated for each point. The resulting spectrum is shown in figure 4.26. For each bin i a flux ϕ_i is obtained between the lower and upper energy limits $E_{\mathrm{b}i}$ and $E_{\mathrm{b}i+1}$. Each point on the energy spectrum, except for the thermal group, is taken as $E_i \cdot \phi_i/\Delta E_i$, where $E_i = \sqrt{E_{\mathrm{b}i}E_{\mathrm{b}i+1}}$ and $\Delta E_i = E_{\mathrm{b}i+1} - E_{\mathrm{b}i}$. The points are plotted at the geometric mean E_i.

For the thermal group the Maxwellian distribution is shown:

$$\frac{\mathrm{d}\phi(E)}{\mathrm{d}E} = \phi_{th}\frac{E}{(k_B T)^2}e^{-E/k_B T} \tag{4.20}$$

where ϕ_{th} is the thermal flux ($E < 0.4$ eV), k_B is Boltzmann's constant, and T is taken as the temperature of the medium, i.e. 87 K. Note that this distribution assumes the neutrons have been fully thermalized. This is not likely to be the case but the distribution is expected to be approximately as shown with some smooth connection with the next group.

Figure 4.27 shows the cross section for ^{40}Ar (n,γ) ^{41}Ar as a function of energy calculated [46] from data from the ENDF/B-VI dosimetry file. The cross section shows the $1/v$ slope at lower energies and some resonances at the higher energies. The gap in the data between these two sections is a region in which the cross section may be less reliable.

The production rate is given by

$$\Psi = \int_0^\infty \frac{\mathrm{d}\phi(E)}{\mathrm{d}E}\sigma(E)\,\mathrm{d}E\,. \tag{4.21}$$

To determine the production rate of ^{41}Ar the following sum was computed:

$$\Psi = \Psi_{th} + \sum_{i=2}^{n} \phi_i \cdot \sigma(E_i) \tag{4.22}$$

where $\sigma(E_i)$ was obtained from linear interpolation, as shown by the solid line in figure 4.27, at the point E_i. The contribution to the production rate from neutrons in the thermal group, Ψ_{th}, was calculated by

$$\Psi_{th} = \frac{\sqrt{\pi}}{2}\sqrt{\frac{293.6}{T}}\,\sigma_o\phi_{th}, \quad T = 87 \text{ K} \tag{4.23}$$

where σ_o is the thermal cross section ($\sigma_o = \sigma(v_o)$, $v_o = 2200$ m.s^{-1} which is the most probable neutron velocity at $T = 293.6$ K for a Maxwellian distribution). Equation (4.23) is obtained by assuming a $1/v$ cross section and the Maxwellian distribution given in equation (4.20).

To obtain comparisons involving the flux on the slots a routine was written which was called at each boundary crossing. This routine determined if the boundary corresponded to one of the slots. Each particle crossing the boundary was given a weighting of $1/\cos(\theta)$ where θ is the angle between the particle's direction and the normal to the boundary. A further weighting was calculated for each reaction equal to the cross section for that particle at that particular energy. (Cross sections are described in Section 4.4.17.) In this way radial distributions were obtained for the expected production rates of ^{24}Na from ^{27}Al and of ^{115m}In from ^{115}In.

To calculate the average production rate expected in an area corresponding to the area covered by the aluminium and indium disks (rather than in a radial bin) a further weighting as given in equation (4.24) below was applied. This weighting was applied for particles in an annulus with a radial extent equal to that covered by the disk, taking advantage of the azimuthal symmetry of the situation. Note that the geometry is not exactly symmetric in azimuth but the experimental data is consistent with such symmetry in the development of the cascade.

For a particle crossing the plate at radius R from the beam centre, the weight-

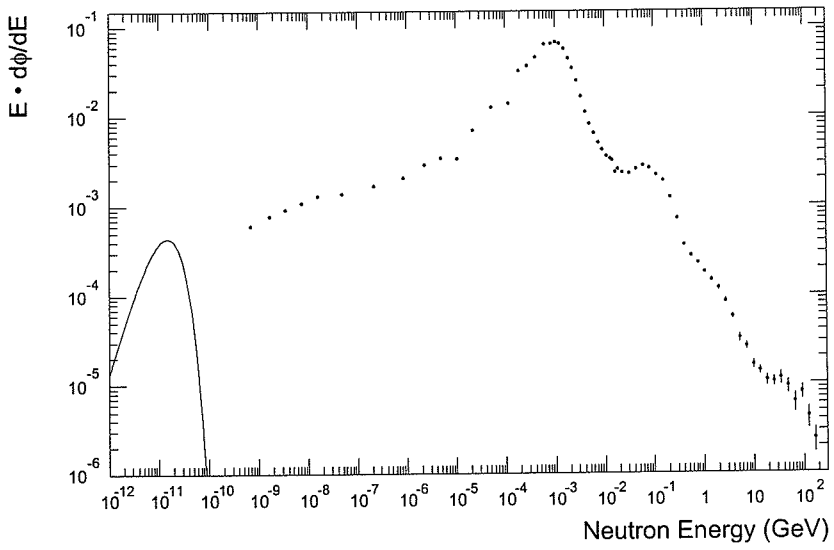

Figure 4.26: Spectrum of neutron flux in the argon surrounding the calorimeter.

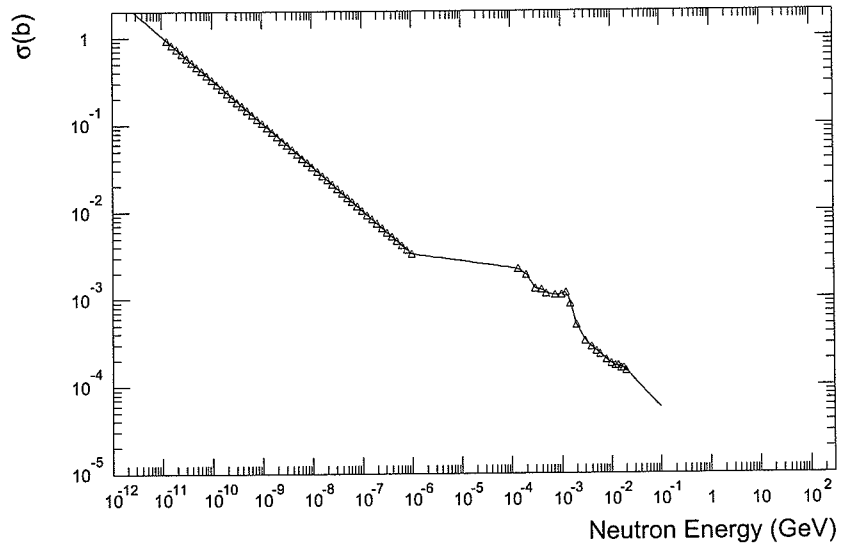

Figure 4.27: Cross section of $^{40}\mathrm{Ar}\,(\mathrm{n},\gamma)\,^{41}\mathrm{Ar}$.

ing w is given by the fraction of the circle of radius R inside the disk. That is, $w = l/2\pi R$ where l is the length of the arc of radius R covered by the disk. This results in the following expression for the weight for a disk of radius r_d with centre at a distance R_d from the beam centre:

$$w = \begin{cases} 1 & \text{for } r_d > R_d \text{ and } R \leq r_d - R_d \\ \frac{1}{\pi} \arccos\left(\frac{R^2 + R_d^2 - r_d^2}{2RR_d}\right) & \text{otherwise.} \end{cases} \tag{4.24}$$

4.4.16 Comparison for Argon Measurements

The FLUKA calculation yielded an argon production rate of $(8.5 \pm 0.2) \times 10^{-4}$ per mole of ^{40}Ar per beam particle, which is 17% lower than the measured value. The comparison is summarized in table 4.16. Section 4.4.22 discusses the comparisons between FLUKA and measurement.

Figure 4.28 shows the running sum as given by equation (4.22). The FLUKA measurement has a 61% contribution from the thermal group, with $\Psi_{th} = (5.2 \pm 0.1) \times 10^{-4}$. The remaining contribution comes from energies up to 50 eV where the cross section is high, and from energies in the range 50 keV to 1 MeV where the neutron spectrum starts to peak. Most of this contribution is in regions where the cross section is reliable. The parts of the cross section which are less reliable are therefore expected to have a minimal effect on the determination of the ^{41}Ar production rate.

Table 4.16: Comparison for ^{41}Ar production rates. Production rates are per mole of ^{40}Ar per beam particle.

Measured	$(10.2 \pm 1.2) \times 10^{-4}$
FLUKA	$(8.5 \pm 0.2) \times 10^{-4}$
Ratio FLUKA/Measured	0.83 ± 0.10

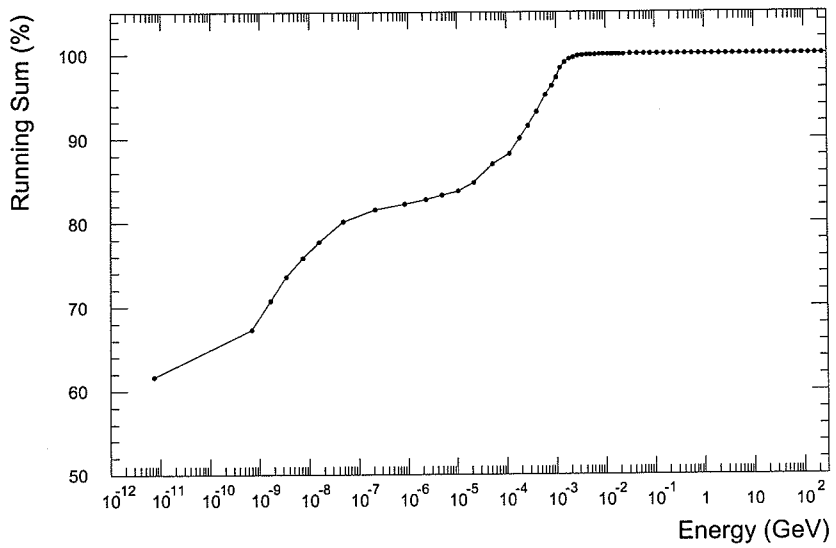

Figure 4.28: Running sum of ^{41}Ar production rate given as percentage of total.

4.4.17 Reaction Cross Sections for Production of ^{24}Na and ^{115m}In.

Figures 4.29 and 4.30 show the cross sections used for production of ^{24}Na and ^{115m}In. These are the same cross sections used in the comparisons made with the Rösti experiments. (See Section 4.2.)

Below 20 MeV cross sections for the neutron-induced reactions, ^{27}Al (n,α) ^{24}Na and ^{115}In (n,n') ^{115m}In were taken from the ENDF/B-VI dosimetry file. Cross sections extrapolated up to 44 MeV by Greenwood [47] were used, and for energies above 50 MeV neutron cross sections were assumed to be constant.

Proton and charged pion induced reactions are also important in aluminium. Cross sections for the reaction ^{27}Al(p,3pn) ^{24}Na were taken from Hitz and Ramsey [48] for energies from 40 to 100 MeV, from Tobailem *et al.* [49] from 100 to 220 MeV, and from Baker *et al.* [50] at 28 GeV and above. The cross sections for production of ^{24}Na from ^{27}Al by π^- and π^+ are those recommended by Dropesky *et al.* [51].

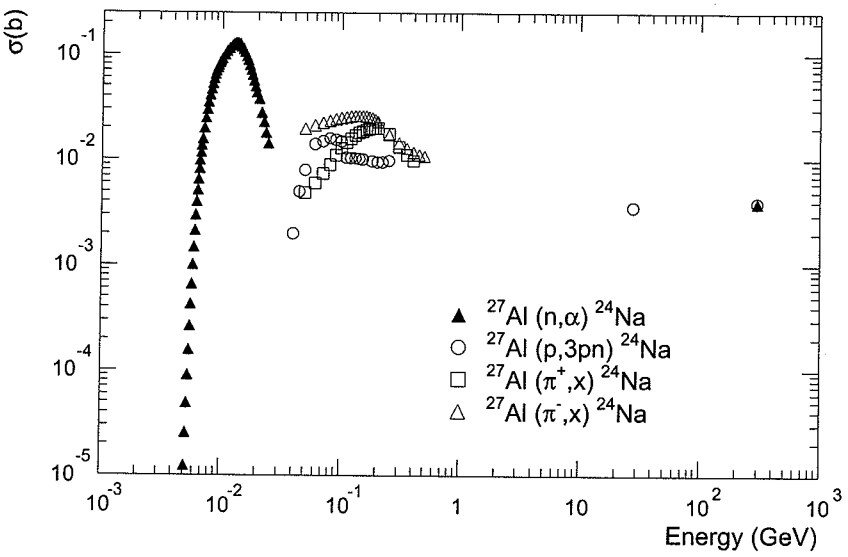

Figure 4.29: Cross section for production of ^{24}Na from ^{27}Al.

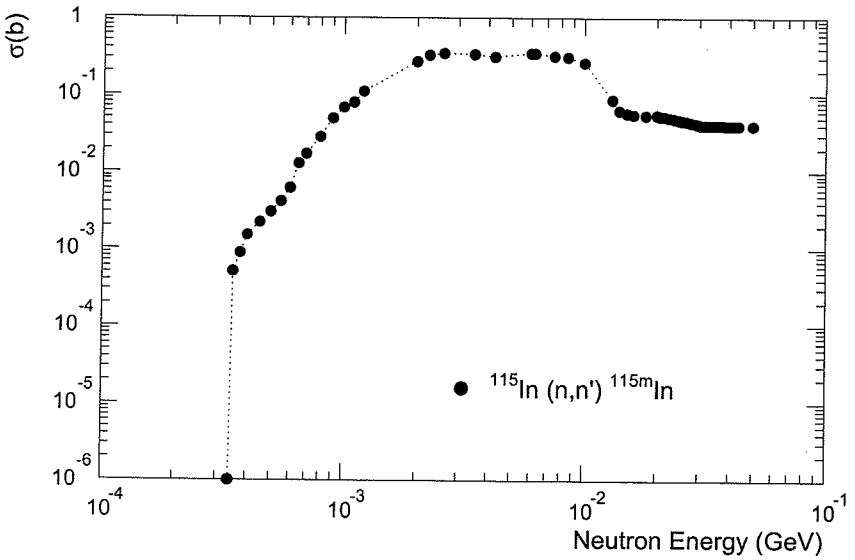

Figure 4.30: Cross section for production of ^{115m}In from ^{115}In.

4.4.18 Comparison of Results for Production of ^{24}Na and ^{115m}In.

Figure 4.22 shows the radial distributions in slots 3 and 5 of the production rate of ^{24}Na from ^{27}Al obtained with FLUKA and measured from the aluminium disks. Figure 4.23 shows the comparison for the reaction rate of ^{115}In (n,n') ^{115m}In at slot 5. Since this reaction is not sensitive to thermal neutrons, data from all the indium foils were used in this graph. In the plots the dashed histogram is the radial distribution in 0.5 cm radial bins. The solid points are the production rates calculated by FLUKA averaged over the disk as described in Section 4.4.15. These are consistent with the histograms. The open circles are the measured data. The shape of the distribution as obtained by FLUKA compares well with the measurement, however, the FLUKA calculation is systematically lower. Figure 4.31 shows the ratio of the FLUKA calculation to the measured data for each disk. The average ratio was 0.55 ± 0.01 for aluminium on slot 3, 0.63 ± 0.01 for aluminium on slot 5, and 0.62 ± 0.01 for indium on slot 5. The errors on these ratios exclude the 8% error on the beam intensity for ease of comparison. This is a systematic error for all the ratios. These comparisons are discussed in Section 4.4.22.

4.4.19 Comparison of Thermal Neutron Measurements

The difference between data obtained from foils with and without cadmium for gold and indium, as shown in figures 4.19–4.20, showed little radial dependence. The average difference between exponential curves fitted to the data was compared with the average thermal production rate obtained from FLUKA. The average thermal flux ϕ_{th} in a 24 cm radius region of the slot, as obtained from FLUKA, was $(7.8 \pm 0.5) \times 10^{-4}$ n/cm^2 per beam particle. This was used in equation (4.23) to obtain the thermal production rate. The error on the measured difference was estimated by the variation of the cadmium/no cadmium difference with radius (about 9% for ^{116m}In and 17% for ^{198}Au,) a 5% error in the efficiency and a 7.5% error in the beam intensity. The results are summarized in table 4.17. The average ratio of FLUKA/measured for gold and indium was 0.57 ± 0.07. The measured results for copper have not been

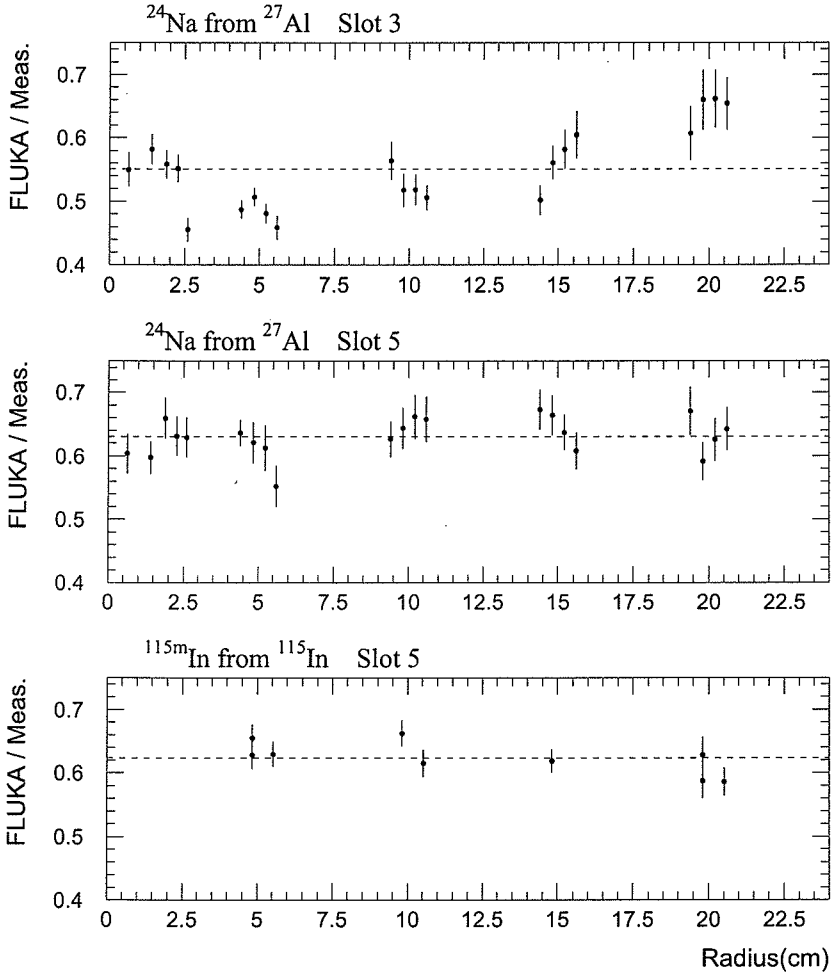

Figure 4.31: Ratio of FLUKA to measured results of production rates of ^{24}Na from ^{27}Al and of ^{115m}In from ^{115}In.

included as the difference between the with and without cadmium data was small, although the value estimated from FLUKA of the thermal production rate for copper seems consistent with what appears in figure 4.21.

Table 4.17: Comparison for thermal neutron flux.

Isotope	Measured Thermal Production Rate	σ_o (b)	FLUKA Thermal Production Rate	FLUKA/ Measured
^{116m}In	0.22 ± 0.03	157	0.12 ± 0.01	0.55 ± 0.08
^{198}Au	0.12 ± 0.02	98.8	0.076 ± 0.005	0.63 ± 0.13
^{64}Cu	–	4.5	0.0034	–

4.4.20 Comparison of Production Rates in Gold, Indium and Copper Foils

The expected production rates in gold, indium and copper were obtained using shielded resonance cross section data for the neutron induced reactions. The cross sections were calculated [52] from resonance parameters taken from ENDF/B VI for Au and In and ENDF/B IV for Cu. They are appropriate for thin foils where the flux outside the foils is not perturbed. The shielding refers to self-shielding in the foils which results from the flux within the foils being depressed at resonance energies. The shielding is significant even in thin foils and is increased due to the reduced doppler broadening at 87 K. The cross sections were calculated to match the energy grouping given by FLUKA and they assume that the resonance is entirely within a group.

The average production rate in a 24 cm radius circle on slot 5 was calculated in the FLUKA simulations. This was done by multiplying the flux ϕ_i in the appropriate neutron energy group with the cross section for that group $\sigma_s(E_i)$. The $1/v$ contribution was also included. The contribution from the thermal group is given in Section 4.4.19 above. The calculation can be represented by

$$\Psi = \Psi_{th} + \sum_{i=2}^{n} \phi_i \cdot \left(\sigma_s(E_i) + \sigma_o \sqrt{E_o/E_i} \right) \tag{4.25}$$

where $E_o = mv_o^2/2$. The other symbols are defined in Section 4.4.15. For the samples enclosed in cadmium the thermal contribution was excluded.

To compare this with the measured data, the average production rate in a 24 cm radius circle was calculated based on the exponential fit to the data. For copper the sum of two exponentials was used. Given a fit to the experimental data with function $f(r)$, the average production rate in a region of radius R is given by

$$\frac{1}{\pi R^2}\int_0^R 2\pi r f(r)\mathrm{d}r \ . \tag{4.26}$$

The comparisons are shown in table 4.18.

Table 4.18: Comparison of production rates in gold, indium and copper foils.

Sample	Measured	FLUKA	FLUKA/ Measured
In/No Cd	0.76	0.54	0.70
In/With Cd	0.54	0.42	0.76
Au/No Cd	0.54	0.39	0.73
Au/With Cd	0.40	0.32	0.78
Cu/No Cd	0.023	0.010	0.44
Cu/With Cd	0.019	0.0068	0.36

4.4.21 Study of the Effects of Material Composition

One uncertainty in the calculation was the composition and density of the wood. To investigate the sensitivity of the wood to the calculation, two runs were performed with the density of wood equal to 0.5 and 1.1 g/cm^3.

In the simulations materials such as iron and lead were assumed to be pure which is not likely to be the case. Small amounts of other elements in these materials can have a significant effect. For example, lead typically has about 4% antimony by weight.

Table 4.19 shows the comparison of the results from these different cases. Table 4.20 shows the results relative to the reference configuration in which $\rho_{\text{wood}} = 0.8$ g/cm^3 and pure lead is used.

Table 4.19: Comparison of ^{41}Ar production rate, average thermal neutron flux on slot 5, and ratio of FLUKA to measured values of production rate of ^{24}Na and ^{115m}In. The 8% error on the beam intensity has been excluded for the ratios. Production rate units are $\times 10^{-4}$ per mole of parent atom per beam particle. Thermal flux units are $\times 10^{-4}$ n/cm^2 per beam particle.

	$\rho_{\text{wood}} = 0.8$ Pure Pb	$\rho_{\text{wood}} = 1.1$ Pure Pb	$\rho_{\text{wood}} = 0.5$ Pure Pb	$\rho_{\text{wood}} = 0.8$ 4% Sb in Pb
^{41}Ar Production Rate	8.5 ± 0.2	9.5 ± 0.2	7.5 ± 0.1	7.5 ± 0.2
(Thermal contribution)	(5.2 ± 0.1)	(6.1 ± 0.2)	(4.8 ± 0.1)	(4.7 ± 0.2)
Thermal Flux on Slot 5	7.8 ± 0.5	10.2 ± 0.8	7.0 ± 0.8	7.3 ± 1.4
^{24}Na on Slot 3	0.55 ± 0.01	0.47 ± 0.01	0.54 ± 0.02	0.54 ± 0.01
^{24}Na on Slot 5	0.63 ± 0.01	0.57 ± 0.01	0.67 ± 0.02	0.60 ± 0.01
^{115m}In on Slot 5	0.62 ± 0.01	0.57 ± 0.01	0.60 ± 0.01	0.61 ± 0.01

Table 4.20: Comparison of ^{41}Ar production rate, average thermal neutron flux on slot 5, and ratio of FLUKA to measured values of production rate of ^{24}Na and ^{115m}In. Values are given as the ratio to the reference configuration, i.e., $\rho_{\text{wood}} = 0.8$, and pure Pb.

	$\rho_{\text{wood}} = 1.1$ Pure Pb	$\rho_{\text{wood}} = 0.5$ Pure Pb	$\rho_{\text{wood}} = 0.8$ 4% Sb in Pb
^{41}Ar Production Rate	1.12 ± 0.04	0.89 ± 0.02	0.87 ± 0.04
(Thermal contribution)	(1.17 ± 0.04)	(0.91 ± 0.03)	(0.88 ± 0.05)
Thermal Flux on Slot 5	1.31 ± 0.13	0.90 ± 0.13	0.93 ± 0.19
^{24}Na on Slot 3	0.85 ± 0.03	0.99 ± 0.04	0.98 ± 0.03
^{24}Na on Slot 5	0.90 ± 0.02	1.05 ± 0.04	0.94 ± 0.02
^{115m}In on Slot 5	0.92 ± 0.02	0.96 ± 0.02	0.98 ± 0.02

Increasing the density of wood introduces more moderating material which

results in an increase of neutrons in the thermal and epi-thermal regions and a decrease in the number of neutrons with high energy ($E_n > 10$ keV). The neutron spectrum in the liquid argon in the inner container was observed to show an increase in the flux for energies from the thermal group up to around 10 keV. There was a slight decrease in the flux in the energy range 0.1–10 MeV. This is reflected in the decreased production rate of ^{24}Na and ^{115m}In. The increase in the production rate of ^{41}Ar is predominately due to the increase in the thermal group. The thermal flux in the inner container (as indicated by the thermal contribution in the ^{41}Ar production rate) increased by 17%. In slot 5 the increase was about 30%.

Decreasing the density of the wood has the opposite effect. However, for this configuration there was no significant change in the high energy neutron flux ($E_n > 10$ keV). Subsequently there was little change in the production rates of ^{24}Na and ^{115m}In. The thermal flux decreased by about 10%.

Similar results were observed when 4% antimony was introduced to the lead. The thermal and epi-thermal flux is reduced here due to a large number of resonances in the neutron cross section for Sb up to around 1 keV.

4.4.22 Discussion of BEDLAM Comparisons

The production rate of ^{41}Ar as calculated by FLUKA was 17% lower than the measured value. For this type of simulation, where a cascade is simulated from an initial high energy particle down to the thermal neutrons, agreement to within 20% is very good. For the other comparisons agreement was not as good, with the FLUKA calculations underestimating the measured quantities. This disagreement is of concern and is not fully understood. In all the comparisons, except for the copper foils, FLUKA agreed within 45% of the measured value.

Many of the results calculated with FLUKA, in particular those in Sections 4.4.18 and 4.4.19, underestimated the measured data by roughly the same amount (a factor of 1.6–1.8). This suggests the possibility of a systematic error in the measurements or in the FLUKA simulations.

One quantity that was used in all measurements was the beam intensity, and so errors in this would give rise to systematic differences. The error for the beam intensity was 8% which was dominated by the error in the cross section. The same technique was used for determining the beam intensity in the Rösti runs (see Section 4.2) where a systematic underestimation was not observed. It therefore seems unlikely that any error inherent in the techniques used for determining the beam intensity (for example, a larger error in the cross section) would explain the observed discrepancies. Also, the agreement with the beam intensity calculated using the parallel plate ionization chamber gives confidence in this value.

The production rates of ^{24}Na from ^{27}Al in slots 3 and 5 are independent of the efficiency of the NaI gamma spectrometer. This is because the same spectrometer was used to assay the ^{24}Na in the aluminium sheet used for determining the beam intensity. The same efficiency was therefore used, and so cancels out in the determination of the production rate. The measurements for gold, indium and copper, and the measurement of the ^{41}Ar activity involved separate gamma spectrometers. These measurements are therefore sensitive to errors in the efficiency of their respective gamma spectrometers as well as the efficiency used in calculating the beam intensity.

The ^{41}Ar production rate has a 61% contribution from thermal neutrons. The good agreement for the ^{41}Ar production rate indicates that the thermal neutron flux is being calculated adequately by FLUKA. The thermal flux in slot 5 as calculated by FLUKA is lower than the measured value by a factor 0.57 ± 0.07. Considering the complexity of the simulation where a thermal flux is determined which is a consequence of a high energy cascade and subsequent thermalization of the neutrons, these comparisons are reasonable.

The thermal neutron flux is very sensitive to the setup used. It is interesting to note the large effect the concrete shielding has on the thermal flux. A simulation without the concrete resulted in a reduction in the thermal neutron flux in slot 5 by a factor of 3. The thermal contribution to the production rate of ^{41}Ar was reduced by a factor of 6. Increasing the wood density from 0.8 to 1.1 g/cm^3 introduced more

moderating material and resulted in an increase of 17% in the thermal contribution to the ^{41}Ar production rate.

The production rates calculated by FLUKA for ^{198}Au and ^{116m}In using resonance cross sections gave reasonable agreement, with FLUKA underestimating the measured values by 22–30%. This suggests that the flux in the 0.5 eV–1 keV range is being calculated reasonably by FLUKA. The production rates in the copper foils compared less favourably with FLUKA. This may be partly due to the radial variation of the production rate being large for the copper measurement. (See figure 4.21.) The method used for determining the measured production rate involved fitting a function to the data and calculating the average over the whole slot. Because of the large radial variation this method could lead to large uncertainties. Also, the diameter of the copper foils (3.6 cm) was much larger than for the gold and indium foils (1.6 cm). This would lead to further uncertainty in fits to the copper data.

In Section 4.4.21 a study was made of the effects of uncertainties in the material compositions. Based on these studies the uncertainty due to the compositions of materials used is likely to be around 20–30% for the thermal flux and less than 10% for other quantities.

Chapter 5

Particle Fluxes and Damage in ATLAS

5.1 Introduction

This chapter describes a simulation of the ATLAS detector to determine the particle fluxes expected in the inner detector. The displacement damage to the silicon has been calculated in terms of the equivalent 1 MeV neutron flux that would produce the same damage. Simulations have been made with different detector configurations. Two designs for the inner detector layout have been studied. One is the Cosener's House design which contains a number of barrel transition radiation tracker (TRT) modules interspersed with silicon tracking layers. The other contains a single barrel TRT, with the silicon layers all inside the inner radius of the TRT.

Only radiation levels in the inner detector are given here. Radiation levels in the whole detector have been studied in various papers. See for example Refs. [1, 26, 53].

5.2 Details of the Simulation

Simulations have been carried out with FLUKA. (See Section 4.1 for an overview of FLUKA.)

The neutron fluxes quoted have a minimum neutron kinetic energy cut-off of 150 keV. As the neutron energy drops below 150 keV, the damage cross section drops sharply by more than a factor of 10. Therefore, this energy corresponds approximately to the minimum energy at which neutrons damage silicon. Although it is possible for neutrons below 150 keV to contribute to the damage if the flux in some part of the

spectrum between thermal energies and 150 keV were to increase by a large factor, such an increase is generally not seen in neutron spectra obtained in calorimeter based detectors. Neutron fluxes are often quoted as above 100 keV. There is not a large difference due to this lower threshold; normally less than a 5% increase in the neutron flux.

Hadronic interactions have an energy threshold of 20 MeV for protons and pions and 50 MeV for other hadrons. Below this energy charged hadrons are ranged out to rest. A minimum kinetic energy cut-off of 10 MeV for all particles other than neutrons has been applied. This cut-off will exclude very few particles as can be seen from figure 5.5 which shows the energy spectra for particles in the first silicon layer of the Cosener's House design. Leptons and photons have been discarded in the simulations. These particles make an insignificant contribution to the bulk damage to silicon compared to the damage caused by hadrons.

Because FLUKA is capable of transporting neutrons down to thermal energies (although in this case we are only interested in transporting down to 150 keV) the simulations include the two main components of the radiation environment which result in bulk damage. These are:

1. the secondaries themselves produced in the primary proton-proton collisions, and

2. the "albedo" neutron flux originating from showers in the calorimeter.

5.2.1 The Source Term

The source of secondaries from proton-proton collisions has been generated with the DTUJET90 code [39]. These secondaries have been stored in a file and the order has been randomized to help avoid any selection effects. Single diffractive events are excluded. These events are very forward peaked and have an insignificant contribution to the calculations carried out here. The uncertainty in the source term is estimated to be around 50%, due to the choice of structure functions, and is the major systematic error in the quoted numbers. This uncertainty arises due to the

Table 5.1: Multiplicity of secondaries generated in p-p events by the DTUJET code. [26]

LHC "Standard" Structure Functions

	Multiplicity				
η	Total	Charged	π^0	γ	Strange
0–2	45.	25.	13.	1.1	5.9
2–4	50.	28.	13.	1.1	8.0
4–6	39.	22.	10.	0.8	6.5
6–8	23.	13.	6.1	0.5	3.8
8–10	8.0	4.7	1.9	0.1	1.2
10–∞	0.7	0.4	0.1	0.01	0.08
0–∞	165.	93.	45.	3.7	26.

LHC "Extreme" Structure Functions

	Multiplicity				
η	Total	Charged	π^0	γ	Strange
0–2	71.	41.	21.	1.9	9.1
2–4	75.	42.	20.	1.8	12.
4–6	57.	32.	15.	1.3	9.4
6–8	29.	16.	7.3	0.6	4.9
8–10	8.2	4.7	1.9	0.1	1.3
10–∞	0.7	0.4	0.1	0.01	0.08
0–∞	241.	136.	66.	5.7	37.

extrapolation from existing data, where the structure functions agree, to LHC energies. About a 50% increase is observed in the multiplicity from the use of "extreme" structure functions [26]. This can be seen in table 5.1 which shows the multiplicity for "standard" and "extreme" structure functions for LHC energies. Figure 5.1 shows the multiplicity of charged hadrons as a function of pseudorapidity for the "standard" structure functions.

Annual fluxes are presented which assume a luminosity of 1.7×10^{34} cm^{-2}s^{-1}, an inelastic cross section (single diffraction excluded) of 60 mb and an operating time

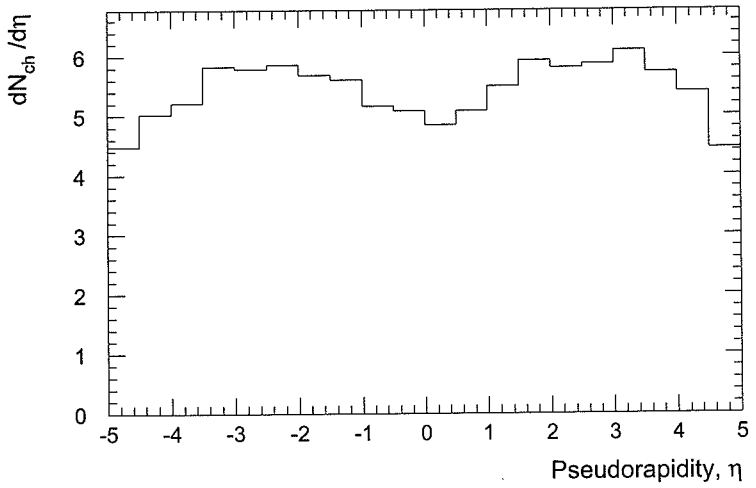

Figure 5.1: Multiplicity of charged hadrons as a function of pseudorapidity as obtained from DTUJET.

per year of 10^7 sec. The uncertainty in the cross section is of the order 10–20%. Systematic errors have not been included in any of the plots presented here.

Estimation of the Charged Hadron Flux

The multiplicity of charged hadrons $\mathrm{d}N/\mathrm{d}\eta$ is approximately flat with respect to the pseudorapidity for $|\eta| < 3$ as seen in figure 5.1. The pseudorapidity is defined as

$$\eta = -\ln\tan(\theta/2) \tag{5.1}$$

where θ is the angle from the beam axis. For a cylinder of radius r, the longitudinal distance z from the interaction point is given by $z = r/\tan\theta$. It follows that

$$\frac{\mathrm{d}N}{\mathrm{d}z} = \frac{\sin\theta}{r}\frac{\mathrm{d}N}{\mathrm{d}\eta}\,. \tag{5.2}$$

The flux ϕ per p-p interaction through the cylinder at a distance z is given by

$$\begin{aligned} \phi &= \frac{1}{2\pi r}\frac{\mathrm{d}N}{\mathrm{d}z}\frac{1}{\sin\theta} \\ &= \frac{1}{2\pi r^2}\frac{\mathrm{d}N}{\mathrm{d}\eta}\,. \end{aligned} \tag{5.3}$$

The $1/\sin\theta$ is due to the increased amount of material that a particle passes through when it transverses the detector obliquely. Since $\mathrm{d}N/\mathrm{d}\eta$ is approximately constant, the flux will be uniform along z in the absence of a magnetic field. From figure 5.1 the plateau has the value $\mathrm{d}N/\mathrm{d}\eta \sim 6$. It follows for a luminosity of 1.7×10^{34} cm^{-2}s^{-1}, an inelastic cross section of 60 mb and an operating time of 10^7 sec, that the charged hadron flux per year is approximately $10^{16}/r^2$ cm^{-2}yr^{-1}, where r is in cm.

Due to the 2 Tesla magnetic field in the inner detector region charged particles with a momentum less than about 300 MeV/c will not hit the barrel calorimeter and may loop a number of times through the inner detector increasing the flux. This increase was found to be about 15% in the first layer at a radius of 11.5 cm and up to 70% for layers at radii around 50 cm.

5.2.2 Description of the Detector

The design of the outer detector is based on the liquid argon option described in the ATLAS Letter of Intent [1]. The geometry used is shown in figure 5.2. The differences expected with the current design of the barrel calorimeter, which consists of Pb-LAr in the EM part and Fe-Scint in the hadronic part, are expected to be small ($<$ 15% decrease) based on studies made by Ferrari *et al.* [26].

The calorimeters have been simulated by a homogeneous mixture of the materials making up those detectors. The electromagnetic calorimeter consists of lead, liquid argon and iron with volume ratios of 1.8 : 3.8 : 0.4 respectively. This is based on the design of the accordion electromagnetic calorimeter described in the Letter of Intent. In this design each converter plate has a 1.8 mm thick sheet of lead which is clad between two 0.2 mm thick sheets of iron. There are 3.8 mm gaps between the

plates which are filled with liquid argon. The hadronic calorimeter consists of iron and liquid argon with a ratio of 12 : 2.5 by volume. The densities of these homogeneous mixtures for the electromagnetic and hadronic calorimeters are 4.82 and 6.76 g/cm^3 respectively. The walls of the cryostat have also been included. The end-caps give coverage to $|\eta| = 2.8$ which is less than the coverage of $|\eta| < 3$ specified in the Letter of Intent. Studies described in Section 5.3.4 show that there is not a significant decrease in the fluxes due to this smaller coverage.

The inner detector region is in a 2 Tesla magnetic field parallel to the beam axis.

Two variations of the inner detector barrel layout were studied. The first was the Cosener's House design. (See Section 2.2.2.) In this design barrel TRT modules are located between radii 55.5–76.5 cm and between 82.5–103.5 cm with longitudinal extent $z = \pm 95$ cm. Two short TRT units are located between radii 33–49.5 cm which extend from $|z| = 50$ to 95 cm. Silicon layers are placed at 52, 53, 79, 81 and 105 cm radius, each with a longitudinal extent of $z = \pm 95$ cm. This layout is shown in figure 5.2.

The second design simulated differed from the Cosener's House design by using a single barrel TRT with radial extent 70–110 cm. This arrangement contains silicon layers at radii of 50, 60, and 69 cm. A diagram of this layout is shown in figure 5.3.

Both arrangements have silicon layers at 11.5, 14.5, 20, and 30 cm. All the silicon layers, except for the first three, extend from $z = \pm 95$ cm. The first three layers extend from $z = \pm 35$, ± 40, and ± 55 cm. A thickness of 300 μm has been used. This does not take into account the effects of material in the supports. A simulation of the Cosener's House design was carried out with 1 mm thick layers of silicon rather than 300 μm to simulate the material in the supports. The effect was not found to be significant.

In both arrangements the end-cap TRT has an inner radius of 50 cm and an outer radius of 100 cm and extends from $z = 105$–330 cm. The TRT modules are assumed to contain polyethylene (CH_2) of density 0.059 g/cm^3. The MSGC wheels

have not been included.

Wheels of detectors are included at $z = 58.5$, 70, 96, and 109 cm. The ones at 58.5 and 70 cm extend from 15–22.5 cm. The others extend from 15–25 cm. These wheels are referred to as GaAs wheels although they have been simulated with silicon of 300 μm thickness. The use of silicon rather than GaAs is not expected to have any effect on the fluxes obtained.

The Cosener's House design has a moderator placed on the inside of the barrel calorimeter vessel and the calorimeter entrance face in the end-cap region. The moderator is 5 cm thick in the barrel region and 10 cm thick in the end-cap region. This has been assumed to be polyethylene (CH_2) of density 0.92 g/cm^3.

In the "single barrel TRT" design four moderator configurations have been simulated to determine the effectiveness of the various parts of the moderator in reducing the "albedo" neutron flux.

The configurations are:

- Configuration A: No moderator
- Configuration B: 10 cm moderator in the end-cap region only
- Configuration C: 10 cm end-cap moderator + 5 cm barrel moderator for $|z| > 100$ cm
- Configuration D: 10 cm end-cap moderator + 5 cm barrel moderator for all z.

5.3 Results

Neutron, proton, anti-proton, charged pion, and charged and neutral kaon fluxes were obtained in each silicon layer and each GaAs wheel. For the silicon layers, the full longitudinal extent was used when determining the flux and so the fluxes reported are the average over the whole layer. Similarly for the GaAs wheels, the fluxes are averaged over the full radial extent. Fluxes were calculated by writing a routine that was called at each boundary crossing. The contribution to the flux was

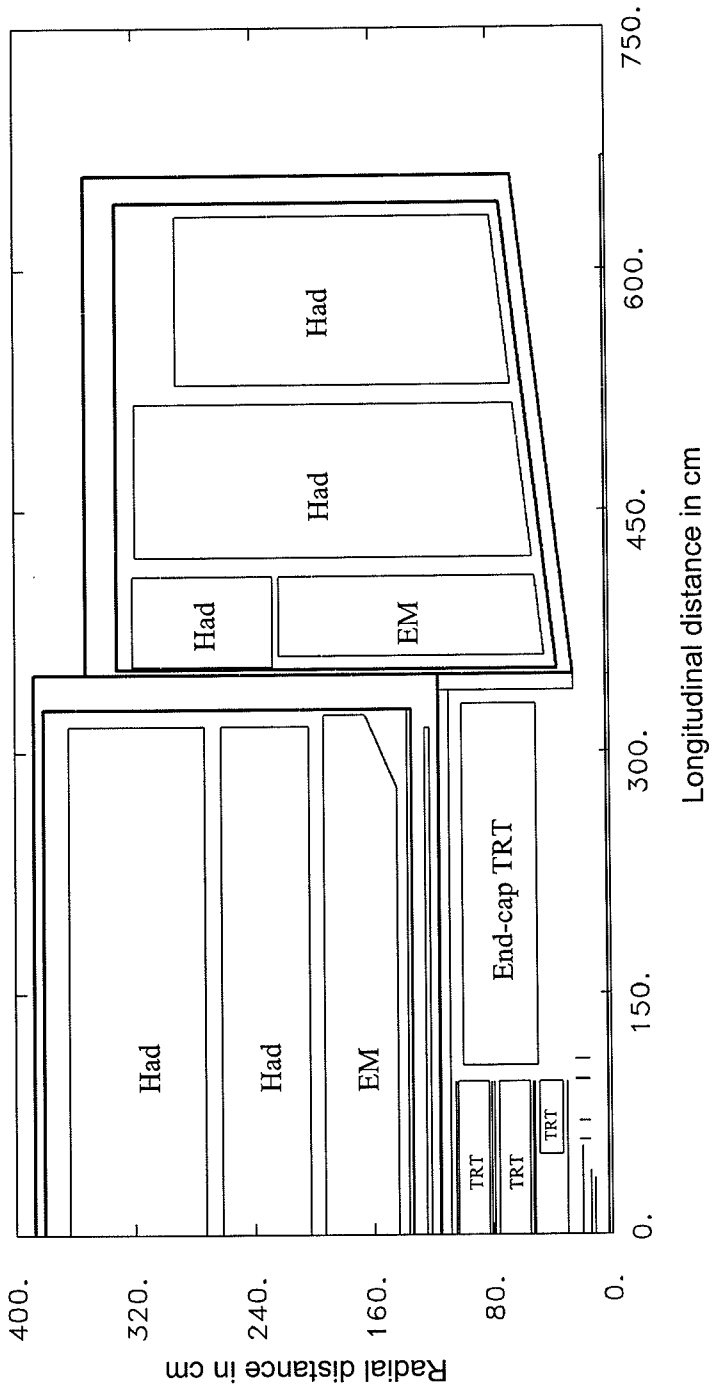

Figure 5.2: Geometry of the ATLAS detector used in the simulations with the Cosener's House design for the inner detector.

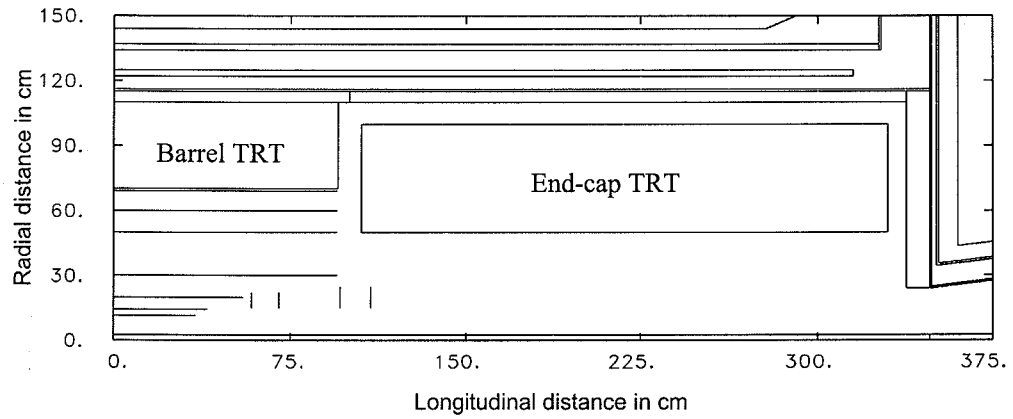

Figure 5.3: Inner detector region showing the layout used for the Single TRT design.

given by $1/\cos(\theta)$ where θ is the angle the direction of the particle makes with the normal to the boundary.

The variation of flux over the detectors was studied. Figure 5.4 shows the z variation of the neutron flux, charged particle flux and total damage for the Cosener's House design. The z variation of charged hadron fluxes in the silicon layers was such that the maximum was generally about 10% higher than the average, with fluxes observed to increase with z. For neutron fluxes the statistical variations dominated and the maximum was in general within 20% of the average. The maximum total damage for a layer was generally within 20% of the average, and for most cases the deviation was around 10–15%. The radial variation for the GaAs wheels roughly follows the radial variation observed for the average flux in the silicon layers and the maximum is expected to be about that obtained in the layer at r=14.5 cm.

To determine the damage that would result from such fluxes, the equivalent 1 MeV neutron flux that would produce the same damage in silicon detectors has been calculated. As stated in Section 3.4 the displacement damage is approximately proportional to the non-ionizing energy loss (NIEL). Figure 3.2 shows the NIEL in silicon as a function of energy for different particles. The equivalent 1 MeV neutron flux has been calculated by normalizing this plot to 1 MeV neutrons and folding the data in with the corresponding particle flux energy spectrum. Examples of these

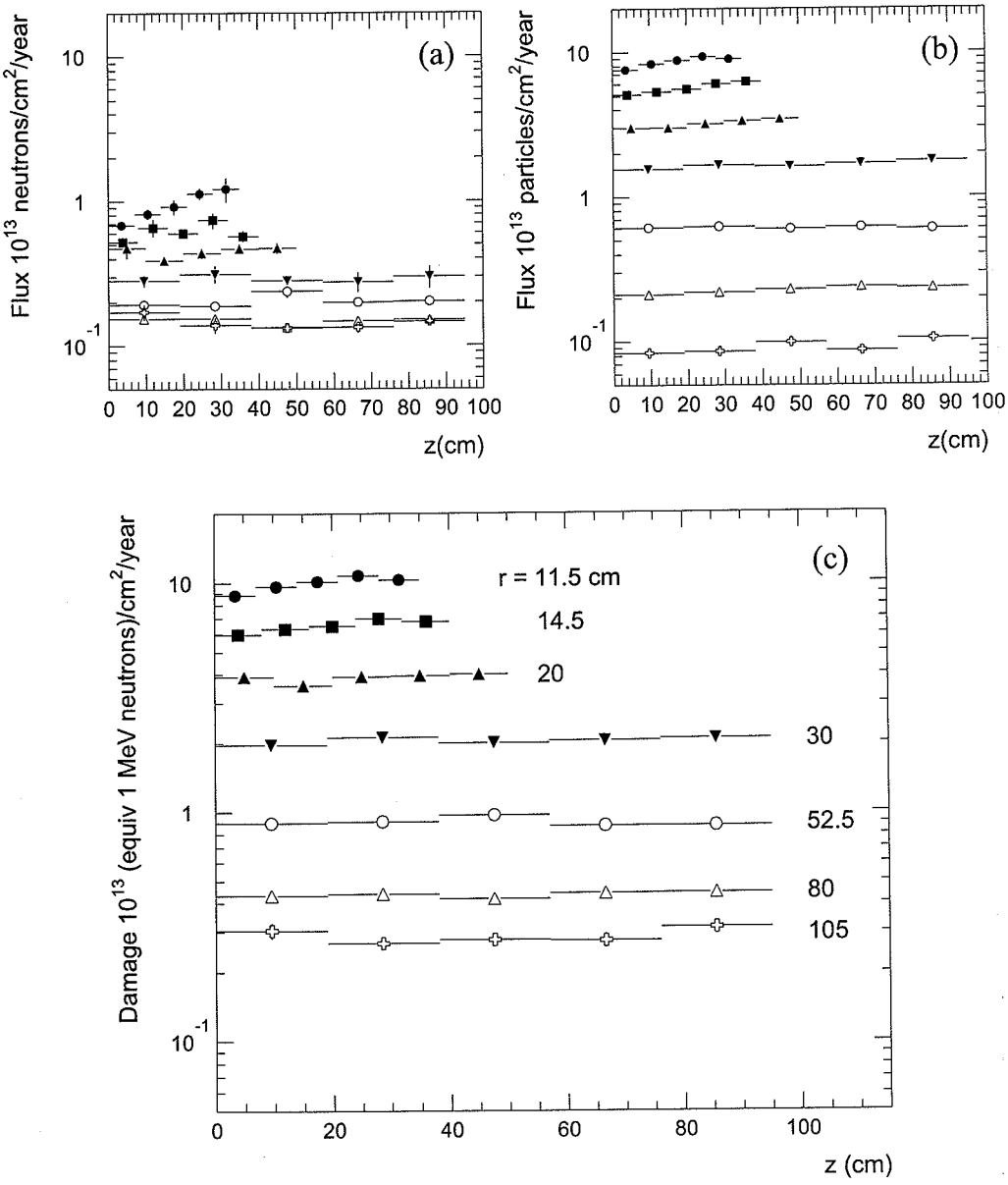

Figure 5.4: Variation with longitudinal distance z from interaction point for (a) neutron flux, (b) charged hadron flux, and (c) total damage in equivalent 1 MeV neutron flux. Data are for silicon layers in the Cosener's House design with radii as indicated in figure (c). The average has been taken for the pairs of layers at radii 52 & 53 cm and at radii 79 & 81 cm.

spectra are shown in figures 5.5 and 5.6. Damage from neutrons, protons, anti-protons, charged pions and kaons (sum of charged and neutral kaons) have been calculated separately. The total damage has been calculated as the sum of the damage from these particles. The kaon damage has been calculated using the proton NIEL data, and so is expected to be slightly over estimated.

5.3.1 Particle Fluxes and Damage

The particle fluxes and damage (in equivalent 1 MeV neutron flux) in the ATLAS detector with the two variations of the inner detector layout are given in tables 5.4–5.7. These results are presented graphically in figures 5.7–5.10. These values were obtained using the complete moderator.

The data for the GaAs wheels are included in the plots and are plotted as the first four points with increasing z from left to right.

Most values have a statistical error below 10%. This error was obtained from 5 or more independent runs comprising of about 6000 secondaries from p-p collisions each. Error bars corresponding to these statistical errors are included on the plots where they are larger than the symbols. Systematic errors as discussed in Section 5.2.1 are not included.

Both the Cosener's House design and the single barrel TRT design showed similar radial variation of the particle fluxes and the neutron-equivalent flux. The charged hadron flux approximately follows a $1/r^2$ distribution. The pion flux dominates making up 85% of the charged hadron flux. The proton and antiprotons have similar fluxes for the inner radii. For larger radii the proton flux is much higher than for antiprotons. This is due to the contribution of protons produced in showers in the calorimeter (i.e. back-splash).

The neutron flux is approximately uniform throughout the inner detector. The "albedo" neutrons make up the majority of this flux. For the inner radii part of the neutron flux is made of neutrons produced in the beam p-p interactions. For the outer layers it is almost all "albedo".

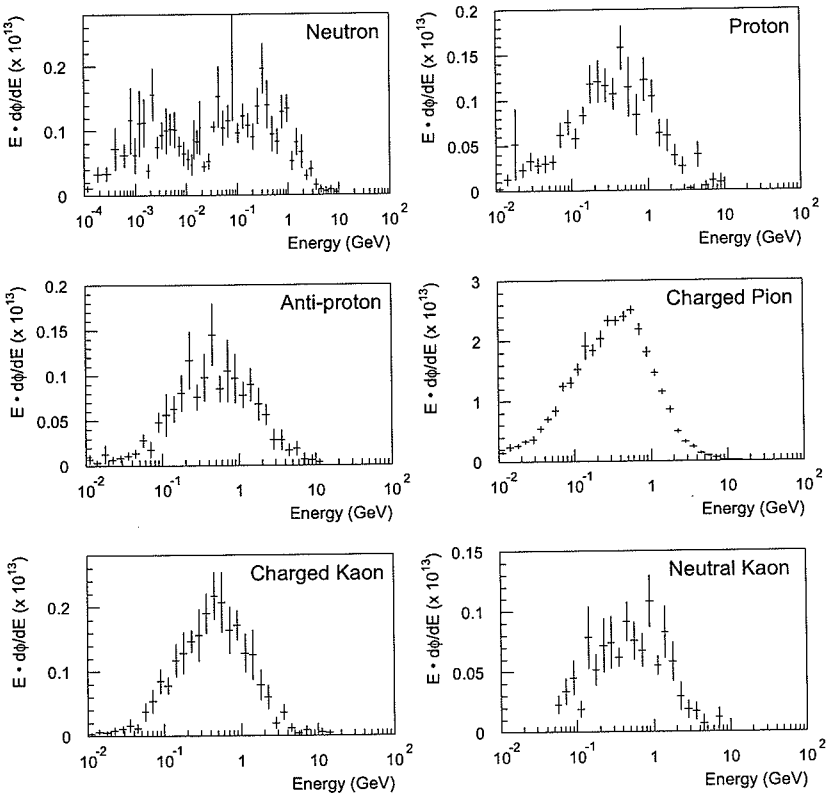

Figure 5.5: Flux energy spectra for different particle species in the first layer of the Cosener's House design with complete moderator.

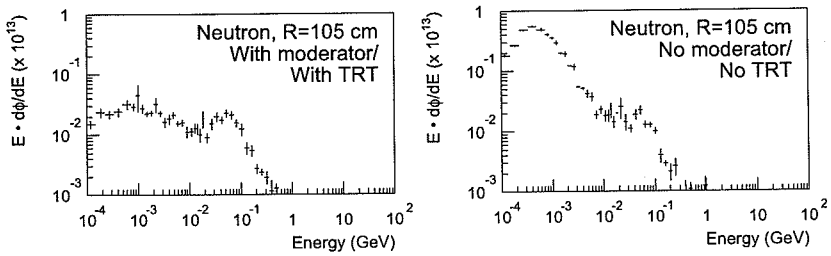

Figure 5.6: Neutron flux energy spectra in the outer layer of the Cosener's House design, comparing configurations with moderator/with TRT and no moderator/no TRT.

For the inner layers, the total 1 MeV neutron-equivalent damage is due mainly to charged hadrons. Further out this contribution reduces and around a radius of 80 cm there is an equal contribution from the neutrons and charged hadrons. For larger radii the neutron contribution dominates, although there is still a significant contribution from charged hadrons.

5.3.2 Relative Effect of Moderator and TRT on Neutron Fluxes

The radiator in the barrel TRT plays a significant role in moderating the "albedo" neutrons. Figure 5.11 shows the comparison of neutron fluxes with the following configurations:

1. No Barrel TRT and No Moderator.
2. With Barrel TRT and No Moderator.
3. With Barrel TRT and With Moderator.

Figure 5.12 shows this comparison for the total neutron-equivalent damage. This data is also given in tables 5.8 and 5.9.

The effect of the moderator on the neutron spectrum is shown in figure 5.6. The moderator is very effective in "removing" the neutrons in the energy range 100 keV to 10 MeV (that is, reducing them to energies below 100 keV where they no longer damage the silicon). For higher energies the flux is not significantly affected.

The TRT clearly reduces the total neutron flux. For example at the radius of 52 cm (inside the barrel TRT), the neutron flux is reduced by a factor of 2 from the no moderator/no TRT simulation. The moderator produces a further reduction of a factor 3. In the total neutron-equivalent damage this effect is diluted by the charged hadrons (mainly pions) which dominate at radii less than 50 cm. For the inner layers at radii less than about 30 cm the introduction of the moderator has little effect in reducing the total neutron-equivalent damage. At the outermost layer, which is outside the barrel TRT, the TRT is not as effective as for those layers within

the TRT. For example, the introduction of the barrel TRT causes a 30% decrease of the neutron flux in the outer layer and a 50% decrease for the layer at r=80 cm.

A simulation that was carried out with a 5 cm thick end-cap moderator, gave about the same fluxes as with a 10 cm thick end-cap moderator. This may no longer be the case if the density of the end-cap TRT is reduced, in which case a thicker end-cap moderator could be beneficial. A study of these effects is described in Section 5.3.4.

5.3.3 Comparison of Different Moderator Configurations in the Single Barrel TRT Design

A comparison of the neutron fluxes in the single barrel TRT design with the four moderator configurations described in Section 5.2.2 above, is summarized in table 5.10 and figure 5.13. The comparison of the total damage in equivalent 1 MeV neutron flux is given in table 5.11 and figure 5.14.

The effect of the moderator is quite dramatic on the neutron flux calculated. For example the full moderator reduces the neutron flux by a factor of 4 in the radial region 50–70 cm. However, with the dilution of the neutron damage by the addition of the damage caused by protons, pion and kaons, the overall effectiveness of the moderator is reduced. With the full moderator the neutron-equivalent damage is reduced by a factor of 2. Removing the moderator from the central barrel region ($|z| < 100$ cm), the neutron flux increases about a factor of two while the total neutron-equivalent damage is only increased by approximately 20–30%. Layers with $r < 30$ cm do not benefit from the introduction of the moderator.

Simulations were also carried out with the moderator in the end-cap region being 5 cm thick rather than 10 cm. The resulting difference for neutron fluxes in the 50–70 cm radial range was insignificant in configuration B. In configuration C there was around a 10–15% increase, and in configuration D there was about a 20–30% increase.

5.3.4 Effect of TRT Density, Thickness of End-Cap Moderator and End-Cap Coverage

In the above simulations the calorimeter covered $|\eta| < 2.8$. The effect of changing the coverage to $|\eta| < 3$ was studied. Also studied was the effect of changing the density of the TRT. The TRT (previously with a density of 0.059 g/cm^3) was simulated with a density of 0.025 g/cm^3 and with no TRT present. The effect of having either a 5 or 10 cm thick end-cap moderator was also compared. The comparison for neutron fluxes at r=79 cm in the Cosener's House design is given in table 5.2.

It can be seen from this table that the effect of changing the η coverage of the end-cap calorimeter from 2.8 to 3 is insignificant. For the case where there is no moderator and no barrel TRT, the presence of the end-cap TRT has a significant effect on reducing the neutron flux. At r=79 cm decreasing the density of the end-cap TRT from 0.059 to 0.025 g/cm^3 gave an increase of 40%. Removing the end-cap TRT resulted in a further increase by a factor of 2. For the cases where the moderator is present, the increase is still significant but not quite as large. This is because the neutrons are already moderated to some extent. The effect of the thickness of the end-cap moderator increases as the TRT is removed. For a TRT with a density of 0.059 g/cm^3, changing the thickness from 10 cm to 5 cm has little effect. For a density of 0.025 g/cm^3 there is about a 17% increase, while for no TRT there is a 50% increase.

These variations have an insignificant effect for charged hadrons since their contribution comes predominantly from secondaries produced in the p-p interactions.

5.4 Comparison with a Different Event Generator and Transport Code

Mouthuy [54] has calculated fluxes in the inner tracking layers using the event generator Pythia 5.6 with Jetset 7.3 along with the transport code Geant 3.16. Table 5.3 shows the comparison of fluxes in the first layer. The values from Mouthuy

Table 5.2: Comparison of the effect of the TRT density, the thickness of the end-cap moderator and the end-cap calorimeter coverage. Neutron fluxes are given at r=79 cm in the Cosener's House design and are in units of 10^{13} n/cm^2/yr.

	With Barrel TRT With Moderator End-cap mod. 10 cm	With Barrel TRT With Moderator End-cap mod. 5 cm	No Barrel TRT No Moderator
$\|\eta\| < 2.8$	0.15	0.16	1.2
$\|\eta\| < 3$	0.14	0.16	1.3
TRT $\rho = 0.025$	0.18	0.21	1.8
No TRT	0.24	0.36	3.5

were originally for a luminosity of 10^{34} cm^{-2}s^{-1} and an inelastic cross section of 80 mb. These have been scaled to the parameters used in this thesis. For the neutron flux, Mouthuy adds 0.38×10^{12} n/cm^2/yr as the contribution from the "albedo" neutron flux since Geant is not able to transport the low energy neutrons. The comparison is observed to be quite close which suggests that the event generators DTUJET and Pythia are in close agreement.

Table 5.3: Comparison between fluxes from this work and from Mouthuy [54] for the inner silicon layer. Fluxes are in units of 10^{13} particles/cm^2/yr.

Particle Type	This Work	Mouthuy
n	0.95	0.70+0.38
p	0.41	0.58
$\pi^{\pm}$	7.3	6.7
$K^{\pm}$	0.53	0.55
K^0_L	0.25	0.28

5.5 Conclusion

Accurate modelling of the ATLAS detector has been carried out using the FLUKA package. Both primary particle production and "albedo" particle fluxes have been simulated to obtain total fluxes expected in the inner detector tracking layers.

Total fluxes, averaged over the inner detector layers, are calculated to vary from near 10^{14} equivalent 1 MeV neutrons per cm^2 per year at the innermost radius considered (11.5 cm), to 10^{13} at r=40–50 cm, further reducing with increasing radius.

The neutron moderating effect of the TRT was compared with that of the moderator in the Cosener's House design. The TRT produces a significant reduction in the neutron flux in the inner detector.

A layout with a single barrel TRT was studied. Calculations show very similar fluxes in the inner barrel region to those calculated for the Cosener's House design. Removal of the moderator from the central barrel region, was shown to have only a 20–30% effect on the total expected radiation damage in the silicon layers, which in this design are all inside the inner radius of the barrel TRT. This could have important consequences for the barrel layout if the additional radial space becomes essential for the active detector elements. With this design, the equivalent 1 MeV neutron flux of 10^{13} cm^{-2} per year occurs at a radius of 40–50 cm.

5.6 Discussion of Uncertainties

It should be kept in mind that there are large uncertainties in the fluxes quoted here.

- The largest of these is the 50% uncertainty in the source term as discussed in Section 5.2.1.
- There is about a 10-20% uncertainty in the inelastic cross section. Data from Ref. [55] suggests that an inelastic cross section (excluding single diffraction) of 71 mb may be more appropriate. (See Ref. [56] for details.)

- The accuracy of FLUKA as discussed in Section 4.2 is estimated to be around ±20%. In some comparisons, including those described in Section 4.4, up to a factor 2 discrepancy has been observed with FLUKA underestimating the measured quantity. This uncertainty will mainly affect the neutron contribution.
- There will be uncertainties in the damage calculated due to uncertainties in the NIEL data. In particular, there is very little experimental data on the damage caused by pions. The uncertainty in the NIEL corrections is not well known and is taken to be 20%.
- Variations in the detector configuration can have large effects on the neutron fluxes. This is particularly the case when hydrogenous material is involved. Charged hadron fluxes which mainly come from the p-p beam collisions are not sensitive to these variations. So in the inner layers, where the charged hadron flux dominates, the damage will not vary significantly with any design variation.

Since these uncertainties are not statistical errors, but rather they are an attempt to quantify the extent to which these numbers are reliable, it is not possible to follow any standard statistical analysis to obtain an overall uncertainty in the fluxes. Nevertheless, an upper bound has been estimated by adding these uncertainties in quadrature. The non-neutron contributions are mainly due to the direct flux from particles produced in the p-p collisions. Therefore, only the uncertainties in the source term (50%), the inelastic cross section (20%), and the NIEL corrections (20%) are important for the non-neutron contribution. Adding these errors in quadrature gives an error of approximately 60%. The upper limit for the non-neutron contribution of the 1 MeV neutron-equivalent flux has therefore been taken as a factor 1.6 higher than the calculated flux. The lower bound is assumed to be the calculated flux divided by 1.6. For the neutron contribution the uncertainty in the FLUKA simulation is important since this contribution is mainly due to the production of "albedo" neutrons. A conservative estimate of a factor 2 in the FLUKA simulation is assumed based on the discrepancies seen in Section 4.4. Since this is now the dominant error, the overall error for the neutron contribution of the 1 MeV neutron-equivalent flux

has been taken as a factor of 2. That is, the upper limit is found by multiplying by 2 and the lower bound is found be dividing by 2.

Table 5.4: Annual particle fluxes for different particle species in the Cosener's House design with complete moderator. Units are 10^{13} particles/cm^2/yr.

Region	n Flux	p Flux	$\bar{p}$ Flux	$\pi^{\pm}$ Flux	$K^{\pm}$ Flux	K^0_L Flux
S1 Si r=11.5 cm	0.95	0.41	0.34	7.3	0.53	0.25
S2 Si r=14.5	0.62	0.26	0.21	4.9	0.32	0.15
S3 Si r=20	0.45	0.16	0.11	2.8	0.17	0.079
S4 Si r=30	0.29	0.079	0.051	1.5	0.073	0.035
S5 Si r=52	0.20	0.032	0.015	0.55	0.021	0.012
S6 Si r=53	0.20	0.035	0.015	0.53	0.020	0.011
S7 Si r=79	0.15	0.013	0.0053	0.21	0.0093	0.0050
S8 Si r=81	0.14	0.013	0.0053	0.19	0.0088	0.0048
S9 Si r=105	0.14	0.0075	0.0023	0.078	0.0043	0.0025
G1 GaAs z=58.5	0.41	0.23	0.16	3.2	0.23	0.12
G2 GaAs z=70	0.39	0.25	0.17	3.2	0.23	0.14
G3 GaAs z=96	0.37	0.21	0.16	3.0	0.21	0.11
G4 GaAs z=109	0.38	0.20	0.16	3.0	0.21	0.11

Table 5.5: Annual damage in silicon due to different particle species and the total damage for the Cosener's House design with complete moderator. Damage is expressed as the equivalent 1 MeV neutron flux. Units are 10^{13} (1 MeV) neutrons/cm^2/yr.

Region	n Damage	p Damage	$\bar{p}$ Damage	$\pi^{\pm}$ Damage	Kaon Damage	Total Damage
S1 Si r=11.5 cm	1.3	0.74	0.57	6.1	1.3	9.9
S2 Si r=14.5	0.84	0.47	0.35	4.1	0.78	6.5
S3 Si r=20	0.63	0.30	0.18	2.3	0.42	3.9
S4 Si r=30	0.41	0.15	0.084	1.2	0.18	2.0
S5 Si r=52	0.30	0.065	0.027	0.46	0.055	0.91
S6 Si r=53	0.30	0.069	0.026	0.44	0.053	0.89
S7 Si r=79	0.21	0.026	0.0093	0.17	0.025	0.45
S8 Si r=81	0.21	0.029	0.0092	0.16	0.024	0.42
S9 Si r=105	0.19	0.016	0.0040	0.064	0.012	0.29
G1 GaAs z=58.5	0.51	0.37	0.23	2.7	0.51	4.3
G2 GaAs z=70	0.48	0.37	0.24	2.6	0.52	4.2
G3 GaAs z=96	0.46	0.31	0.22	2.5	0.44	3.9
G4 GaAs z=109	0.48	0.29	0.22	2.5	0.43	3.9

Table 5.6: Annual particle fluxes for different particle species in the Single TRT design with complete moderator. Units are 10^{13} particles/cm^2/yr.

Region	n Flux	p Flux	$\bar{p}$ Flux	$\pi^{\pm}$ Flux	$K^{\pm}$ Flux	K^0_L Flux
S1 Si r=11.5 cm	1.0	0.42	0.34	7.3	0.53	0.30
S2 Si r=14.5	0.63	0.30	0.21	4.8	0.34	0.19
S3 Si r=20	0.42	0.16	0.11	2.7	0.17	0.099
S4 Si r=30	0.36	0.087	0.050	1.5	0.076	0.045
S5 Si r=50	0.19	0.032	0.017	0.58	0.024	0.014
S6 Si r=60	0.18	0.026	0.011	0.40	0.017	0.0098
S7 Si r=69	0.16	0.016	0.0084	0.28	0.013	0.0076
G1 GaAs z=58.5	0.43	0.25	0.16	3.4	0.23	0.14
G2 GaAs z=70	0.48	0.28	0.18	3.2	0.23	0.14
G3 GaAs z=96	0.47	0.24	0.15	2.9	0.21	0.12
G4 GaAs z=109	0.45	0.23	0.15	3.0	0.22	0.12

Table 5.7: Annual damage in silicon due to different particle species and the total damage for the Single TRT design with complete moderator. Damage is expressed as the equivalent 1 MeV neutron flux. Units are 10^{13} (1 MeV) neutrons/cm^2/yr.

Region	n Damage	p Damage	$\bar{p}$ Damage	$\pi^{\pm}$ Damage	Kaon Damage	Total Damage
S1 Si r=11.5 cm	1.6	0.79	0.56	6.1	1.4	10.
S2 Si r=14.5	0.92	0.56	0.35	4.0	0.87	6.7
S3 Si r=20	0.61	0.31	0.18	2.3	0.45	3.8
S4 Si r=30	0.55	0.17	0.082	1.3	0.20	2.3
S5 Si r=50	0.26	0.066	0.030	0.48	0.066	0.90
S6 Si r=60	0.25	0.057	0.020	0.33	0.046	0.70
S7 Si r=69	0.23	0.033	0.015	0.23	0.035	0.54
G1 GaAs z=58.5	0.54	0.44	0.23	2.8	0.55	4.6
G2 GaAs z=70	0.56	0.45	0.26	2.6	0.54	4.4
G3 GaAs z=96	0.61	0.37	0.21	2.4	0.46	4.0
G4 GaAs z=109	0.58	0.34	0.21	2.5	0.46	4.1

Table 5.8: Comparison of annual neutron fluxes in different detector configurations of the Cosener's House design. Units are 10^{13} particles/cm^2/yr. Configuration numbers correspond to those given in fig. 5.11.

Region	Configuration		
	1	2	3
S1 Si r=11.5 cm	1.9	1.4	0.95
S2 Si r=14.5	1.6	1.2	0.62
S3 Si r=20	1.5	1.1	0.45
S4 Si r=30	1.3	0.77	0.29
S5 Si r=52	1.3	0.65	0.20
S6 Si r=53	1.2	0.61	0.20
S7 Si r=79	1.2	0.55	0.15
S8 Si r=81	1.1	0.52	0.14
S9 Si r=105	1.1	0.72	0.14
G1 GaAs z=58.5	1.6	1.0	0.41
G2 GaAs z=70	1.4	0.85	0.39
G3 GaAs z=96	1.3	0.95	0.37
G4 GaAs z=109	1.4	1.0	0.38

Table 5.9: Comparison of annual total damage in equivalent 1 MeV neutron flux in different detector configurations of the Cosener's House design. Units are 10^{13} (1 MeV) neutrons/cm^2/yr. Configuration numbers correspond to those given in fig. 5.12.

Region	Configuration		
	1	2	3
S1 Si r=11.5 cm	11.	10.	9.9
S2 Si r=14.5	7.3	7.3	6.5
S3 Si r=20	4.6	4.6	3.9
S4 Si r=30	2.7	2.4	2.0
S5 Si r=52	1.7	1.3	0.91
S6 Si r=53	1.6	1.2	0.89
S7 Si r=79	1.2	0.77	0.45
S8 Si r=81	1.2	0.73	0.42
S9 Si r=105	1.0	0.75	0.29
G1 GaAs z=58.5	5.1	4.9	4.3
G2 GaAs z=70	5.1	4.6	4.2
G3 GaAs z=96	4.5	4.3	3.9
G4 GaAs z=109	4.7	4.4	3.9

Table 5.10: Comparison of annual neutron fluxes in different detector configurations of the Single TRT design. Units are 10^{13} particles/cm^2/yr. Configuration letters correspond to those given in fig. 5.13.

Region	Configuration			
	A	B	C	D
S1 Si r=11.5 cm	1.6	1.2	1.1	1.0
S2 Si r=14.5	1.2	0.95	0.86	0.63
S3 Si r=20	1.0	0.71	0.62	0.42
S4 Si r=30	0.77	0.58	0.45	0.36
S5 Si r=50	0.73	0.49	0.36	0.19
S6 Si r=60	0.66	0.47	0.34	0.18
S7 Si r=69	0.61	0.44	0.31	0.16
G1 GaAs z=58.5	0.92	0.75	0.44	0.43
G2 GaAs z=70	1.0	0.72	0.55	0.48
G3 GaAs z=96	1.0	0.64	0.56	0.47
G4 GaAs z=109	1.2	0.77	0.51	0.45

Table 5.11: Comparison of annual total damage in equivalent 1 MeV neutron flux in different detector configurations of the Single TRT design. Units are 10^{13} (1 MeV) neutrons/cm^2/yr. Configuration letters correspond to those given in fig. 5.14.

Region	Configuration			
	A	B	C	D
S1 Si r=11.5 cm	11.	10.	10.	10.
S2 Si r=14.5	7.2	7.0	6.7	6.7
S3 Si r=20	4.5	4.1	4.0	3.8
S4 Si r=30	2.4	2.3	2.2	2.3
S5 Si r=50	1.4	1.2	1.0	0.90
S6 Si r=60	1.1	0.99	0.84	0.70
S7 Si r=69	0.94	0.83	0.70	0.54
G1 GaAs z=58.5	4.6	4.5	4.5	4.6
G2 GaAs z=70	5.1	4.5	4.5	4.4
G3 GaAs z=96	4.5	4.1	4.0	4.0
G4 GaAs z=109	4.6	4.3	4.3	4.1

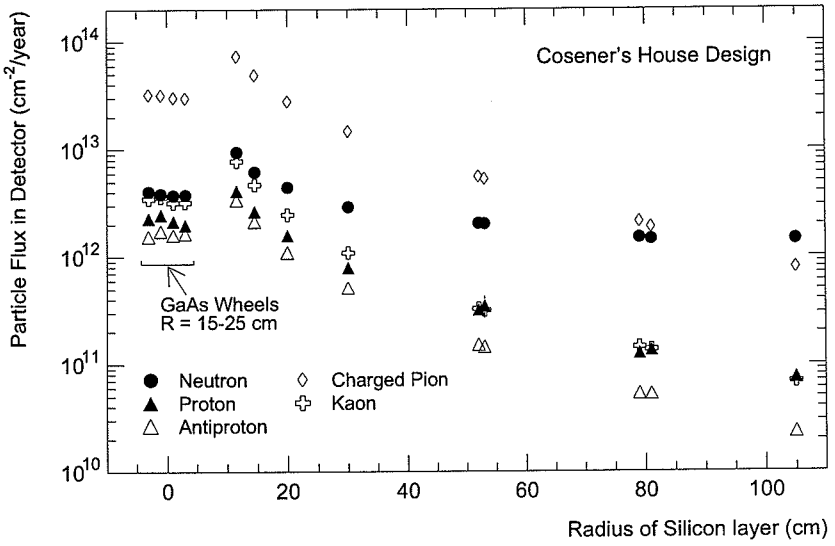

Figure 5.7: Annual neutron, proton, anti-proton, charged pion and kaon fluxes in the Cosener's House design with complete moderator.

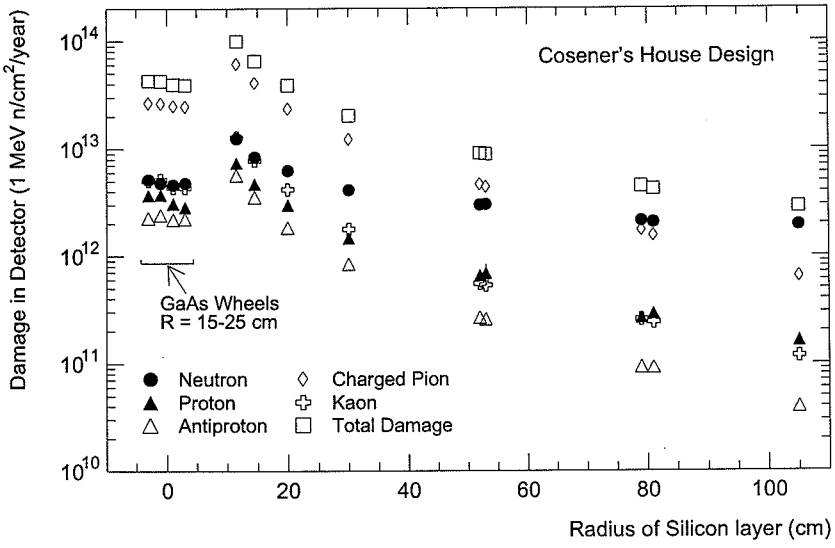

Figure 5.8: Annual damage in equivalent 1 MeV neutron flux in silicon caused by different particle species and the total damage. Cosener's House design with complete moderator.

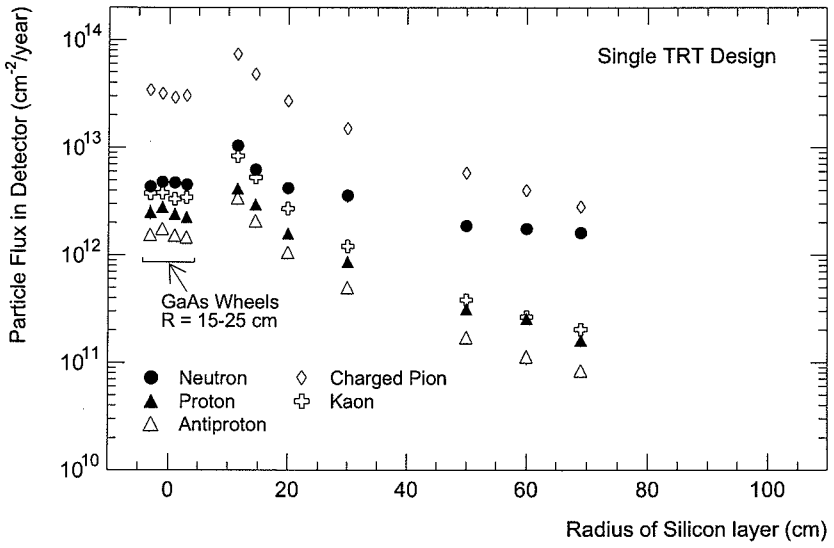

Figure 5.9: Annual neutron, proton, anti-proton, charged pion and kaon fluxes in the Single TRT design with complete moderator.

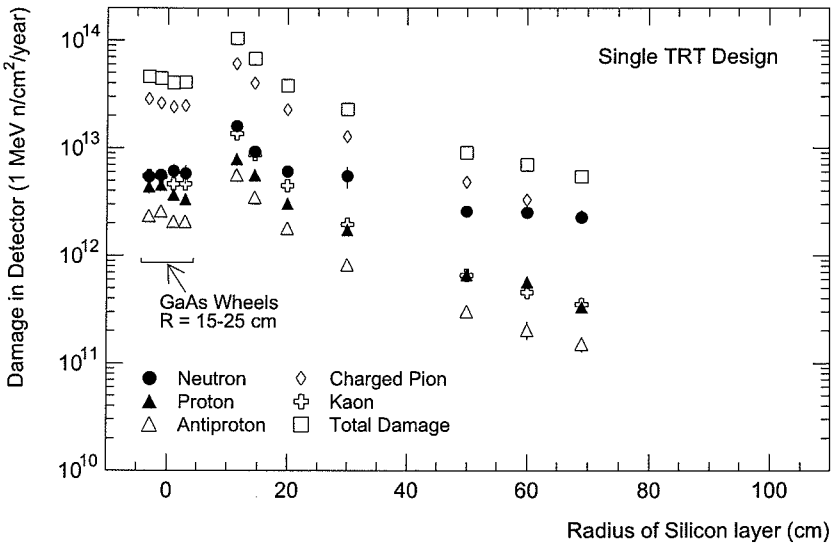

Figure 5.10: Annual damage in equivalent 1 MeV neutron flux in silicon caused by different particle species and the total damage. Single TRT design with complete moderator.

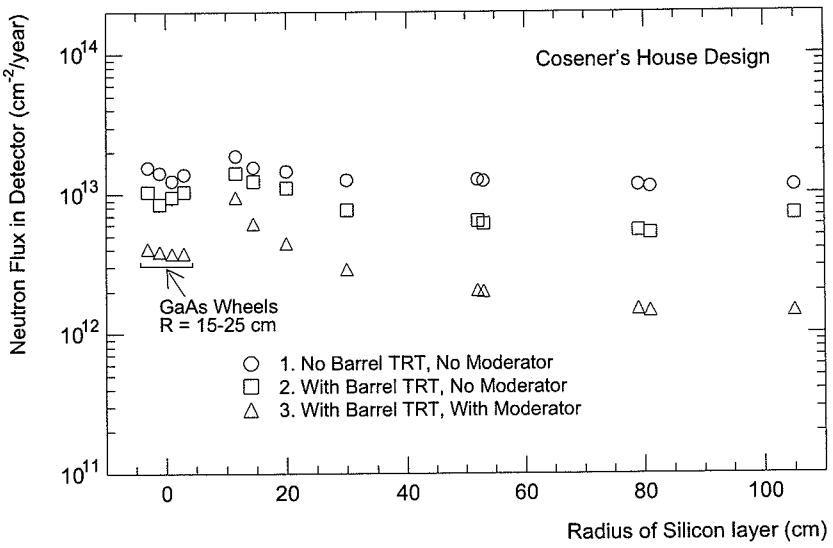

Figure 5.11: Comparison of annual neutron fluxes for different configurations of the Cosener's House design.

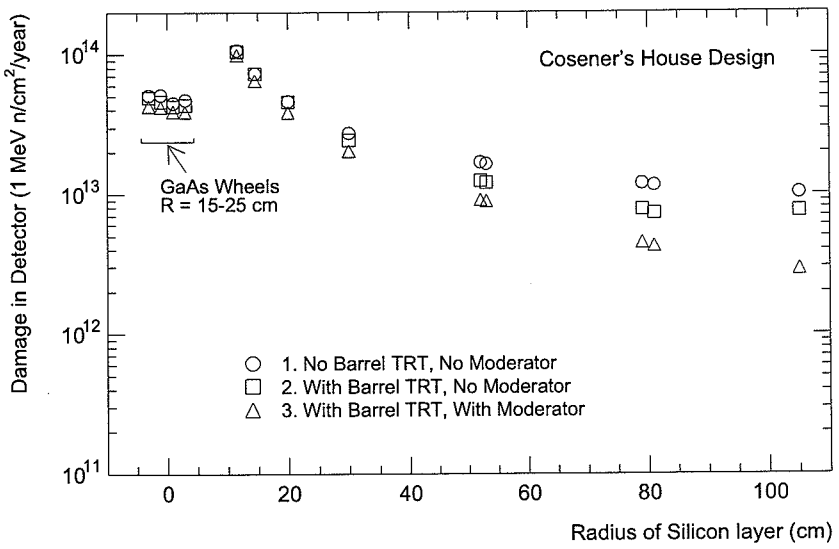

Figure 5.12: Comparison of annual total damage for different configurations of the Cosener's House design. Damage is given as the equivalent 1 MeV neutron flux.

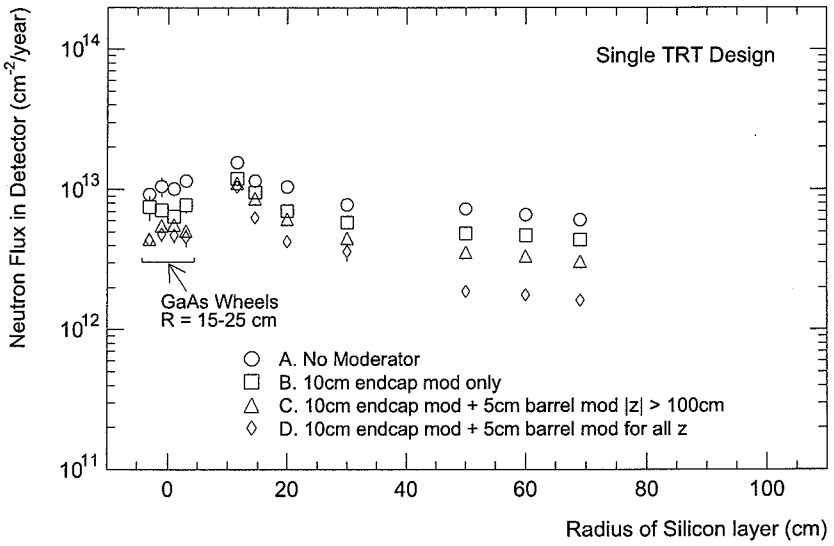

Figure 5.13: Comparison of annual neutron fluxes for different configurations of the Single TRT design.

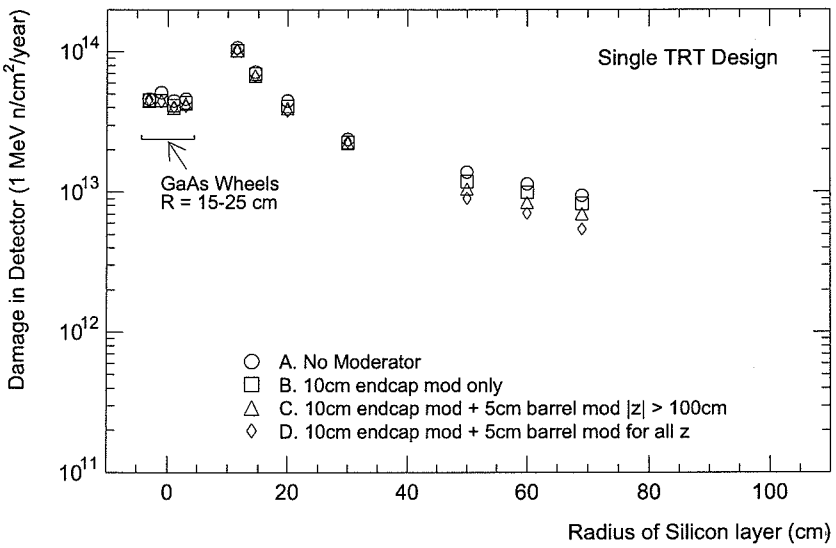

Figure 5.14: Comparison of annual total damage for different configurations of the Single TRT design. Damage is given as the equivalent 1 MeV neutron flux.

Chapter 6

Predictions for Silicon Operation in ATLAS

6.1 Introduction

In this chapter, predictions have been made of the increase in leakage current and depletion voltage during a possible 10 year LHC scenario. These predictions are based on the fluxes in the inner detector as calculated for the Cosener's House design in Chapter 5 along with results from radiation damage studies. Results of the neutron irradiations as described in Chapter 3 have been used to estimate changes in leakage currents at 20°C. This has been compared with results from another group. For the changes of leakage current at 0°C and for the change in depletion voltage, data compiled by the RD2 collaboration have been used.

6.2 Operating Limits for Silicon

The foreseen maximum limits for depletion voltage, leakage current and charge collection efficiency as given by the RD2 collaboration [57] are given below.

- Depletion voltage $\leq$ 150 V. During operation the detectors will need to be over-biased in order to achieve better charge collection efficiency. The operating voltage should remain below 200 V.

- Leakage Current $\leq$ 2 μA. This limitation is mainly to keep power dissipation less than 20% of the power dissipation of the amplifier. If extra cooling is

provided this limitation could be increased to ≤ 5 μA.

- The charge collection efficiency should be $\geq 70\%$ from a mip (minimum ionizing particle) signal. With a leakage current below 5 μA and this charge collection efficiency the signal to noise ratio should be greater than 8:1. (See Section 3.5.3.)

6.3 An LHC Scenario

It is expected that the LHC will initially run at low luminosity, not reaching maximum design luminosity for a number of years. For the purpose of predicting the degradation of the silicon the luminosity for the first ten years has been assumed to be

- 10^{31} cm^{-2}s^{-1} for year 1.
- 10^{32} cm^{-2}s^{-1} for year 2.
- 10^{33} cm^{-2}s^{-1} for year 3.
- 10^{34} cm^{-2}s^{-1} for years 4 and 5.
- 1.7×10^{34} cm^{-2}s^{-1} for years 6–10.

The average luminosity over 10 years for this scenario is about 10^{34} cm^{-2}s^{-1}. The running time per year is expected to be around 10^7 sec spread over about 7 months.

Leakage currents can be reduced by operating the detectors at low temperature. Keeping the detectors at low temperature also slows down the reverse annealing of the effective impurity concentration and hence prolongs the detectors useful lifetime. For the latter reason it is necessary to keep warm up periods (for maintenance) to a minimum. A possible yearly operating scenario could be:

- Beam on for 7 months. Temperature: 0°C.
- No beam for 1 month. Temperature: 0°C.
- No beam for 1 month. Warm up period with temperature: 20°C.
- No beam for 3 months. Temperature: 0°C.

Scenarios where the temperature is always at 20°C and always at 0°C have also been studied.

6.4 Prediction of the Increase in Leakage Current

For a given set of self annealing parameters and damage coefficient the leakage current can be calculated as a function of time as described in Section 3.6. It is useful to calculate the increase in leakage current in a time interval in which the flux is constant. The current I is given by

$$I = \sum I_i \tag{6.1}$$

where I_i corresponds to the component which anneals with time constant τ_i. The change in I_i in a time interval Δt (which does not necessarily need to be small) with constant flux $\mathrm{d}\Phi/\mathrm{d}t$ is given by

$$\Delta I_i = \left(A_i \, \tau_i \, \alpha \; Vol \, \frac{\mathrm{d}\Phi}{\mathrm{d}t} - I_i \right) \left(1 - e^{-\Delta t/\tau_i} \right) . \tag{6.2}$$

Using these equations the leakage current can be calculated as a function of time by an iterative process. This has been done for a flux time profile corresponding to the LHC luminosity scenario proposed in the previous section.

Running at 20°C

The self annealing parameters and damage coefficient obtained from Melbourne Irradiation 1 (see Section 3.9) were used to predict the leakage current for running at 20°C. This set of parameters will be referred to as the Melbourne set. The damage coefficient from Melbourne Irradiation 1 has been used rather than the one calculated from Melbourne Irradiation 2 for reasons discussed in Section 3.11. The self annealing parameters and damage coefficient as obtained by the Hamburg group have also been used for comparison. This set has been modified so that after about 100 days no further annealing takes place reflecting the uncertainty in the behaviour for longer periods. Unless otherwise stated references to the Hamburg set will refer to this modified set. The damage coefficients used were 1.4×10^{-16} A/cm for the Melbourne set and 8.0×10^{-17} A/cm for the Hamburg set. The self annealing parameter sets are

given in table 6.1. Figure 6.1 shows each parameter set as given by

$$I(t)/I_0 = \sum A_i e^{-t/\tau_i} \tag{6.3}$$

where I_0 is the leakage current increase in the absence of self annealing.

Table 6.1: Self annealing parameters.

Melbourne Set		
i	τ_i (min)	A_i
1	∞	0.255
2	3.54×10^4	0.159
3	2440	0.196
4	63	0.390

Old Hamburg Set		
i	τ_i (min)	A_i
1	6.70×10^5	0.396
2	1.47×10^4	0.201
3	1090	0.131
4	119	0.116
5	17.8	0.156

Hamburg Set (Modified)		
i	τ_i (min)	A_i
1	∞	0.320
2	1.0×10^5	0.076
3	1.47×10^4	0.201
4	1090	0.131
5	119	0.116
6	17.8	0.156

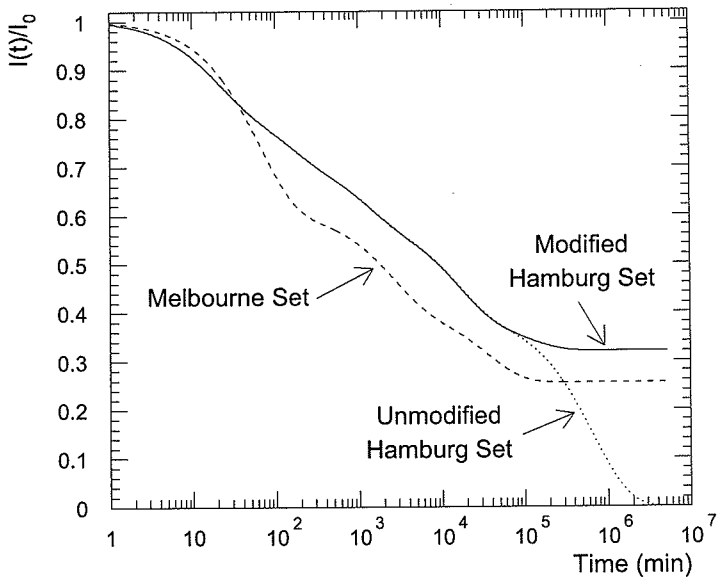

Figure 6.1: Comparison of different self annealing parameter sets.

Figure 6.2 shows the ratio $I(t)/I_0$ in an LHC scenario in which the luminosity

is the same in each year, with a running period of 7 months per year. Here, I_0 is the leakage current increase expected at the end of 10 years if no self annealing took place. Since annealing is occurring continuously during operation, types of damage with time constants much less than a year do not contribute greatly. This is seen in figure 6.2 where, except for the unmodified Hamburg set, the ratio after 10 years is equal to the constant term in the self annealing parameter set. Because of this, the final leakage current (after a fluence Φ) can be estimated as

$$I = \alpha_\infty \cdot \Phi \cdot Vol \tag{6.4}$$

where $\alpha_\infty = A_1\alpha$ and A_1 is the constant term in the parameter set. For the Melbourne set $\alpha_\infty = 3.6 \times 10^{-17}$ A/cm and for the Hamburg set $\alpha_\infty = 2.6 \times 10^{-17}$ A/cm.

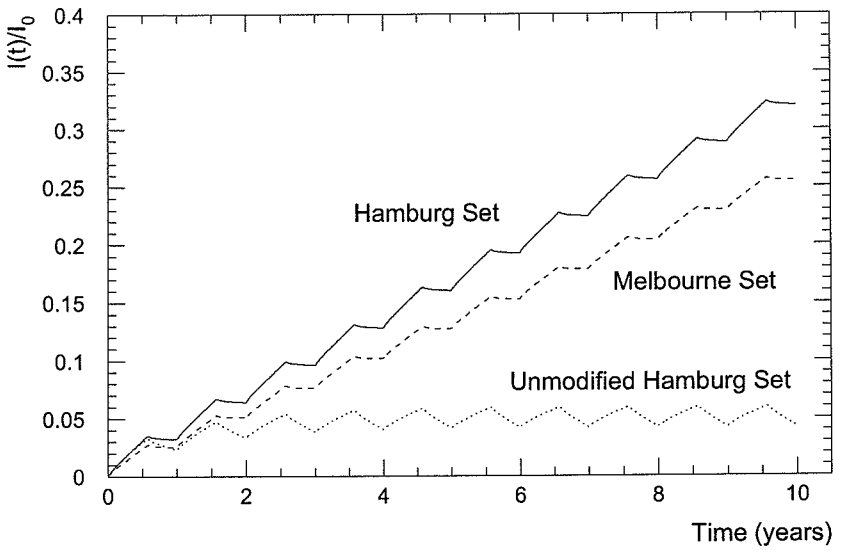

Figure 6.2: Ratio of leakage current I to I_0, where I_0 is the current increase expected at the end of 10 years if no self annealing took place. Shown are the ratios predicted using the self annealing parameter set from Melbourne Irradiation 1 (Melbourne set), the modified Hamburg set and the unmodified Hamburg set.

Running at 0°C

For 0°C running the damage coefficient, $\alpha_{0^\circ} = 2.2 \times 10^{-17}$ A/cm, obtained by Dortmund [19] has been used. The Hamburg annealing set has been used since in Ref. [19] the rate of annealing for the 0°C data was observed to be approximately the same as that predicted by the Hamburg set. This does not mean that the same damage mechanisms are annealing at 0°C and 20°C, only that the overall annealing rates are similar.

Running with a 1 Month Warm Up

A warm up period is likely to result in lower currents than if the detectors are kept constantly at 0°C due to an increased rate of annealing at higher temperatures. To estimate the leakage currents for the scenario where there is a 1 month warm up period, the following procedure was used.

During both cold and warm operation (but not during the transition from one to the other) ΔI is given by equations (6.1) and (6.2). The parameters A_i and τ_i are not necessarily the same for both temperatures. The value of α is the one corresponding to operation at the temperature being considered. For the warm periods both the Melbourne and Hamburg sets have been used. For the cold periods the parameters used are the same as for 0°C running as described above.

To determine the current after transition between different temperatures, the temperature dependence as given in equation (3.29) is used. From this equation $I_{0^\circ}/I_{20^\circ} = 0.15$. After transition the current must be divided up into its constituents I_i. This is done as follows.

After transition from cold to warm, the part of the current I_g gained during the previous irradiation is calculated. That is the difference between the current directly after warm up and the current at the end of the previous warm up period. The ratio $I_g/I_{0,g}$ is determined where $I_{0,g}$ is the current that would have been gained without annealing in a warm irradiation of the same fluence as the previous irradiation. This ratio can be thought of as the remaining fraction of the damage that would have been

produced in a warm irradiation. Other damage that would anneal immediately at 20°C (i.e., damage not seen in 20°C irradiations) is assumed to have had sufficient time to anneal out completely at 0°C. Also damage that anneals with the shorter time constants at 20°C is assumed to be completely or partially annealed at 0°C. The remaining fractions A_i^* of the different damage types are found so that

$$\sum A_i^* = I_g/I_{0,g} \tag{6.5}$$

where the index i corresponds to the indices in the self annealing parameter set. Each A_i^* in turn, from the longest to shortest time constant, is given the value A_i so that the ratio $I_g/I_{0,g}$ is not exceeded. The next coefficient is assigned the remainder. Any other coefficients are assigned zero. For example if $I_g/I_{0,g} = 0.5$ and the Melbourne parameter set is being used, then $A_1^* = 0.255$, $A_2^* = 0.159$, $A_3^* = 0.086$, and $A_4^* = 0$. The components of the current are then given by

$$I_i = A_i^* I_{0,g} + I_{i,p} \tag{6.6}$$

where $I_{i,p}$ are the components from the previous warm up period.

After the transition from warm to cold, the remaining damage is assumed to be stable. (It may, however, continue annealing in the next warm up period.) All the current is assigned to the constant term I_1. The other components are set equal to zero.

The Predictions

The expected leakage currents in layer 5 of the Cosener's House design (this layer has the highest leakage current increase) for the LHC scenario as proposed in Section 6.3 are shown in figures 6.3 and 6.4. Figure 6.3 shows predictions made using the Melbourne set for 20°C operation (including the 1 month warm up period) while figure 6.4 shows the predictions made using the Hamburg set. Predictions made for 0°C, 20°C, and 1 month warm up scenarios are shown. The leakage currents

scale with flux and sensitive volume. Silicon detectors in layer 5 have a sensitive volume of 7.02×10^{-3} cm^3 and receive a fluence (over 10 years) of 5.7×10^{13} (equiv. 1 MeV neutrons)/cm^2. Leakage currents at the end of 10 years are 14 and 2.8 μA for 20°C (using the Melbourne set) and 0°C scenarios respectively. The same values are obtained using equation (6.4).

For the scenario where there is a 1 month warm up, after this warm up the currents are higher than those for the irradiation at 20°C. This is due to damage that would have annealed out at room temperature being stable or annealing more slowly at cold temperatures. Annealing follows with currents approaching the level obtained for the 20°C irradiation. The extra annealing results in the currents for the 1 month warm up scenario being less than if the detectors were kept at 0°C continuously. The leakage currents at the end of 10 years for the 1 month warm up case are only slightly higher than what would be obtained if operated continuously at 20°C for 10 years and then cooled down to 0°C. For example in layer 5, using the Melbourne set, the leakage current at the end of 10 years is 14.2 μA for the 20°C scenario. Cooling the detector down (i.e., multiply by $I_{0°}/I_{20°} = 0.15$) results in a current of 2.13 μA. For the 1 month warm up scenario the final current is 2.19 μA. This suggests that a 1 month warm up period is sufficient time to get most of the benefit from room temperature annealing.

The increase in leakage current at the end of running each year is given as a function of radius in figures 6.5, 6.6 and 6.7 for 20°C, 0°C, and 1 month warm up running respectively. The values are taken directly after the end of the beam on period (i.e., after 7 months). It is at this time that the currents are highest, after which time some annealing takes place. For 20°C operation the Melbourne set has been used. This includes the warm up periods in the 1 month warm up scenario. Figure 6.8 shows the 1 month warm up scenario predicted using the Hamburg set for the warm periods. Using the Hamburg set gives values a factor 1.2 lower for the final years.

The sensitive volume of the detectors are those given in table 2.1. Layer 5 has

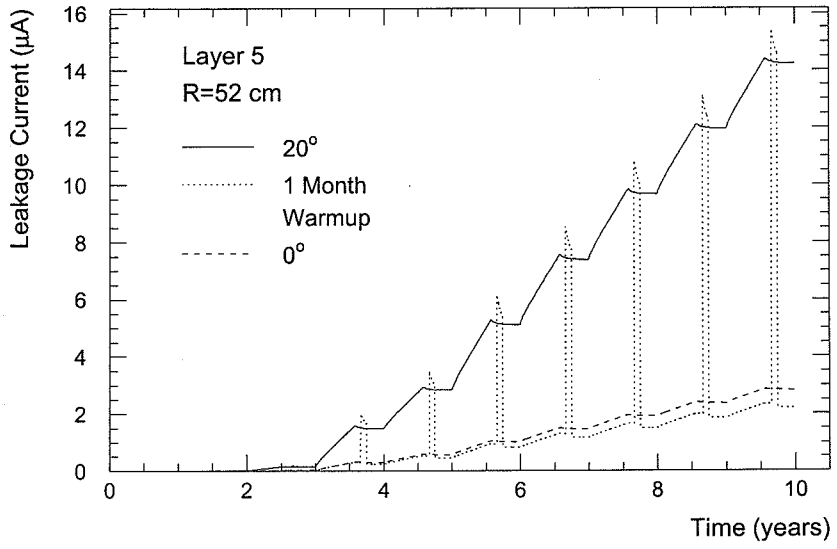

Figure 6.3: Predicted leakage current in layer 5 for a 10 year LHC scenario. Data is shown for three temperature scenarios: operation at 0°C, at 20°C and 0°C with 1 month warm up to 20°C. The Melbourne set has been used for 20°C operation.

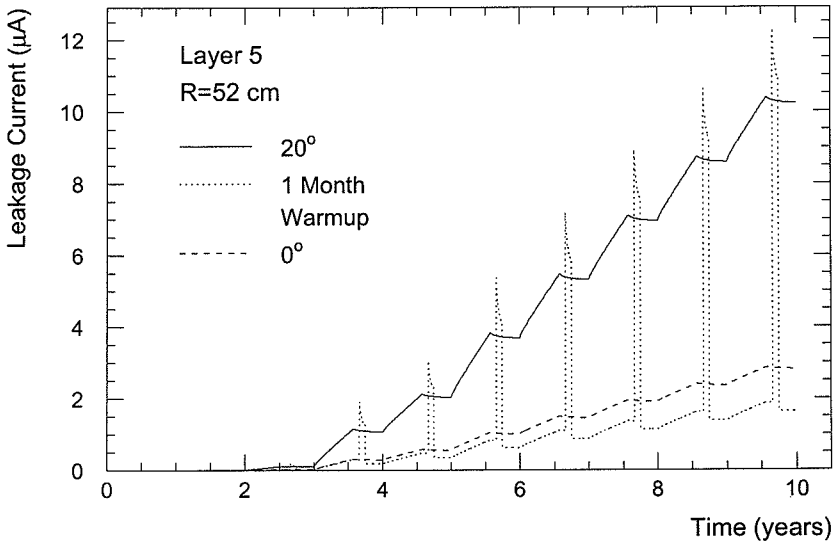

Figure 6.4: As in figure 6.3, except that the Hamburg set has been used for 20°C operation.

the highest leakage current increase. Although layers at smaller radii receive higher fluxes, they have smaller sensitive volumes than the outer layers.

For 20°C the maximum limit of 2 μA is exceeded in the outer layer in 7 years. Layers 5 and 6 exceed this limit after 5 years and exceed 5 μA after 6 years. It is clear from this that cooling is essential. For 0°C running, the currents remain below 2 μA for all layers, except 5 and 6, after 10 years of operation. Layers 5 and 6 reach the limit after 8 years with layer 5 reaching a maximum of 2.9 μA after 10 years. A 1 month warm up period improves the situation. For this temperature scenario layers 5 and 6 remain within the limit for 9 years, reaching a maximum of 2.3 μA after 10 years. Using the Hamburg set in the 1 month warm up scenario, the currents remain below 2 μA for the 10 years, reaching a maximum of 1.9 μA in layer 5.

6.5 Prediction of the Change in Depletion Voltage

The change in the effective impurity concentration N_{eff}, for times much greater than the irradiation time, is given by equation (3.13). In the long term running of the LHC the reverse annealing will occur during the irradiation. The predicted N_{eff} was calculated numerically. Consider the following quantities:

N_D: Part of the donor concentration. These are neutralized during irradiation with a rate $\frac{dN_D}{dt} = -cN_D\frac{d\Phi}{dt}$.

N_A: Concentration of acceptor like defects. These are created during irradiation with a rate $\frac{dN_A}{dt} = +\beta_s\frac{d\Phi}{dt}$.

N_x: Concentration of neutral defects which later combine to form an acceptor like defect. These are created during irradiation with rate $\frac{dN_x}{dt}^+ = +\beta_n\frac{d\Phi}{dt}$ and are removed at a rate $\frac{dN_x}{dt}^- = -kN_x^2$.

N_y: Concentration of acceptor like states created by the combination of neutral type defects N_x with a rate $\frac{dN_y}{dt} = -\frac{dN_x}{dt}^- = kN_x^2$.

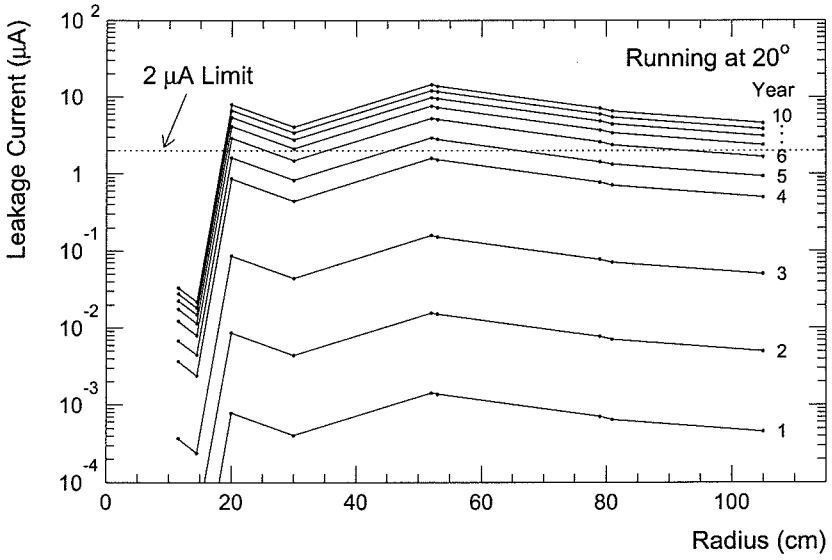

Figure 6.5: Predicted leakage currents at the end of running each year as a function of radius. This data assumes operation at 20°C at all times. The Melbourne set has been used.

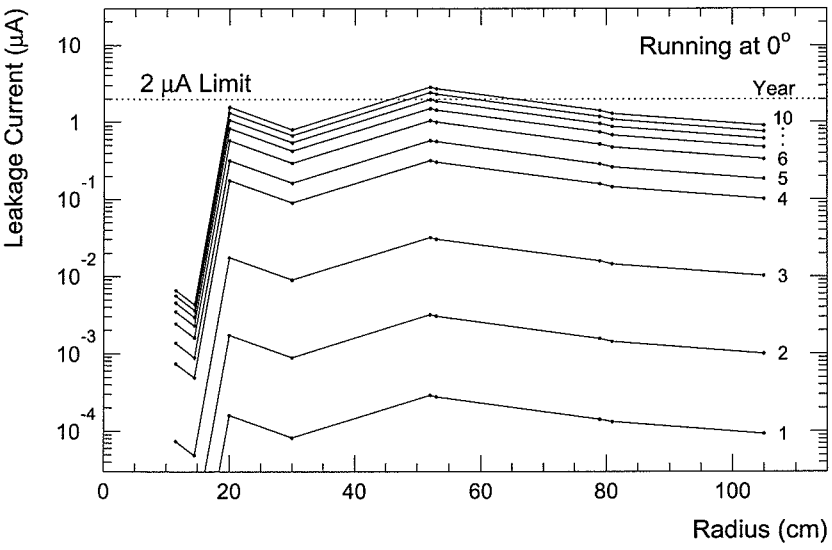

Figure 6.6: Predicted leakage currents at the end of running each year as a function of radius. This data assumes operation at 0°C at all times.

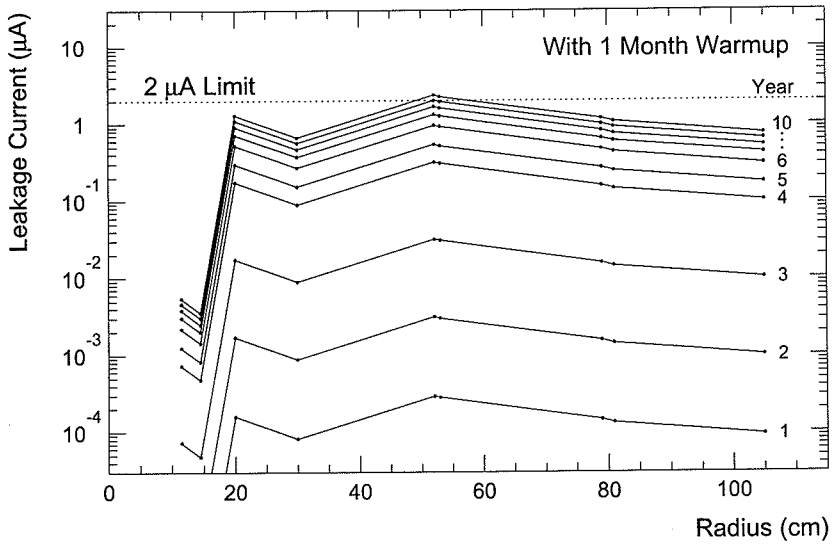

Figure 6.7: Predicted leakage currents at the end of running each year as a function of radius. This data assumes operation with a 1 month warm up period of 20°C each year. The temperature at all other times is 0°C. The Melbourne set has been used for the 20°C periods.

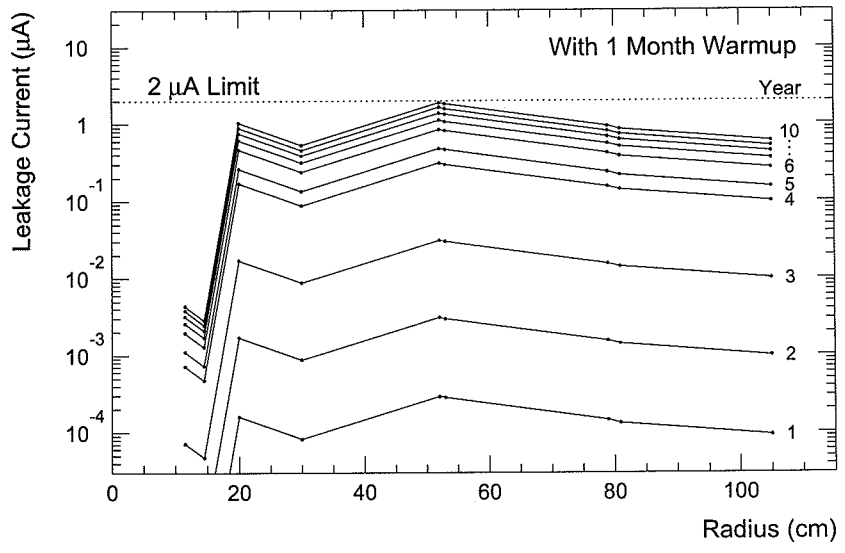

Figure 6.8: As in figure 6.7, except that the Hamburg set has been used for the 20°C periods.

The time was divided into small intervals ΔT. In a time ΔT the change in fluence is given by $\Delta\Phi = \frac{d\Phi}{dt}\Delta t$. The changes in the above quantities in time ΔT are:

$$\begin{aligned}
\Delta N_D &= -N_D(1 - e^{-c\Delta\Phi}) \\
\Delta N_A &= +\beta_s \Delta\Phi \\
\Delta N_x &= +\beta_n \Delta\Phi - kN_x^2 \\
\Delta N_y &= +kN_x^2
\end{aligned}$$

where k=k(T) as given in equation (3.12). The initial values are $N_D(0) = N_0^*$, $N_A(0) = N_y(0) = N_x(0) = 0$. The value of N_{eff} is given by

$$N_{eff} = N_{eff,0} - N_0^* + N_D - N_A - N_y \tag{6.7}$$

where $N_{eff,0}$ is the effective impurity concentration before irradiation. The depletion voltage is then calculated using equation (3.7). The values used for $N_{eff,0}$, N_0^*, β_s, β_n, and c are given in table 3.1.

Figure 6.9 shows the expected depletion voltage for a few layers of the Cosener's House design. Three temperature scenarios have been considered. One with operation at 0°C at all times, one with 0°C at all times except for a 1 month warm up period at 20°C and one with 20°C at all times. The thickness of the detectors has been taken as 300 μm for all layers except layers 1 and 2 for which the thickness was 150 μm. The depletion voltage is observed to initially decrease until it reaches zero after which it increases. This inflection corresponds to the silicon changing from n-type to p-type. (See Section 3.5.2.) The effect of the different temperature scenarios is quite dramatic on the depletion voltage as a result of the strong dependence reverse annealing has with temperature.

Figures 6.10–6.12 show the depletion voltage expected at the end of each year as a function of radius. The three temperature scenarios are shown. The thickness of the detectors was taken as 300 μm for all layers. For the actual depletion voltage in the first 2 layers it is necessary to divide by 4. Because of this layer 3 has the highest

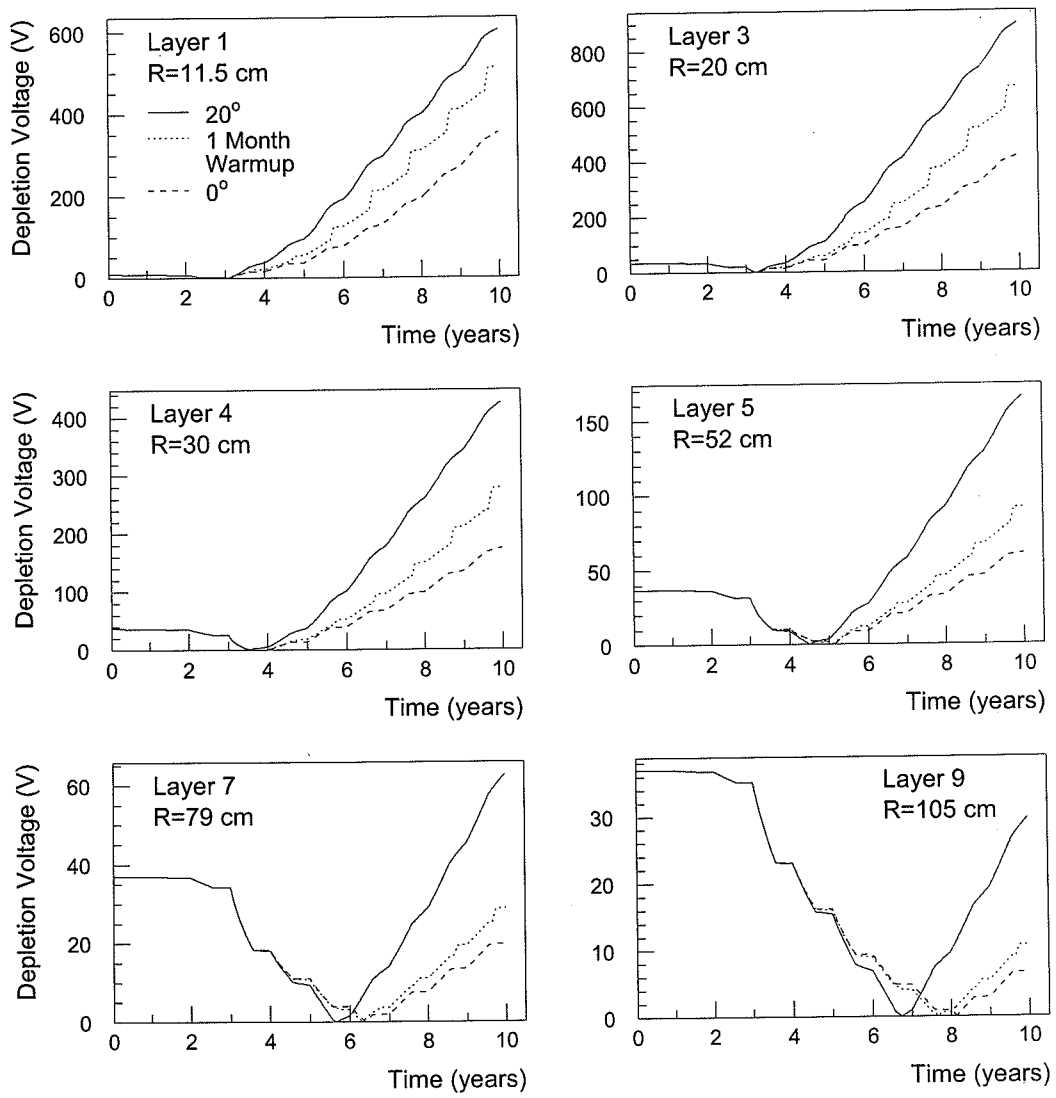

Figure 6.9: Prediction of the depletion voltage in a 10 year LHC scenario for different silicon layers.

increase in depletion voltage. The inflections in these plots are due to type inversion. For running at 20°C the depletion voltage remains below the 150 V limit after 10 years operation for layers with a radius greater than 55 cm. Operating the detectors at 0°C with a 1 month warm up reduces this minimum radius to 42 cm. Without the warm up period, layers with radius greater than 33 cm remain below the limit.

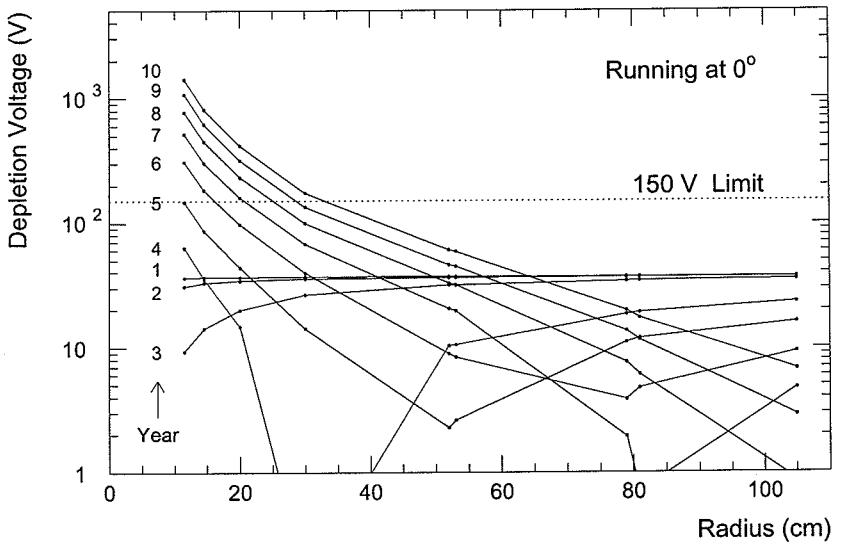

Figure 6.10: Predicted depletion voltage at the end of each year as a function of radius. This data assumes operation at 0°C at all times. The thickness for all layers is 300 μm.

6.6 Predictions with Different Luminosity Scenarios

The predicted depletion voltage and leakage current will be dependent on the LHC luminosity scenario. Five luminosity scenarios were studied (Scenario 1 is the one described in Section 6.3). These were as follows (luminosities are in units of $cm^{-2}s^{-1}$):

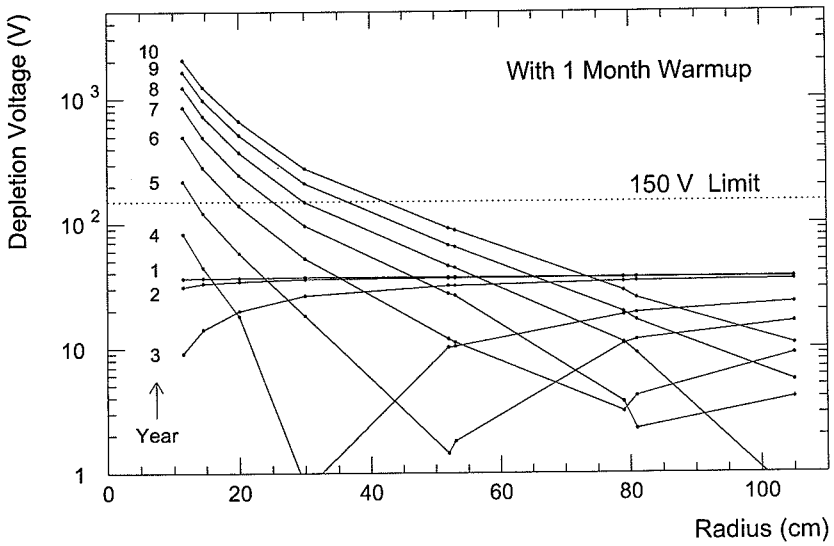

Figure 6.11: Predicted depletion voltage at the end of each year as a function of radius. This data assumes operation with a 1 month warm up period of 20°C each year. The temperature at all other times is 0°C. The thickness for all layers is 300 μm.

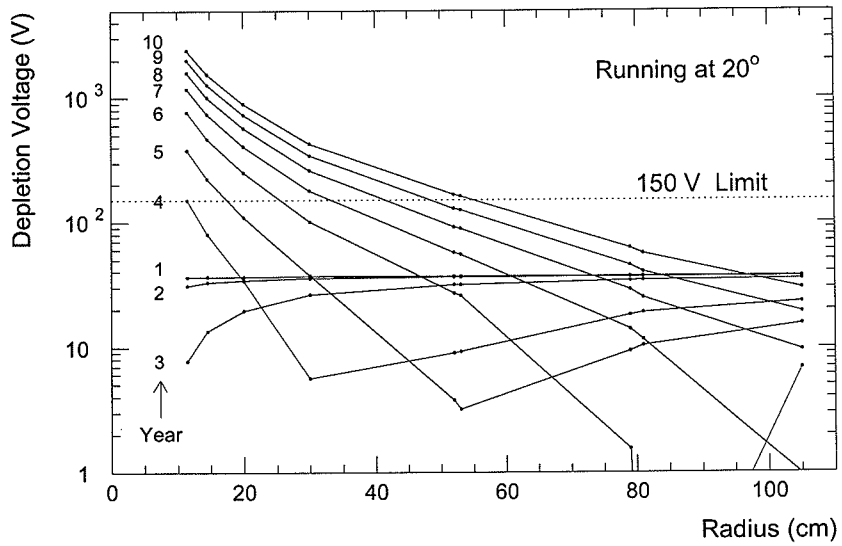

Figure 6.12: Predicted depletion voltage at the end of each year as a function of radius. This data assumes operation at 20°C at all times. The thickness for all layers is 300 μm.

Scenario 1:	1 yr at 10^{31}, 1 yr at 10^{32}, 1 yr at 10^{33}, 2 yrs at 10^{34}, 5 yrs at 1.7×10^{34}	Average: 1.06×10^{34}
Scenario 2:	10 yrs at 10^{34}	Average: 1.0×10^{34}
Scenario 3:	3 yrs at 10^{33}, 7 yrs at 10^{34}	Average: 0.73×10^{34}
Scenario 4:	3 yrs at 10^{33}, 7 yrs at 1.7×10^{34}	Average: 1.22×10^{34}
Scenario 5:	10 yrs at 1.7×10^{34}	Average: 1.7×10^{34}

The leakage current and depletion voltage at the end of 10 years running for the 5 scenarios are shown in figures 6.13 and 6.14. The leakage currents after 10 years are approximately proportional to the integrated luminosity. For the depletion voltage, the final value varies roughly with the integrated luminosity although they are not proportional. For scenarios 1 and 2, which both have about the same integrated luminosity (6% higher for scenario 1), the final depletion voltages are almost identical. Luminosity scenarios which have higher luminosity during the earlier years will have a larger final depletion voltage than for a luminosity scenario which has the same integrated luminosity but where the luminosity is higher during the final years. This is because the reverse annealing has had more time to take effect on the damage produced in the first few years. The resulting difference, however, is not large (about 6%) for the variations between scenarios 1 and 2.

6.7 Estimate of the Uncertainty in the Predictions

The predictions given in the previous sections have all used the "best guess" values for all parameters. A number of uncertainties must be considered. These are:

- The uncertainty of the fluxes as calculated in Chapter 5. An estimate of these uncertainties is given in Section 5.6. For the neutron contribution, the upper limit on the flux is obtained by multiplying by a factor of 2 and the lower limit by dividing by a factor of 2. Similarly, for the limits on the non-neutron contribution a factor of 1.6 is used.

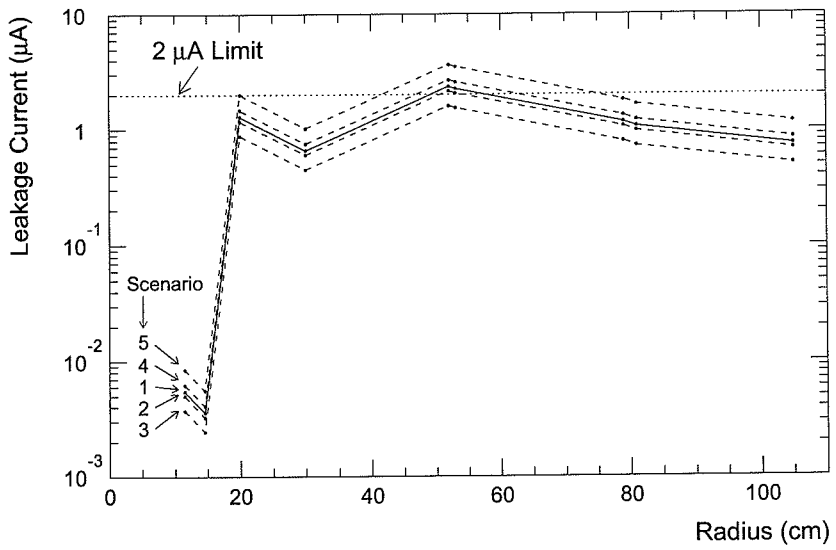

Figure 6.13: Predicted leakage current at the end of running in the 10th year as a function of radius. Data is shown for five different LHC luminosity scenarios (see text). Scenario 1 (solid line) has a similar integrated luminosity to that of scenario 2.

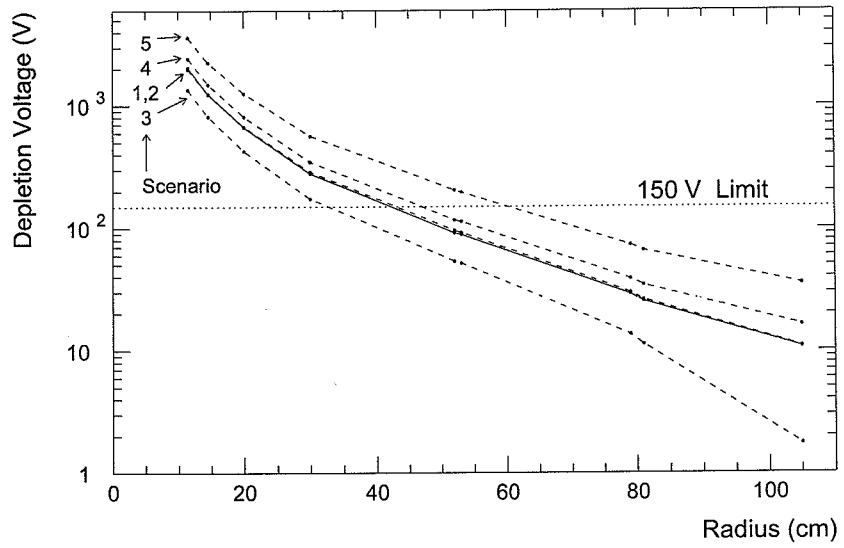

Figure 6.14: Predicted depletion voltage at the end of 10 years as a function of radius. Data is shown for five different LHC luminosity scenarios (see text). Scenario 1 (solid line) has a similar integrated luminosity to that of scenario 2. The thickness for all layers is 300 μm.

- The uncertainty in the effective impurity concentration parameters. To obtain the upper limit the upper or lower limit of each parameter is used such that it results in an increase in $|N_{eff}|$. Similarly for the lower limit; the limits are chosen which result in a decrease in $|N_{eff}|$. In effect, the errors are added linearly and so they are conservative.

- The luminosity scenario. The previous section gives some indication of the sensitivity to the luminosity and has not been considered in this section.

Figure 6.15 shows the upper and lower limits due to the uncertainty in the flux for the leakage current at the end of running in the 10th year. A 1 month warm up scenario has been assumed with the Melbourne set used for the warm periods. Figure 6.16 shows the upper and lower limits of the depletion voltage after 10 years. The limits correspond to the uncertainty in the flux and the uncertainty in the effective impurity concentration parameters. Also shown is a case where both the fluxes and effective impurity concentration parameters are at their extremes. In effect, the errors are added linearly. This will be a conservative procedure as the two sources of uncertainty are uncorrelated and so it is unlikely that both will be at their extremes.

6.8 Discussion and Conclusions

Using the "best guess" values for all parameters, layers with $r > 42$ cm will be operable for 10 years. The limiting quantity that determines the survivability of silicon is the depletion voltage. However, the leakage currents for the intermediate layers (around a radii of 50 cm) exceed the 2 μA limit after 10 years reaching a value of 2.3 μA. Using the Hamburg parameters, the currents remain below this limit for the full 10 years. These currents are well below the 5 μA limit which may be possible if extra cooling is provided. The intermediate layers have the highest increase in leakage current despite the inner layers receiving higher fluxes. This is due to the larger pad sizes used for the outer layers. In current designs of the ATLAS inner detector the pad sizes have been reduced which will result in lower leakage currents.

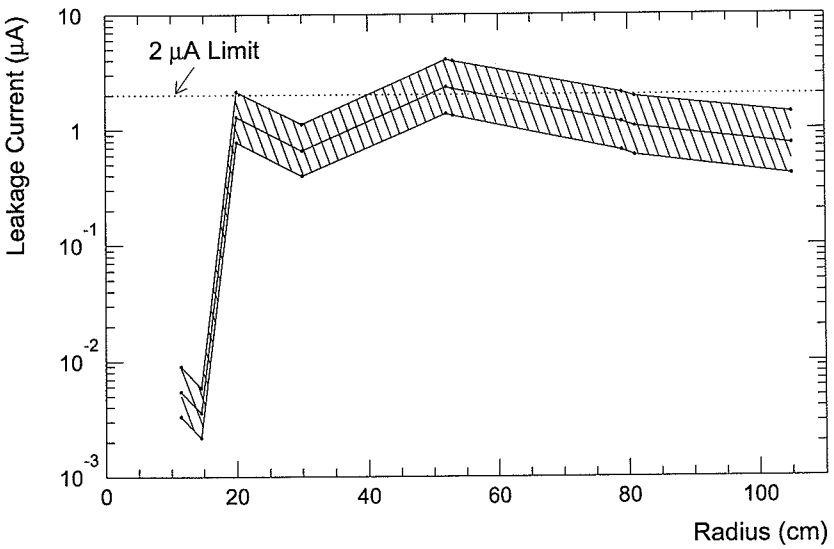

Figure 6.15: Upper and lower limits for the predicted leakage current at the end of running in the 10th year as a function of radius. Shown are the upper and lower limits as estimated by taking the extremes of the fluxes. A 1 month warm up period has been assumed with the Melbourne set used for the warm periods.

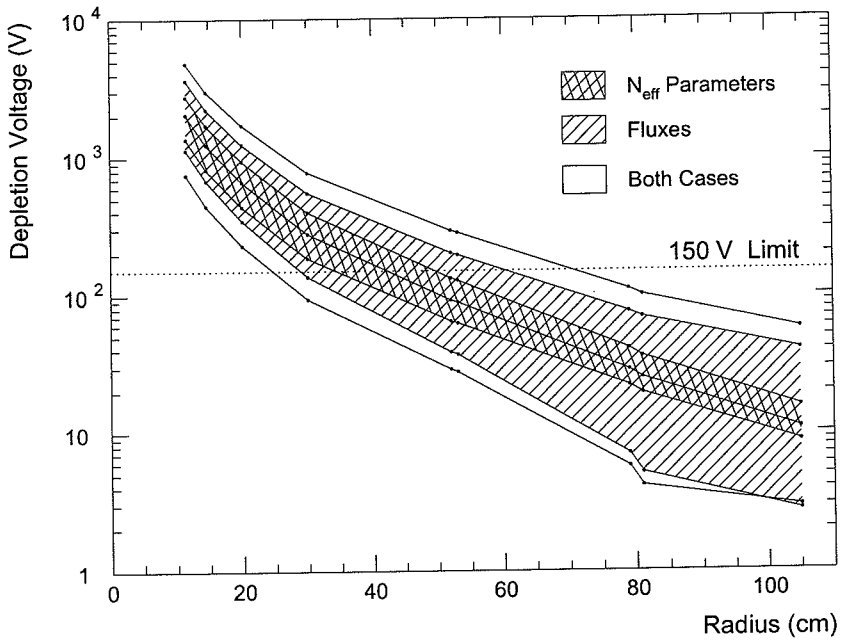

Figure 6.16: Upper and lower limits for the predicted depletion voltage at the end of 10 years as a function of radius. Shown are the upper and lower limits as estimated by taking the extremes of the effective impurity concentration parameters, the extremes for the fluxes, and a linear combination of these. A 1 month warm up period has been assumed. The thickness for all layers is 300 μm.

There are many uncertainties. With the effective impurity concentration parameters and fluxes at their extremes, silicon detectors with $r < 70$ cm may not be operable for the full 10 years. With only the fluxes at their maximum, this gives a minimum radius of 60 cm. The leakage currents are likely to remain below 5 μA even with the fluxes at their extremes. A 2 μA limit, however, could easily be exceeded.

The inner layers according to these predictions are unlikely to be operable for the full 10 years. For layer 3 the depletion voltage reaches 150 V after an integrated luminosity of about 4×10^{41} cm^{-2} in the case of a 1 month warm up. For luminosity scenario 1 this occurs after 6 years.

Since both the Cosener's House design and the single barrel TRT design studied in Chapter 5 showed similar radial variation of the fluxes, results here are applicable for both designs. Clearly the pad geometry and detector thickness must be taken into consideration when studying different designs.

Chapter 7

Conclusion

The damage to silicon detectors due to neutrons was studied by monitoring leakage currents in two neutron irradiations. In both experiments, the detectors were kept under bias with leakage currents monitored both during and after the irradiations. The currents were observed to reduce after the irradiation due to self annealing. This annealing was parameterized enabling damage coefficients to be determined which were corrected for self annealing. The first experiment, Melbourne Irradiation 1, yielded a damage coefficient of $(1.4 \pm 0.3) \times 10^{-16}$ A/cm. In this experiment the temperature was measured but not controlled and data was normalized to 20°C. Currents were monitored for up to 80 days enabling the long term annealing to be measured. This resulted in a damage coefficient $\alpha_\infty = 3.6 \times 10^{-17}$ A/cm due to the unannealed fraction. Data from this experiment was used to predict leakage currents in possible LHC scenarios.

The second experiment, Melbourne Irradiation 2, in which the temperature was maintained at 20°C, yielded a lower damage coefficient of $8\text{–}9 \times 10^{-17}$ A/cm. Variation was observed in the short term annealing in supposedly identical pads. The ratio of the decrease in current after 10 hours of annealing to the current at the end of the irradiation varied from 13–25%. This variation led to a variation in the damage coefficient obtained. Since the irradiation was around an hour, the short term annealing could be accurately determined, allowing an accurate correction for the self annealing to be made. Because of this, and since the experiment was done under more controlled conditions, the damage coefficient corrected for self annealing obtained in Melbourne Irradiation 2 is considered to be a more accurate value than the

one obtained in Melbourne Irradiation 1. The difference in the two irradiations was possibly due, in part, to an overestimation in the short term annealing in Melbourne Irradiation 1 in which the irradiation was over 3 days. The long term annealing is not sensitive to the components with short time constants and so Melbourne Irradiation 1, which gave information about the long term annealing, was used for the LHC predictions.

Two experiments were performed to test the validity of the Monte Carlo code FLUKA. In the first experiment comparisons were made between the neutron fluxes calculated using FLUKA and those measured in an operating detector UA2. The results were inconclusive due to contributions suspected to be from beam losses. This comparison highlighted the importance of eliminating such contributions in the LHC. These contributions, however, are unlikely to be a problem since the design of the LHC incorporates efficient beam collimaters which will reduce beam losses to an insignificant level at full luminosity.

In the second experiment a calorimeter-like structure, which was comprised of lead plates immersed in a tank of liquid argon, was irradiated with a 205 GeV/c hadron beam. The isotope ^{41}Ar, which is radioactive, is produced when argon is exposed to low energy neutrons. Good agreement was found for the ^{41}Ar production rate with the simulation agreeing with the experiment to within 20%. Comparisons with other dosimeters placed throughout the "calorimeter" were less favourable, although all were within a factor of two. All comparisons had FLUKA underestimating the measured value. Measurements that were sensitive to neutrons in the 1–10 MeV range agreed within 37–45%. The thermal flux as measured by gold and indium foils agreed within 45%. Comparisons which were sensitive to the 0.5–1 keV range as measured by the gold and indium foils gave agreement within 22–30%. Considering the good agreement for the argon activity and the reasonable agreement for the activity measured by the gold and indium foils, the flux from thermal neutrons up to around 1 keV appear to be calculated adequately by FLUKA.

Accurate modelling of the ATLAS detector with FLUKA was carried out. Par-

ticle fluxes in the inner detector region were calculated. Since FLUKA is able to transport low energy neutrons, these fluxes contain the contribution from "albedo" neutrons as well as particles (mostly charged hadrons) coming directly from the p-p beam interactions. Equivalent 1 MeV neutron fluxes were calculated using non-ionizing energy loss data.

Two designs were considered; the Cosener's House design and a design which had all silicon layers within the inner radius of a single barrel TRT module. Both designs showed a similar radial dependence for the fluxes. The 1 MeV neutron equivalent flux was observed to range from $(0.3\text{–}10)\times10^{13}$ cm^{-2}yr^{-1} with 10^{13} cm^{-2}yr^{-1} occurring at r=40–50 cm. These values assume an inelastic cross section of 60 mb and an integrated luminosity of 1.7×10^{41} cm^{-2} per year. In the Cosener's House design the moderating effect of the radiator in the TRT was seen to have a significant effect on reducing the neutron flux. In the single barrel TRT design the removal of the moderator in the $|z| < 100$ cm region was shown to have only a 20–30% increase on the 1 MeV neutron equivalent flux. For the inner radii the charged hadron component dominated. In the outer radii the "albedo" neutron flux dominated, although there was still a significant contribution from charged hadrons.

Fluxes calculated here, along with radiation damage studies including the neutron irradiations described in this thesis, were used to predict the degradation of silicon detectors in LHC scenarios. Although fluxes obtained using the Cosener's House design were used, these had a similar radial variation to the single barrel TRT design. Therefore the results are applicable to both designs. For an average luminosity of 10^{41} cm^{-2} per year the leakage current remained below 2 μA for 9 years reaching 2.3 μA in the 10th year. Allowing for uncertainties in the particle fluxes, it is possible for the leakage currents to remain below 5 μA. The 2 μA limit may be viable but cannot be guaranteed. The limiting factor is the depletion voltage. Using the best estimates of all parameters, the depletion voltage remains below the 150 V limit for 10 years for silicon layers with a radius greater than 40 cm.

With fluxes at the extremes of their uncertainty the depletion voltage remains

below the 150 V limit for $r > 60$ cm. A worst case scenario, with both fluxes and effective impurity concentration parameters at their extremes, gives a minimum radius of 70 cm.

The silicon layer at a radius of 20 cm has the highest increase in depletion voltage. This layer is expected to survive up to an integrated luminosity of 4×10^{41} cm^{-2} which is likely to occur in 4–6 years depending on the initial luminosity.

In conclusion it is possible to operate silicon detectors with $r > 70$ cm for the full 10 years of operation at the LHC. A more optimistic estimate gives a minimum radius of 40 cm. The leakage currents are not likely to be a problem, but they may exceed 2μA for layers around $r = 50$ cm. A 5μA limit is more reasonable. The depletion voltage may be improved by reducing the length of warm up periods or having them at lower temperatures.

Appendix A

Definitions of Flux and Fluence

The terms flux and fluence are used extensively in this thesis. The definition of flux, and some methods for determining it, will be given here. Fluence is the time integrated flux. A detailed explanation of flux and some related concepts can be found in Ref. [58].

If considering particles moving in a single direction normal to a plane detector, then the flux is given by the number of particles passing through the plane per unit area per unit time. For a real detector the measured flux will depend on the interaction probability. For a thin detector, if a particle's direction of travel is not perpendicular to the surface of the detector, the particle will travel through more material and hence have a higher chance of interacting than in the perpendicular case. As shown in figure A.1 the path length of the particle through the material is greater by $1/\cos\theta$ where θ is the angle the particle makes with the normal to the surface. The flux through the detector can therefore be obtained by weighting each particle with $1/\cos\theta$. That is, the flux is given by

$$\text{Flux} = \frac{\sum_i w_i}{A \cdot T}, \qquad w_i = \frac{1}{\cos\theta_i} \tag{A.1}$$

where A is the area of the detector and T is the time interval. This is referred to as inverse cosine weighting.

A definition of flux which can be applied to an arbitrary region is the sum of track-lengths of the particles divided by the region's volume. This gives the average

flux in the region:

$$\text{Flux} = \frac{\text{Total track-length}}{\text{Volume} \cdot T} \,. \tag{A.2}$$

This definition is correct because the track-length is proportional to the interaction probability. The normalization by 1/volume is easily seen to be correct by considering the case of particles moving in a direction perpendicular to the surface of a cuboid. Consider figure A.1: for a flux F perpendicular to the surface A, the total track-length per unit time is $F \cdot A \cdot d = F \cdot Vol.$ In the case of a thin detector the track-length definition of flux gives the same result as the inverse cosine weighting method since the track-length is proportional to $1/\cos\theta$.

When referring above to a measured flux, this assumed that the interaction probability was low. If the interaction probability is high, such that every particle passing through a thin detector is counted, then a more appropriate quantity is the current. The current is the number of particles, regardless of direction, passing through a surface per unit area per unit time. Unlike the usual definition of current, where particles moving in one direction cancel with particles moving in the opposite direction, there is no cancelling out with this definition.

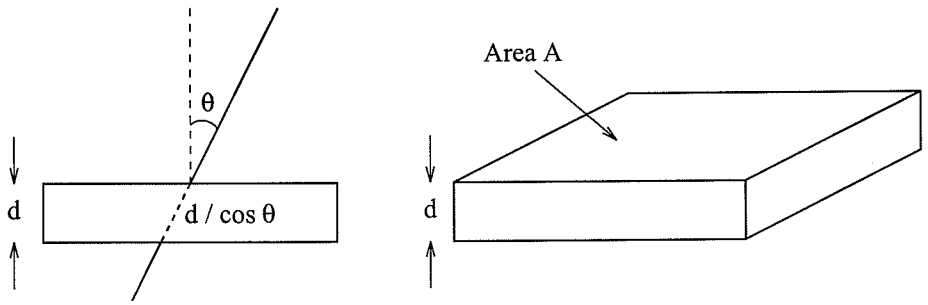

Figure A.1: A thin detector with particle travelling through it with an angle θ to the normal.

Appendix B

Calculation of the Run Uniformity Factor

The Run Uniformity factor as used in Section 4.4 corrects for the non-uniformity in the beam intensity when calculating the production rate of a radioactive isotope.

The production rate of the isotope is proportional to the beam intensity $\mathcal{I}(t)$:

$$\frac{\mathrm{d}N^{+}}{\mathrm{d}t} = P\mathcal{I}(t) \tag{B.1}$$

where $\mathcal{I}(t)$ is given as the number of beam particles per unit time. The proportionality constant P is the production rate per beam particle and is the quantity of interest. The rate of decay is

$$\frac{\mathrm{d}N^{-}}{\mathrm{d}t} = -\lambda N\ . \tag{B.2}$$

The differential equation for N is therefore

$$\frac{\mathrm{d}N}{\mathrm{d}t} = P\mathcal{I}(t) - \lambda N\ . \tag{B.3}$$

The activity is given by $a = \lambda N$. Solving equation (B.3) results in the following expression of the activity for an irradiation starting at time t_s:

$$a(t) = \lambda P\left[\int_{t_s}^{t} \mathcal{I}(t^*)e^{\lambda t^*}\,\mathrm{d}t^*\right]e^{-\lambda t}\ . \tag{B.4}$$

This is analogous to the equations used for self annealing as described in Section 3.6.

Consider an irradiation of uniform beam intensity $\mathcal{I}_u$ between times t_s and t_f

as shown in figure B.1a. The activity at t_f is then given by

$$a_f = P\mathcal{I}_u\left(1 - e^{-\lambda(t_f - t_s)}\right) . \tag{B.5}$$

The saturation activity is

$$a_{sat} = P\mathcal{I}_u . \tag{B.6}$$

In general the beam intensity will vary and the actual start and end of irradiation may differ from the nominal times t_s an t_f (for example, if the actual start and end of irradiation is determined after the nominal times are chosen). Consider a measurement of the activity a_l made a time t_l after the nominal end of irradiation. The saturation activity calculated from this measurement assuming a uniform irradiation over the nominal times is (see Section 4.4.5):

$$a_{sat} = a_l \cdot e^{\lambda t_l} \cdot \frac{1}{1 - e^{-\lambda(t_f - t_s)}} . \tag{B.7}$$

From equation (B.4) the activity a_l is

$$a_l = \lambda P \left[\int_{T_s}^{T_f} \mathcal{I}(t^*) e^{\lambda(t^*)}\, \mathrm{d}t^*\right] e^{-\lambda(t_f + t_l)} \tag{B.8}$$

where T_s and T_f are the start and end of the actual irradiation. From equation (B.7) the saturation activity assuming uniform irradiation over the nominal times is

$$a_{sat} = \frac{\lambda P \left[\int_{T_s}^{T_f} \mathcal{I}(t^*) e^{\lambda t^*}\, \mathrm{d}t^*\right] e^{-\lambda t_f}}{1 - e^{-\lambda(t_f - t_s)}} . \tag{B.9}$$

Equating (B.6) and (B.9) gives the following expression of the uniform beam intensity needed to give the same activity as in the non-uniform irradiation:

$$\mathcal{I}_u = \frac{\lambda \left[\int_{T_s}^{T_f} \mathcal{I}(t^*) e^{\lambda t^*}\, \mathrm{d}t^*\right] e^{-\lambda t_f}}{1 - e^{-\lambda(t_f - t_s)}} . \tag{B.10}$$

The quantity to be extracted is $P = a_{sat}/\mathcal{I}_u$. The uncorrected production rate P' is given by

$$P' = \frac{a_{sat}}{\mathcal{I}_{ave}} \tag{B.11}$$

where $\mathcal{I}_{ave}$ is the beam intensity averaged over the nominal length of the irradiation:

$$\mathcal{I}_{ave} = \frac{\int_{T_s}^{T_f} \mathcal{I}(t)\,\mathrm{d}t}{t_f - t_s}\,. \tag{B.12}$$

The corrected production rate is given by

$$P = \frac{a_{sat}}{\mathcal{I}_u} = \frac{a_{sat}}{\mathcal{I}_{ave}} \cdot \frac{\mathcal{I}_{ave}}{\mathcal{I}_u} = P' \cdot f_{RU} \tag{B.13}$$

where f_{RU} is the Run Uniformity factor:

$$f_{RU} = \frac{\mathcal{I}_{ave}}{\mathcal{I}_u}\,. \tag{B.14}$$

In practice the integrals in equations (B.10) and (B.12) are replaced by a sum. Consider the profile in figure B.1b which has been divided up into a number of uniform irradiations with time limits $t_0 = T_s$, t_1, ..., $t_n = T_f$. The beam intensity between times t_{i-1} and t_i is $\mathcal{I}_i$.

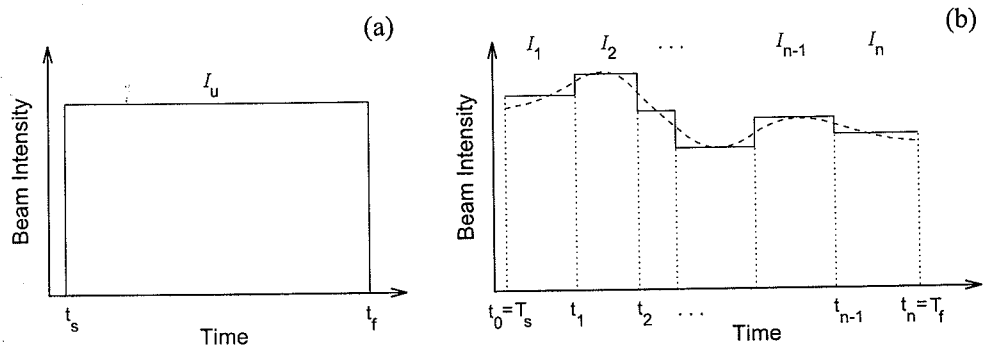

Figure B.1: Beam intensity time profile for (a) a uniform irradiation and (b) a non-uniform irradiation.

The expressions for $\mathcal{I}_{ave}$ and $\mathcal{I}_u$ are given by

$$\mathcal{I}_{ave} = \frac{\sum_{i=1}^{n} \mathcal{I}_i \cdot (t_i - t_{i-1})}{t_f - t_s} \tag{B.15}$$

and

$$\mathcal{I}_u = \frac{\left[\sum_{i=1}^{n} \mathcal{I}_i \left(e^{\lambda t_i} - e^{\lambda t_{i-1}}\right)\right] e^{-\lambda t_f}}{1 - e^{-\lambda(t_f - t_s)}} \,. \tag{B.16}$$

Note that when calculating f_{RU} any quantity proportional to the beam intensity can be used.

Bibliography

[1] The ATLAS Collaboration, *ATLAS Letter of Intent for a General-Purpose pp Experiment at the Large Hadron Collider at CERN*, CERN/LHCC/92–4, LHCC/I 2 (1992).

[2] The ATLAS Collaboration, *The ATLAS Inner Detector, Status Report*, CERN/LHCC/93–24 (March 1993).

[3] V.A.J. van Lint, *The Physics of Radiation Damage in Particle Detectors*, Nucl. Instr. and Meth. **A253**, 453 (1987).

[4] G.C. Messenger, *A Summary Review of Displacement Damage from High Energy Radiation in Silicon Semiconductors and Semiconductor Devices*, IEEE Trans. Nucl. Sci. **39**, 468 (1992).

[5] A. Van Ginneken, *Non Ionizing Energy Deposition in Silicon for Radiation Damage Studies*, FERMILAB report FN-522 (1989).

[6] E. Fretwurst, *et al., Radiation Hardness of Silicon Detectors for Future Colliders*, Nucl. Instr. and Meth. **A326**, 357 (1993).

[7] The RD2 Collaboration, *Progress Report on the RD2 Project*, CERN/DRDC/93-18 (1993).

[8] E. Fretwurst, *et al., Reverse Annealing of the Effective Impurity Concentration and Long Term Operational Scenario for Silicon Detectors in Future Collider Experiments*, Nucl. Instr. and Meth. **A342**, 119 (1994).

[9] G. Lindström, H. Feick and E. Fretwurst, *Status of Data Analysis for Radiation Damage Projections*, RD2 Internal Note, SITP-NO-102 (1994).

[10] F. Lemeilleur, *et al., Electrical Properties and Charge Collection Efficiency for Neutron-Irradiated p-type and n-type Silicon Detectors,* Nucl. Phys. B (Proc. Suppl.) **32**, 415 (1993).

[11] G. Lindström *et al., Radiation Damage in Silicon Detectors, Self Annealing Corrections,* RD2 Internal Note, SITP-NO-002 (Feb 1991).

[12] R. Bardos, G. Gorfine, G. Taylor and S. Tovey, *The Increase in Leakage Current in Segmented Silicon Detectors Exposed to 1.2 MeV Neutrons while Reverse Biased,* RD2 Internal Note, SITP-NO-008 (June 1991).

[13] R. Bardos, G. Gorfine, L. Guy, G. Moorhead, G. Taylor and S. Tovey, *Neutron Damage of Silicon Detectors at 20° C.,* RD2 Internal Note, SITP-NO-037 (June 1992).

[14] H. Liskien and A. Paulsen, *Neutron Production Cross Sections and Energies for the Reactions $^7Li(p,n)^7Be$ and $^7Li(p,n)^7Be^*$,* Atom. Data and Nucl. Data Tables **15**, 57 (1975).

[15] MINUIT, CERN Program Library.

[16] G. Kegel, *Fluences and Energy Spectra of Fast Neutrons from a Proton Irradiated Thick Lithium Target,* Computer Physics Communications **36**, 321–336 (1985).

[17] The RD2 Collaboration, F. Anghinolfi, *et al., Neutron Irradiation of Silicon Diodes at Temperatures of* $+20°C$ *and* $-20°C$, Nucl. Instr. and Meth. **A326**, 365 (1993).

[18] R. Wunstorf, *et al., Results on Radiation Hardness of Silicon Detectors up to Neutron Fluences of* 10^{15} n/cm^2. Nucl. Instr. and Meth. **A315**, 149 (1992).

[19] A. Rolf, *Summary of Results of Radiation Damage Studies in Dortmund,* RD2 Internal Note, SITP-NO-075 (1993).

[20] K. Gill, *et al., Radiation Damage by Neutrons and Photons to Silicon Detectors,* Nucl. Instr. and Meth. **A322**, 177 (1992).

[21] A. Baldini, *et al., Electrical and Spectroscopic Analysis of Neutron-Irradiated Silicon Detectors,* Nucl. Instr. and Meth. **A315**, 182 (1992).

[22] P. Aarnio, A. Fassò, A. Ferrari, H.J. Moehring, J. Ranft, P.R. Sala, G.R. Stevenson and J.M. Zazula, *FLUKA92 User Manual,* (to be published).

[23] P. Aarnio, J. Lindgren, J. Ranft, A. Fassò, and G.R. Stevenson, *FLUKA86 User's Guide* and *Enhancements to the FLUKA86 program (FLUKA87),* CERN Divisional Reports TIS-RP/168 (1986) and TIS-RP/190 (1987).

[24] A. Ferrari, P.R. Sala, R. Guaraldi and F. Padoani, *An Improved Multiple Scattering Model for Charged Particle Transport,* Nucl. Instr. and Meth. **B71**, 412 (1992).

[25] A. Fassò, A. Ferrari, J. Ranft, P.R. Sala, G.R. Stevenson and J.M. Zazula, *A Comparison of FLUKA Simulations with Measurements of Fluence and Dose in Calorimeter Structures,* Nucl. Instr. and Meth. **A332**, 459 (1993).

[26] A. Ferrari, P.R. Sala, A. Fassò and G.R. Stevenson, *Can We Predict Radiation Levels in Calorimeters?,* in: Proc. II Int. Conf. on Calorimetry in High Energy Physics (Capri, 14-18 Oct. 1991), ed. A. Ereditato, World Scientific, Singapore (1992) p. 101., also CERN ATLAS Internal Note, CAL-NO-005 (1991).

[27] G.R. Stevenson, A. Fassò, A. Ferrari and P.R. Sala, *The Radiation Field in and around Hadron Collider Detectors,* IEEE Trans. Nucl. Sci. **39**, 1712 (1992).

[28] M. B. Emmett, *The MORSE Monte-Carlo Radiation Transport Code System,* Oak Ridge National Laboratory Report ORNL-4972 (1975).

[29] J.S. Russ, G.R. Stevenson, A. Fassò, M.C. Nielsen, C. Furetta, P.G. Rancoita and L. Vismara, *Low-Energy Neutron Measurements in an Iron Calorime-*

ter Structure Irradiated by 200 GeV/c Hadrons, Report CERN/TIS-RP/89-02 (1989).

[30] A. Fassò, G.R. Stevenson, M. Bruzzi, C. Furetta, P.G. Rancoita, P. Giubellino, R. Steni and J.S. Russ, *Measurements of Low-Energy Neutrons in an Iron Calorimeter Structure Irradiated by 24 GeV/c Protons*, Report CERN/TIS-RP/90-19 (1990).

[31] G.R. Stevenson, A. Fassò, C. Furetta, P.G. Rancoita, P. Giubellino, J.S. Russ and C. Bertrand, *Measurements of Low-Energy Neutrons in a Lead Calorimeter Structure Irradiated by 200 GeV/c Hadrons*, Report CERN/TIS-RP/91-11 (1991).

[32] The UA2 Collaboration, C.N. Booth, *The UA2 Experiment at ACOL,* Proc. 6th Topical Workshop on Proton-Antiproton Collider Physics, Aachen, 1986, eds. K. Eggert *et al.,* (World Scientific, Singapore, 1987) p. 381.

[33] Product Information, *Pulse Fission Chambers*, 20^{th} Century Electronics Limited.

[34] W. Abson, P.G. Salmon and S. Pyrah, *The Design, Performance and Use of Fission Counters,* Proc. Inst. Elec. Engineers **105B**, Paper No. 2546 M (1958).

[35] H.D. Lemmel, Report IAEA-NDS-100 (1990).

[36] R.C. Raffnsøe (CERN TIS Division), private communication, 1990.

[37] L. Stewart, *Neutron Spectrum and Absolute Yield of a Plutonium-Beryllium Source*, Phys. Rev. **98**, 740 (1955).

[38] L. DiLella, *Calibration of the UA2 Luminosity Monitor,* UA2 Internal Note, $\overline{p}p$-note 549 (1987).

[39] P. Aurenche *et al.*, *Multiparticle Production in a Two-Component Dual Parton Model,* Phys. Rev. **D45**, 92 (1992).

[40] R. Brant, F. Carbonara, E. Cieslak, H. Piekarz, J. Piekarz and J. Zakrzewski, *The Study of Nuclear Fission Induced by High-Energy Protons*, Nuclear Phys. Div. Report CERN 71-2, (1971).

[41] M.H. Simbel, *Phenomenological Analysis of Fission Induced by High-Energy Protons*, Z. Phys. A. – Atomic Nuclei **333**, 177 (1989).

[42] K.H. Hicks, *et al.*, *Fission of Heavy Nuclei Induced by Energetic Pions*, Phys. Rev. **C31**, 1323 (1985).

[43] H.A. Khan, *et al.*, *Fission Induced in ^{nat}U, ^{nat}Pb, ^{197}Au, and ^{165}Ho by 80 and 100 MeV π^+ and π^-*, Phys. Rev. **C35**, 645 (1987).

[44] S.B. Kaufman, M.W. Weisfield, E.P. Steinberg, B.D. Wilkins and D. Henderson, *Nuclear Reactions of ^{197}Au with 11.5 and 300 GeV Protons,* Phys. Rev. **C14**, 1121 (1976).

[45] E. Storm and H.I. Israel, *Photon Cross Sections from 1 keV to 100 MeV for Elements Z=1 to Z=100*, Nucl. Data Tables **A7**, 565 (1970).

[46] A. Fassò (CERN TIS Division), private communication, 1992.

[47] L.R. Greenwood, Report ANL/FPP/TM-115 (1978).

[48] N.M. Hitz and N.F. Ramsey, Phys. Rev. **88**, 19 (1952).

[49] J. Tobailem *et al.*, Report CEA-N-1466(1) (1971).

[50] S.I. Baker *et al.*, Nucl. Instr. and Meth. **A222**, 467 (1984).

[51] B.J. Dropesky *et al.*, Phys. Rev. **C32**, 1305 (1985).

[52] Graham Robinson (ANSTO, Lucas Heights, Australia), private communication, 1992.

[53] Y. Fisyak, *Study of Neutron and γ Backgrounds in ATLAS,* ATLAS Internal Note, CAL-NO-039 (1994).

[54] T. Mouthuy, *Radiation Dose Expected in LHC Inner Detectors: An Update,* ATLAS Internal Note, INDET-NO-028 (Oct 1993).

[55] C. Augier, *et al.*, *Predictions on the Total Cross Section and the Real Part at LHC and SSC,* Phys. Lett. **B315**, 503 (1993).

[56] R.J. Hawkings and A.R. Weidberg, *TRD Occupancies,* ATLAS Internal Note, INDET-NO-026 (1993).

[57] G. Lindström, *Silicon Lifetime Limits,* RD2 Internal Note, SITP-NO-097 (1993).

[58] D.E. Groom, *Flux, Current, and Lambert's Law,* Appendix 9 in *Report of the Task Force on Radiation Levels in the SSC Interaction Regions,* ed. D.E. Groom, SSC Central Design Group Report SSC-SR-1033 (1988).